2009

Numerical investigation of film cooling fluid flow and heat transfer using large eddy simulations

David Houston Leedom
Louisiana State University and Agricultural and Mechanical College

NUMERICAL INVESTIGATION OF FILM COOLING FLUID FLOW AND HEAT TRANSFER USING LARGE EDDY SIMULATIONS

A Thesis

Submitted to the Graduate Faculty of the
Louisiana State University and
Agricultural and Mechanical College
in partial fulfillment of the
requirements for the degree of
Master of Science in Mechanical Engineering

in

The Department of Mechanical Engineering

by
David Houston Leedom
B.S., Louisiana State University, 2007
May 2009

Dedication

To my parents and everyone else along the way who have provided me with inestimable assistance in terms of encouragement, discipline, examples set, sage advice, money, and time.

Acknowledgements

I gratefully acknowledge the financial support of the Clean Power and Energy Research Consortium (CPERC, funded through the State of Louisiana) and the financial support of the United States Air Force Office of Scientific Research (AFOSR). Additionally, I would like to thank the Louisiana Board of Regents for their support in the form of a generous fellowship. The extensive computations would not have been possible without resources made available by the LSU Center for Computation and Technology (CCT), LSU Information Technology Services (ITS), and the Louisiana Optical Network Initiative (LONI); these resources are greatly appreciated.

I would also like to thank Ashoke De and Somnath Roy for their assistance in learning the code, as well as the rest of the guys in the office (Timur and Anvar Gilmanov, Kedar Jathar, Prasad Kalghatgi, and Hessam Babaee) for being available for explanations and discussions.

Finally, I'd like to thank Dr. Sumanta Acharya for providing me with the resources and information necessary to do this research.

Table of Contents

Abstract

Large eddy simulations of film cooling from discrete holes inclined at 35° with a feeding plenum chamber are performed at a density ratio of 2 and blowing ratios from 0.5 to 2.0 in order to gauge the suitability and performance of different hole shapes. Cylindrical holes at length to diameter ratios of 1.75 and 3.5 as well as shaped holes (laterally diffused and console holes) at a length to diameter ratio of 3.5 are simulated issuing into a laminar crossflow at a Reynolds number of approximately 16,000 based on freestream velocity and hole diameter. The domain extends 15 hole diameters downstream of a single coolant hole, and periodic boundary conditions on the lateral faces of the domain are used. The results are validated in terms of the flow field and surface adiabatic effectiveness to experiments for cylindrical hole cases. Horseshoe vortices, DSSN vortices, and hairpin vortices are resolved and isolated. Jetting is found to have significant effects on effectiveness in cylindrical hole cases (with less jetting at the exit plane and better cooling performance from the longer holes) and shaped hole cases (with a laterally split jetting action occurring around a central recirculation region). The performance of the shaped holes is dramatically better than the performance of the cylindrical holes in terms of surface adiabatic effectiveness, with the console holes performing slightly better than the laterally diffused holes. In terms of aerodynamic loss, the console and cylindrical hole far outperformed the laterally diffused hole.

1 Introduction

1.1 Film Cooling

Increasing the efficiency of a gas turbine engine can have benefits in terms of saved money, reduced environmental emissions, and performance (increased range and power in an aircraft application). By a thermodynamic analysis of the Brayton cycle, one can show that increasing the temperature at the turbine inlet yields higher efficiency. Even modest increases in efficiency (on the order of one percent) can have a significant economic impact when spread over an entire airline fleet or a power generation facility. While increasing the turbine inlet temperature, one must be careful to avoid the destruction of the turbine section via thermal material failure. Many techniques have been developed to protect the blades and vanes of the turbine from hot gases; these techniques include coatings, blowing cool air through internal blade passages to dissipate heat, and blowing cool air out over the surface of the blade to form a protective layer. The last technique is known as film cooling.

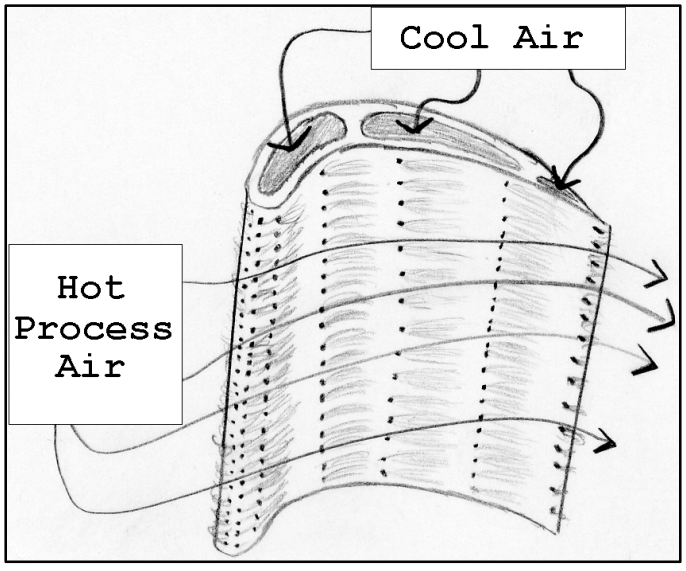

Figure 1.1: Illustration of film cooling on the surface of a turbine blade

The objective of film cooling is to inject just enough coolant to evenly thermally protect the surface; excess coolant causes losses due to cooling of the hot process air, losses in aerodynamic efficiency from the slowing of the air over the blade, and losses from the energy required to compress the film cooling air in the compressor section. Film cooling would be most efficiently implemented via a porous surface that effuses just enough coolant at every point to keep the surface cool. Since such a porous material is not suited for making a turbine blade, another efficient possibility is a two-dimensional, spanwise slot that would effuse cooling air evenly over the area behind it. The difficulty with this arrangement is structural, that is, how to support each chordwise section of blade independently. For this reason, several rows of discrete cooling holes are spaced along the span of a blade in an attempt to replicate the performance of a slot.

The simplest geometry to create for a film cooling hole is a cylindrical hole with constant cross sectional area. This geometry, while easy to drill, is not the optimum arrangement to thermally protect the area behind the hole. The cooling jet is prone to blowing off of the surface and otherwise providing a nonuniform film behind it. Slightly changing the shape of the hole can allow the discrete holes to provide a more efficient film. These non-cylindrical holes are known as shaped holes. The search for a hole shape that is manufacturable, structurally sound, and more efficient is ongoing.

The shapes that are currently state of the art are holes that act as diffusers toward their exits in order to lower the vertical momentum of the jet and provide a more even coating of cool air on the surface. One problem with this arrangement is that the aerodynamic losses (excess drag on the blade due to injection of a significant amount of slowly moving coolant air) from the diffused holes take back some of the efficiency gained by film cooling in the first place. Modern

manufacturing techniques allow shapes that are even more complex and possibly more efficient than the industry standard expanded exit holes (see Figure 1.2 for examples).

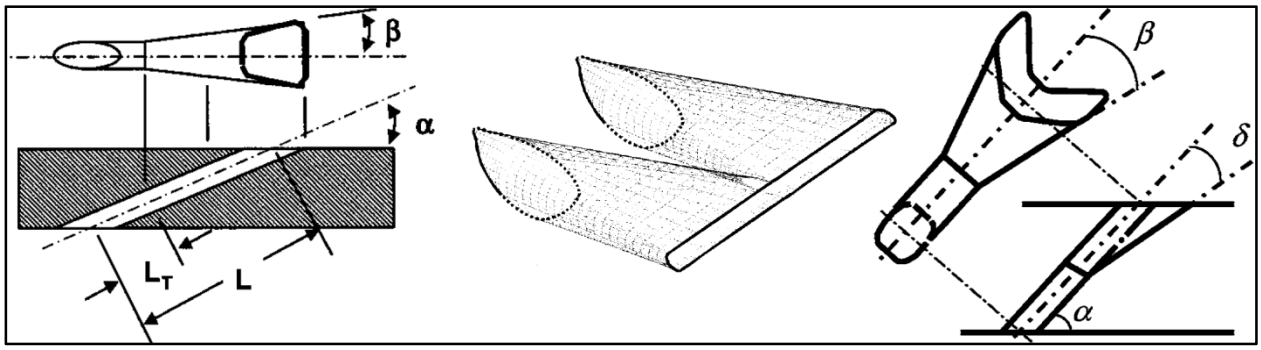

Figure 1.2: Industry standard expanded exit hole (left, Bunker 2005), Console holes (middle, Sargison et al. 2002a), and arrowhead shaped holes (right, Okita and Nishiura 2007)

Since direct, accurate observation of the film in an operating gas turbine is difficult, hole shapes are studied in simulated conditions. One can perform physical experiments at representative operating conditions or perform numerical simulations. The experiments and simulations are often simplified or ideal arrangements, such as observing a single cooling hole instead of a row, or ignoring the difference of density between the coolant jet and the crossflow. As long as the important phenomena are captured in the experiment or simulation, usable data to gauge the performance of a hole geometry can be gleaned.

1.2 Large Eddy Simulations

Large eddy simulation (LES) is a numerical modeling technique for solving the Navier-Stokes equations which govern fluid flow. In contrast to the Reynolds Averaged Navier-Stokes (RANS) technique (which averages fluctuations in the flow temporally), LES filters fluctuations spatially. This allows LES to fully resolve fluctuations larger than the filter width (in this study, the grid

spacing) and model the effects of smaller fluctuations via a sub-grid scale model. In this study, LES will be used to investigate film cooling.

The advantage of LES is that it is a middle ground between RANS and Direct Numerical Simulation (DNS). RANS predicts all of the turbulence in a flow using a turbulence model, while DNS fully resolves all of the important scales of turbulence down to the Kolmogorov scales (where the turbulence is dissipated into thermal energy). RANS is much less computationally expensive than DNS, but provides much less accurate results. LES is a middle ground because it resolves the fluctuations to the extent made possible by the grid and only models the smallest fluctuations (which are more universal in nature, and therefore more easily modeled). Thus, the turbulence which affects the flow the most is resolved with LES without the intensely fine grid requirements of DNS.

1.3 Outline of Thesis

- Chapter 1 provides a basic introduction to film cooling and LES in the context of this study.
- Chapter 2 provides insight into the state of the art (via discussions of other published works) and motivations for this study.
- Chapter 3 is a study of flow fields and effectiveness from shaped and cylindrical holes with length to diameter ratios of 1.75 to 3.5, a density ratio of 2, and varied blowing ratio.
- Chapter 4 is a previously published LES film cooling flow field study examining cylindrical and shaped holes with higher length to diameter ratios (L/D = ~5).

2 Literature Review

2.1 Film Cooling

Film cooling from a tangential slot is ideal, but rows of discrete holes are used because the continuous slot does not provide adequate structural strength (Bunker 2005). As little cool air as possible should be added to the mainstream flow; if too much is added, the loss of process air and the added aerodynamic losses from the coolant air would outweigh the advantages of the higher turbine inlet temperature (Walters and Leylek 2000b). When discrete coolant injection holes are used, hole shape can have a significant effect on the quality of the film effused and the extent to which the film thermally protects the surface of the part. Many shaped hole geometries have been investigated including the industry standard laterally and/or longitudinally diffused holes, trenched holes (Waye and Bogard 2007), arrowhead shaped holes (Okita and Nishiura 2007), holes with leading edge tabs (Nasir et al. 2003), and console holes (Sargison et al. 2002a). A review paper by Bunker (2005) gives a general overview of the state of the art.

2.2 Flow Field Features

The behavior of film cooling holes and the more general case of a jet in crossflow have been studied for many years. These flows are typically characterized by a series of coherent flow structures that contribute to the mixing process.

For a round, laminar jet in crossflow (low Reynolds number), the counter-rotating vortex pair (Cortelezzi and Karagozian 2001) is the dominant feature in the flow field downstream of the jet. It is illustrated in Figure 2.1. The time-averaged flow field still exhibits this counter-rotating vortex pair in the case of the round, turbulent jet in crossflow (high Reynolds number), but the unsteady nature of the jet is complex. Many distinct features of the instantaneous flow field have been isolated and are discussed here.

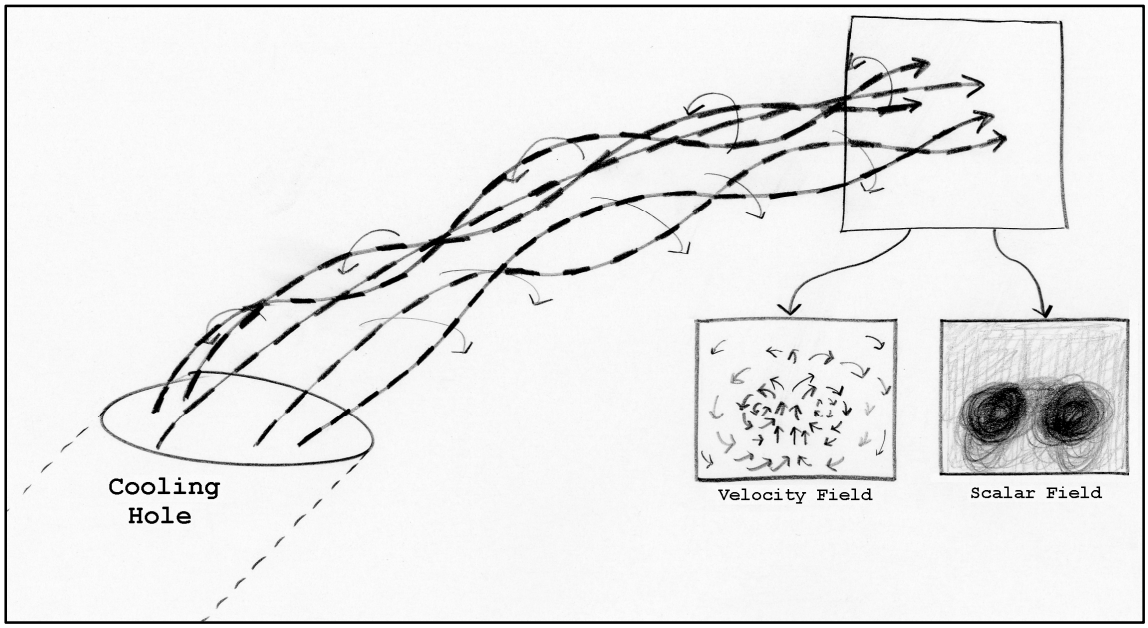

Figure 2.1: Conceptual illustration of the counter-rotating vortex pair

The horseshoe vortex is a recirculation in front of the effused jet whose vorticity is perpendicular to the flow. The vortex extends laterally and its vorticity curves around the leading edge of the hole and turns parallel to the flow near the surface. Figure 2.2 shows the recirculation associated with the front of the horseshoe vortex, and Figure 2.3 shows the vortex wrapping around the front of the cooling hole and extending in the streamwise direction.

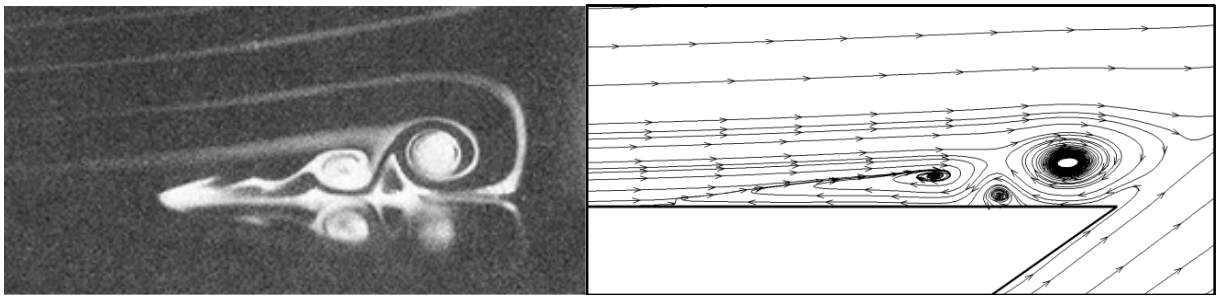
Figure 2.2: Horseshoe vortex, centerline visualizations of streamlines, experimental on the left (Baker 1991), simulation from the current study on the right

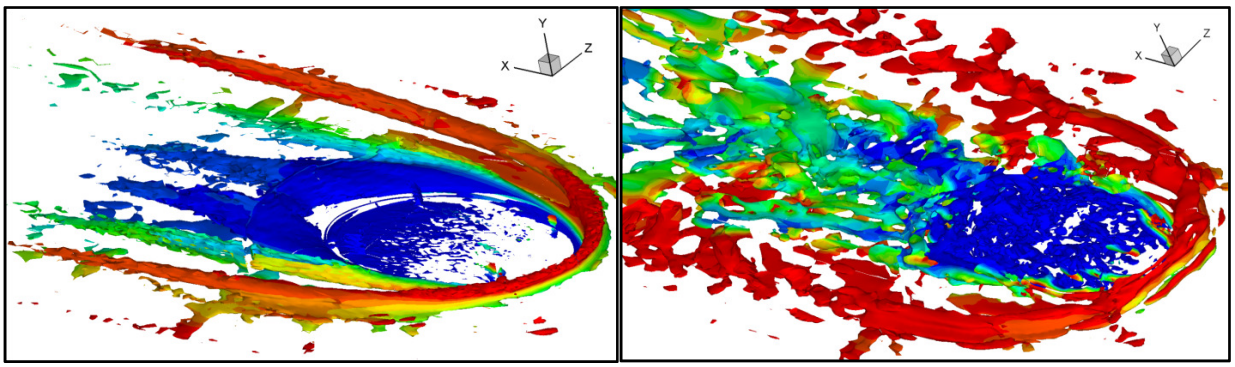

Figure 2.3: Horseshoe vortex visualizations (Laplacian of pressure) for a round jet in crossflow simulation in the current study, time averaged on the left and instantaneous on the right

The downstream spiral separation node (DSSN) vortices are associated with jet blow-off and recirculation behind the effused jet. The DSSN vortices can be described as recirculation regions behind the cooling hole which are quite close to the surface and have vorticity in a direction normal to the surface. Figure 2.4 shows the recirculation region behind the jet in the centerline plane of a simulation. As shown in Figure 2.5, taking a slice of a flow field with this sort of blow-off parallel to the surface through this recirculation will show DSSN vortices.

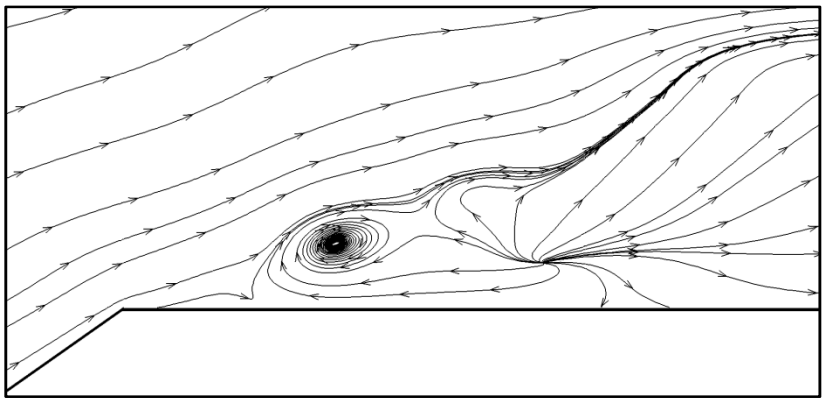

Figure 2.4: Streamtraces in a centerline slice of an instantaneous flow field showing jet blow-off and recirculation behind a round cooling hole in the current study

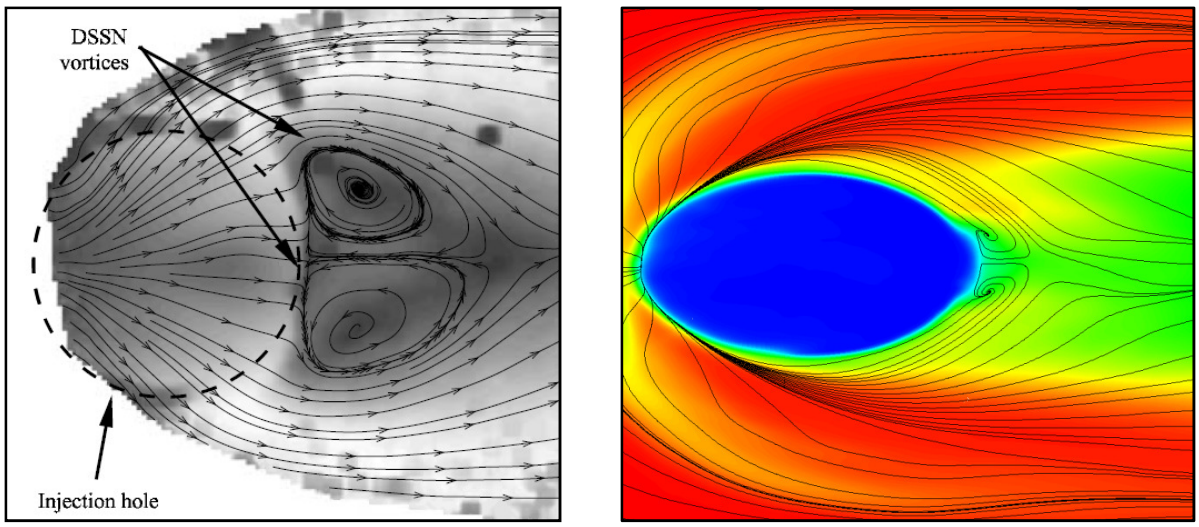

Figure 2.5: DSSN vortices as illustrated by streamlines in a plane close to the cooled surface by Peterson and Plesniak (2004, left, vertical jet), and the present study (right, 35° jet)

Hairpin vortices are periodic vertical structures observed in effused jets in crossflow (Tyagi and Acharya 2003). Figure 2.6 illustrates these structures and shows their distinctive shape. A conceptual model put forth by Morton and Ibbetson (1996, shown in Figure 2.7) shows one possible mechanism for the creation of such a vortex. The "legs" of these hairpin vortices affect the surface temperatures because their circulation pulls hot fluid from the crossflow underneath the vortex and toward the centerline of the jet. This entrainment is detrimental to film cooling performance.

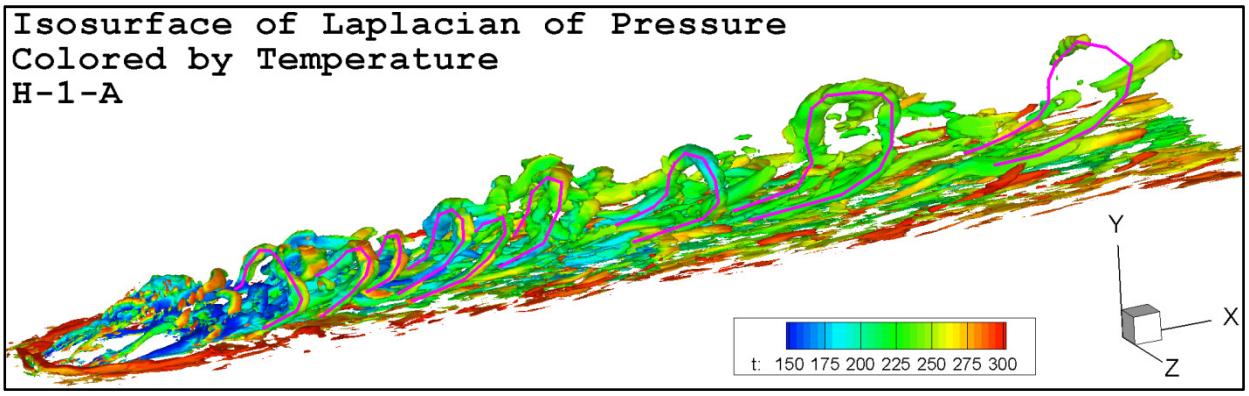

Figure 2.6: Hairpin vortices as observed in the current study colored by temperature and highlighted in purple

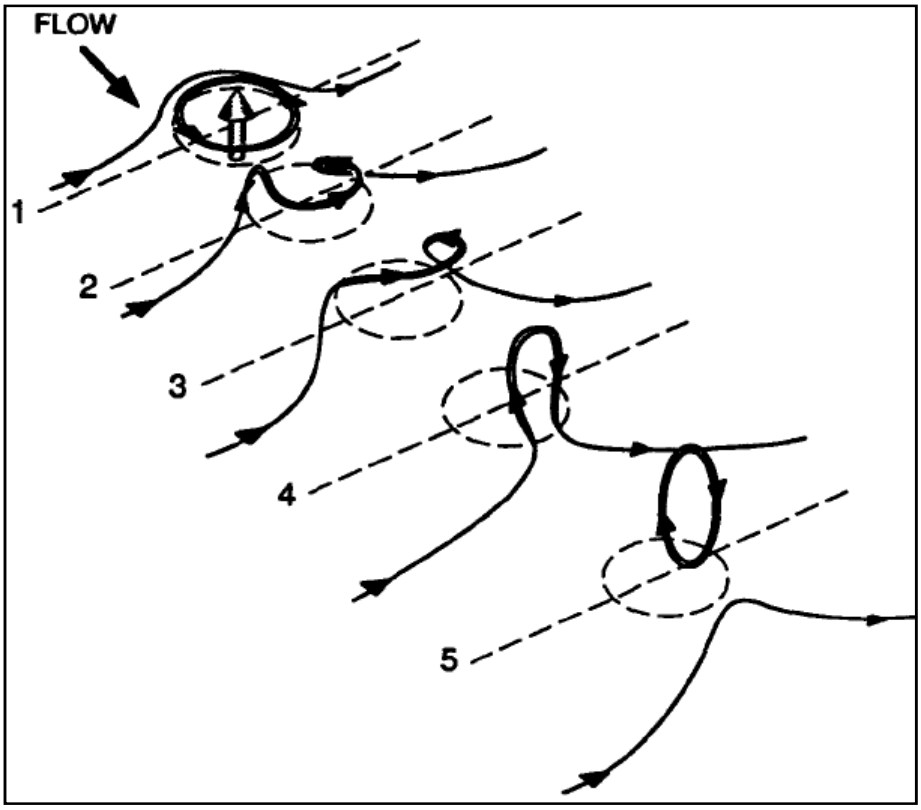

Figure 2.7: Conceptual model by Morton and Ibbetson (1996) showing filaments of vorticity and how they are folded to create the hairpin vortex shape

2.3 Large Eddy Simulations

Large Eddy Simulations (LES) were first suggested by Smagorinsky (1963) for use in weather simulations. Turbulence modeling via the Reynolds Averaged Navier-Stokes (RANS) equations has been extensively used to predict the behavior of turbulent fluid flows. RANS filters the Navier-Stokes equations in time, while LES filters them spatially. A key mathematical identity was presented by Germano, et al. (1991); this identity provides a way to use two different filters to provide a better guess at the Smagorinsky constant at any given location in a flow. Before this, the Smagorinsky coefficient was typically held constant over the flow domain, leading to errors in the calculation of eddy viscosity. LES, by resolving the larger eddies in the flow, can be viewed as a middle ground between RANS (which models all turbulence) and Direct

Numerical Simulation (DNS, which resolves all turbulence down to the Kolmogorov scales where the fluid motion is dissipated into heat). As computers become more powerful, LES becomes more practical as an alternative to RANS.

2.4 Results in Open Literature

This section details some of the prominent studies done on film cooling using LES and the experimental studies used as benchmark validation cases for these studies. The studies are arranged by type (experimental, RANS, LES, DNS, etc.) in approximate chronological order. Studies of holes and hole shapes with a relatively short length to diameter ratio (less than about 4), moderate blowing ratios (.2 to 1.5), inclination angles of about 35°, and which include a feeding plenum chamber are included. LES results should provide more and better information than RANS studies to justify the extra computational effort required compared to turbulence modeling.

2.4.1 Experimental Studies

Pietrzyk et al. (1989) utilize particle image velocimetry (PIV) to describe the flow field associated with a film cooling flow (including a feeding plenum chamber). Mean flow field quantities as well as turbulence statistics are presented for a row of jets at a Reynolds number based on hole diameter and freestream flow conditions of about 16,000. The results from blowing ratios of 0.25, 0.5, and 1.0 for cylindrical holes inclined at 35° with a pitch of 3 hole diameters are reported, and the density ratio for each case is unity. The measurements are restricted to the centerline plane of the film cooling jet up to 30 hole diameters downstream of the cooling hole row. A correlation between regions of high velocity gradients and high levels of turbulence is made.

The further study of Pietrzyk et al. (1990) expands on the previous study, including further description of the flow field. Scope is broadened to include density ratios up to 2.0 as well as unity. The density ratio was varied to 2.0 by decreasing the temperature of the jet to half the temperature of the freestream air using liquid Nitrogen, thus doubling the density of the jet. Blowing ratios of 0.25 and 0.5 only are presented, again only at the centerline plane of the hole out to 30 hole diameters downstream of the row of holes. A detailed description of the boundary layer upstream of the holes is provided. Dr. Bogard has been gracious enough to share the complete PIV database compiled during this study for use in validation of the current study.

Sinha et al. (1991) uses much the same experimental setup, but measures the surface adiabatic effectiveness downstream of the hole instead of the flow field. A surface thermocouple technique designed to minimize conduction effects from the surrounding surface is used to glean the surface effectiveness data. The paper causes some confusion by reporting in text that the length to diameter ratio of the holes is changed to 1.75 (half that in the previous studies), while reporting in a figure that the length to diameter ratio is 3.5 (as it was in the previous studies). After a telephone conversation with one of the authors, it was determined that the new plate used by Sinha et al. (1991) did indeed have a length to diameter ratio of 1.75. Blowing ratios are varied from .25 to 1.0 for density ratios from 1.2 to 2.0. The changes in blowing ratio are accomplished by changing the jet flow rate, and the changes in density ratio are accomplished via changing the temperature of the jet. Details of the conditions under which the jet blows off of the surface and reattaches are documented, and centerline adiabatic effectiveness data as well as lateral effectiveness profiles and laterally averaged effectiveness are provided out to 60 hole diameters downstream of the hole. This study is frequently used as a benchmark for validation

of other studies attempting to predict surface adiabatic effectiveness for similar operating conditions.

Another pair of studies utilizing the experimental setup of Pietrzyk et al. (1990) involves the measurement of surface adiabatic effectiveness by Schmidt et al. (1996) and surface heat transfer coefficient by Sen et al. (1996) from compound angle holes. Round holes with a length to diameter ratio of 4 and no compound angle were used as a control group. The results, when compared to the surface adiabatic effectiveness data from Sinha et al. (1991) show similar results for centerline effectiveness at low blowing ratios. However, at a higher blowing ratio (1.0), evidence of the distinct jet blow off and reattachment is absent for the longer delivery tube case.

Lutum and Johnson (1999) experimentally study the effects of hole length to diameter ratio on the effused jet's film cooling potential. Length to diameter ratio is varied from 1.75, as employed in the experiments of Sinha et al. (1991), to 18. Thermochromic liquid crystal and a CCD camera are used to deduce the surface adiabatic effectiveness. Longer coolant channels are observed to have better surface film cooling effectiveness properties. The under-performance of the shorter holes is exaggerated at higher blowing ratios.

The study of Sargison et al. (2002a) presents a patented shaped film cooling geometry called a console. The name console is an apt portmanteau of "*con*verging *s*lot h*ole*." The hole begins with a typical round hole profile, then is smoothly lofted into a uniform, thin slot on the surface that intersects the neighboring consoles. Unlike the laterally diffused geometry (which slows the jet through an increase in cross sectional area as it reaches the surface to prevent penetration of the jet), the cross sectional area the console decreases as it approaches the surface. Assuming that the flow is subsonic through the console, this reduction acts as a nozzle and increases the velocity of the coolant jet. This increase in jet velocity is shown to reduce the aerodynamic

losses incurred due to film cooling by providing similar surface coverage to the laterally diffused hole while avoiding the large pocket of slowly moving air that a diffused geometry creates. Cylindrical holes, laterally diffused holes, a uniform slot, and console holes are all experimentally examined in a wind tunnel at a Reynolds number based on hole diameter and freestream velocity of 36,000. The density ratio was less than one, this owed to the fact that hot air was ejected into a cooler mainstream in this particular experimental setup. Comparisons were made between the different geometries by setting the ideal momentum flux ratio equal in each case (which ends up being the same as setting the plenum total pressures equal). Surface adiabatic effectiveness and surface heat transfer are measured via liquid-crystal paint on a uniform heat flux plate controlled by heaters. The authors claim good agreement with previous experimental studies based on results for the round hole only; the agreement is far from definite. Attention is drawn to the fact that the Conada effect helps to keep the cooling jet attached to the film cooled surface after turning the corner out of the console.

A second study of the console geometry Sargison et al. (2002b) uses a different experimental arrangement, this one a nozzle guide vane outfitted with consoles and tested in an environment with engine-representative Reynolds number, Mach number, and density ratio. A further publication Sargison et al. (2005) includes largely qualitative experimental data which characterize the behavior of the effused jets from shaped holes in terms of penetration and aerodynamic losses. Two methods are used to measure penetration: a fine mesh covered with temperature-sensitive liquid crystal and a CO_2 fog in the jet. Both methods utilize a digital camera system and computer program to process the data. No surface measurements are reported. Thermal penetration profiles are similar for the slot and the console, while the cylindrical hole's tendency to blow off of the surface at higher blowing ratios is confirmed.

In the study of Okita and Nishiura (2007), an industrial group at Ishikawajima-Harima Heavy Industries, studies a new film cooling geometry, the arrowhead shaped hole, via experiments and numerical simulations. The experimental investigation is not on a flat plate, but on the suction and pressure surfaces of an airfoil at engine-representative Mach number and Reynolds number. The control in the experiment is a laterally and forward diffused hole geometry. The surface effectiveness data is gleaned via a mass transfer analogy by using photoluminescent paint sensitive to the partial pressure of Oxygen, then using pure Nitrogen as coolant and air in the freestream. The estimated error of this method is claimed to be 9%; no comparison to other published data is attempted. This arrowhead geometry is of particular interest to the present study because it has some of the same characteristics as the console such as a slot shaped exit (albeit one bent into an arrow shape) and a smaller cross-sectional area than typical diffused exit shaped holes. Further, some results of the present study suggest that film penetration at the edges of the console hole (where it meets the next hole at the surface) is excessive, and the arrowhead shape may help to mitigate this tendency, helping to economize the use of coolant.

Nasir et al. (2003) investigate the effects of leading edge tabs experimentally. Different tab orientations are investigated, and some exit velocity profiles are shown to quantify the changes in the flow field. Downstream surface effectiveness data is collected; this data shows that horizontal and downward angled tabs increase the film cooling effectiveness downstream of the hole. It is noted that the tab would not fare well in actual film cooling applications. The tab is only presented as an example of how the flow field can be positively manipulated.

A set of studies, an experimental investigation by Dhungel et al. (2007) and a RANS investigation by Heidmann and Ekkad (2008), describe the performance of the same novel film cooling configuration. These two studies utilize anti-vortex holes, a pair of smaller holes that

begin in the injection tube and intersect the surface in front of and on both sides of the otherwise conventional cylindrical hole. Experiments are performed for several permutations of the anti-vortex hole. Some favorable configurations are suggested in the experiments in terms of heat transfer coefficient and surface adiabatic effectiveness. The RANS investigation details the vorticity downstream of the hole, but provides poor validation to the experiments.

Thole et al. (1998) investigate the flow fields from shaped and round holes in a high-speed wind tunnel (Mach number .25-.3). One notable feature is that the inlet to the coolant hole is also a high-speed crossflow aligned with the mainstream flow. Validation to the data of Pietrzyk et al. (1989) is provided for a plenum crossflow velocity of zero. LDV is used to examine the flow field. Contours of the first and second order statistics of velocity are presented inside the coolant delivery tubes and downstream of the injection. Regions of maximum turbulence are shown to be at the jet exit in the case of the diffused geometries, but for the cylindrical case the maximum turbulence levels occur downstream. Gritsch et al. (1998) use the same experimental arrangement, but this time with modifications to control jet temperature and measure surface adiabatic effectiveness (via infrared cameras and thermocouples) at high Mach numbers (.6 - 1.2). Effects on the effused jet's surface adiabatic effectiveness field of crossflow at the hole inlet and its orientation to the coolant hole are illustrated via contour plots. It is noted that at transonic velocities, the coolant jet has markedly different characteristics than for the subsonic case.

A study of several diffused hole shapes Gritsch et al. (2005) is performed by one of the same individuals as the previous study and another group. 20 various combinations of lateral diffusion and forward diffusion angles are examined in a wind tunnel at a freestream Mach number of .3 with an infrared camera. Hole pitch is varied (from 4 to 8 hole diameters), as well as hole length

(from 7.5 to 11.5 hole diameters) and compound angle. Density ratio is 1.7, and blowing ratio is varied from 0.5 to 2.5. Length to diameter ratio is reported to have only a "small" effect on the effused jet's cooling effectiveness, but no "short" cooling holes are included in the study. Most hole geometry changes are reported to have only a "weak impact on laterally averaged film cooling effectiveness," which is not surprising considering the small changes in geometry considered in the study.

Baldauf et al. (2001) experimentally investigate surface adiabatic effectiveness. Local surface temperature data downstream of a row of inclined, cylindrical, six diameter long holes is collected using Infrared thermography calibrated with surface thermocouples. The material used for the test plate has a low thermal conductivity, and a finite-element solver makes corrections for conduction errors. Approximations of the effects of radiative heat transfer are made and applied to the data as well. Data is collected for a variety of different hole pitches (2, 3, and 5 hole diameters), and indicates that beyond a pitch of five hole diameters the jets have negligible interaction. The lowest angle holes (30°) have the best film cooling performance, which is no surprise as the shallower the injection angle, the closer to tangential blowing the case becomes. Optimum blowing ratio is reported to be unity or slightly lower.

The study of Saumweber et al. (2003) is a similar study, but this one investigates shaped holes, higher freestream turbulence intensity levels, and measurements of surface heat transfer. Freestream turbulence is detrimental to surface effectiveness at lower blowing ratios, but enhances it at higher blowing ratios for the round holes. Freestream turbulence is detrimental to surface effectiveness at all tested blowing ratios for the shaped (diffused) holes. Increasing the integral length scale by 66% caused a small positive change in surface effectiveness. Forward diffusion of the hole shape is not reported to have any advantage over the shaped hole with only

lateral diffusion. This observation lends some weight to the claims in the console hole papers that the Conada effect helps to "turn the corner" at the top of shaped holes with lateral diffusion (such as the console hole). A follow-up study by Saumweber and Schulz (2004) similarly investigates the effects of a second row of shaped holes.

An investigation into freestream effects Saumweber and Shulz (2008c) yields an important insight into the function of the fan shaped hole. A separation region in the center of the downstream wall of the diffuser is observed computationally and experimentally to split the coolant jet and effuse a non-uniform lateral velocity profile. This profile, which features decreased coolant flow at the center plane and increased flow at the lateral edges, has been observed in the current study for the laterally diffused and the console holes. The study also investigates how the effused profile changes at high Mach numbers and with changes in freestream turbulence intensity. Another similar study, Saumweber and Schulz (2008a), details the effects of plenum crossflow on the flow inside the delivery tube and in the effused jet. Fluent RANS results and experiments are used, but not extensively validated against each other. Cylindrical holes and laterally diffused holes are observed. Asymmetric surface film cooling effectiveness fields are observed experimentally and computational studies indicate that the vortex pair usually observed in the delivery tube is replaced by a single swirling vortex at higher plenum crossflow velocities.

Saumweber and Schulz (2008b) detail the effects of geometry changes on a laterally diffused geometry and a cylindrical geometry. The "bimodal effectiveness pattern" resulting in decreased effectiveness at the center of the jet effused from the laterally diffused holes is noted to be less prevalent at lower diffuser angles. The effects of hole inclination angle are also discussed.

The study of Jumper et al. (1991) is notable because it attempts to study the effects of high (14-17%) freestream turbulence levels on an effused jet in crossflow. A wall jet is used to create the turbulent crossflow, which is blown over a row of coolant holes. For lower Reynolds number cases (Re_D=~20,000), it is noted that in the near field (less than 20 hole diameters downstream of the injection holes) the high freestream turbulence (17%) cases outperform other studies with lower freestream turbulence in terms of surface adiabatic effectiveness close to the holes (x/d<20). Farther from the holes, the surface adiabatic effectiveness of the jet tended to decay with distance faster than the low turbulence cases. The higher Reynolds number cases (Re_D=~85,000) with high freestream turbulence have dramatically lower performance in terms of surface adiabatic effectiveness than other studies performed with less freestream turbulence over the entire cooled domain. The results indicate that at higher freestream turbulence levels, Reynolds number is a very important factor in determining film cooling performance.

Ekkad et al. (1997) measure surface film cooling effectiveness and heat transfer effects from compound angle, round holes. A "transient liquid crystal technique" is used to deduce the surface heat transfer and adiabatic effectiveness downstream of the hole with a freestream turbulence level of 8.5 percent. A blowing ratio close to unity is found to provide the best film cooling effectiveness for the zero compound angle holes inclined at 35° to the surface. The Reynolds number based on hole diameter is notably low, 2500.

2.4.2 RANS Studies

Walters and Leylek (1997) begin a set of computational studies using turbulence modeling in a commercially available flow solver (Fluent RAMPANT). The grids used are unstructured, tetrahedral meshes mimicking the details of conditions (blowing ratios and density ratios) and geometries simulated by Pietrzyk et al. (1990) and Sinha et al. (1991) as discussed in this thesis. Adaptive mesh refinement methods (adding increasing refinement in areas with high gradients)

were used to generate meshes containing approximately 200,000 cells. The computational domain extended downstream of the hole to 15 hole diameter. Two geometries are used, one with a length to diameter ratio of 3.5 and one with 1.75. The jetting effect in the coolant delivery tube due to the sharp transition from the plenum to the tube is described. Details of the differences in the flow fields in the coolant delivery tube between the two geometries are discussed. Farther from the hole (over 10 hole diameters downstream), the surface adiabatic effectiveness is well predicted, but the blow off and reattachment effects closer to the hole at higher blowing ratios is not captured.

The previous study begins a four-part series addressing film cooling using the Fluent RAMPANT code and turbulence models. The first study in the series by Walters and Leylek (2000a) includes details of the same geometries and operating conditions as Walters and Leylek (1997). A two-layer model is used in addition to the wall function methodology from the previous paper. The two-layer model successfully resolves some of the jet blow off and reattachment effects (along with a pocket of reversed flow directly behind the coolant jet) and brings the surface adiabatic effectiveness plots closer to the experimentally measured values in the near field, but still leaves much to be desired in this respect.

McGovern and Leylek (2000) use the same Fluent code to analyze compound angle holes at higher blowing ratios (1.25 to 1.88) and at a density ratio of 1.6. No validation to experiments is provided for the compound angle holes, and compound angle holes are beyond the scope of this study.

The third study in this series is by Hyams and Leylek (2000) and is of special interest because it deals with the same subject matter as this thesis – comparisons of shaped film cooling geometries via computational methods. The same Fluent code is used in this study, with density

ratios of 1.6 and blowing ratios of 1.25 to 1.88 in most cases. Forward diffused holes, laterally diffused holes, cylindrical holes with shaped inlet regions, and cusp-shaped holes are compared to the plain cylindrical geometry. Validation to experimental data generated by Schmidt et al. (1996) for the surface adiabatic effectiveness is provided for the cylindrical hole for two blowing ratios and shows reasonable agreement. Details of the flow field and plots of the surface adiabatic effectiveness and heat transfer are shown. A discussion of induction lift and its effect on the design of shaped film cooling holes is provided.

Brittingham and Leylek (2000) investigate shaped geometries combined with compound angles. Validation to experimental data generated by Schmidt et al. (1996) for the surface adiabatic effectiveness is provided for the cylindrical hole and forward diffused hole and shows reasonable agreement.

This series of studies lays a framework for a successful computational study of shaped film cooling holes. It was discussed here because the present study is of the same vein, but uses an in-house code instead of Fluent, slightly different geometries, and large eddy simulations instead of RANS.

Jones et al. (2005) investigate the suitability of turbulence modeling (specifically, a four equation model) for film cooling simulation. The turbulence model is first validated with respect to flow field via comparisons to experimental data. The effects of a variable Prandtl number are investigated in terms of agreement with experimental jet temperature data and surface temperature data.

The console geometry is investigated in a computational study by Azzi and Jubran (2007) utilizing a two-layer, anisotropic RANS turbulence model. Good agreement is shown with the laterally averaged surface effectiveness data and the spanwise surface effectiveness data by

Sinha et al. (1991) for the cylindrical hole. Little in-depth analysis of the flow fields is performed, but a tendency of the jet effused from the console hole to penetrate the crossflow excessively where the jets from two adjacent consoles meet is shown. No comparisons to data from the experiments of Sargison et al. (2002a) are included. This is possibly due to the differences in geometry (most notably length to diameter ratio of the holes) and operating point (Azzi and Jubran (2007) set the blowing ratio, while Sargison et al. (2002a) set the ideal momentum flux ratio).

2.4.3 LES Studies

Tyagi and Acharya (2003) perform LES of film cooling, but utilize a different code than is used in the present study. Differences include that the code is a serial code (as opposed to Chem3D's multiblock, parallel implementation), the code is fourth-order accurate in space and third-order accurate in time (as opposed to Chem3D being second-order accurate in space and time), the code uses a dynamic mixed model for the computation of subgrid stresses (as opposed to Chem3D's use of a dynamic Smagorinsky model), and that the code is incompressible with a scalar transport equation (as opposed to Chem3D's compressible solver.) To prevent the number of unused grid points in the calculation from becoming unmanageable, the grid only extends down the delivery tube one hole diameter (with the bottom of the domain parallel to the exit plane). Inlet conditions from a RANS calculation are used at the bottom of the flow domain, and a random perturbation generator is used to generate the turbulence for the delivery tube inlet. Validations of velocity profiles as well as centerline surface adiabatic effectiveness profiles are presented. Coherent structures are plotted and the temporally averaged behavior of the counter-rotating vortex pair is traced back to the legs of hairpin vortices. Roller vortices and upright wake vortices are also identified. Instantaneous distributions of wall adiabatic effectiveness are examined.

Iourokina and Lele (2005) begin a series of studies by introducing a two-code approach to large eddy simulations of film cooling. A compressible, fourth-order code based in Cartesian coordinates is used in the region outside the delivery tube, while a low Mach number, second-order accurate code based in cylindrical coordinates is used in the delivery tube and cylindrical feeding plenum chamber. The dynamic Smagorinsky model (the same model used in Chem3D) is used in the subgrid scale modeling for both codes. The delivery tube, plenum chamber, and crossflow are all independent domains linked together by overlapping grids. The solutions at each time step are forced (by interpolation from one grid to the other and vice versa) to match in the intersecting volumes. The method is tested on various benchmark problems, including a convecting Taylor vortex, flow over a flat plate, and a normal jet in crossflow.

Iourokina and Lele (2006a) continue with a study in which an implementation of the spatially developing turbulent boundary layer presented by Lund et al. (1998) is incorporated into the two-code approach for the simulation of freestream turbulence. The experimental setup of Pietrzyk et al. (1989) is simulated in order to provide validation of the flow field. A density ratio of .95 and a blowing ratio of .7 are used to allow comparison to both the flow field data of Pietrzyk et al. (1989) and the heat transfer data with high freestream turbulence of Bons et al. (1996). Details of the flow field are discussed, but no significant surface effectiveness or heat transfer data is presented. The crossflow domain is limited to a very small region outside of the cooling hole, only 5 hole diameters long in the flow direction total. The group continues with another study by Iourokina and Lele (2006b) which includes more examination of the flow field characteristics for the small domain and an attempt at validation of the centerline surface heat transfer data to Sinha et al. (1991) at a low blowing ratio without significant jet detachment.

Peet and Lele (2008) further examine the flow field. This analysis is carried out accompanied by extensive validation of the flow field (including both first and second order statistics) to experiments done by Pietrzyk et al. (1990). Comparisons of film cooling effectiveness to the experiments of Sinha et al. (1991) are made with good results in the near field (up to three hole diameters downstream of the hole). Over two million cells are used in the small crossflow region simulated indicating that something close to direct numerical simulation (DNS) with the fourth-order scheme is taking place. Because the filter width is dependent on the grid spacing, smaller scales of turbulence are being resolved when the grid spacing is smaller. If the Kolmogorov scales (the scales at which the fluctuations are dissipated into heat) are resolved, the simulation is indeed doing DNS.

The results of this group are important to this study because Chem3D also uses the dynamic Smagorinsky model for LES, and the goals of this study are certainly aligned with the present study. The use of three separate domains and two separate codes certainly provides some contrast. The higher order of accuracy of the discretizations used in this group's work is also to be highlighted against Chem3D and the code used by Renze et al. (2008a), both of which are only second order accurate.

The LES study of Guo et al. (2006) simulates two simple geometries, a normal jet in crossflow and a 30° inclined jet in crossflow. Both jets are issued through a plate 12 hole diameters thick with a feeding plenum chamber at the bottom. Two blowing ratios (.48 and .1) are simulated, and no mention of density ratio is made (which leads the reader to suspect that it is unity). A spatially developing turbulent boundary layer simulation is carried out independently from the jet simulation and is used to generate turbulent inlet boundary conditions via the method of Lund et al. (1998). The flow fields are examined in detail, but not compared to any

other studies. The paper appears to be a proof of concept for the LES code and implementation of the turbulent inflow generation procedure for a film cooling geometry.

Renze et al. (2007) utilize the same code and spatially developing turbulent inlet boundary conditions, but this time simulate an inclined hole and a shaped hole (laterally and forward diffused) at a single blowing ratio (.43) and density ratio (1.53, consistent with CO_2 injected into air). The length to diameter ratios were still very large in this case, owing to the 12 hole diameter thick plate simulated. Comparisons of the mean velocity and second order statistics of velocity are made to an experimental study and show good agreement. Results of surface adiabatic effectiveness are plotted using the mass transfer analogy and plotting the mixture fraction of CO_2. Results are claimed in text to corroborate cited experimental investigations, but no data from the experimental investigations is presented as a benchmark to validate.

Renze et al. (2008a) present validation of many cases, beginning with a propane-burning combustor using the same code that is later used for film cooling. Large eddy simulations for a cylindrical hole at blowing ratios from 0.15 up to 0.5 with density ratios of unity and 1.53 are performed. Validation to an experimental PIV study is provided and shows good agreement for first and second order statistics of velocity. The impact of the varied velocity ratio and density ratio are investigated in some detail, with basic physics of the jet in crossflow being the chief subject of discussion. A comparison to the experimental work of Sinha et al. (1991) is made, but with a different blowing ratio and different geometry than the experiments. Renze et al. (2008b) appear to present results quite similar to Renze et al. (2008a). The newer study focuses strictly on the cylindrical hole presented in the previous studies using the same code as the previous studies. No distinctly new data is presented, save a comparison of surface adiabatic effectiveness to the data of Sinha et al. (1991) for a blowing ratio of 0.5. This comparison is highly suspect

first because of the much longer coolant delivery tube, and second because the blowing ratio is not the same (0.43 versus 0.5).

This group's work is meaningful to the present study for several reasons. This group uses LES in a parallel, multi-block, curvilinear mesh, second-order accurate code which uses an implicit, dual-timestep solution algorithm with the recycling turbulent inlet as specified by Lund et al. (1998) to study film cooling from cylindrical and shaped holes. This is all the same as the present study. Differences are that Chem3D utilizes a different convective scheme (weighted essentially non-oscillating as opposed to their advective upstream splitting method), a different implementation of LES (a dynamic Smagorinsky model as opposed to their MILES technique), and a different temporal differencing method (Adams-Bashforth as opposed to their five-step Runge-Kutta method).

2.4.4 DNS Studies

Muppidi and Mahesh (2005) study a normal cylindrical jet in crossflow using DNS. Important flow features are investigated including the horseshoe vortex, hovering vortex, and jet exit profile. Effects of crossflow profile and velocity ratio (equal to blowing ratio in this case at density ratio unity) on these features are presented. A scaling law for the jet trajectory is presented, but has little use for film cooling operations. The next study by Muppidi and Mahesh (2007) involves DNS of a normal, round jet. More discussion of jet exit profile (first and second order statistics) and condition are presented.

Muppidi and Mahesh (2008) simulate not only the flow field, but also the transport of a scalar in a normal, round jet. The jet is at a very high blowing ratio (5.7) making the results of the study of limited usefulness to the present study. There is a discussion of counter-gradient diffusion due to pressure gradients that could possibly be exploited to increase performance in film cooling applications.

2.5 Motivation and Goals

Computational tools are needed to help understand flow physics in order to improve film cooling performance and efficiency. Because RANS has not been shown to provide precise, accurate predictions of film cooling performance (as evidenced in the literature review), LES and DNS are looked to as more accurate tools for numerical investigations. While DNS is by definition more accurate than LES (because it uses no subgrid scale model and resolves all important scales of turbulence), its burdensome computational cost makes it impractical. LES is therefore presented as a middle ground that provides better results at an acceptable computational cost. The flow physics of jets issued from shaped cooling holes are not well understood, with the experimental studies mostly focusing on surface temperature measurements. At this point, most open-literature CFD studies of shaped holes utilize RANS. There are few LES studies of shaped holes, and there are no LES studies of console holes save those presented in this thesis. Motivation for this study stems from the need to better understand the flow physics of jets issued from shaped film cooling holes and the desire to comparatively study cylindrical and shaped holes on an equal footing.

The goals of this study are to modify and use the Chem3D code with LES to:

- Help establish LES as a useful tool in the study of film cooling
- Perform a systematically validated LES study for cylindrical holes
- Provide insight into the flow field features captured for shaped geometries
- Use gleaned data to explain performance trends and suggest improvements to existing shaped hole geometries

3 Simulations of Round and Shaped Hole Film Cooling

3.1 Introduction

This chapter will investigate the effects of hole shaping, length to diameter ratio, and blowing ratio on a simulated row of discrete film cooling holes operating at a density ratio of 2. This investigation will also identify the key flow field features, investigate how they come about, and discuss how they affect the effectiveness of the film cooling jets.

3.2 Numerical Method

An in-house, multiblock, body-fitted code (Chem3D) is used in this investigation; the code is fully parallel and reads multiblock grids with hexahedral cells. The compressible Navier-Stokes equations are solved in their compressible-conservative form on a generalized, curvilinear coordinate system using a finite volume based discretization and preconditioning to resolve the mismatch between acoustic and convective speeds at the low Mach numbers simulated. The spatial discretizations used are second order accurate and use a weighted, essentially non-oscillating (WENO) convective scheme. Brief details of the equations solved may be found in this section, and more information and details about the code are available from Harvey (2003).

A vector representation of the compressible, conservative Navier-Stokes equations solved is presented in (3.1). Scalar inviscid and viscous fluxes (with viscous fluxes indicated by the subscript v) are defined in (3.3), and the conserved variable vector is defined in (3.2). The components of the stress tensor (τ_{ij}) are defined in (3.4). The energy fluxes (q_{ie}) are defined in (3.5). The effective dynamic viscosity, effective thermal conductivity, and enthalpy are represented by μ_e, k_e, and h respectively.

$$\frac{\partial}{\partial t}\vec{Q} + \frac{\partial}{\partial x}\left(\vec{E} - \vec{E}_v\right) + \frac{\partial}{\partial y}\left(\vec{F} - \vec{F}_v\right) + \frac{\partial}{\partial z}\left(\vec{G} - \vec{G}_v\right) = \vec{S} \tag{3.1}$$

$$\vec{Q} = [\rho u, \rho v, \rho w, E_t]^T \tag{3.2}$$

$$\begin{aligned}
\vec{E} &= [\rho u^2 + p, \rho uv, \rho uw, (E_t + p)u]^T \\
\vec{E}_v &= \left[\tau_{xx}, \tau_{xy}, \tau_{xz}, u\tau_{xx} + v\tau_{xy} + w\tau_{xz} + q_{x_e}\right]^T \\
\vec{F} &= [\rho vu, \rho v^2 + p, \rho vw, (E_t + p)v]^T \\
\vec{F}_v &= \left[\tau_{yx}, \tau_{yy}, \tau_{yz}, u\tau_{yx} + v\tau_{yy} + w\tau_{yz} + q_{y_e}\right]^T \\
\vec{G} &= [\rho wu, \rho wv, \rho w^2 + p, (E_t + p)w]^T \\
\vec{G}_v &= \left[\tau_{zx}, \tau_{zy}, \tau_{zz}, u\tau_{zx} + v\tau_{zy} + w\tau_{zz} + q_{z_e}\right]^T
\end{aligned} \tag{3.3}$$

$$\begin{aligned}
\tau_{xx} &= 2\mu_e \frac{\partial u}{\partial x} - \frac{2}{3}\mu_e \left(\frac{\partial u}{\partial x} + \frac{\partial v}{\partial y} + \frac{\partial w}{\partial z}\right) & \tau_{xy} &= \tau_{yx} = \mu_e \left(\frac{\partial u}{\partial y} + \frac{\partial v}{\partial x}\right) \\
\tau_{yy} &= 2\mu_e \frac{\partial v}{\partial y} - \frac{2}{3}\mu_e \left(\frac{\partial u}{\partial x} + \frac{\partial v}{\partial y} + \frac{\partial w}{\partial z}\right) & \tau_{xz} &= \tau_{zx} = \mu_e \left(\frac{\partial u}{\partial z} + \frac{\partial w}{\partial x}\right) \\
\tau_{zz} &= 2\mu_e \frac{\partial w}{\partial z} - \frac{2}{3}\mu_e \left(\frac{\partial u}{\partial x} + \frac{\partial v}{\partial y} + \frac{\partial w}{\partial z}\right) & \tau_{yz} &= \tau_{zy} = \mu_e \left(\frac{\partial v}{\partial z} + \frac{\partial w}{\partial y}\right)
\end{aligned} \tag{3.4}$$

$$q_{x_e} = k_e \frac{\partial T}{\partial x} + \rho h \qquad q_{y_e} = k_e \frac{\partial T}{\partial y} + \rho h \qquad q_{z_e} = k_e \frac{\partial T}{\partial z} + \rho h \tag{3.5}$$

Large eddy simulations (LES) resolve the larger scales of turbulence and use a subgrid scale model to account for the contributions of the smaller scales of turbulence (which are assumed to be more universal in nature). The governing equations are filtered spatially to yield the governing equations for LES. An eddy viscosity subgrid scale model accounts for the contributions of the turbulence scales too small to be resolved. A box filter is used, meaning that the filter width is equal to cell width at any given location in the domain. The eddy viscosity model is of the dynamic Smagorinsky type; the Smagorinsky coefficient value for each cell at each time step is solved for by additionally using a test filter with twice the width of the box filter, then using the Germano identity.

A second order, implicit, dual timestepping scheme is used for temporal differencing. The essence of the method is that many explicit pseudo-time steps (sub-iterations) are performed at each physical time step (iteration). After each sub-iteration, data is exchanged between neighboring blocks. The result is that with enough sub-iterations per iteration, each physical time step is well resolved. In order to accurately capture the evolution of the flow features, the physical time step was chosen for each grid so that the CFL number was restricted to be about .8 in the most refined portions of each grid. The physical time step expressed as a nondimensional quantity ($\Delta t^* u_{inf}/D$) is 0.0139.

Each case is initialized until all initial transient conditions have washed out and a semi-steady state operating condition is reached (usually approximately 10,000 time steps). Time averaging is then begun, and first and second order statistics for all relevant quantities (velocity, temperature, and pressure) are collected. Averaging continues until acceptable statistical convergence is achieved; this usually requires 10,000-12,000 time steps (equivalent to 12-15 domain flow-through times or about 300 hole diameters traveled by the mainstream flow). The Louisiana State University cluster Tezpur as well as the Louisiana Optical Network Initiative clusters Eric, Louie, Oliver, and Poseidon are used to perform these calculations.

3.3 Problem Setup

3.3.1 Geometries

Three geometries are examined: the simple round hole, the laterally diffused hole, and the console hole. All have a length to diameter ratio of 3.5 except for the round hole, which is run at a length to diameter ratio of both 3.5 and 1.75. All holes are inclined to the surface at an angle of 35 degrees and have a pitch (lateral spacing) of 3 hole diameters. Figure 3.1 shows three dimensional representations of the shaped geometries in this study.

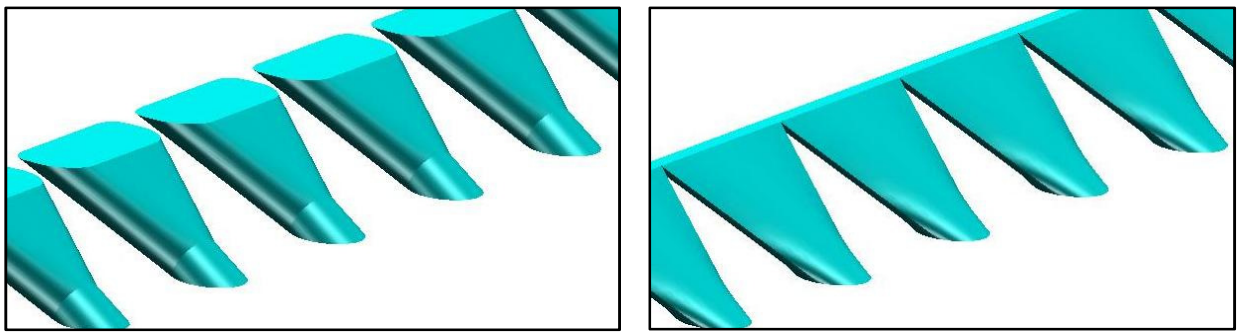

Figure 3.1: Three dimensional representations of the laterally diffused (left) and console (right) hole shapes

Figure 3.2 shows dimensioned drawings of each geometry. Note that all of the holes begin with the same cylindrical profile, and that the hole diameter is 12.7 mm. The consoles meet at the surface to form a uniform .35D slot; the profiles at the surface and top of the plenum chamber are connected ("lofted") with a series of straight lines. This ensures that the geometry is more easily manufacturable (even if it is much more complex than drilling the round hole). Similarly, the laterally diffused hole is created by beginning with the round hole and cutting out the upper portion with a "stub" cylindrical hole left extending out of the plenum chamber. The stub is cut off normal to the direction of the tube. The round profile at the top of the stub is connected to the laterally diffused surface profile via straight lines to create the diffuser. Each side of the diffuser diverged from the centerline at an angle of 14.5 degrees. The area ratios (exit area divided by inlet area) are 0.7636, 3.016, and unity in the console, laterally diffused, and round hole cases respectively. These area ratios may be used to calculate the true blowing ratio in the shaped geometries, as will be discussed later.

The plenum domain extends 3D in the lateral direction (matching the crossflow pitch, as shown in Figure 3.3). The crossflow domain extends 7 hole diameters upstream and 15 hole diameters downstream of the center of the hole exit at the surface. The flow domain extends 12 hole diameters vertically from the surface. The coordinate system is nominally centered at the

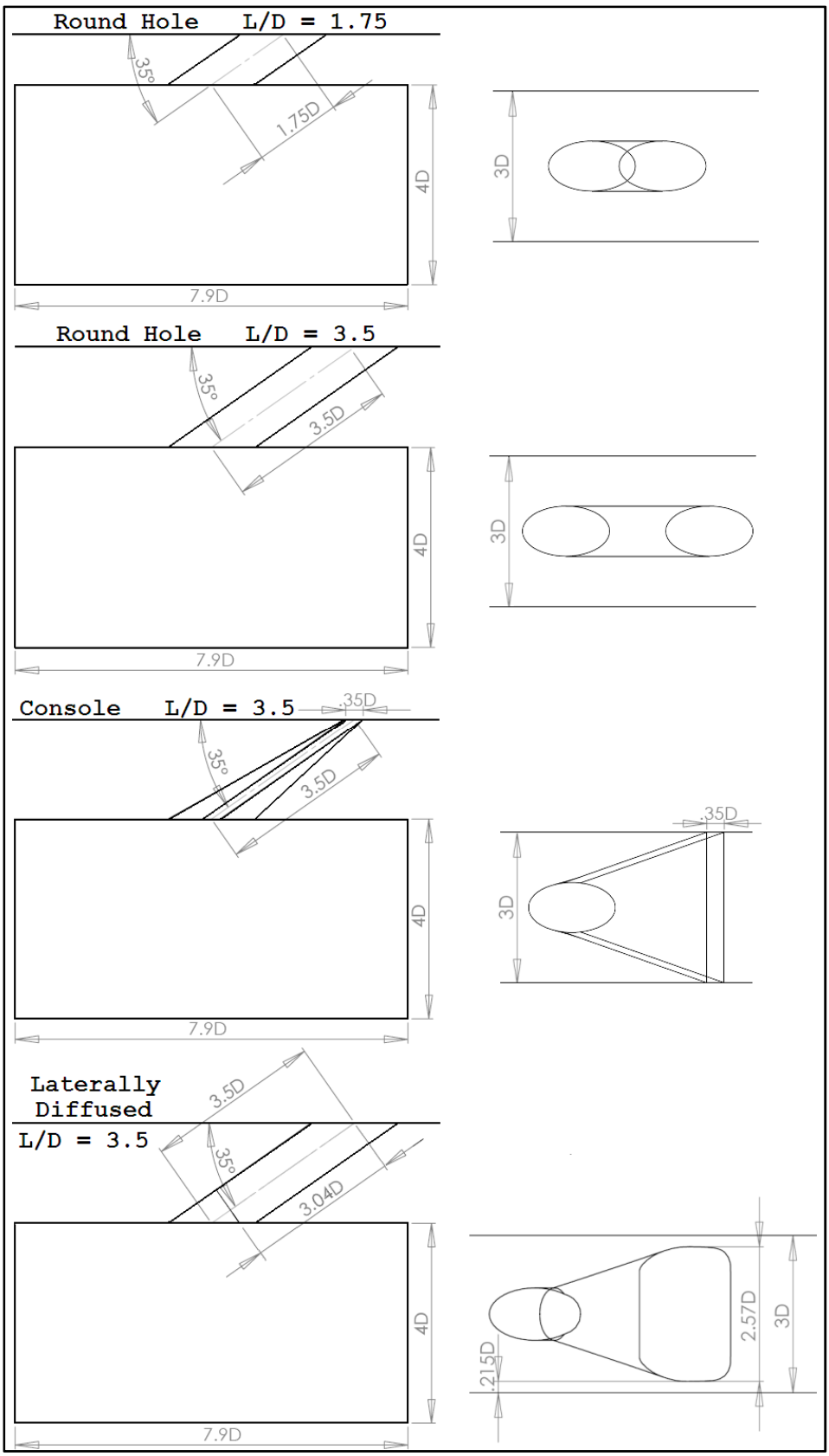

Figure 3.2: Dimensions of holes and plenum chambers, side view (left) and top view (right)

middle of the hole exit profile in each case, but because the experimental data used for validation sometimes uses a different x direction datum (the leading edge or trailing edge of the hole), occasionally the x datum is reported in the same way as the experiments in order to keep the reported locations integer values of x/D. When this is done, it will be noted.

3.3.2 Key Operating Parameters

There are several key nondimensional parameters used to describe the jet in crossflow. These ratios are defined in 3.6, 3.7, 3.8, and 3.9.

$$VR = \frac{v_{jet}}{v_{cross}} \tag{3.6}$$

$$DR = \frac{\rho_{jet}}{\rho_{cross}} \tag{3.7}$$

$$BR = \frac{\rho_{jet} v_{jet}}{\rho_{cross} v_{cross}} \tag{3.8}$$

$$MR = \frac{\rho_{jet} {v_{jet}}^2}{\rho_{cross} {v_{cross}}^2} \tag{3.9}$$

The velocity ratio (VR, 3.6) is a simple measure of the jet velocity with respect to the crossflow velocity. The density ratio (DR, 3.7), similarly, is a measure of the density of the jet with respect to the crossflow (held constant at 2.0 for all cases in this study). The density ratio in an operating gas turbine is greater than unity because the coolant is cooler and therefore denser than the hot process gas. The blowing ratio (BR, 3.8) is sometimes referred to as the mass flux ratio, and it is simply the velocity ratio multiplied by the density ratio. The momentum ratio

(MR, 3.9), sometimes referred to as the momentum flux ratio, is a measure of the kinetic energy of the jet relative to the mainstream.

3.3.3 Boundary Conditions

Figure 3.3 illustrates some of the boundary conditions used in the simulations. Not shown are the adiabatic, no-slip wall boundary conditions used in the plenum chamber, hole, and cooled surface as well as the periodic boundaries on the z faces of the crossflow (effectively simulating an infinite row of holes). The inlet of the crossflow domain is Dirichlet for both velocity and temperature, with a uniform velocity outside the boundary layer. Within the boundary layer, the velocity field obeys 3.10 (where the boundary layer thickness of 0.512 hole diameters is indicated by δ). This profile was chosen to closely match the experiments of Pietrzyk et al. (1990) at the locations measured upstream of the hole. For lack of a realistic inlet turbulence generator, turbulence quantities are not represented, but the mean profile is simulated closely. This can be observed in the plots upstream of the hole in Appendix B and Table 3.3, which shows relative boundary layer thicknesses. The inlet at the base of the plenum chamber is Dirichlet for velocity and temperature, and is uniform with a vertical velocity that is varied to enforce the blowing ratio. The temperature of the crossflow is 300K and the jet is 150K, yielding the density ratio of 2. The freestream velocity is 20 m/s, yielding a Reynolds number based on hole diameter and freestream conditions of about 16,000. In order to compare geometries in an equitable fashion, mass flow rates of coolant are equalized between the geometries. Thus, a blowing ratio of 1 for the round hole indicates a true blowing ratio of 1, but for the console and laterally diffused hole this indicates an equal coolant mass flow rate to the round hole case with that blowing ratio. Indeed, to glean the true blowing ratio for the shaped holes, the blowing ratio should be divided by the area ratio of the shaped holes reported in 3.3.1.

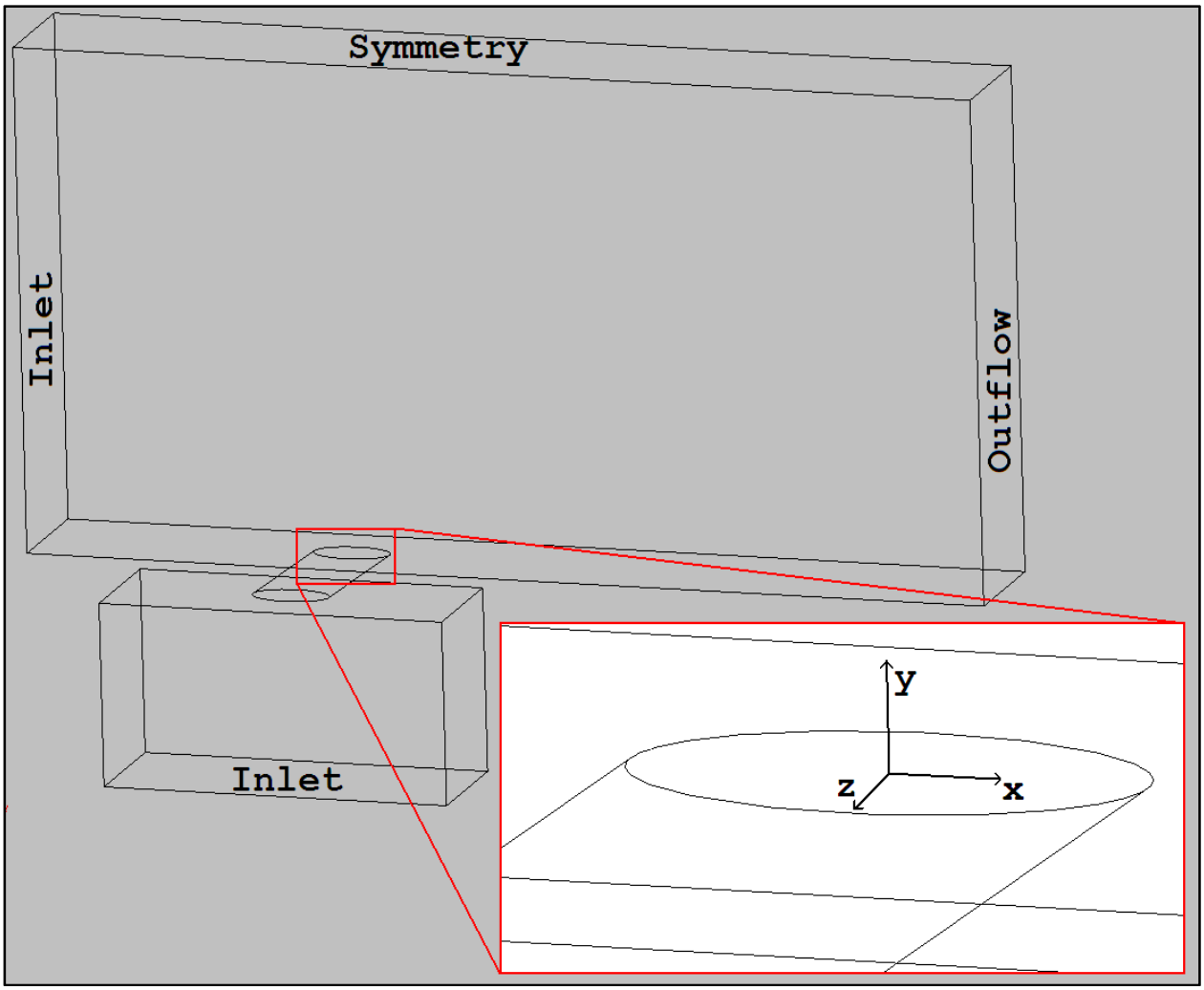

Figure 3.3: Layout of the coordinate system and key boundary conditions

The names of the runs (H-1, J-05, etc.) are descriptive in that the letter provides the geometry (H for the longer cylindrical hole, I for the console, J for the laterally diffused, and K for the shorter cylindrical hole) and the number provides the blowing ratio. The only exceptions are the GI runs, which are all the shorter cylindrical hole geometry (the same as K) but have different grid refinements. Thus, GI-3 could have been called K-1, but was not for fear of confusion. The A suffix occasionally used throughout the study indicates the density ratio is 2, but since the density ratio is fixed for the study this letter is irrelevant and may safely be ignored.

$$u(y) = u_{inf}\left(\frac{y}{\delta}\right)^{1/5.5} \qquad \delta = .512D \tag{3.10}$$

Table 3.1

Run Guide – Round Holes							
Run	Geometry	Cells	L/D	BR	DR	VR	Purpose
GI-1	Cylindrical	.341M	1.75	1	2	0.5	Grid Independence Study, Eff. Validation
GI-2	Cylindrical	1.675M	1.75	1	2	0.5	Grid Independence Study, Eff. Validation
GI-2a	Cylindrical	2.234M	1.75	1	2	0.5	Grid Independence Study, Eff. Validation
GI-3	Cylindrical	5.146M	1.75	1	2	0.5	Grid Ind. Study, BR Eff. Study, Eff. Validation
GI-4	Cylindrical	11.888M	1.75	1	2	0.5	Grid Independence Study, Eff. Validation
K-05	Cylindrical	5.146M	1.75	0.5	2	0.25	BR Eff. Study, Eff. Validation
K-2	Cylindrical	5.146M	1.75	2	2	1	BR Eff. Study, Eff. Validation
H-05	Cylindrical	5.089M	3.5	0.5	2	0.25	BR/Shape Flow Field Study, Flow Validation
H-1	Cylindrical	5.089M	3.5	1	2	0.5	BR/Shape Flow Field Study, Flow Validation
H-2	Cylindrical	5.089M	3.5	2	2	1	BR/Shape Flow Field Study

Table 3.2

Run Guide – Shaped Holes							
Run	Geometry	Cells	L/D	BR	DR	VR	Purpose
I-05	Console	5.325M	3.5	0.5	2	0.25	BR/Shape Flow Field Study
I-1	Console	5.325M	3.5	1	2	0.5	BR/Shape Flow Field Study
I-2	Console	5.325M	3.5	2	2	1	BR/Shape Flow Field Study
J-05	Lat. Diff.	6.246M	3.5	0.5	2	0.25	BR/Shape Flow Field Study
J-1	Lat. Diff.	6.246M	3.5	1	2	0.5	BR/Shape Flow Field Study
J-2	Lat. Diff.	6.246M	3.5	2	2	1	BR/Shape Flow Field Study

Table 3.3

Boundary Layer Upstream of the Hole					
	δ/D	δ*/D	θ/D	Re_θ	Re_δ
LES	0.497	0.102	0.0567	920.	1660
Exp.	0.52	0.089	0.059	946	1600

3.3.4 Grids

Once the geometries are generated in a commercial CAD program (SolidWorks), the files are saved in STEP format and imported into Ansys ICEM 11, a grid generator. Within ICEM, blocking is manually created and associated with the geometry. This blocking must consist of logically rectangular blocks, and it is sometimes a challenge to make them conform to a complex shape (like a console or laterally diffused geometry). 1:1 face matching is required in Chem3d, placing more restriction on the choice of blocking. To avoid domain decomposition issues when the problem is run on many processors, care should also be taken to ensure that no blocks with either a very large or very small number of cells are created. It is quite time consuming to adjust the number of points on each edge, locations of block vertices, and edge bunching ratios to yield a usable grid with no cells too highly skewed or folded inside out. Once the mesh is created in ICEM via this highly iterative generation process, it is exported in CFX-4 format (due to licensing restrictions, this was the only ASCII format that ICEM supported). A converter program was written by Jathar and Leedom (2006) to change the ASCII CFX-4 format into the ASCII Product Development Corporation GridPro format that Chem3D reads directly.

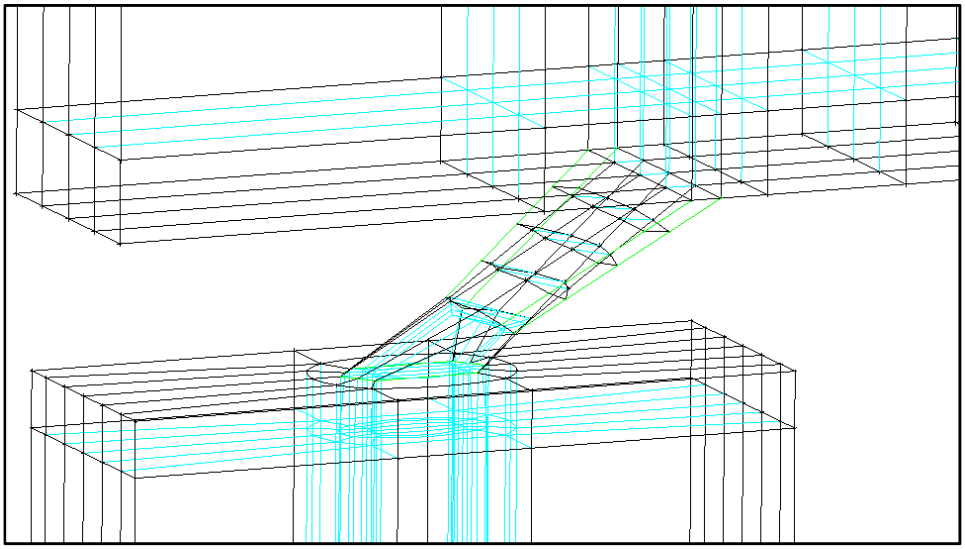

Figure 3.4: Manually created blocking for the console hole grid

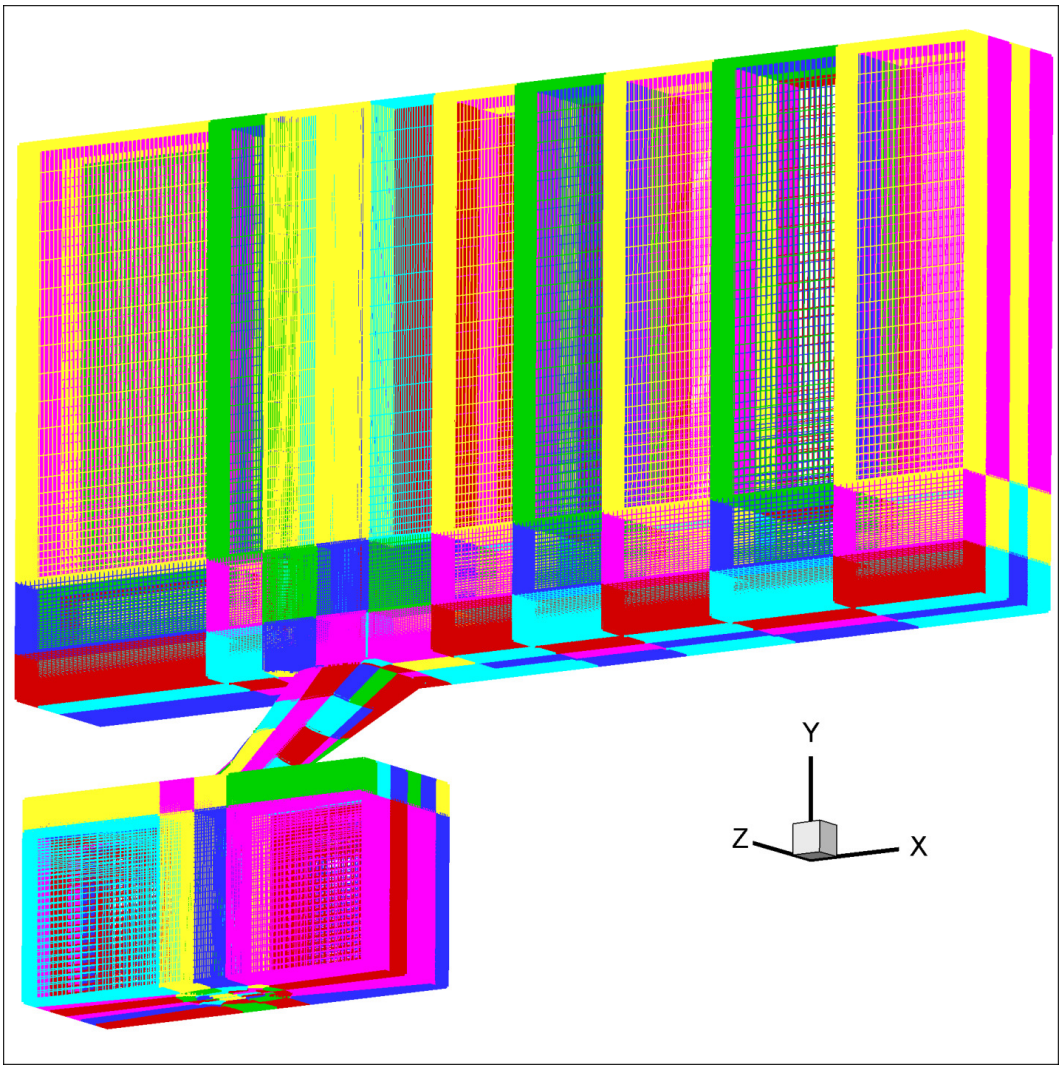

Figure 3.5: Example of a multiblock grid - laterally diffused geometry

In order to find the correct grid refinement level, a grid independence study is performed. A systematic method for determining three grid refinement levels for comparison is used. First, a "fine" grid is created, in this case having 11.89 million cells. Next, a scale factor of 1.322 is chosen to provide an even spacing between the coarsened grid levels. Scaling the grid by this factor in each direction causes the number of cells to change by a factor of $(1.322)^3$, meaning that the medium and coarse grids have 5.14 million and 2.23 million cells, respectively. These grid refinement levels correspond to runs GI-4, GI-3, and GI-2a as shown in the boundary conditions

section. Two other coarser grid refinement levels, .341 million cells and 1.675 million cells, are run in order to gain a clearer idea of what the trends are. Once the time-averaged solutions are obtained on the three grid refinement levels, both the flow field and the temperature field are sampled at various points. A determination of whether or not convergence has been reached can be made based on these observations. It should also be noted that since the filter width changes with the grid cell width, the equations being solved are not exactly the same at all refinement levels.

Figure 3.6, Figure 3.7, and Figure 3.8 show the results of the grid independence study; they indicate that adequate convergence of the surface adiabatic effectiveness and mean flow field have been reached at the 5.15 million cell level. This is purely a comment on the quality of the

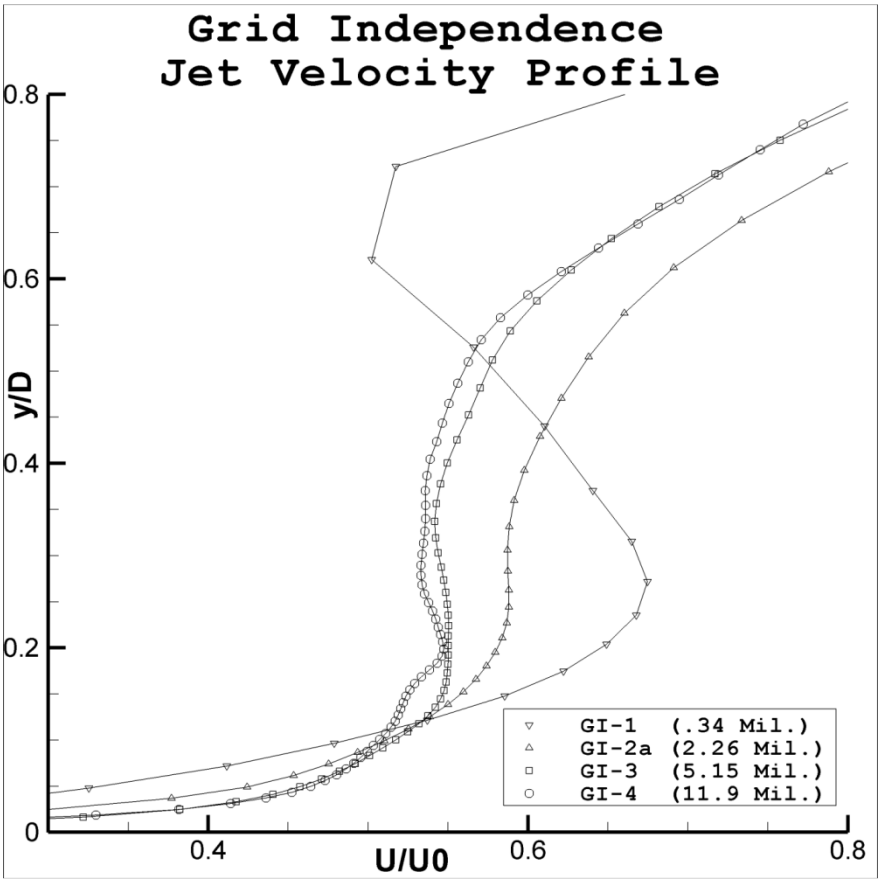

Figure 3.6: Centerline u velocity profile at x/D=3

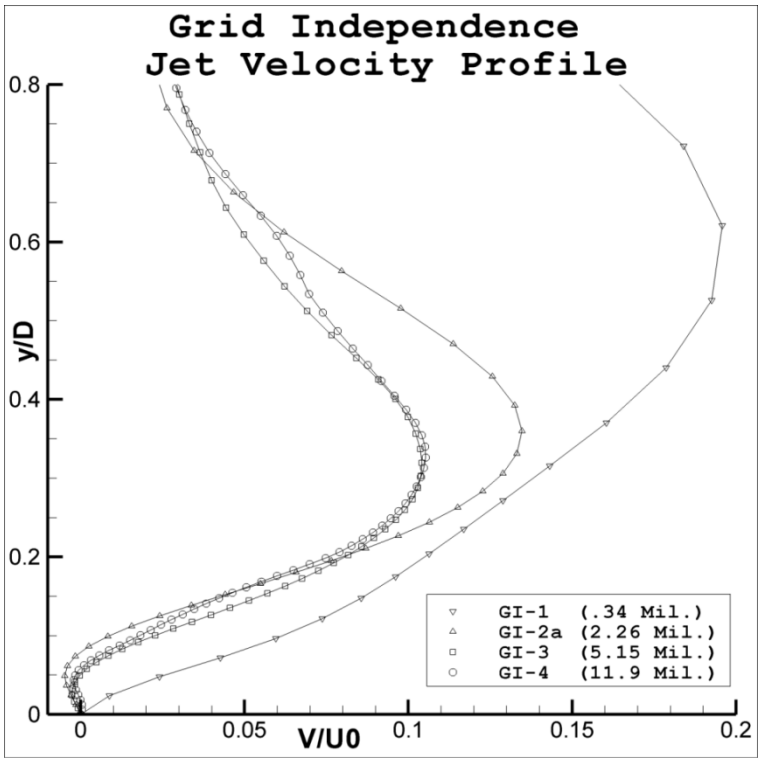

Figure 3.7: Centerline v velocity profile at x/D=5

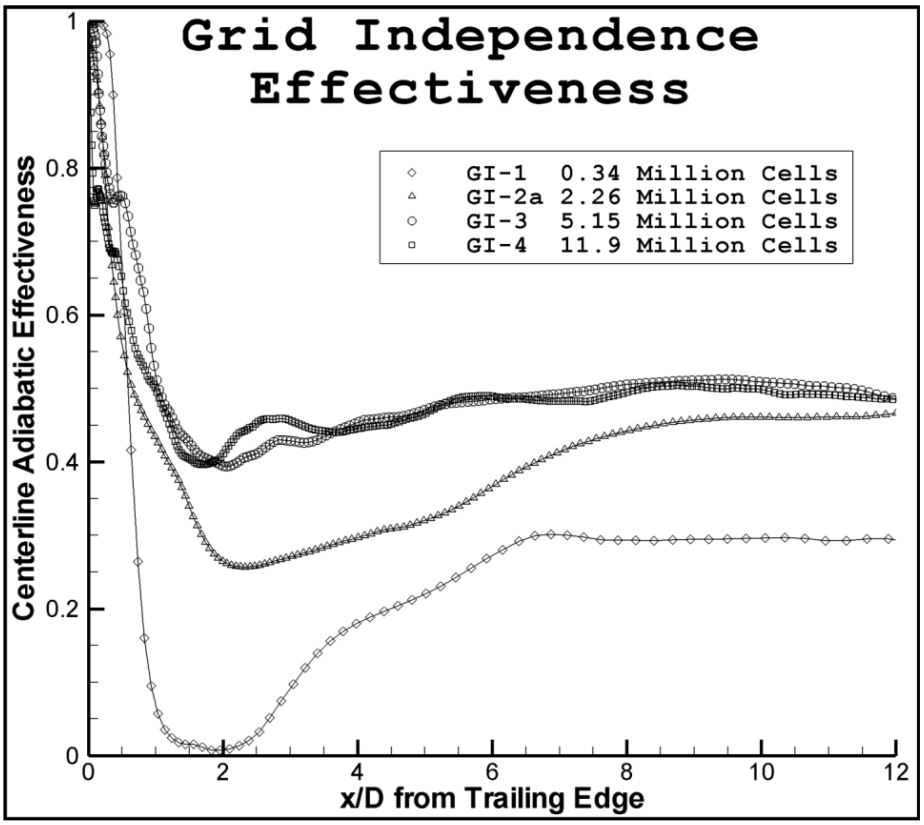

Figure 3.8: Grid independence study results

convergence in the case of surface adiabatic effectiveness, as the code converges to values overpredicting effectiveness by ~25% in the near field. This discrepancy will be addressed later in the validation section. The waves in the 11.88 million cell results are a consequence of the shorter time-averaging interval chosen (in light of the computational cost of running such a fine grid for long periods, it was decided that the data shows the trend well enough for the purposes of this grid independence study).

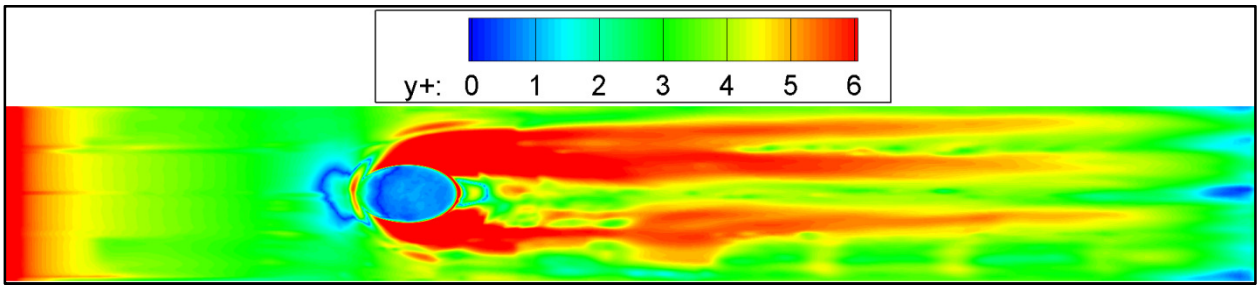

Figure 3.9: Typical distribution of first surface cell y+ values for a round-hole production grid

For the production grids, the flow domain is decomposed into zones in order to facilitate parallel solution; the domain is decomposed into 280 zones for the cylindrical cases, 230 for the console cases, and 368 zones for the laterally diffused cases. The mainstream flow of the cylindrical hole grid case (grid H) with a length to diameter ratio of 3.5 has 277, 96, and 86 cells in the x, y, and z directions respectively; the console and laterally diffused holes have approximately the same distributions. The grid is refined near the wall to provide a first cell height y^+ of about 3 upstream of the hole (as detailed in Figure 3.9). The distribution is nonuniform because the wall shear is not constant over the surface. Using du/dy from ahead of the hole to calculate viscous sublayer units, in the x-direction the mesh spacing values ranged from 5 near the hole to 12 near the end of the flow domain in x^+ units, and in the z-direction mesh spacing values were about 13 throughout the domain in z^+ units.

3.4 Validation

3.4.1 Flow Field Validation

The validation of the flow field is done with respect LDV data created in the study of Pietrzyk et al. (1990). Flow field validation is done for the blowing ratios of 0.5 and unity in the cylindrical hole case with a length to diameter ratio of 3.5. Due to the extensive nature of the plots, they are shown in their entirety in the appendix with only selected results shown in this section. The experimental results were thoughtfully provided by Dr. David Bogard, and are an expanded set generated in the experimental study of Pietrzyk et al. (1990). It should be noted that in this section, x/D refers to distance downstream of a datum located at the leading edge of the hole.

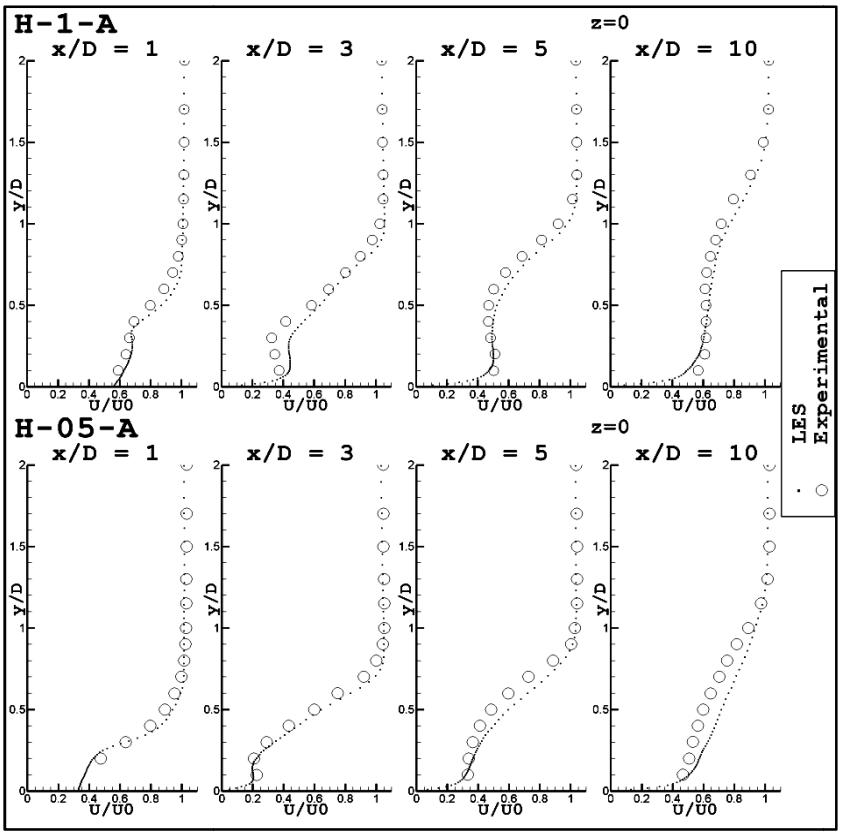

Figure 3.10: Mean u velocity profile validation

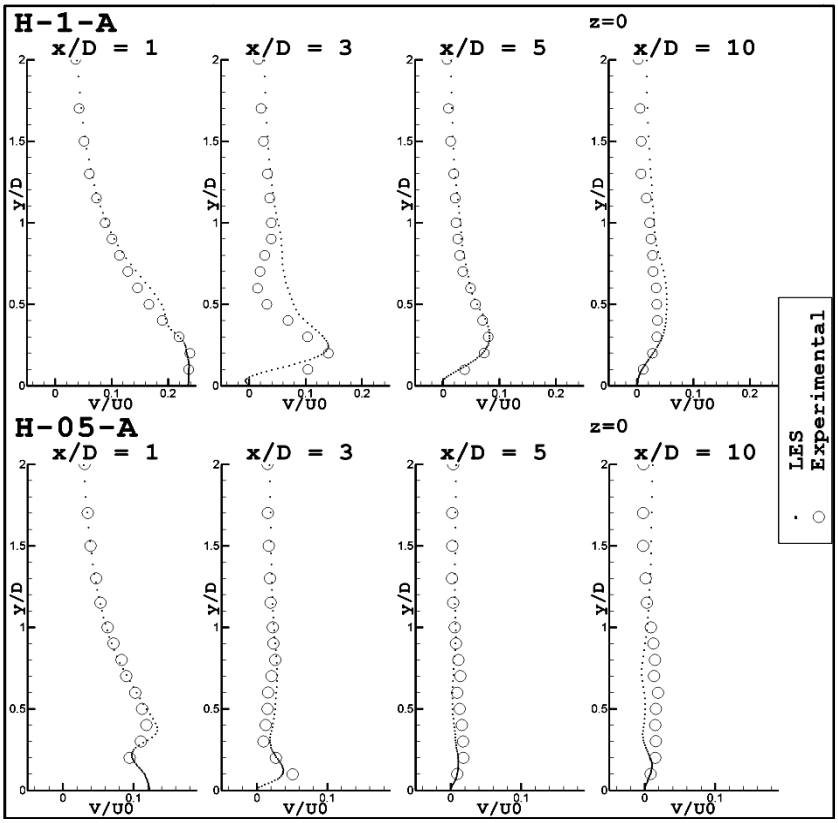

Figure 3.11: Mean v velocity profile validation

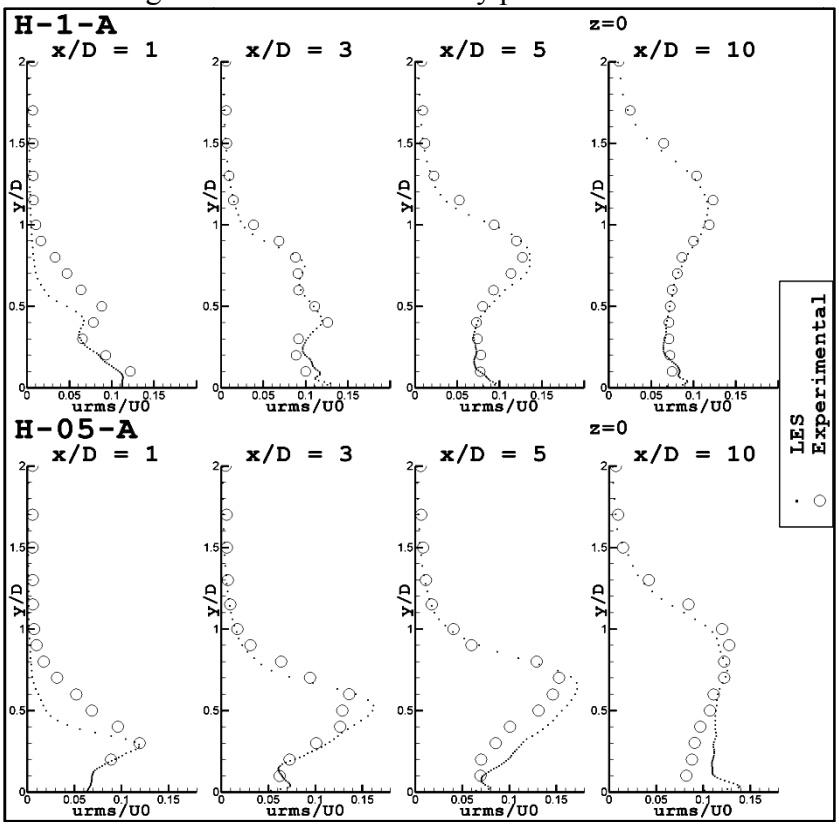

Figure 3.12: Root-mean-square of u velocity validation

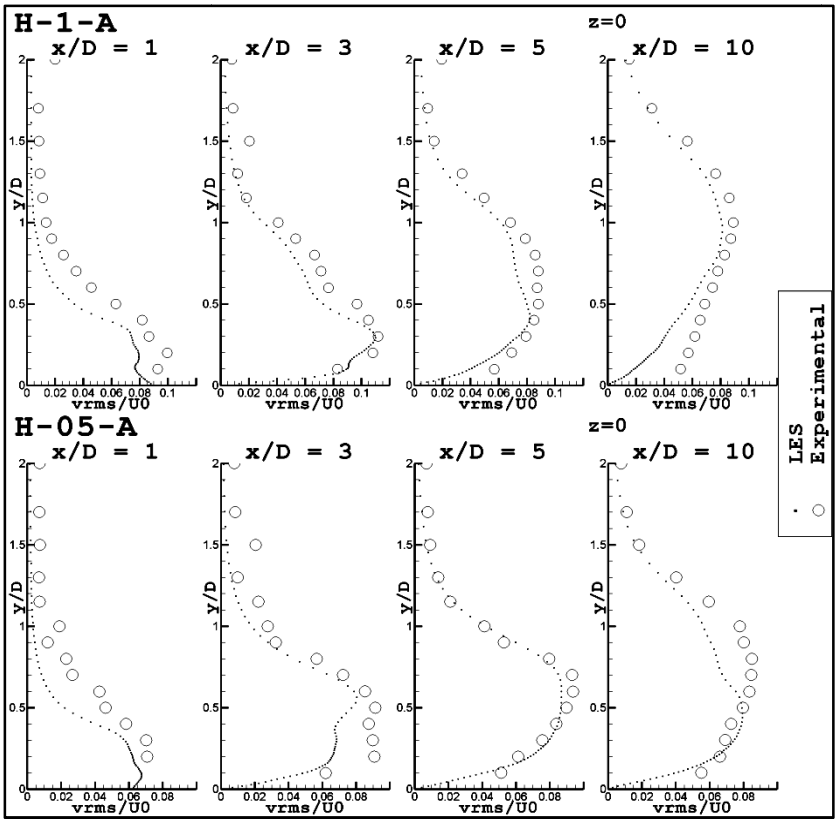

Figure 3.13: Root-mean-square of v velocity validation

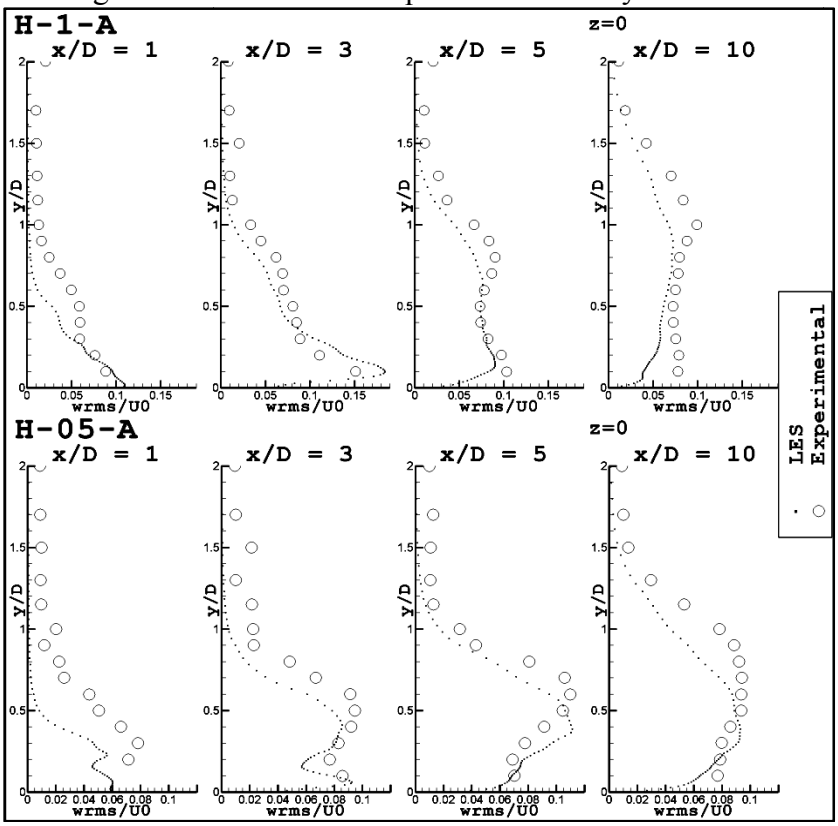

Figure 3.14: Root-mean-square of w velocity validation

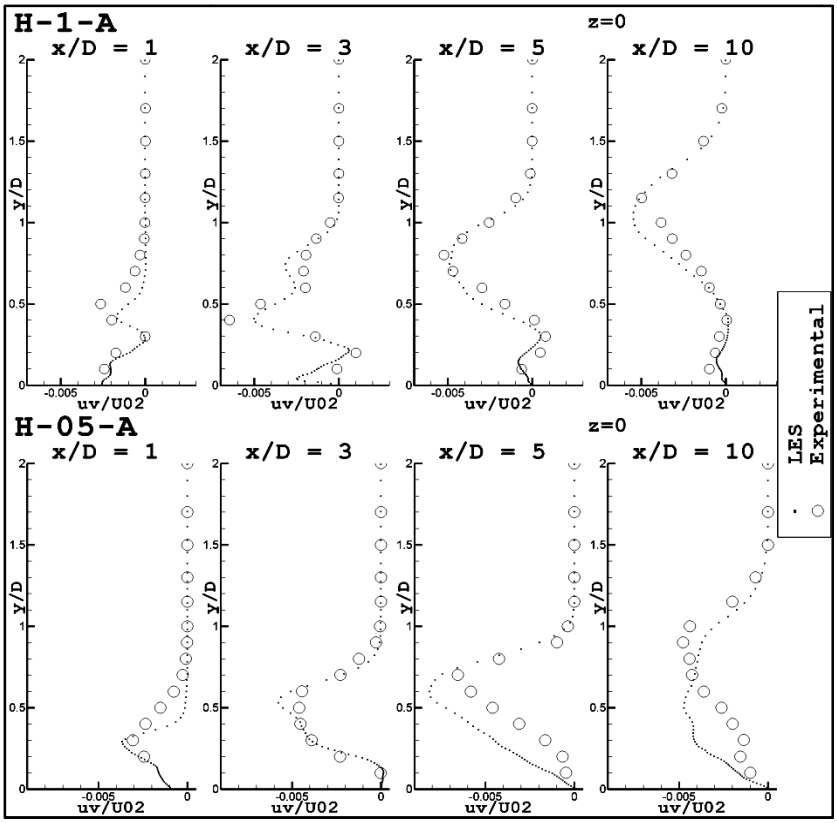

Figure 3.15: uv shear stress validation

The first order statistics (mean velocities u and v) in the centerline profiles (Figure 3.10 and Figure 3.11) show excellent agreement. The largest deviations in the first order statistics between the experimental and LES results are shown at about three hole diameters downstream of the leading edge of the hole (where the x datum is located in these experiments). The shear layer moves closer to the surface and the wake is shorter in the lower blowing ratio case just as measured in experiments (Figure 3.10). The vertical velocity is also correctly predicted to be lower for the lower blowing ratio cases (Figure 3.11). The second order statistics (u'^2, v'^2, w'^2, and $u'v'$) also show excellent agreement (Figures 3.12-15), but LES underpredicts the fluctuations upstream of the hole and back to about 1 hole diameter downstream of the leading edge of the hole. This can be shown in these figures in the consistent underprediction of root-mean-square velocity quantities above a y/D value of about .25, and in the appendix at the

upstream profiles. This is a result of the crossflow inlet condition being a laminar one, rather than completely replicating the turbulent conditions upstream of the hole in the experiments. This is not seen to be a great impediment in these simulations because the LES profiles of second order statistics fill out and agree nicely at locations farther downstream. As a side note, the fact that the profiles do fill out and agree farther downstream indicates that most of the turbulence created in these film cooling cases (at similar operating conditions, upstream turbulence levels, Reynolds numbers, density ratios, etc.) comes from the interaction of the jet and crossflow, not the upstream conditions. It would be interesting to fully replicate the upstream conditions and compare the results to see how the profiles change, but this is beyond the scope of the current study.

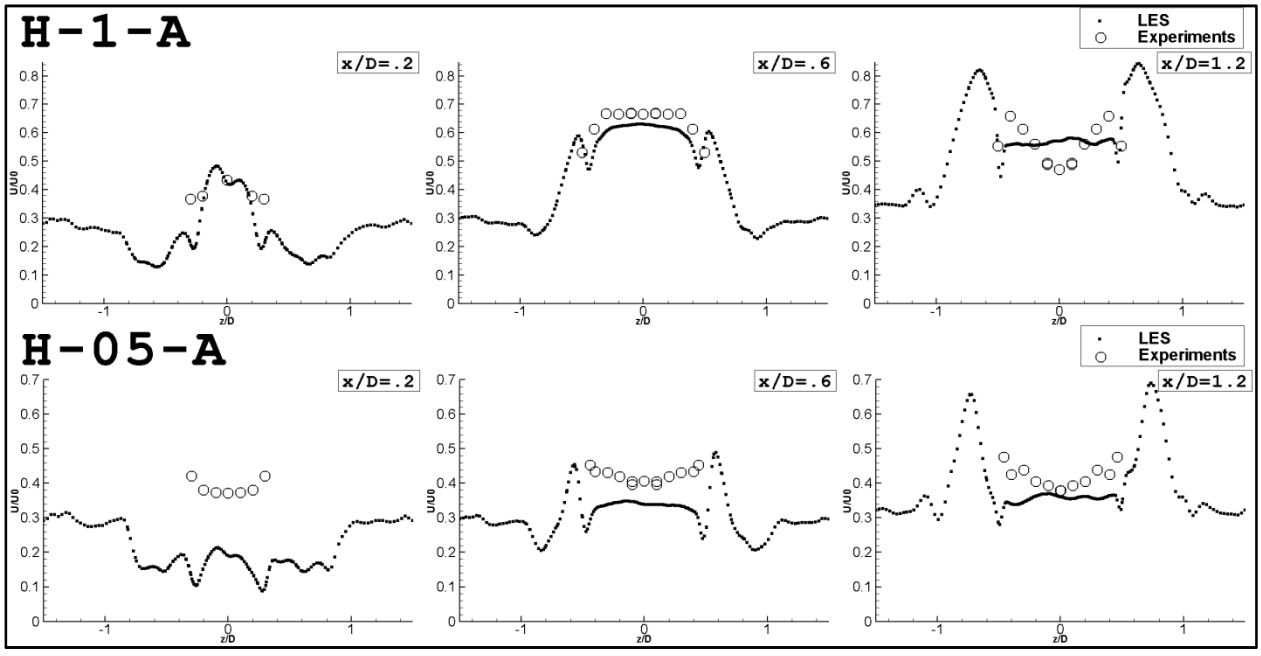

Figure 3.16: Mean u velocity profile above hole exit validation

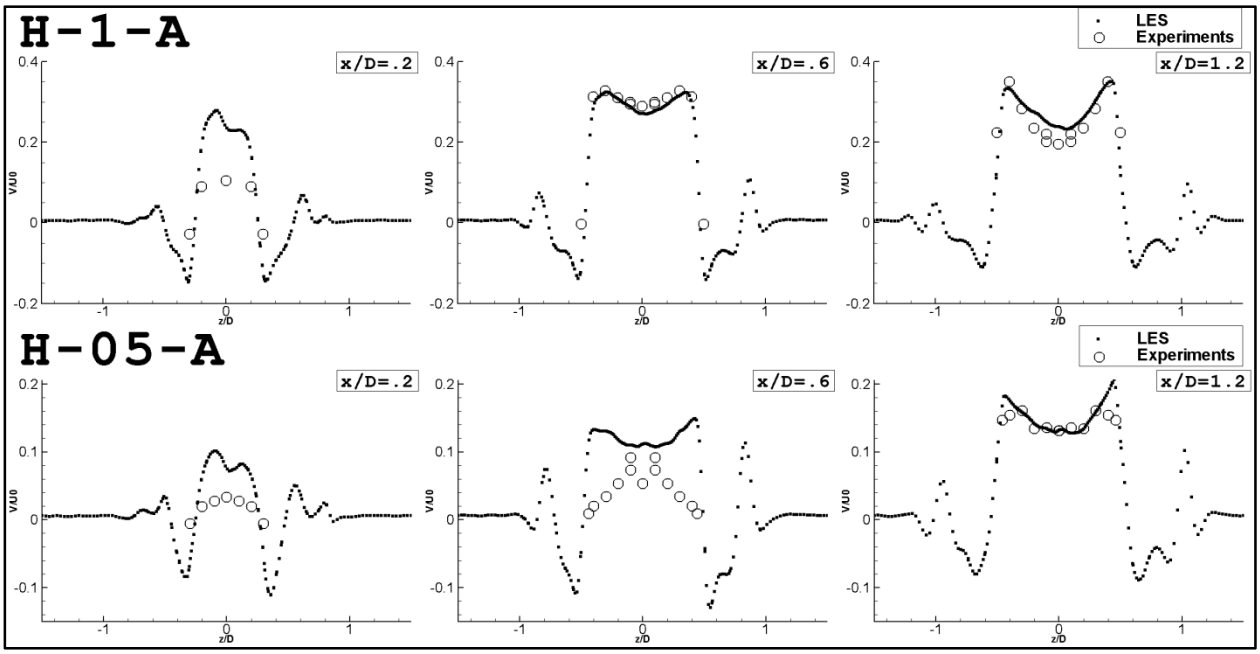

Figure 3.17: Mean v velocity profile above hole exit validation

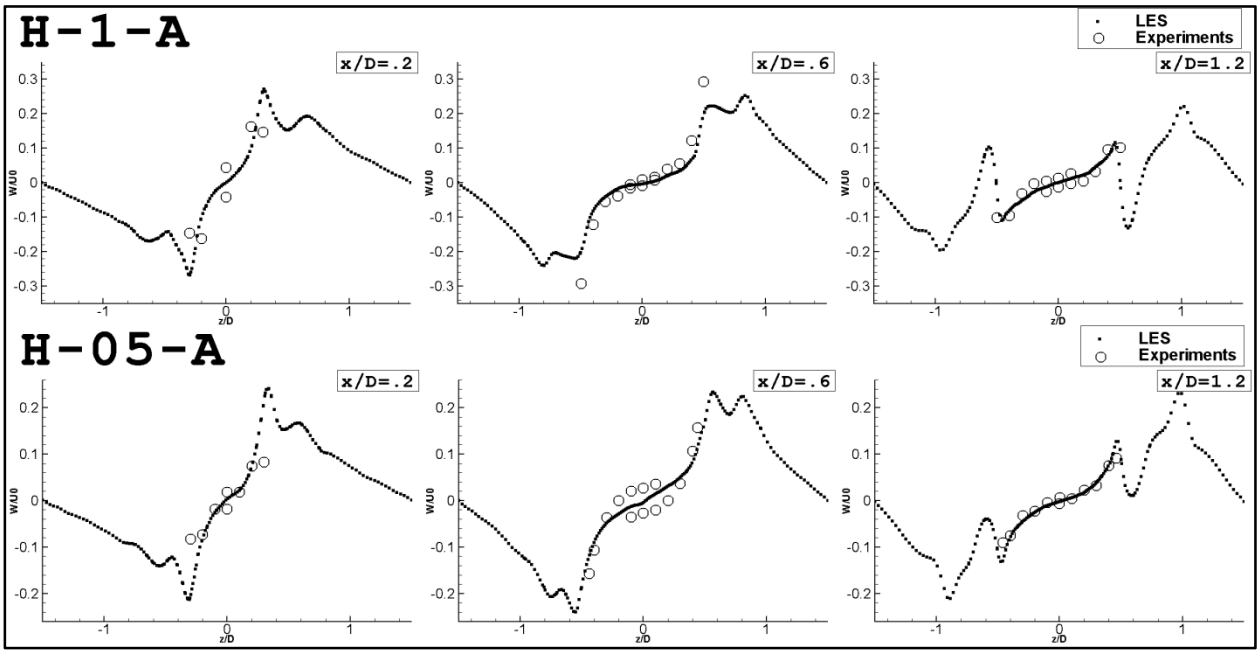

Figure 3.18: Mean w velocity profile above hole exit validation

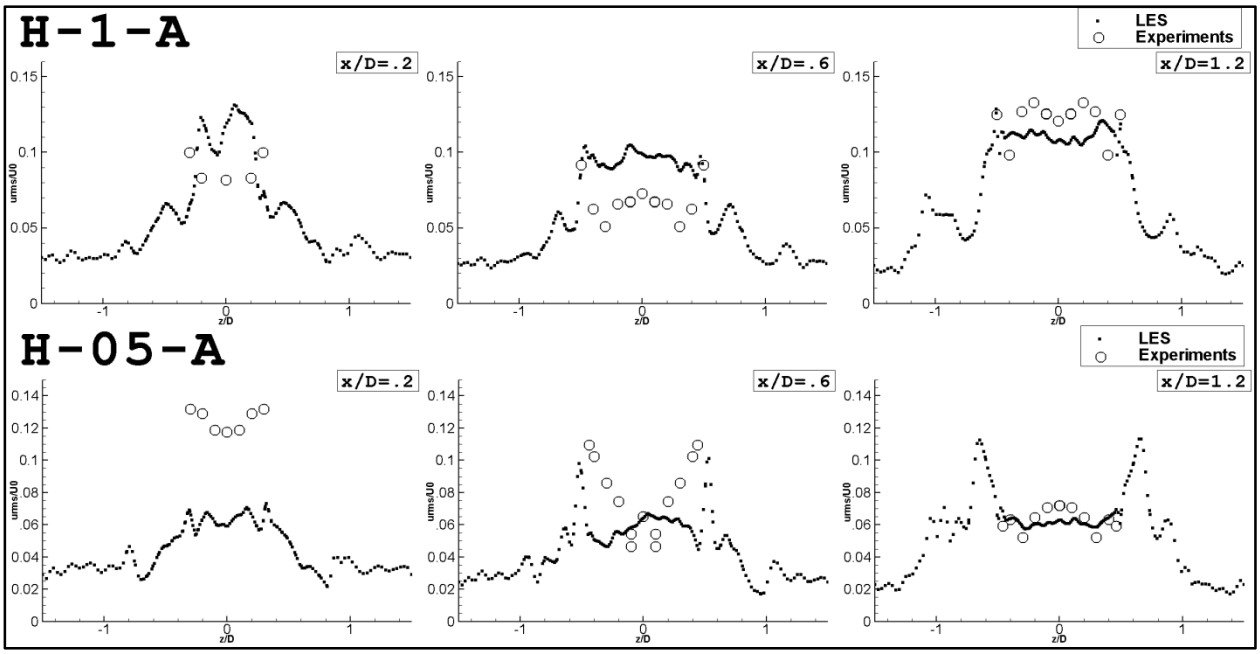

Figure 3.19: Root-mean-square of u velocity above hole exit validation

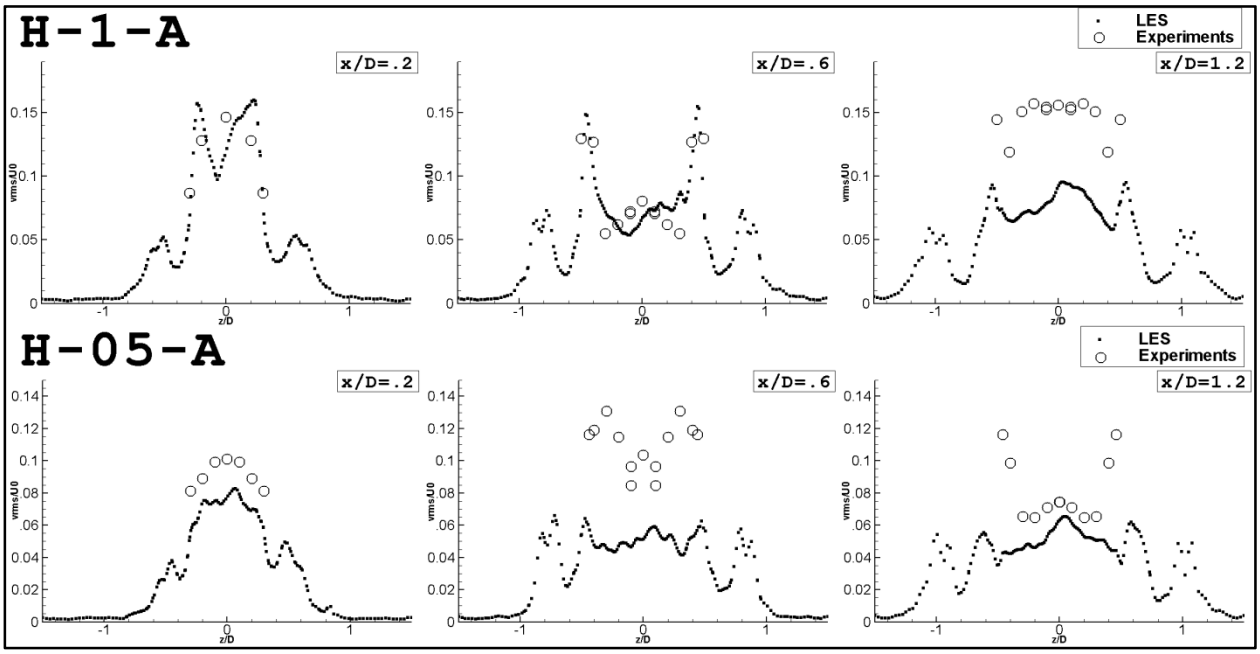

Figure 3.20: Root-mean-square of v velocity above hole exit validation

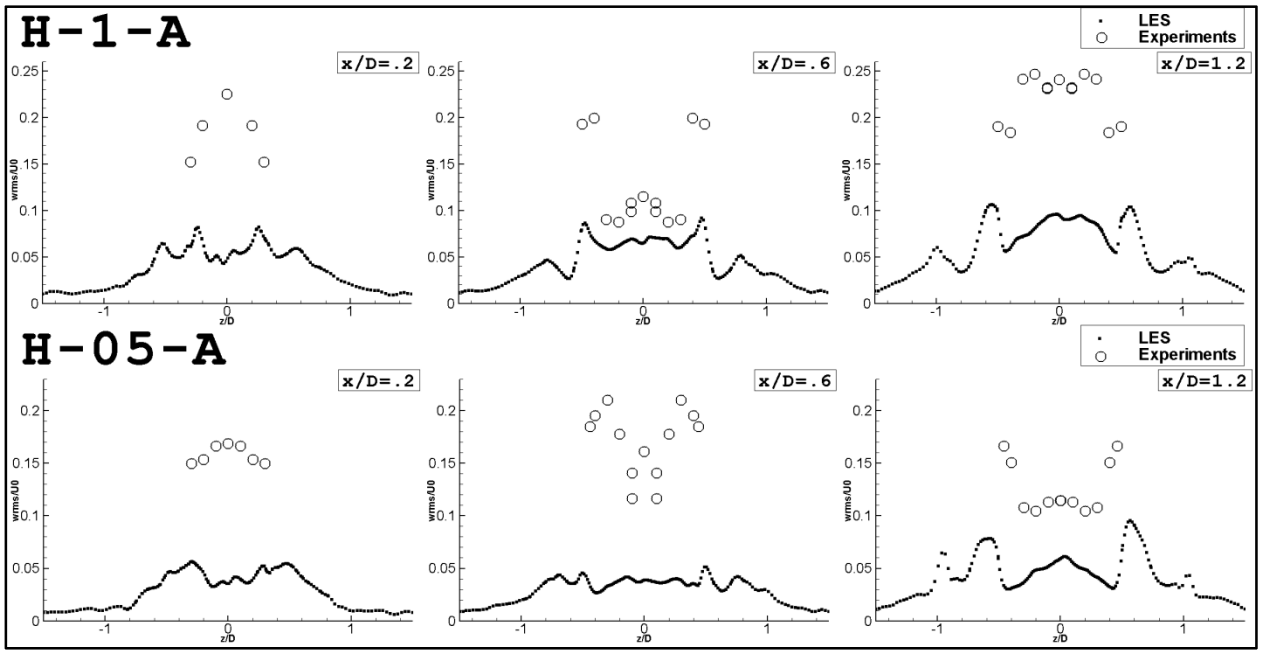

Figure 3.21: Root-mean-square of w velocity above hole exit validation

The LES results at the hole exit are further plotted against the experimental data from Pietrzyk et al. (1990) and shown in Figures 3.16-21. The first order statistics in the data above the hole exit show good agreement with experiments. The mean u velocity profiles shown agree generally with the exceptions of slight variations in profile shape and a gross underprediction in the x/D=.2 location of the blowing ratio 0.5 case. The v velocity profiles indicate that the jetting effect is slightly exaggerated close to the front of the hole, but the profiles agree nicely at locations farther from the front. The w velocity profiles have outstanding agreement. With the exception of the leading edge of the hole in the blowing ratio 1 case, the profiles of root-mean-square of velocity all either agree or underpredict (sometimes underpredicting significantly) the amount of fluctuation in velocity at the hole exit. The underprediction is most severe in the root-mean-square of w velocity plots. The most probable cause of this underprediction is the lack of upstream turbulence. The horseshoe vortex is a dominant feature in these results. If freestream

turbulence levels were higher, the horseshoe vortex may not have been as stable and more fluctuation may have been introduced into the jet at the leading edge.

More extensive comparisons to experimental results are provided in the appendix so that the reader is free to draw his or her own conclusions about the quality of agreement relative to the experimental data

3.4.2 Surface Adiabatic Effectiveness Validation

In this section, the surface adiabatic effectiveness validation is presented with respect to the experimental study of Sinha et al. (1991). In order to conform to the experimental study, all x/D locations reported in this section will be reported relative to a datum located at the trailing edge of the hole on the surface.

The adiabatic effectiveness in the blowing ratio 1 case (plotted in Figure 3.22) is overpredicted (both in terms of centerline effectiveness and laterally averaged effectiveness), with greater overprediction as locations father from the hole are observed. One possible explanation is that the lack of realistic inlet turbulence reduces the mixing of the coolant and crossflow air as it moves downstream, thus leading to better film cooling performance. One could also argue that the inlet turbulence at these downstream locations is not a significant factor because the second order velocity statistics (previously discussed) agree very well at these downstream locations. Another possibility is that the increased Δx grid spacing as the grid approaches the outflow (as described in section 3.3.4) is not fine enough to capture some vital turbulence or mixing phenomena close to the wall. Since the LES filter width is proportional to the grid spacing, a finer grid would resolve more turbulence and leave less to be modeled by the subgrid scale model. A future study of a similar grid with a uniform Δx distribution would be instructive.

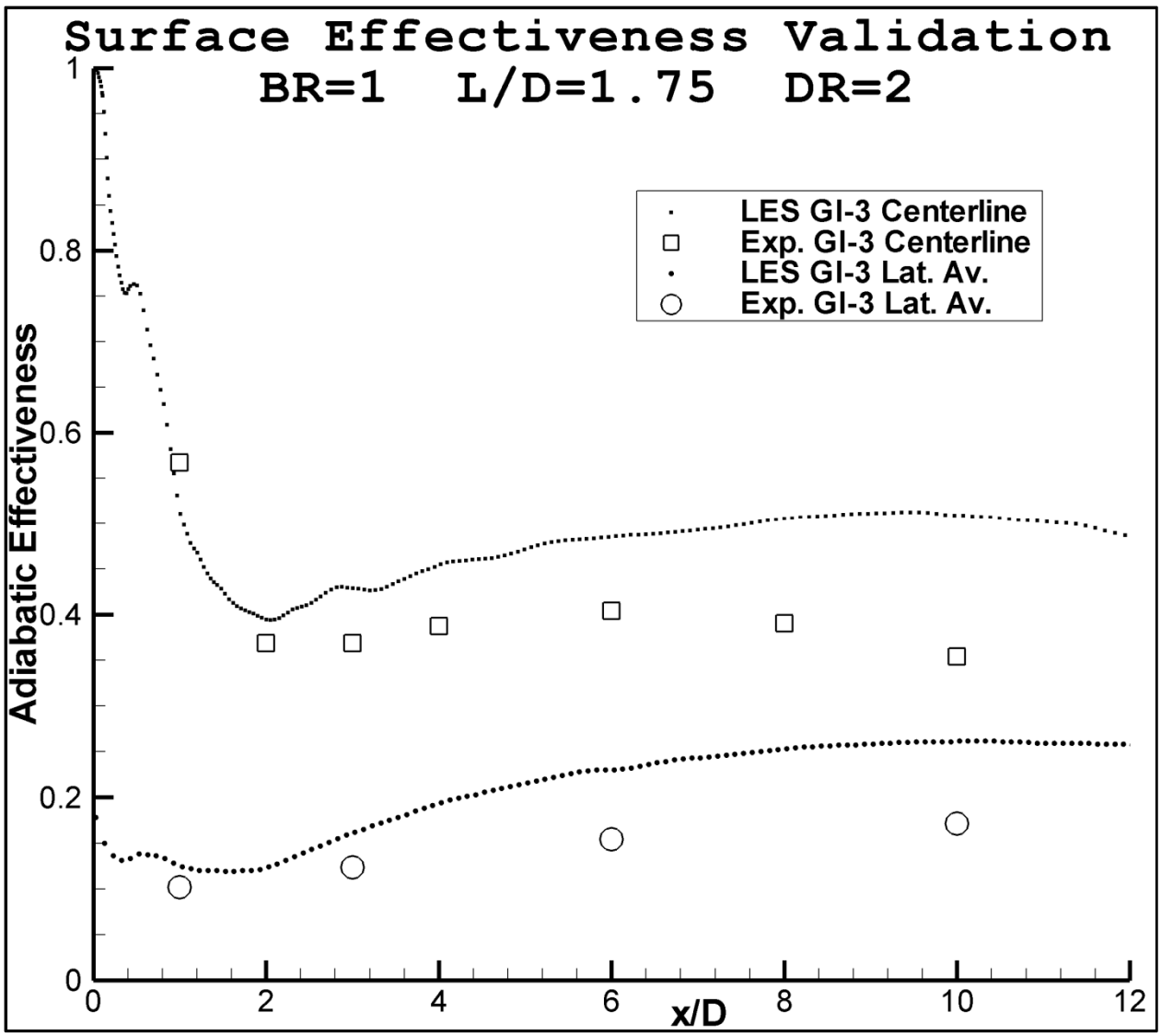

Figure 3.22: Validation of case GI-3

Comparisons of the agreement obtained in this study to previous computational studies are plotted in Figure 3.23. Surface adiabatic effectiveness is not a simple thing to predict for a turbulent jet in crossflow. While the agreement with the experimental data is not excellent, it is an improvement when compared to previous computational studies. For the case shown in Figure 3.23, jet blow off and reattachment are not captured in the previous studies, but are captured in the present study.

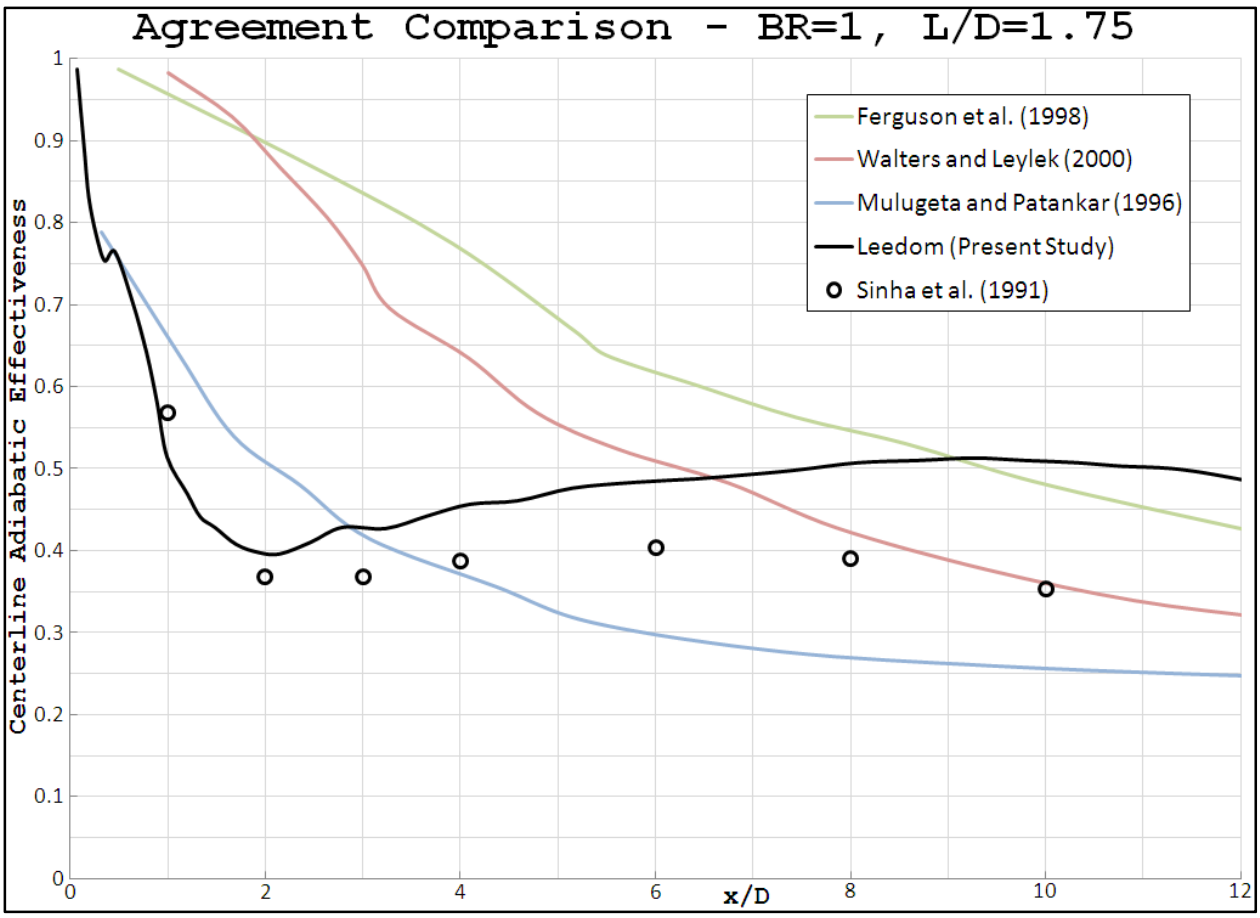

Figure 3.23: Agreement comparisons to other studies

The lateral profile closer to the hole (plotted in Figure 3.24) shows excellent agreement to experiments, but the profile close to the outflow only shows a qualitative agreement. There is a rounded, overpredicted peak at the centerline that tapers down to similar levels at z locations halfway in between two holes.

The overprediction of film cooling adiabatic effectiveness is further exaggerated in the lower blowing ratio (BR=0.5) case (Figure 3.25). The centerline effectiveness is poorly represented, but the gross error in the laterally averaged effectiveness can be attributed to the more prominent role of the horseshoe vortex observed in the local adiabatic effectiveness plots and temperature fields. The horseshoe vortex takes cool air from the leading edge of the jet and deflects it far to the sides of the jet, where mixing farther downstream brings it to the surface. The horseshoe

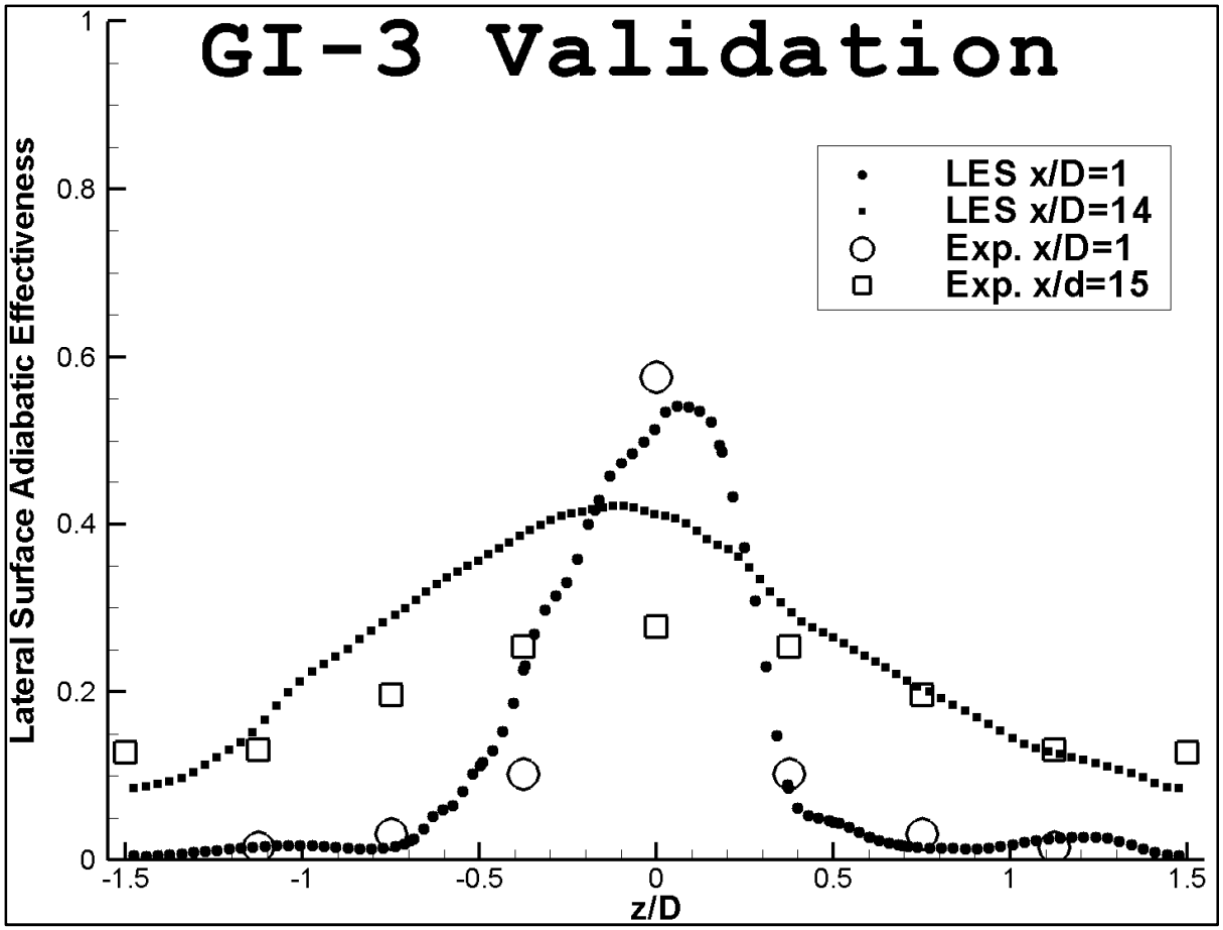

Figure 3.24: Lateral surface effectiveness profiles, BR=1, L/D=1.75

vortex is less dominant in the temperature field as the blowing ratio is increased. Since the horseshoe vortex plays a key role and the horseshoe vortex emanates from the leading edge of the hole, one logical explanation is that the turbulence at the inlet of the crossflow domain in the experimental case affected the horseshoe vortex and decreased its tendency to help cool downstream. The lateral effectiveness profiles shown in Figure 3.26 again agree qualitatively with the experimental data (same shape, same trends), but consistently overpredict performance.

The surface adiabatic effectiveness validation presented in this section show that while agreement is not perfect, the data is still usable for further analysis.

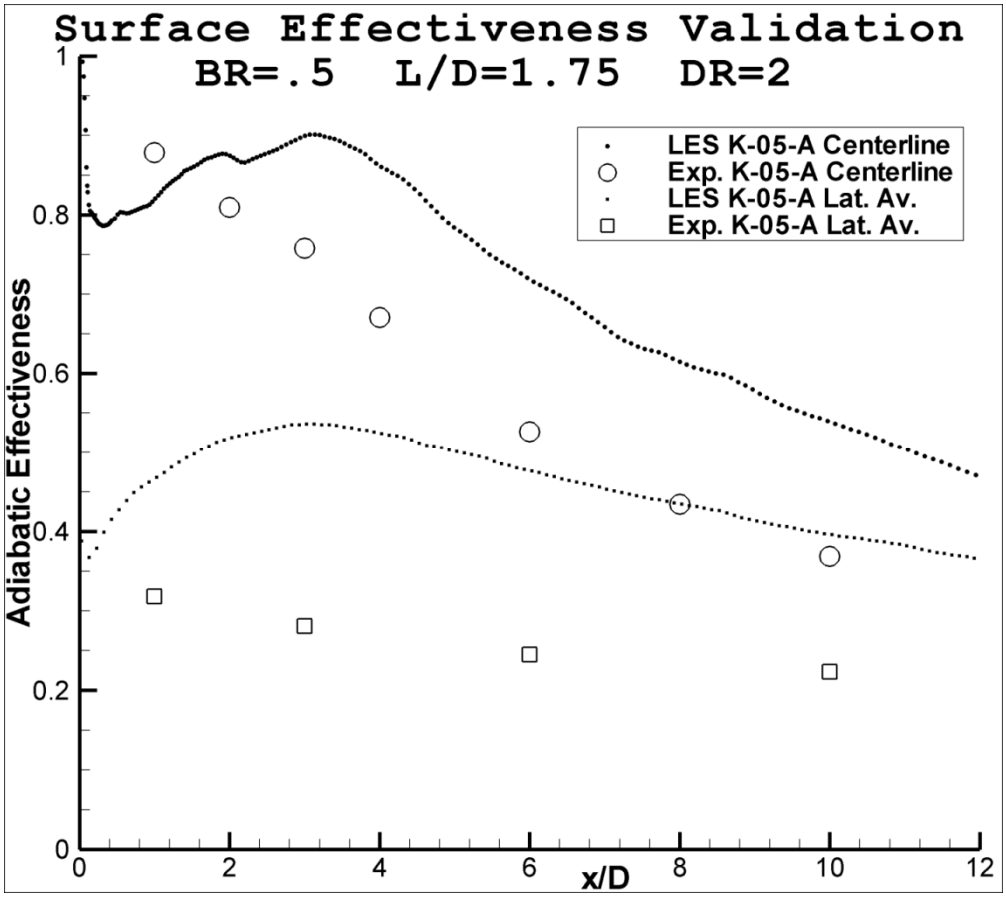

Figure 3.25: Validation of case K-05

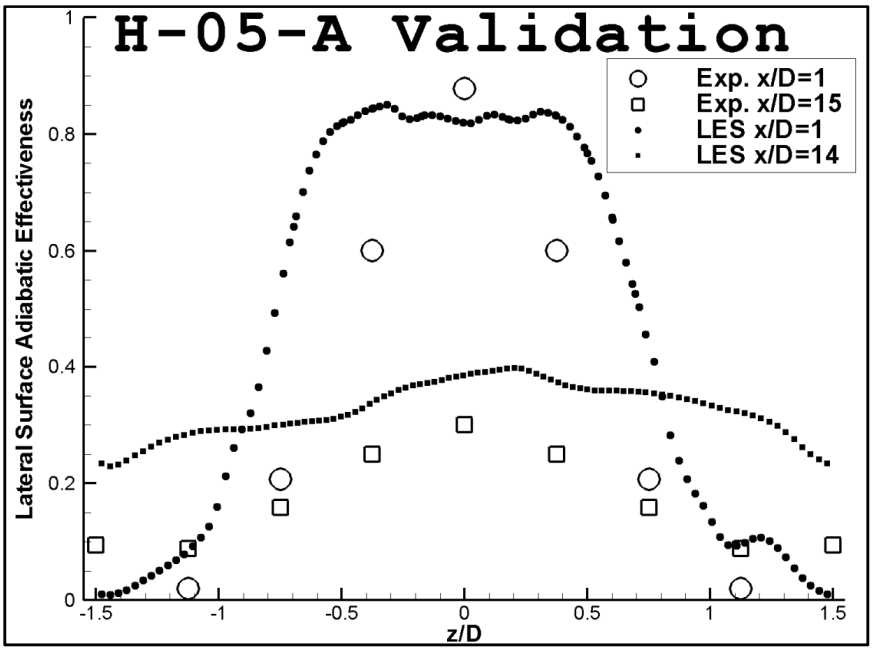

Figure 3.26: Lateral surface effectiveness profiles, BR=0.5, L/D=1.75

3.5 Round Hole Results

3.5.1 Results

This section will present results from all cylindrical hole runs. All scatter plots (such as Figure 3.27) are reported with the x/D datum located at the trailing edge of the cooling hole, while the surface contour plots (Figure 3.31, for example) are reported with the x/D datum being located at the center of the hole exit.

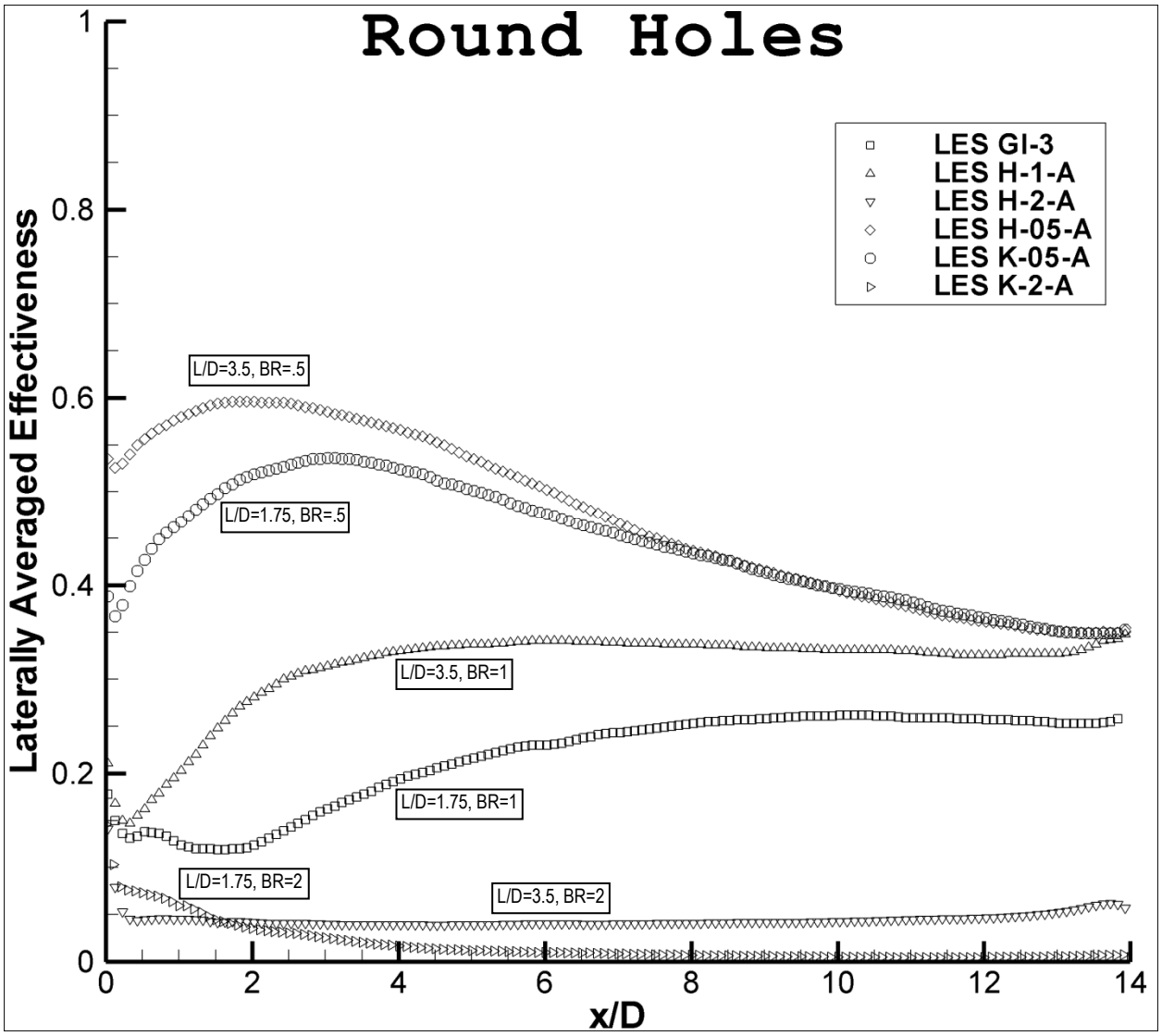

Figure 3.27: Comparisons of laterally averaged effectiveness with varied L/D and blowing ratio

Figure 3.27 shows the laterally averaged adiabatic effectiveness profiles for all of the production round hole cases in this study. The jet in the blowing ratio 2 case experiences blow off over the entire domain; this blow off phenomenon may be observed in Figure 3.29. The delivery tubes 3.5 hole diameters long tend to outperform the 1.75 hole diameter lengths, especially at x/D locations closer to the hole. This confirms the trend noted by Lutum and Johnson (1999) and shown in Figure 3.28 of better performance for the longer delivery tubes. The blowing ratio 0.5 cases show markedly better performance closer to the hole than their higher blowing ratio counterparts, which can be explained by the decreased penetration of the jet into the crossflow in the lower blowing ratio cases. While twice as much coolant is effused in the blowing ratio 1 cases, the excess vertical momentum carries it farther from the surface, rendering a decrease in performance. Towards the outflow of the domain, the performance of the blowing ratio 1 jets approach the performance of the blowing ratio 0.5 jets. If the decay trends continue, the blowing ratio 1 case will have better performance in the far field because of the larger amount of coolant, but this is beyond the outflow of this simulation.

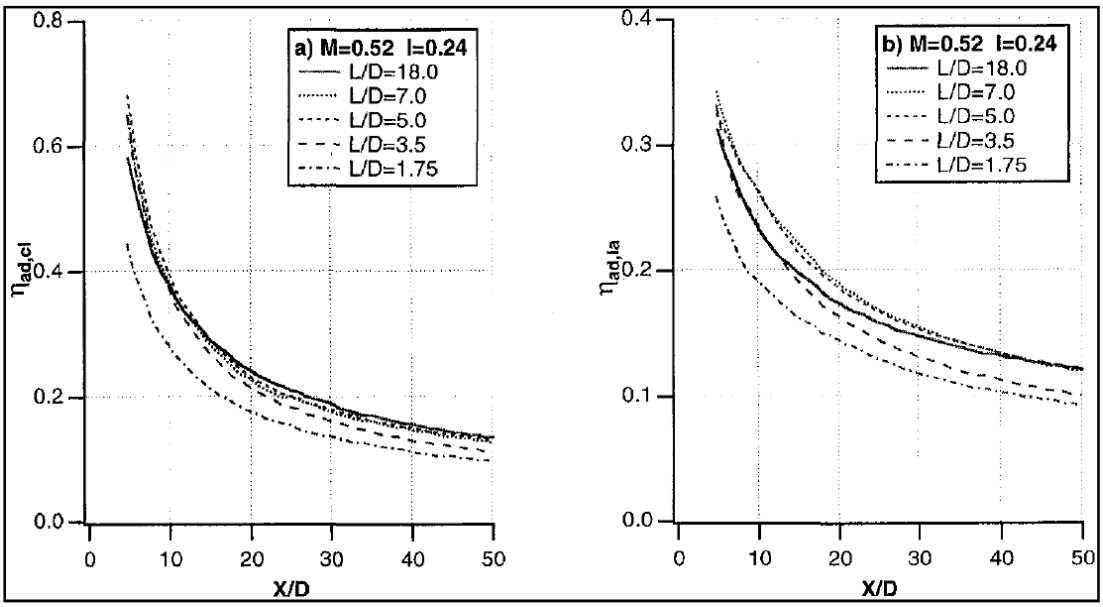

Figure 3.28: Trend of lower adiabatic effectiveness performance from shorter holes shown by Lutum and Johnson (1999), centerline (a) and laterally averaged (b)

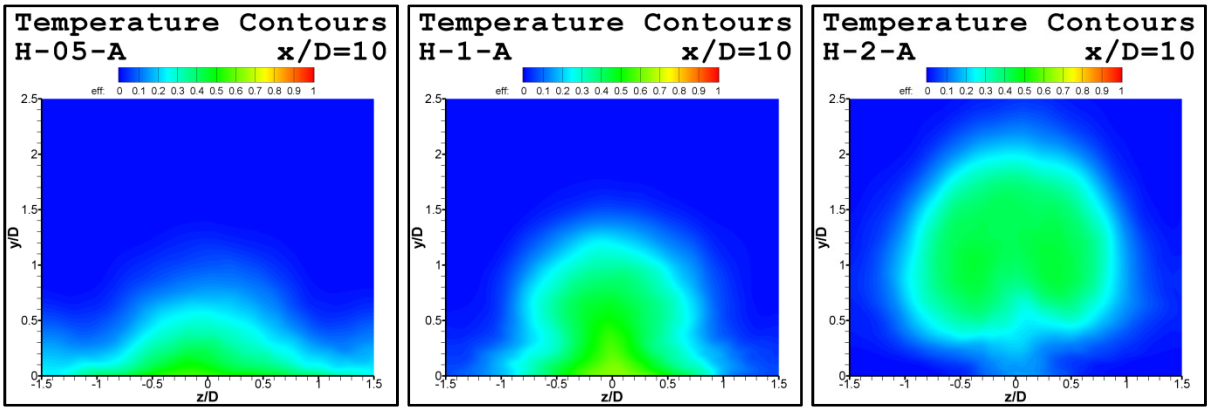

Figure 3.29: Jet blow-off in the round hole, L/D=3.5 cases - left to rght, BR=0.5, BR=1, BR=2

The blow off tendency of the cylindrical hole jet at higher blowing ratios is illustrated in Figure 3.29, which shows the vertical development of the jet 10 hole diameters downstream of the hole. This blow off is the cause of the abject failure of the blowing ratio 2 jets to adequately cool the surface (see Figure 3.30 and compare the contour plots to Figure 3.31). These figures also show the generally superior performance of the L/D=3.5 tubes as compared to the L/D=1.75 tubes. Not only is the surface effectiveness directly behind the hole better for the longer tubes, but the horseshoe vortex and overspill of coolant from the lateral sides of the hole provide more effective cooling for the longer holes. The blow off in the shorter tubes is also illustrated to be more pronounced at any given x/D location.

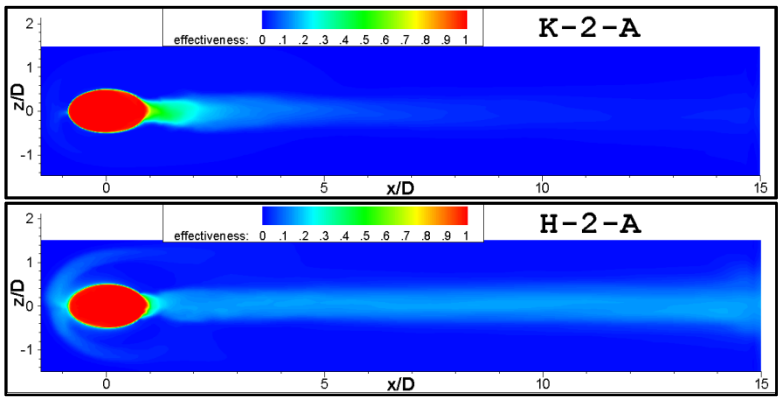

Figure 3.30: Blowing ratio 2 with round hole, L/D=1.75 (top), L/D=3.5 (bottom)

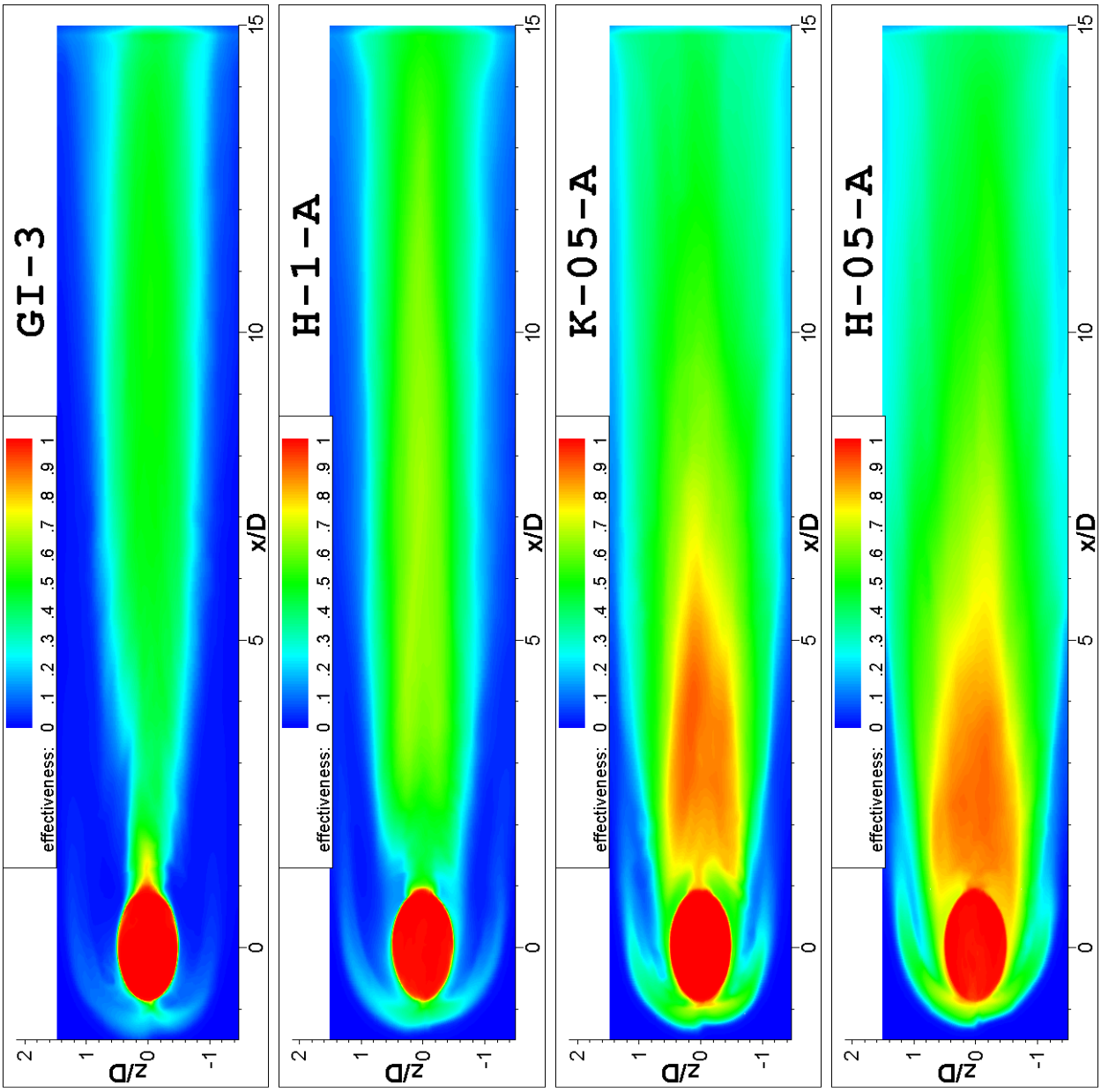

Figure 3.31: Left to right: BR=1, L/D=1.75; BR=1, L/D=3.5; BR=.5, L/D=1.75; BR=.5, L/D=3.5

3.5.2 Horseshoe Vortex

The horseshoe vortex is clearly visible in both time-averaged and instantaneous results as shown in Figure 3.32 and Figure 3.33.

The horseshoe vortex is not a completely steady phenomenon. The vortex shows up in the time averaged results, but it is only a mean location of the stronger vortices which are constantly

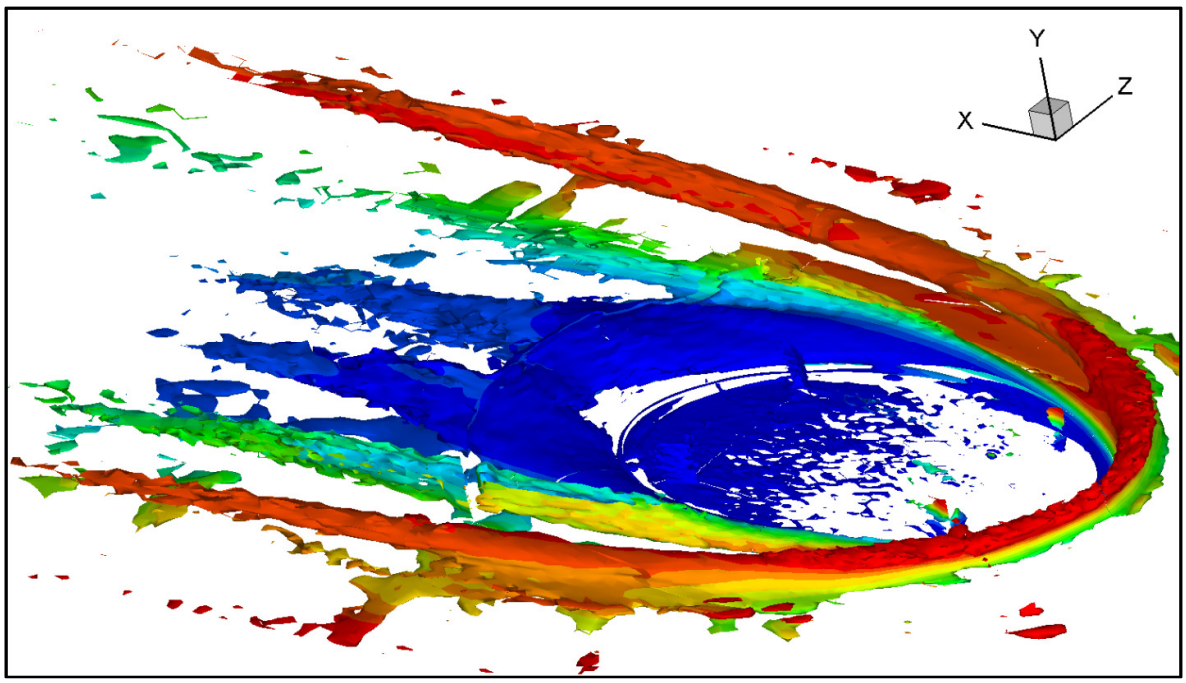

Figure 3.32: Averaged results, H-05 run, isosurface of pressure Laplacian colored by temperature

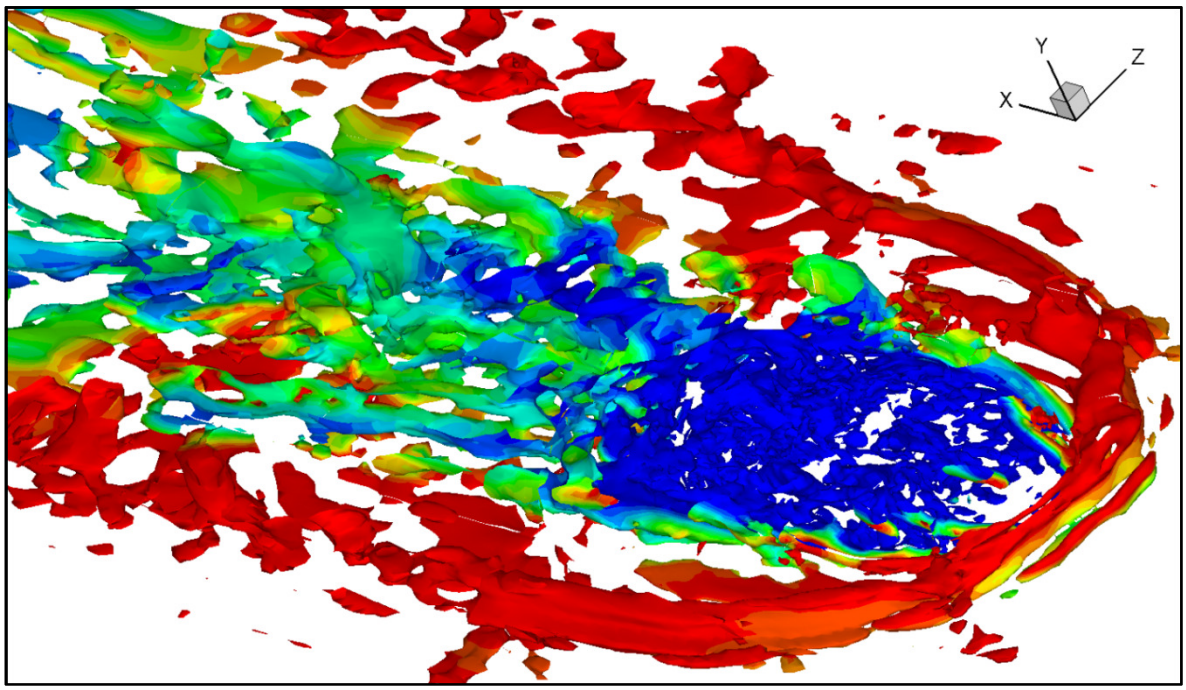

Figure 3.33: Instantaneous results, H-05, isosurface of pressure Laplacian colored by temperature

being shed and evolving. An example of this evolution is shown in Figure 3.34, where the vortices are each given letters and tracked. In the first frame, vortex A and C correspond to the two vortices that are dominant most of the time. Vortex B (which rotates in the opposite

direction) becomes stronger as time passes and interacts with the stronger vortex A, pushing under it. Vortex A is then absorbed into vortex C, which takes up the same location that vortex A had occupied. Vortex D, which at the beginning of the time series was very weak and farther upstream, moves to take vortex C's former location and becomes stronger. By the end of the time series, we see that the evolution is complete with vortices C, F, D, and E replacing vortices A, B, C, and D from the first frame.

This delicate interaction between the vortices could be easily disturbed by a perturbation at the inlet of the crossflow domain, making this one of the most highly suspect behaviors (as mentioned in the validation section.) The contour plot serving as the background for the streamlines is the temperature field, with red being the hot crossflow temperature and blue being the coolant temperature. Note how the horseshoe vortex pulls coolant from the leading edge of the jet and deposits it on the surface upstream of the hole. Since the horseshoe vortices then extend laterally and stay close to the surface, they are easily visible on the local surface effectiveness plots (Figure 3.31).

3.5.1 Delivery Tube Behavior

The profiles of velocity at the exit plane affect the cooling effectiveness plots downstream of the hole; the profiles at the exit plane are a result of the flow field in the delivery tube. The flow field in the delivery tube is not uniform at the Reynolds numbers of interest here. Jetting is the generic name given to the tendency of part of the delivery tube to carry most of the coolant in a jet smaller than the tube. Figure 3.35, Figure 3.36, and Figure 3.37 attempt to document the average behavior of this jetting effect. The v velocity color contours are shown, and slices are taken perpendicular to the y axis so that the contours are proportional to the volume flow rate (and mass flow rate, since the density is largely constant within the tube.) Thus, the red areas

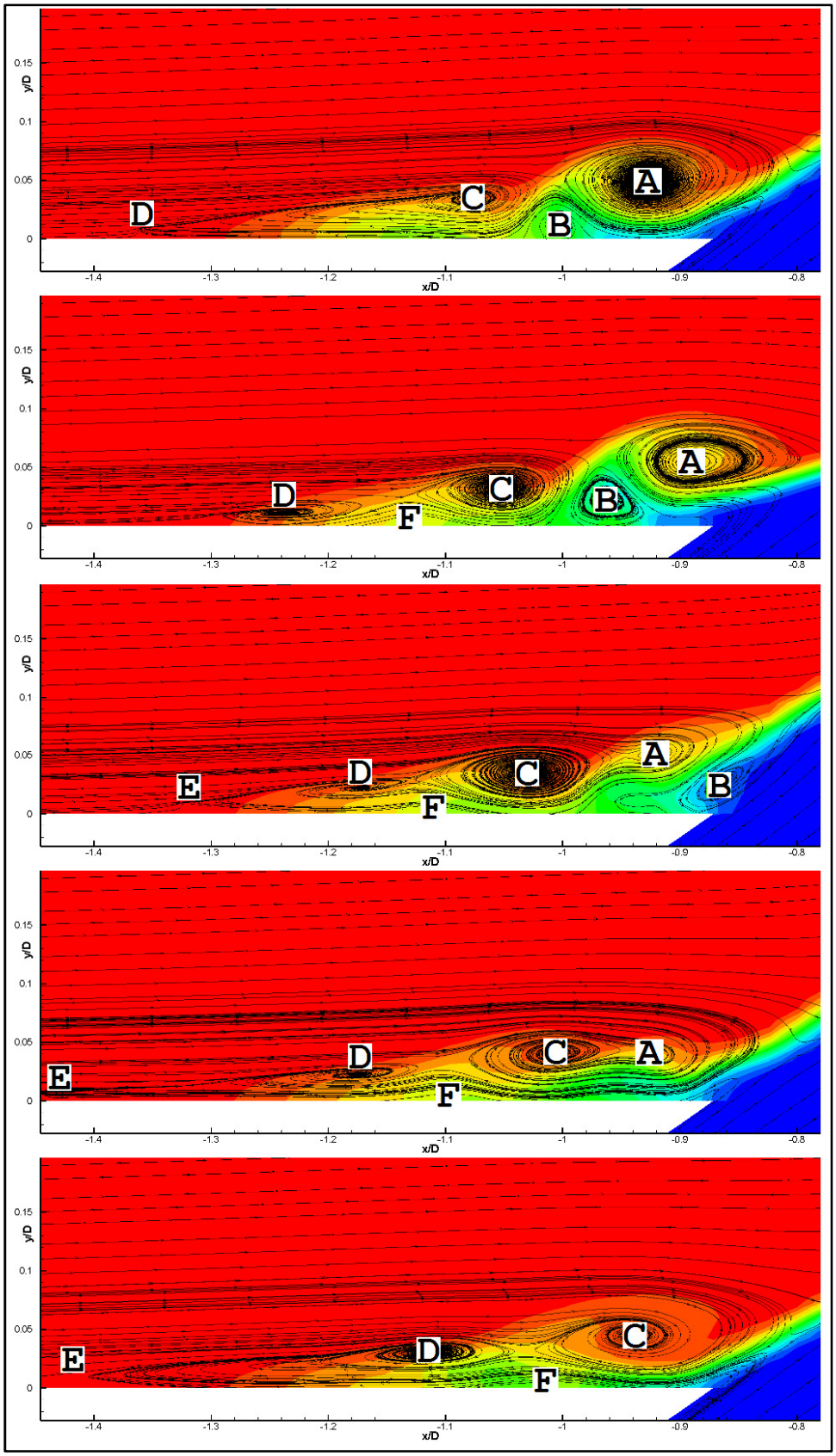

Figure 3.34: Horseshoe vortex evolution - streamlines on a temperature contour plot

indicate the jetting region and the blue areas indicate areas where the flow is either stagnant or recirculating.

The contour plots at the exit plane of the L/D=1.75 case are less uniform than similar plots of the L/D=3.5 case (both having a blowing ratio of 1, Figure 3.35). The plots of flow within the tube indicate that at the entrance to the tube, similar characteristics are exhibited in both tube

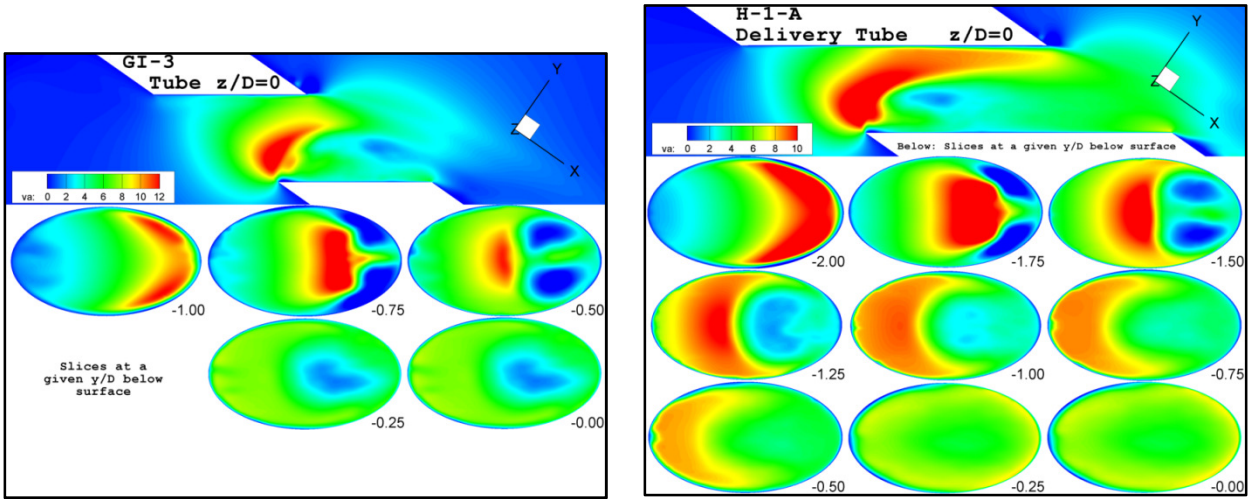

Figure 3.35: Jetting in the blowing ratio 1 cases, L/D=1.75 (left) and L/D=3.5 (right)

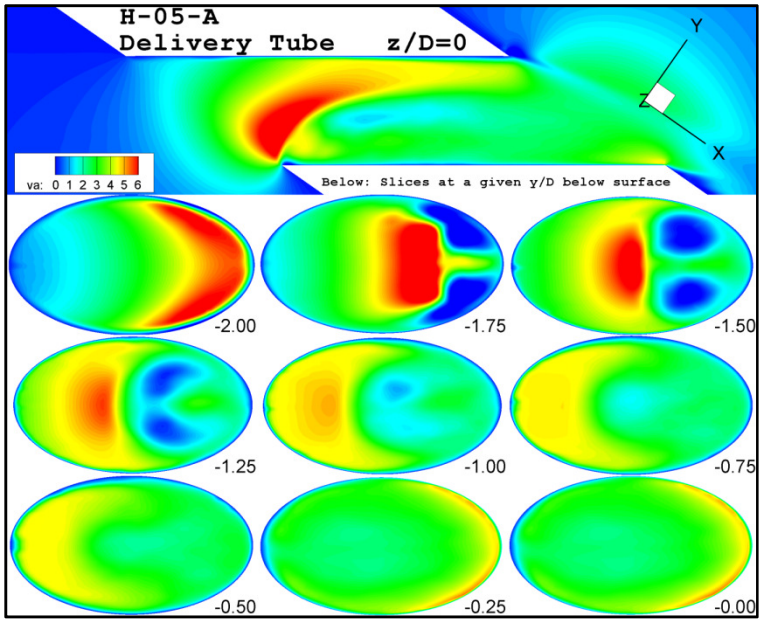

Figure 3.36: Jetting in the blowing ratio 0.5, L/D=3.5, round hole case

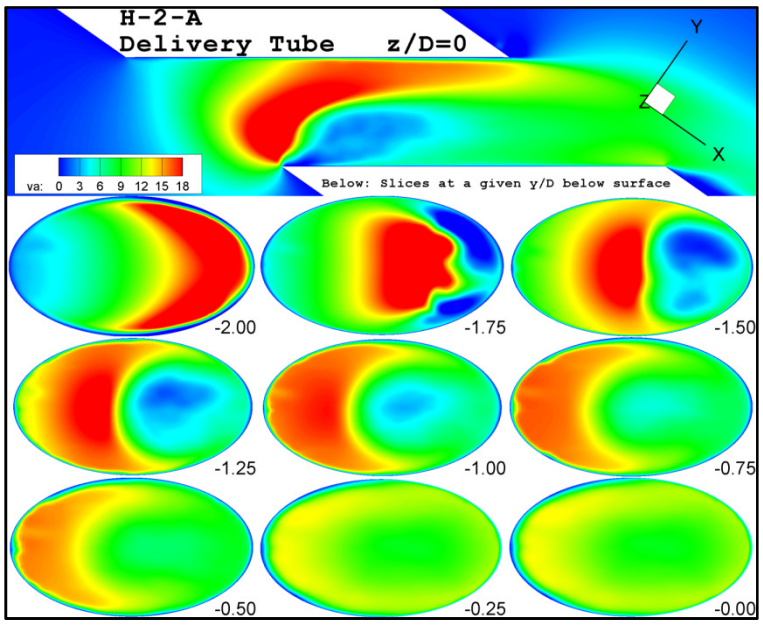

Figure 3.37: Jetting in the blowing ratio 2, L/D=3.5, round hole case

lengths. The shape of the jetting region is quite similar in both cases, but the extra 1.75 hole diameters of the longer delivery tube allow the jetting effect to dissipate somewhat and the contours become more uniform. The jetting, it may thus be inferred, is not beneficial to the film cooling performance of the hole. In fact, as evidenced and discussed previously, the longer delivery tube consistently has better performance, especially closer to the hole.

The similar plots at L/D=3.5 and varied blowing ratio indicate that the jetting effect is more prominent at higher blowing ratios. This is to be expected, as the jetting is due to the inertia of the fluid entering the hole. As the local Reynolds number is increased (by increasing the velocity of the fluid in the tube), the inertial forces dominate the flow even more, with the net result being a stronger jetting effect. Additionally, the recirculation regions occur in two distinct pockets which merge into one farther up the hole. This behavior should be noted and kept in mind when investigating the shaped geometries later.

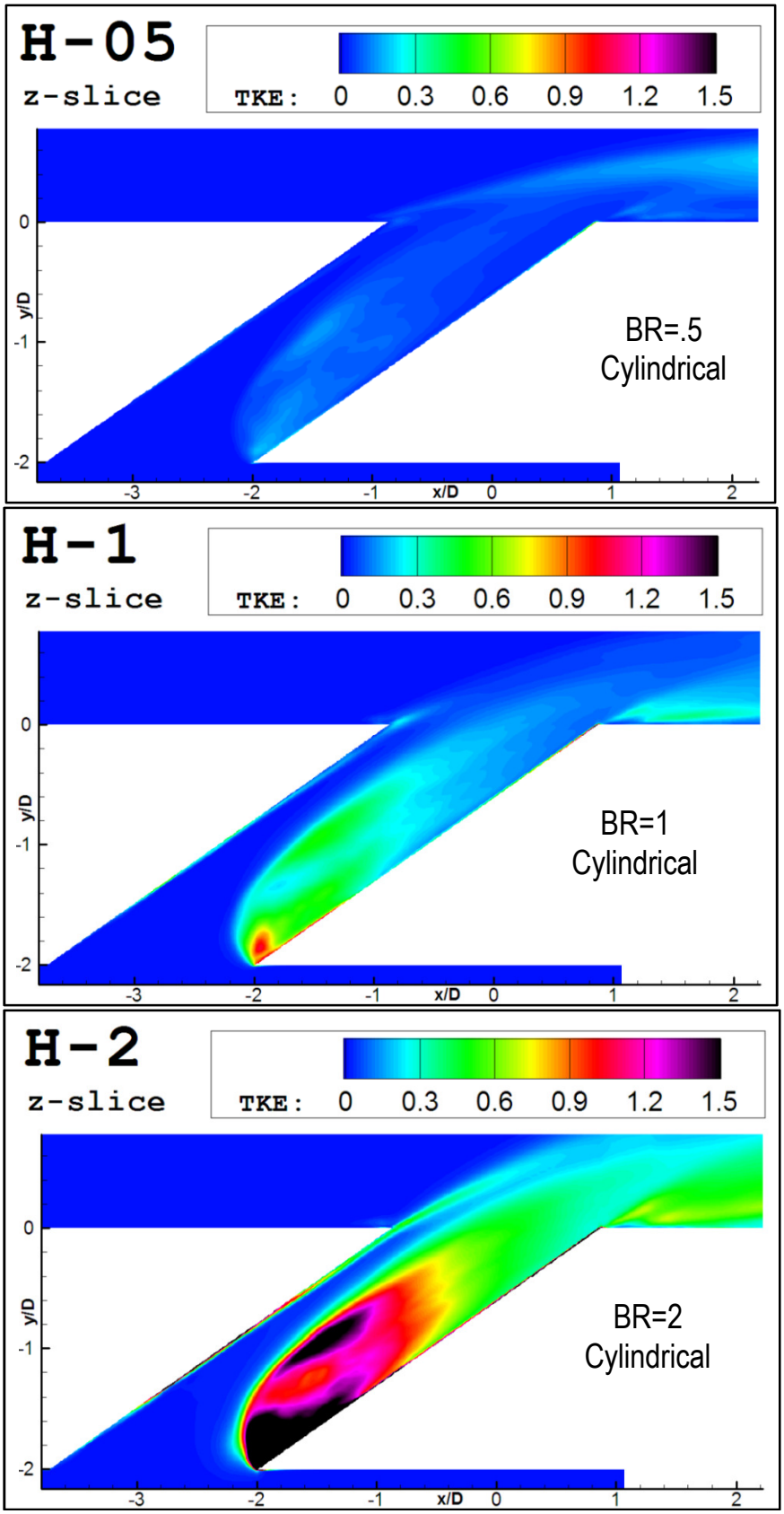

Figure 3.38: Turbulent kinetic energy within the hole (z=0 slices)

The turbulent kinetic energy in the cooling hole is illustrated in Figure 3.38. The lower blowing ratio cases tend to have less turbulence within the delivery tube, which is consistent with a lower Reynolds number based on jet velocity. The jetting effect near the front of the hole appears to induce a more laminar flow, while the separated flow at the back side of the hole shows more turbulent characteristics. This separation is a result of the sharp turn the coolant is required to make on the downstream side of the tube as the coolant enters the tube. Surprisingly, the turbulence in the delivery tube is higher than that found in the shear layer between the jet and the crossflow in all cases except for the lowest blowing ratio (BR=0.5) case. More plots of the turbulent behavior in the delivery tube and in the crossflow are provided in Appendix C.

3.5.2 Jet Blow-Off, Recirculation, and DSSN Vortices

Figure 3.39, Figure 3.40, and Figure 3.41 show the trailing edge phenomena that affect film cooling effectiveness. Blow off (where the jet penetrates the crossflow and crossflow fluid becomes entrained below the jet) and recirculation aft of the hole (which generally accompanies blow off in the form of a vortex behind the jet with vorticity in the z direction) are relatively well understood. DSSN vortices are discussed and illustrated in section 2.2, but may briefly be described as twin vortices behind the jet on the surface behind the hole with vorticity in the y direction. These features may be observed in Figure 3.39, Figure 3.40, and Figure 3.41. These figures show temperature contours and streamlines at the symmetry plane and a plane slightly above the surface.

The first things to notice in these plots are the color contours of temperature in the z/D=0 plots. For the blowing ratio 0.5 case (Figure 3.39), the jet turns the corner at the hole exit and follows the surface, resulting in good film cooling effectiveness. Figure 3.40 shows the jet blowing off of the surface in the blowing ratio 1 case, with the hot and cold air mixing and becoming entrained underneath the jet. Figure 3.41 shows the jet blowing off the surface more

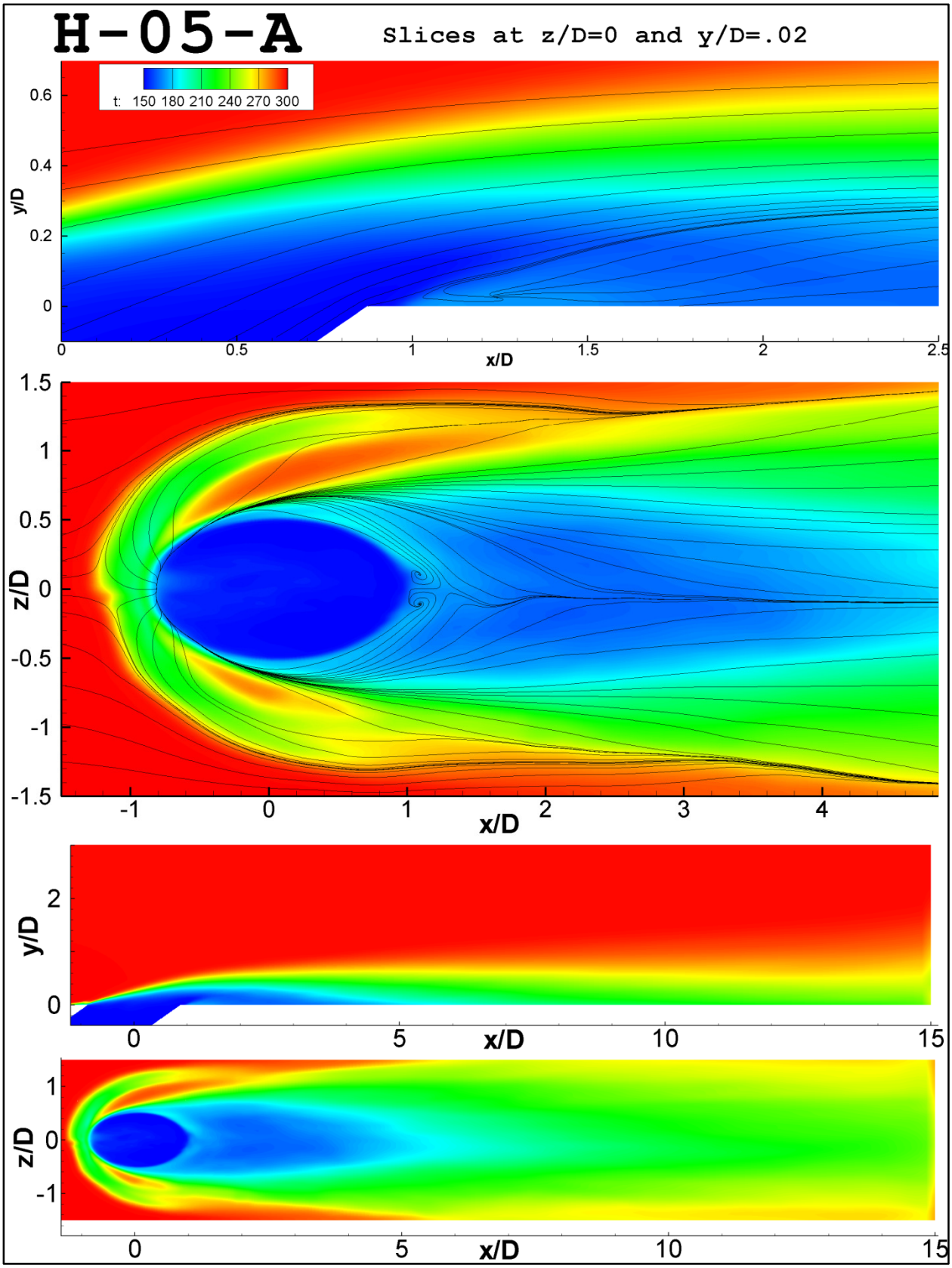

Figure 3.39: Streamlines and temperatures, BR=0.5, L/D=3.5

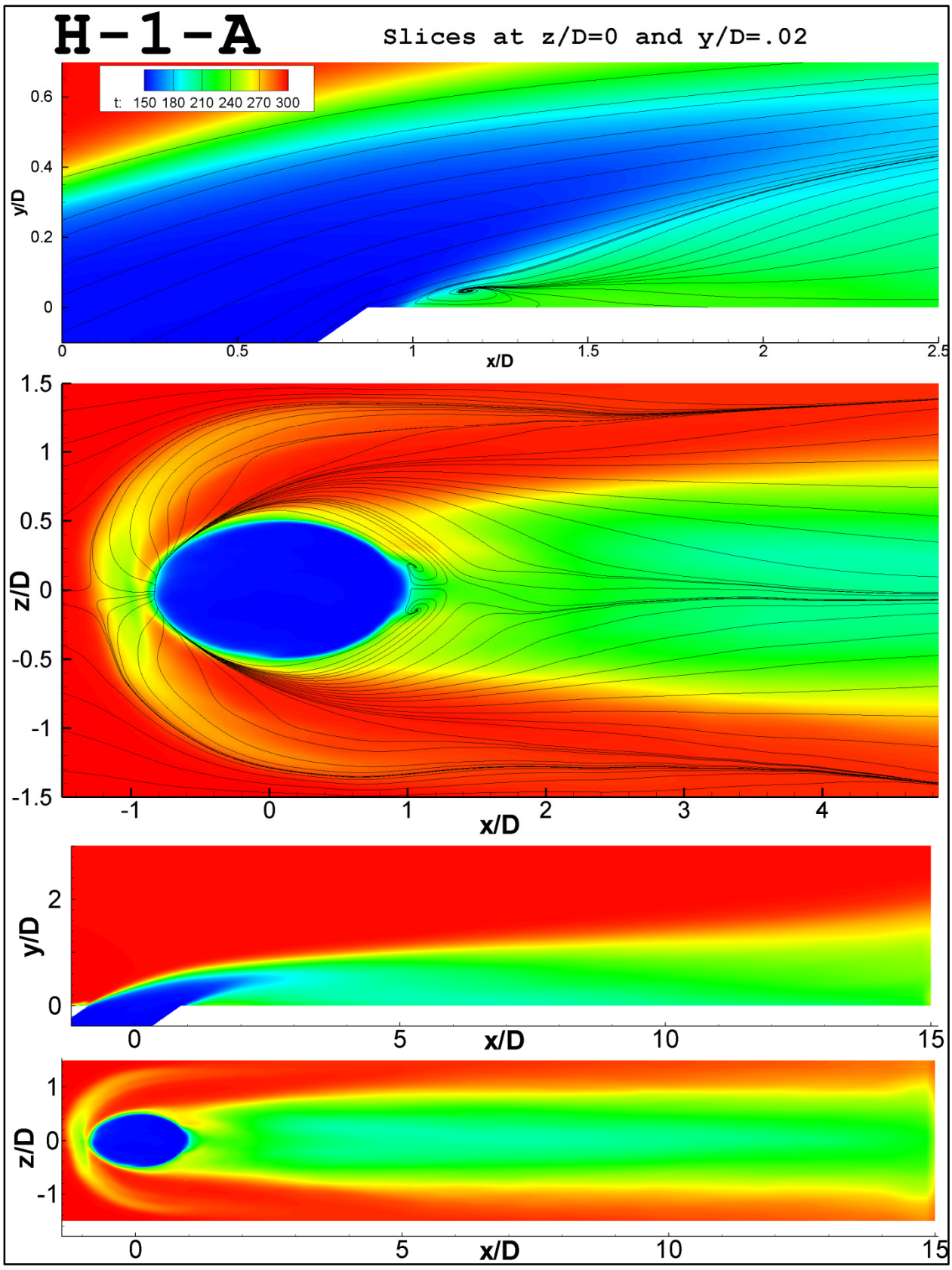

Figure 3.40: Streamlines and temperatures, BR=1, L/D=3.5

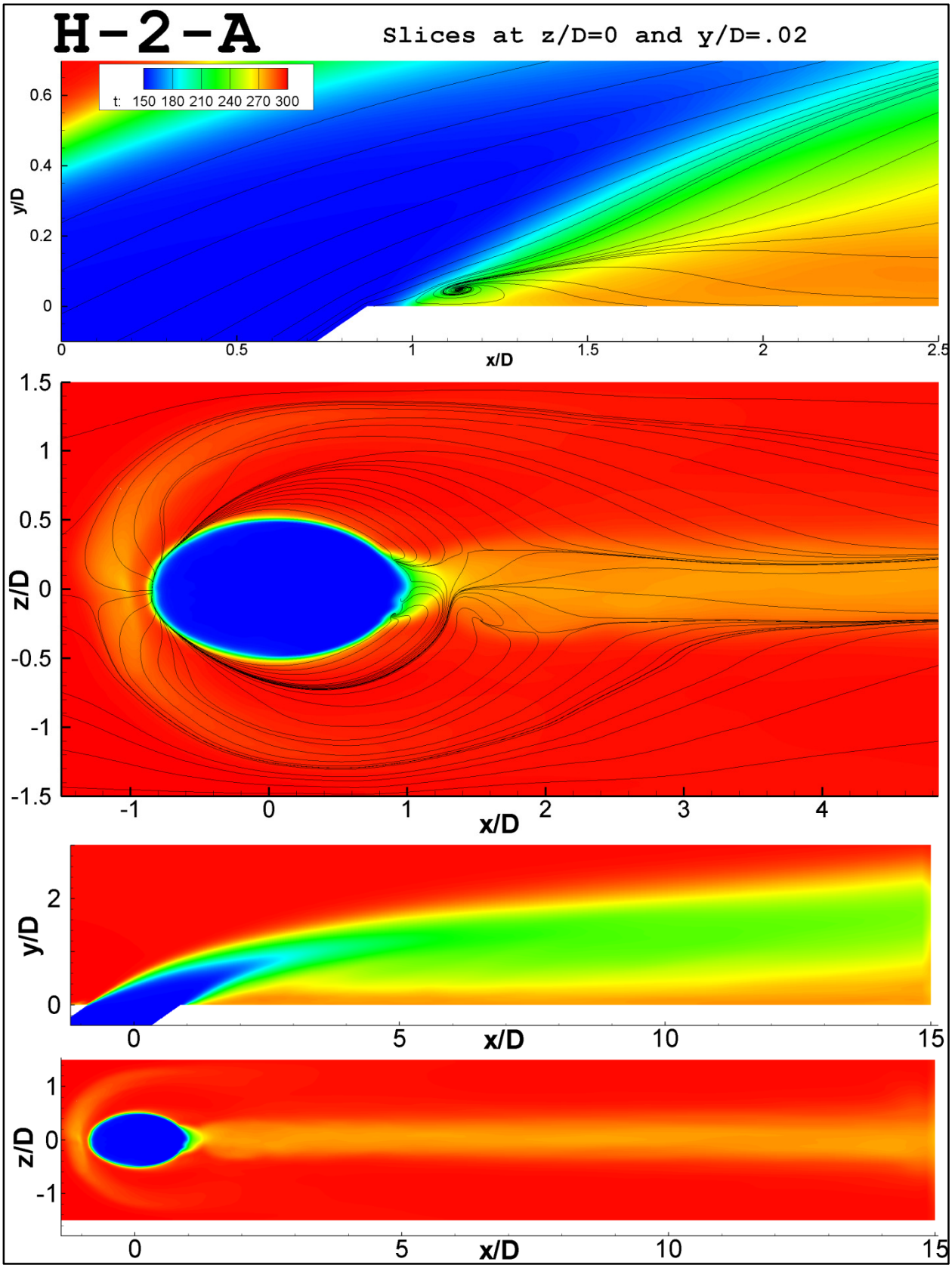

Figure 3.41: Streamlines and temperatures, BR=2, L/D=3.5

vigorously in the blowing ratio 2 case, with the jet clearly staying close to the 35° inclination over most of the domain shown in this figure. The fluid entrained beneath the jet is of even higher temperature than the blowing ratio 1 case.

The z/D=0 slice in each figure also shows the recirculation region in each case. The recirculation becomes larger and more prominent as the blowing ratio is increased, but even in the lowest blowing ratio case of 0.5 it is still present. The DSSN vortices are easily visible in the streamlines of the lower slice of each figure, taken just above the surface. The fluid that becomes entrained below the jet comes from around the sides and forms these vortices. The one measurement of the strength of these vortices to alter the solution is how far behind the hole they extend to. In the lower blowing ratio case, the recirculation only reaches downstream .2 hole diameters, but this increases to .4 and about .7 hole diameters in the BR=1 and BR=2 cases respectively. Measurement in the BR=2 case is difficult due to the asymmetry of the solution. Also note that the center of circulation of the DSSN vortices moves from the trailing edge of the hole in the BR=0.5 case to sit farther apart and farther upstream as the blowing ratio is increased.

The instantaneous behavior that leads to the DSSN vortex pattern on the average plots shown is isolated in Figure 3.42 for the BR=1 case. The semi-transparent isosurfaces of temperature (at T=250K) show the three-dimensional shape of the jet and its effect on the surface temperatures (using the same contour temperature scales as Figure 3.40) at four time steps. The crossflow wraps around the jet as it would a vertical obstruction, bringing process gas and coolant around to become entrained underneath the jet. This is not a laminar operation, and the coolant that wraps around the hole is shed from the body of the jet periodically. Some of the shed coolant vortices are tracked with letters in both an isometric view and on a smaller, normal surface temperature plot (temperature contour levels are the same as those in Figure 3.40). Vortex A

travels around and is amalgamated into the fluid entrained beneath the jet; since this entrainment is very close to the surface, this parcel of coolant (and the other shed vortices near the surface) does much more to cool the surface than a parcel which is convected far from the surface in the mainstream flow of the jet. Vortex C is weaker than the others tracked and dies out between frames 3 and 4, while vortices A, B, and D are more typical. If more coolant could be induced to shed into the area where these vortices exist, it stands to reason that cooling effectiveness would increase because of the increased volume of coolant in the entrainment region under the jet.

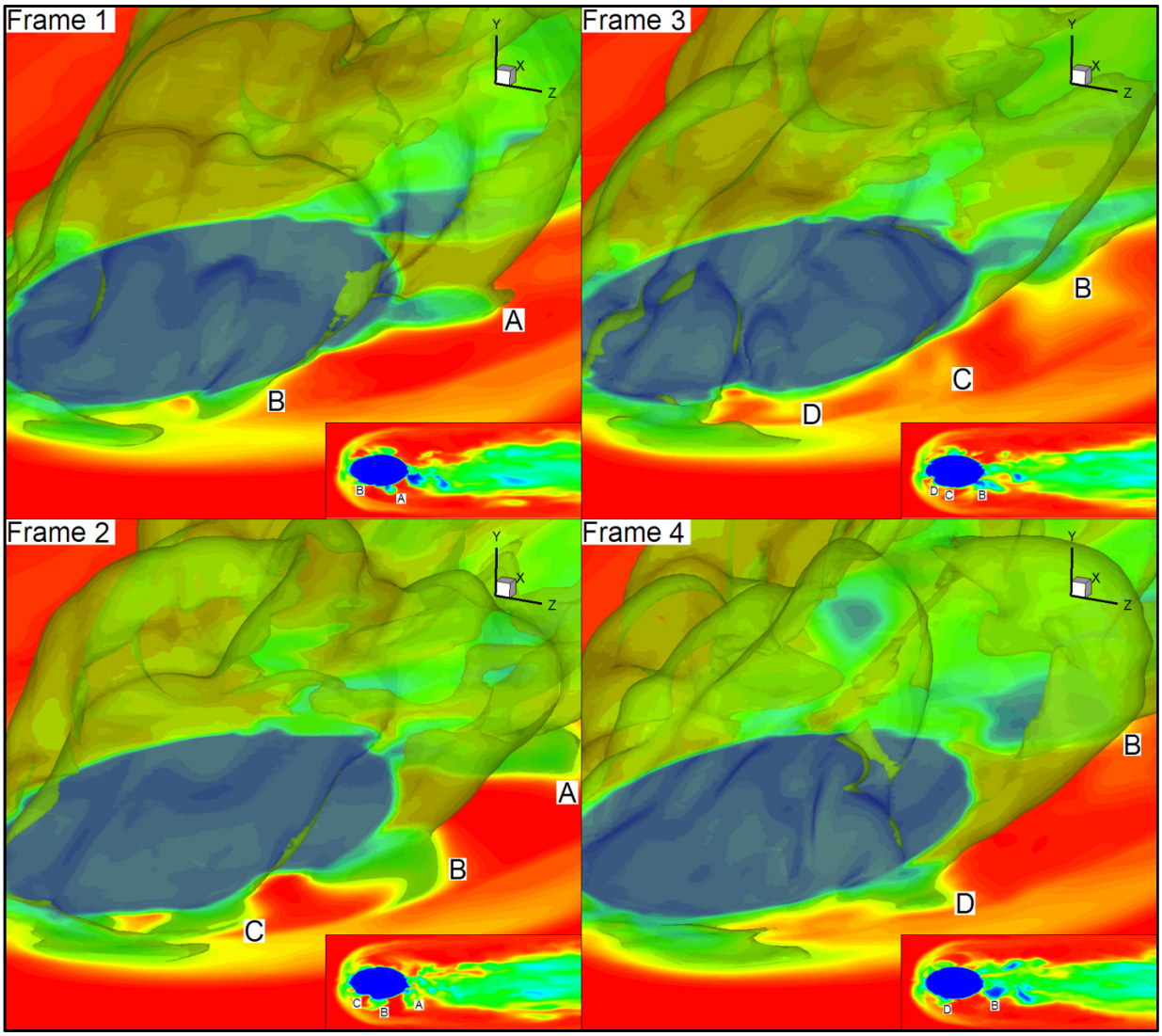

Figure 3.42: Time series of coolant wrapping around hole into wake – BR=1

3.6 Shaped Hole Results

3.6.1 Results

Surface adiabatic effectiveness results are shown first as scatter plots of laterally averaged effectiveness with x location (Figure 3.43-47). It should again be noted that all measurements are made from the same location at the trailing edge of the round hole, which is located .872 hole diameters aft of the center of the hole in each case. This is done to allow comparison to the plots in the validation section, which adopted this convention from the experimental results provided

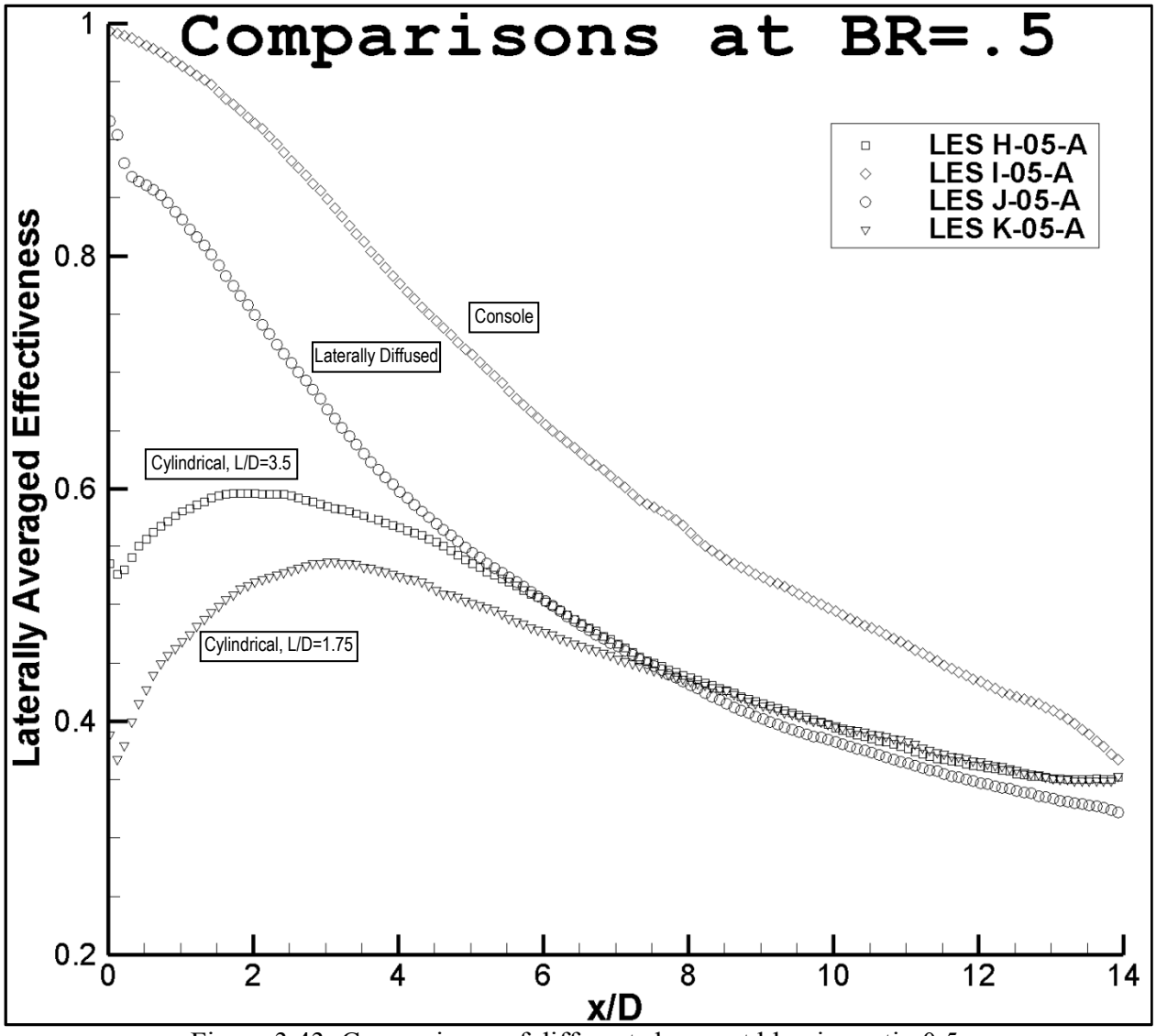

Figure 3.43: Comparisons of different shapes at blowing ratio 0.5

by Sinha et al. (1991). Centerline adiabatic effectiveness is not shown because while the maximum effectiveness at a given x location in the cylindrical hole case may be at the centerline, this is not the trend in the shaped holes. Thus, such a comparison of centerline effectiveness was not felt to be appropriate.

The comparisons of laterally averaged adiabatic effectiveness (Figure 3.43, Figure 3.44, and Figure 3.45) are discussed here. The first thing to note is that the console hole consistently outperforms the other geometries, with the second place finisher being the laterally diffused

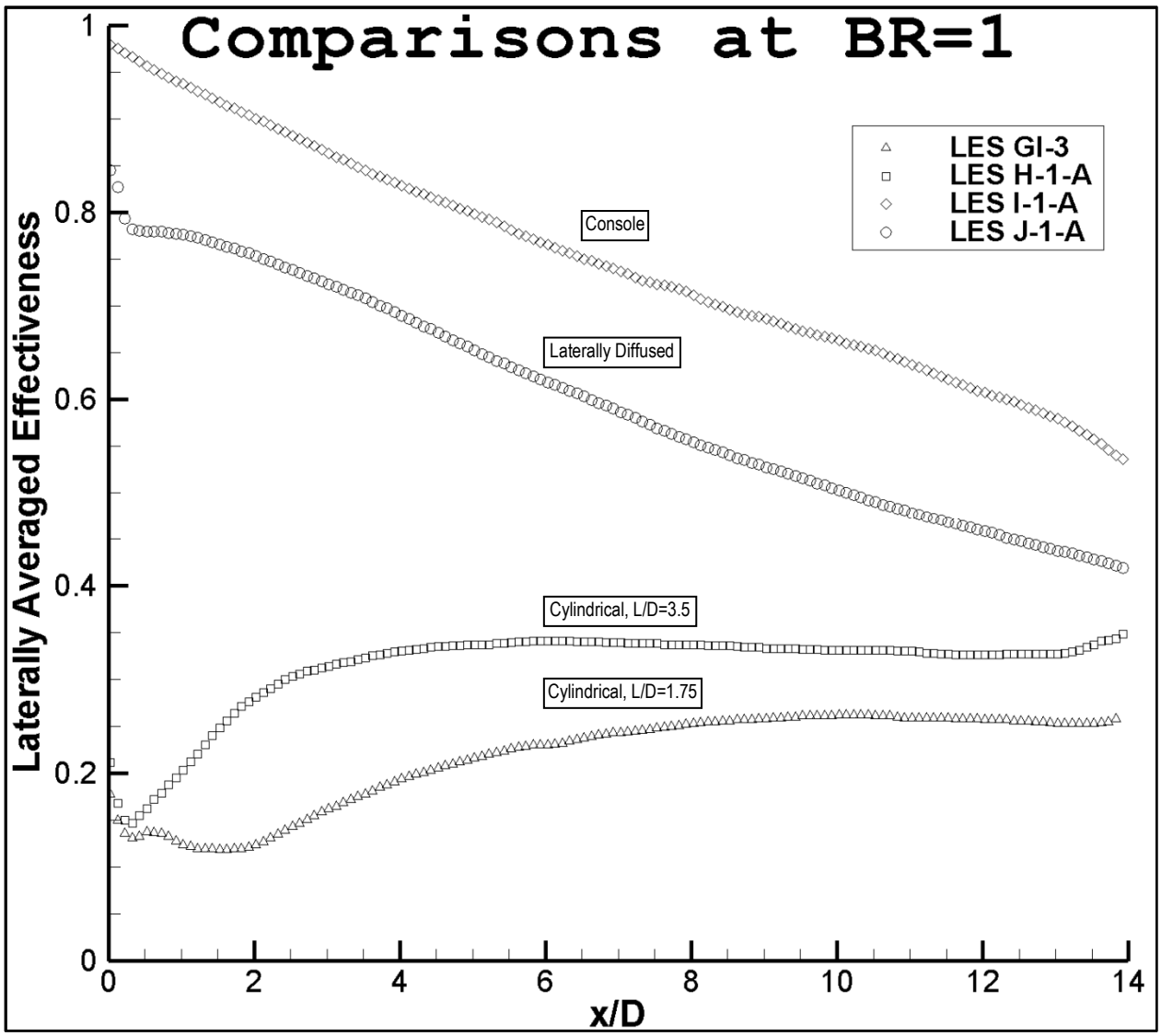

Figure 3.44: Comparisons of different shapes at blowing ratio 1

geometry, which consistently performs at 80-90% as compared to the console. The cylindrical holes are more fickle in that as the blowing ratio is increased, their performance as compared to the other geometries loses more and more ground as the cylindrical hole jet blows off of the surface with increasing blowing ratio.

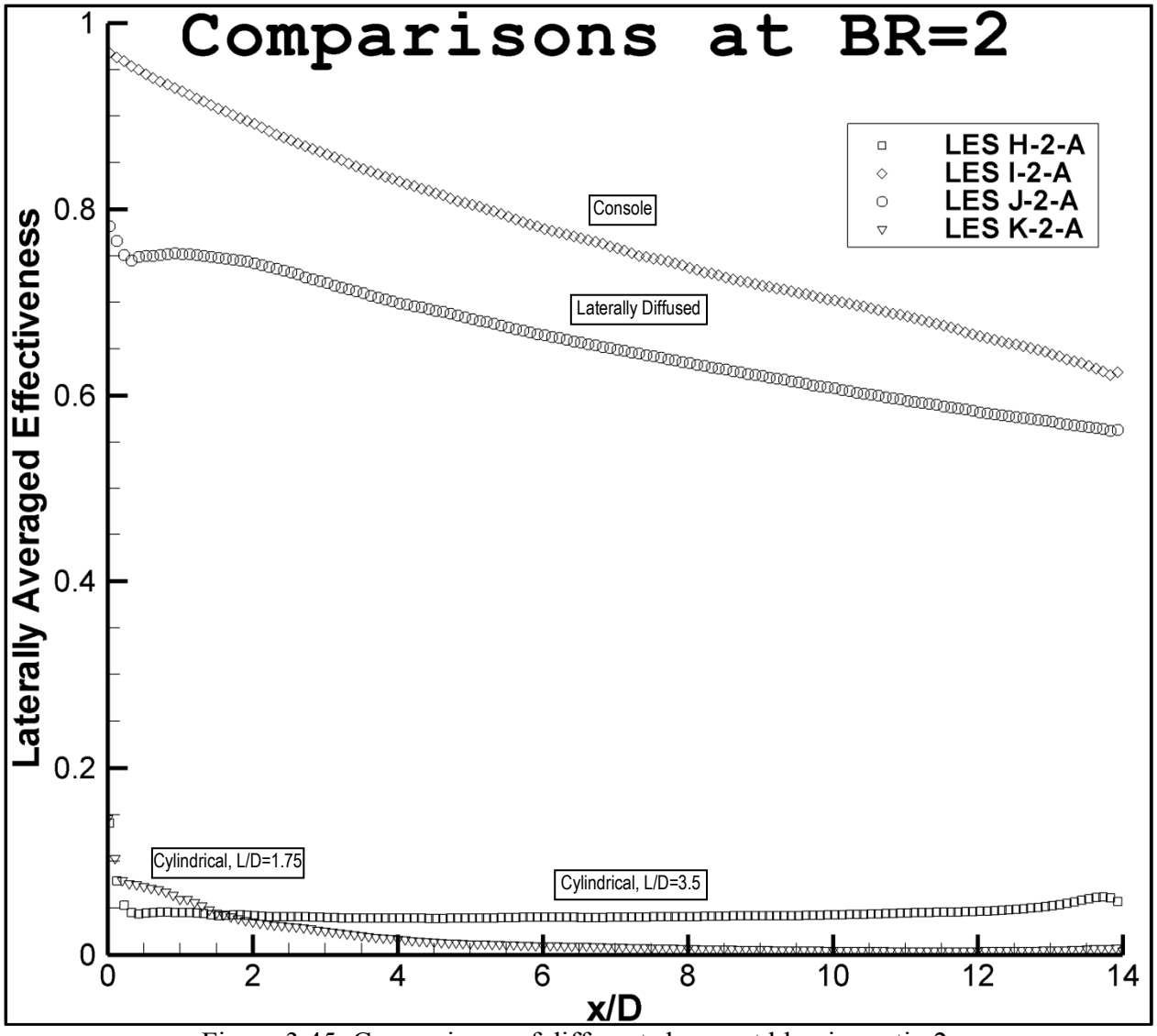

Figure 3.45: Comparisons of different shapes at blowing ratio 2

For the laterally diffused holes (Figure 3.46), increasing the blowing ratio seems only to decrease the decay rate of effectiveness with x, with only a small penalty indicated quite near to

the jet. This indicates that the increased blowing ratio and the corresponding increase in coolant mass flow rate is helping film cooling performance. Contrast this with the performance of the round holes (Figure 3.27) at increasing blowing ratio, where the increased coolant mass flow rate is not as important for the surface effectiveness as the hot air being entrained under the jet which undermines the film cooling performance.

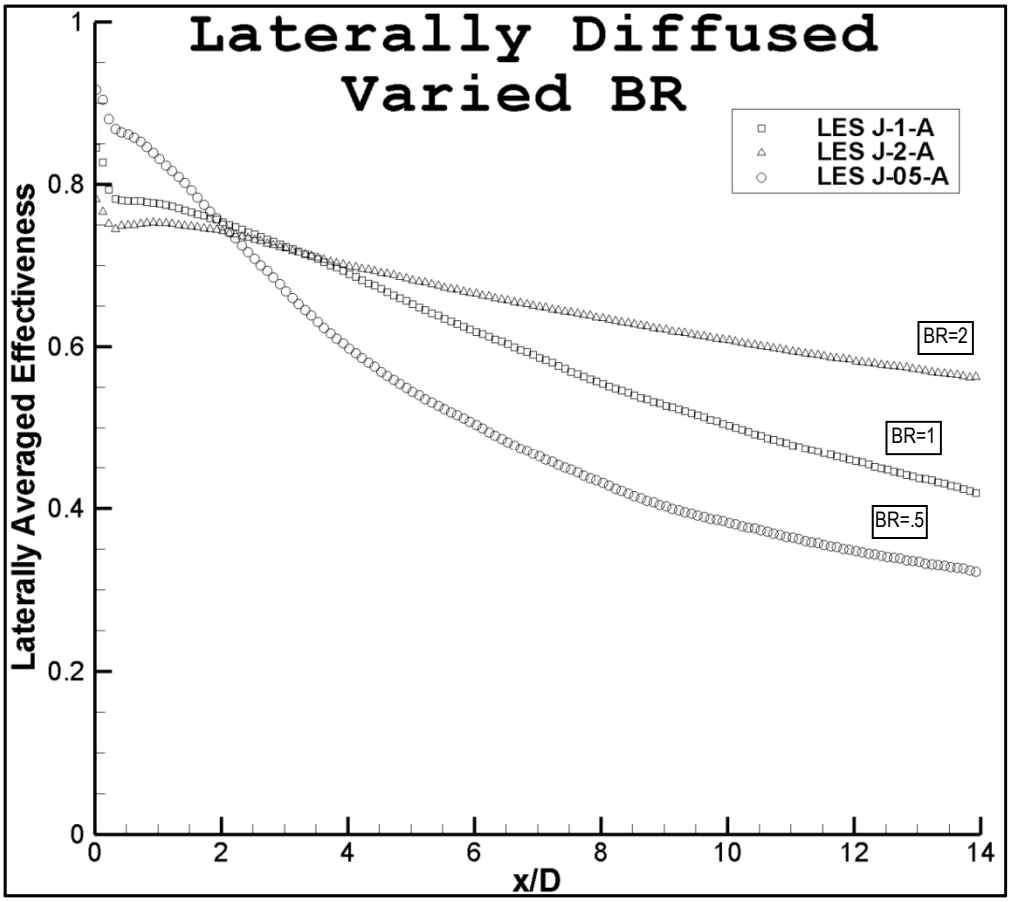

Figure 3.46: Laterally diffused geometry

For the console holes (Figure 3.47), in the same vein as the laterally diffused holes, increasing the blowing ratio seems only to decrease the decay rate of effectiveness with x. The small penalty near the hole indicated in the laterally diffused geometry with increasing blowing ratio is even less prevalent. This indicates that the increased blowing ratio and the corresponding

increase in coolant mass flow rate is helping film cooling performance, again similar to the laterally diffused geometry. Again, this is in stark contrast to the performance of the cylindrical holes (Figure 3.27).

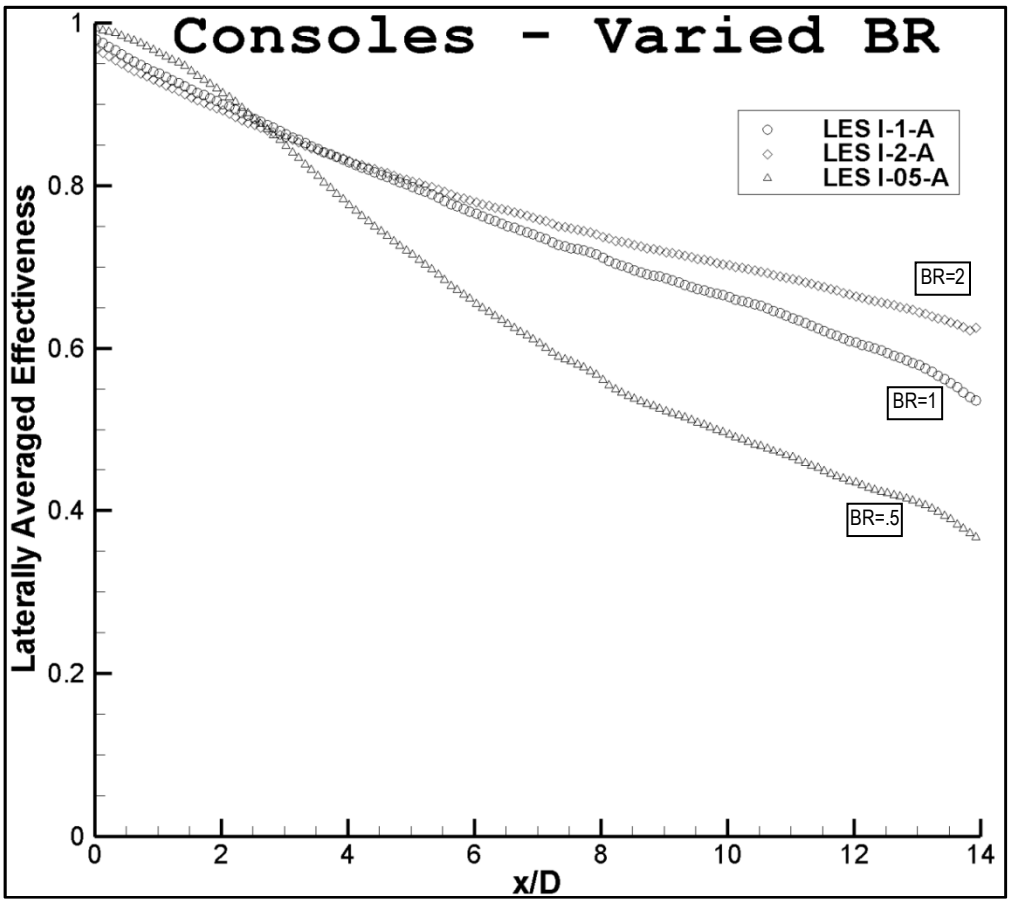

Figure 3.47: Console geometry

The local surface adiabatic effectiveness plots in Figure 3.48 show the excellent performance and resistance to blow off at high blowing ratios (as compared to the round hole). It should also be noted that the best performance of the console is not shown at the centerline (as it was in the round hole), but at the periodic boundaries downstream of where the console meets the next console. This is further explored later in this study, but it suffices to mention now that performance near the z=0 centerline of the console hole is poor compared with the performance near the z=pitch/2 locations.

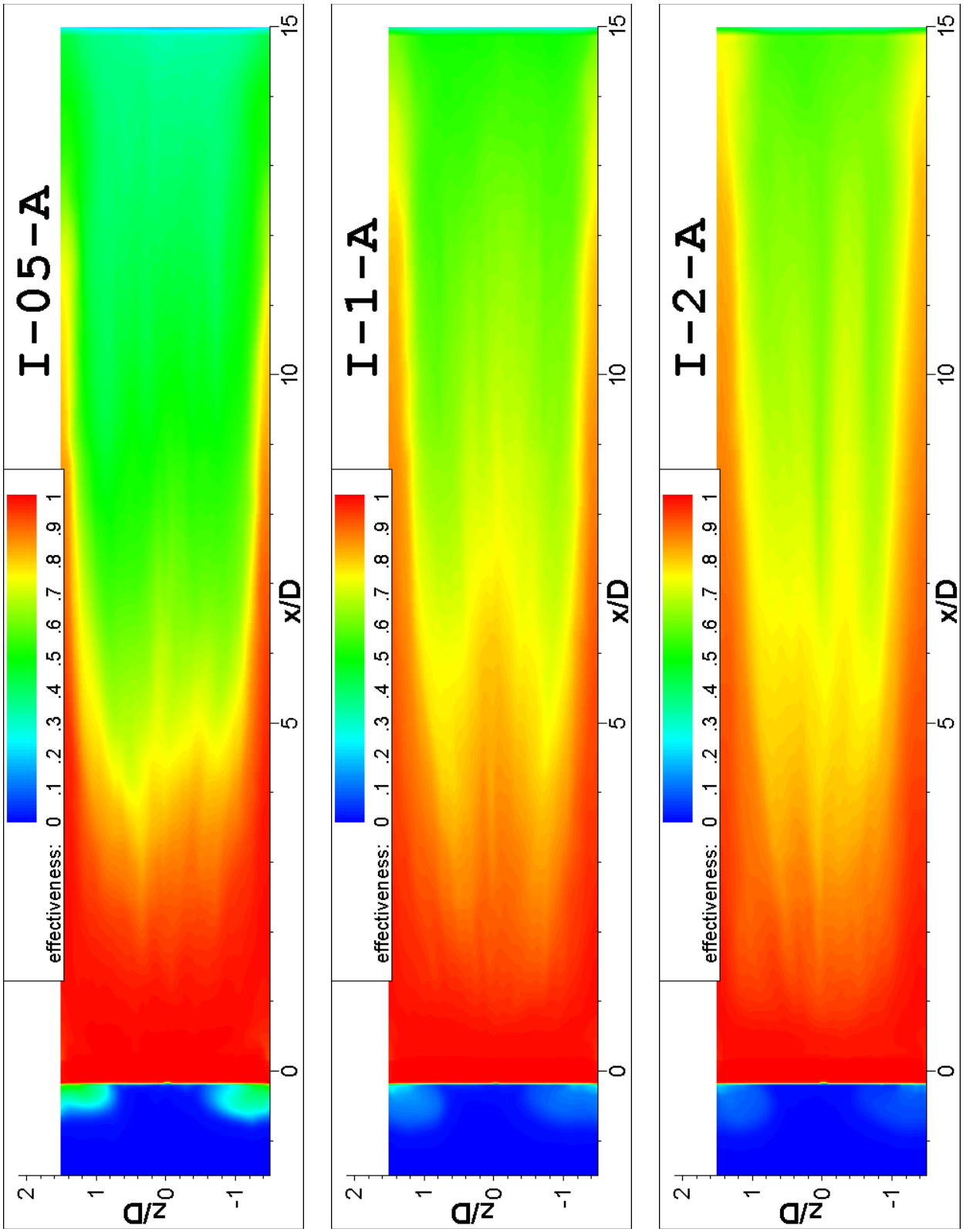

Figure 3.48: Console surface adiabatic effectiveness plots, blowing ratios of 0.5 (left), 1.0 (middle), and 2.0 (right)

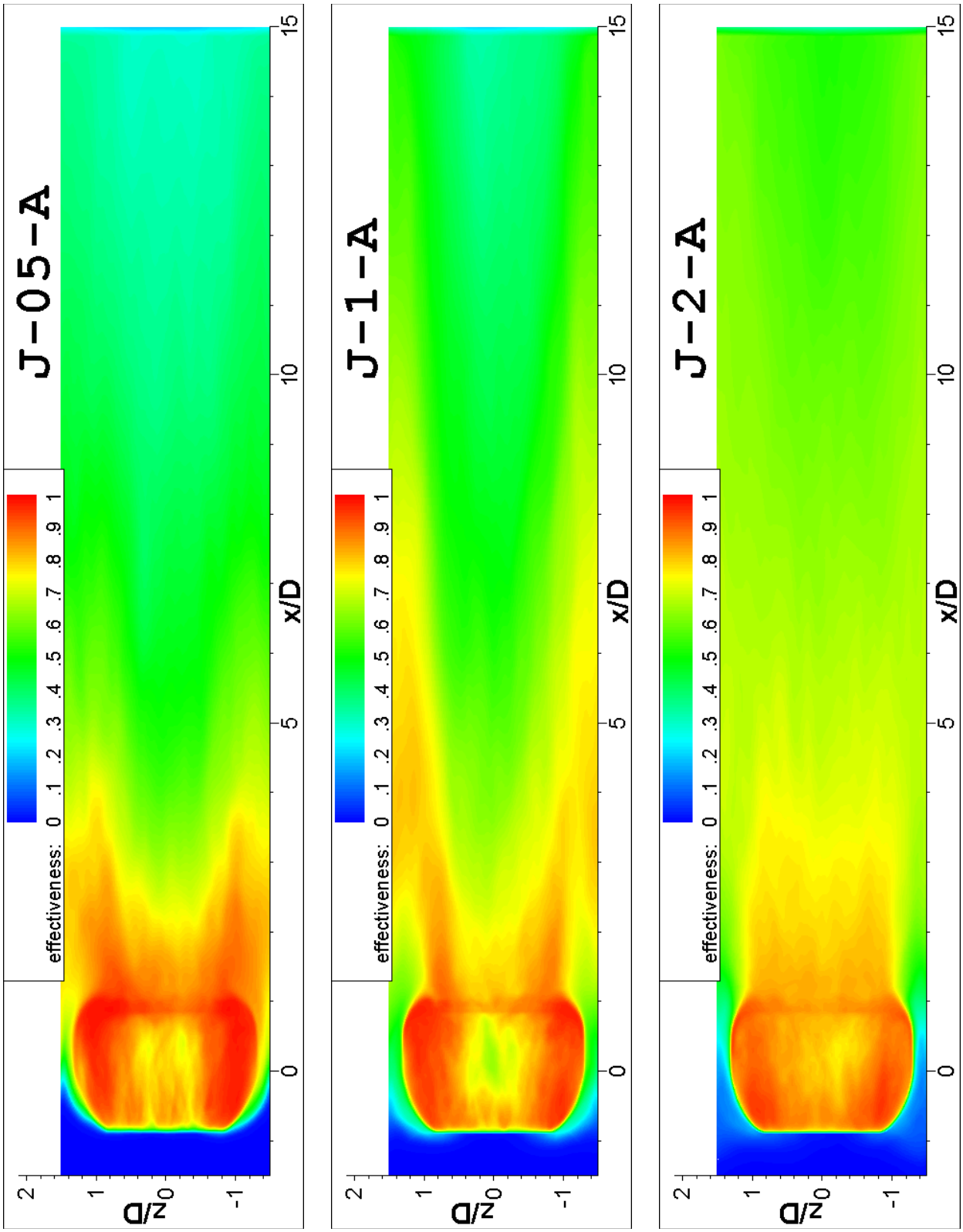

Figure 3.49: Laterally diffused hole surface adiabatic effectiveness plots, blowing ratios of 0.5 (left), 1.0 (middle), and 2.0 (right)

The local surface adiabatic effectiveness plots for the laterally diffused geometry in Figure 3.49 show the good performance and resistance to blow off at high blowing ratios (as compared to the round hole). At lower blowing ratios, the performance of the laterally diffused hole is similar to the console hole in that the best performance is not at the z=0 centerline, but downstream of the sides (laterally) of the hole. This effect is not as pronounced as in the console hole case, and when blowing ratio is increased to 2 in the laterally diffused case this trend is reduced (resulting in a more uniform lateral profile). This dual peak trend is reported in the study of Saumweber and Shulz (2008c) and shown in Figure 3.50. This can be explained by examining the behavior of the fluid in the delivery tube.

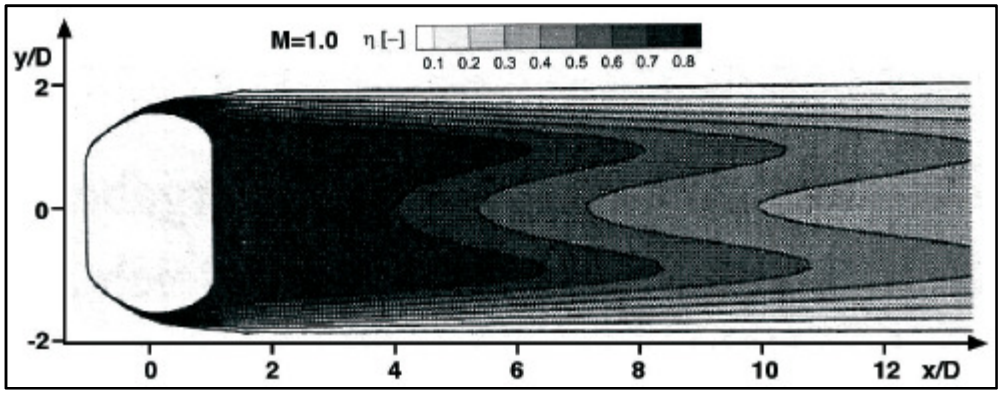

Figure 3.50: Result from Saumweber and Shulz (2008c) showing the lack of performance in terms of adiabatic effectiveness near the z=0 plane from the laterally diffused hole

3.6.2 Delivery Tube Behavior

The behavior inside the delivery tube is important because this is a key factor in the behavior of the jet at the exit plane. This, in turn, is a key factor in the downstream film cooling effectiveness of the jet. First, the exit plane behavior of the jet will be examined.

Jetting within the delivery tube in the cylindrical hole cases was discussed earlier in section 3.5.1. The tendency for the jet to shift toward the leading edge of the hole in the cylindrical

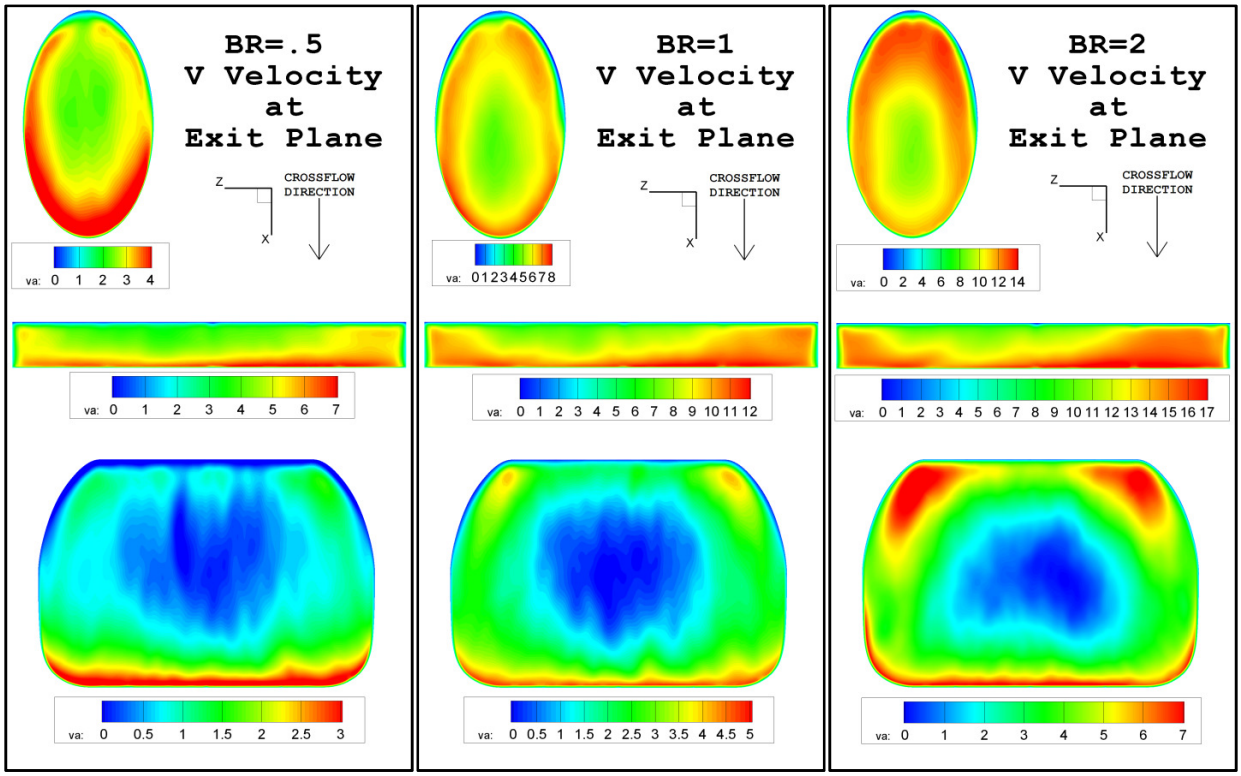

Figure 3.51: Exit plane vertical velocity contour plots at varied blowing ratios

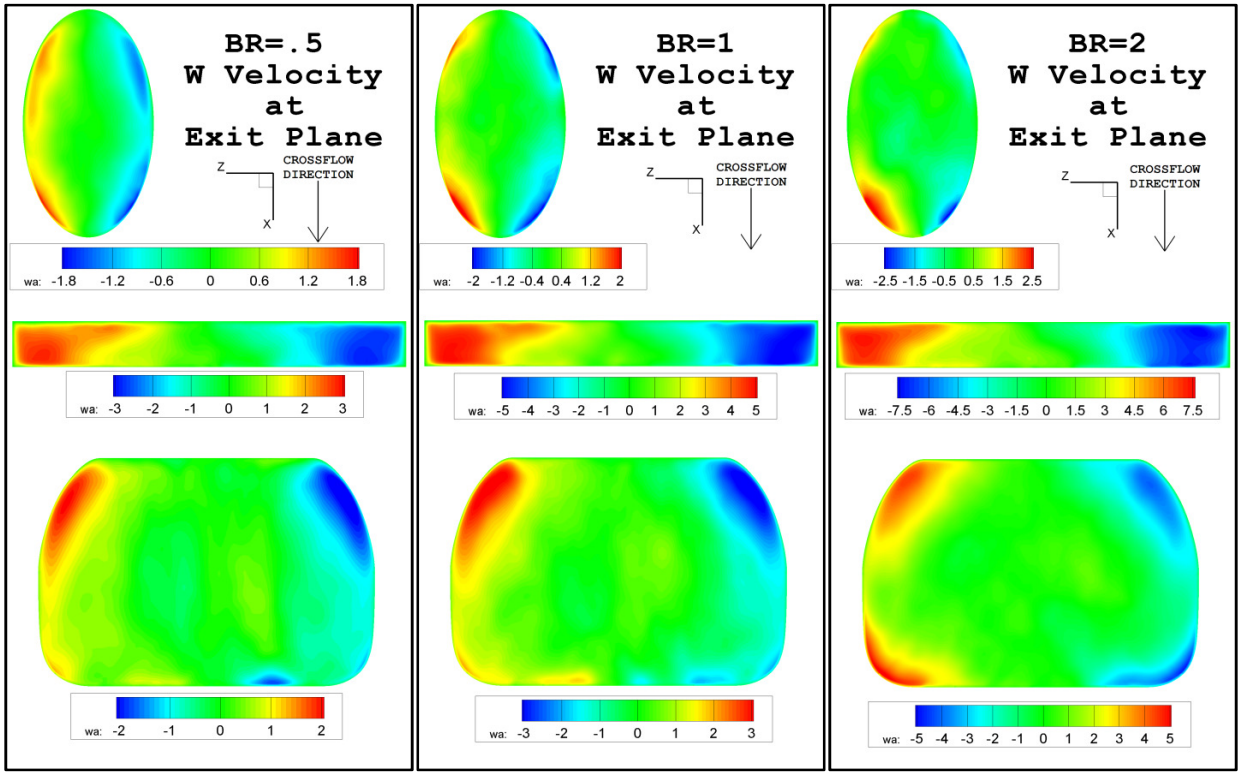

Figure 3.52: Exit plane lateral velocity contour plots at varied blowing ratios

L/D=3.5 case as the blowing ratio is increased is confirmed in Figure 3.51. This same tendency toward more coolant flow at the upwind side of the hole at higher blowing ratios is also confirmed for the laterally diffused geometry.

The lateral components of velocity at the exit plane (shown in Figure 3.52) indicate that there is a strong lateral flow away from the centerline of the jet at the sides. This is not a problem (it in fact may be an advantage) in the laterally diffused geometry because the holes are spaced apart to give the coolant that spills off of the sides a place to go. In the console case, the console hole butts directly up to the next hole, yielding two opposing jets that are trying to blow against each other into the same space. The net result of this is an upward jet at the intersections of the two consoles. This upward jet in the console case will be further documented in this study in terms of jet penetration and other effects.

The reason for the deficit in vertical velocity noted in Figure 3.51 at the center of the laterally diffused hole becomes clearer after observing the large recirculation region at all blowing ratios at the top of Figure 3.53. The jetting effect at the front of the hole is further aggravated by the diffuser action of the shape slowing the fluid. Indeed, if the diffused hole did not meet the crossflow at the top but continued upward, the jetting and recirculation effect would likely be further exacerbated because the crossflow fluid appears to impart some of its momentum on the fluid still in the hole. The center column of Figure 3.55 clearly shows the stagnation between the jetting region and the recirculation region in the throat of the diffuser. The velocity profile in the direction of the tube appears to fill out at the top of the hole, but this is mostly due to the momentum that the crossflow imparts on the fluid in the hole. This is evidenced by Figure 3.51 which clearly shows almost nil vertical velocity (and therefore, coolant flow) in the center of the tube exit.

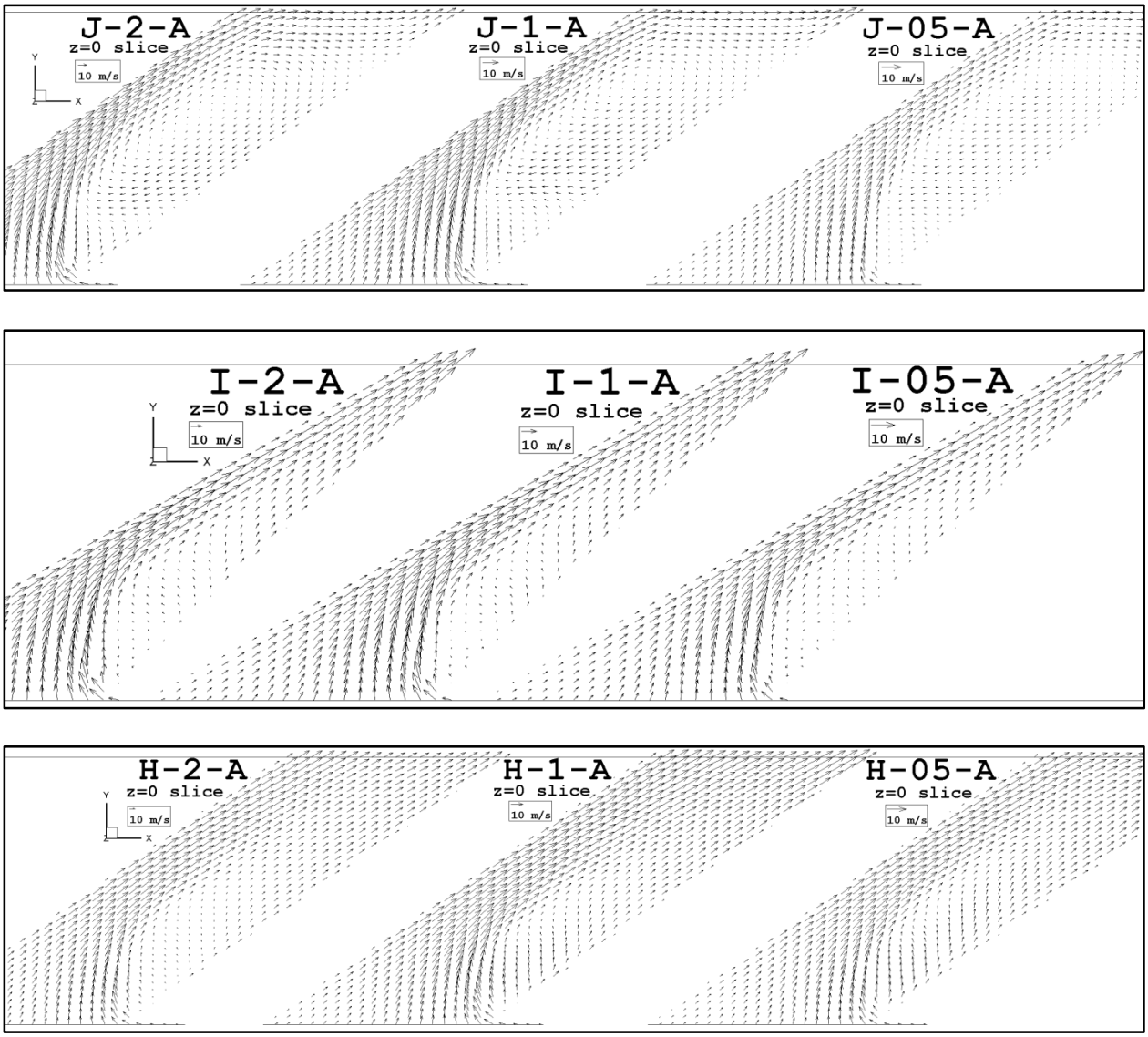

Figure 3.53: Recirculation and stagnation regions illustrated in the laterally diffused geometry (top), console geometry (middle), and cylindrical hole (bottom)

The same jetting and recirculation region phenomenon is observed in the console hole, but since the hole is acting as a nozzle the recirculation is dissipated and reduced to an area of stagnation which resolves itself far in advance of reaching the surface. The more critical observation in the console case is the lateral (z) component of the fluid motion. A lateral split of the jetting around the central stagnation region occurs as the coolant travels up the console. This lateral splitting can be observed in Figure 3.55, but is more apparent in Figure 3.54. This lateral

splitting is a key characteristic because it is one of the most obvious reasons for the egregious penetration of the console's jet into the crossflow that will be presented later. The fact that there is a significant lateral component of velocity directing these split jets into the split jets of neighboring holes (see Figure 3.52). When these split jets meet, significant penetration of the crossflow occurs; this will be further explored later in this study.

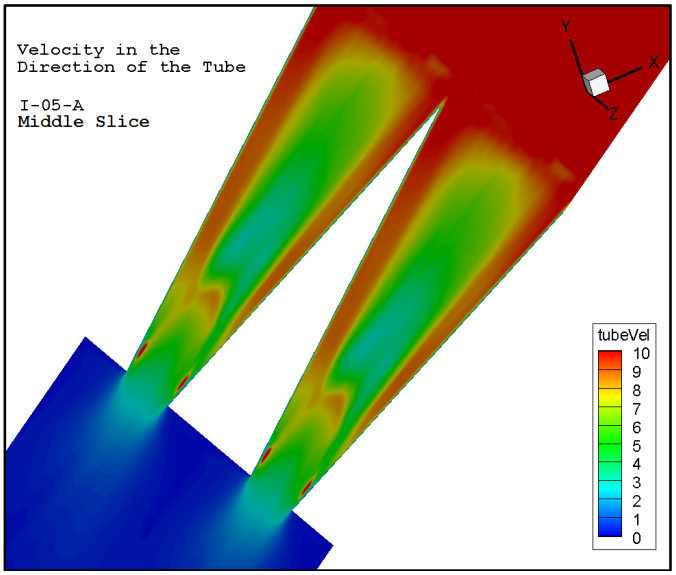

Figure 3.54: Evidence of split jetting in the console hole (m/s)

The turbulence quantities in the shaped holes are illustrated in Figure 3.56 and Figure 3.57. The lower blowing ratio cases tend to have less turbulence within the delivery tube (similar to the cylindrical holes). The jetting effect near the front side of the hole does not appear to induce as laminar a flow as in the cylindrical hole case; this may simply be explained in that the jetting is split laterally around the plane plotted (z=0). The separation region that forms as a result of the sharp turn at the hole entrance fosters turbulence (just as it did in the cylindrical cases), but the more laminar jetting region is not located at the symmetry plane of the jet for either shaped geometry simulated.

Surprising observations visible in Figure 3.56 and Figure 3.57 are that in all but the lowest blowing ratio cases, the turbulent intensity in the delivery tube is much higher than the turbulence in the shear layer between the jet and crossflow. The console shape induces more laminar flow toward the exit of the hole, as opposed to the laterally diffused hole which induces more turbulent conditions toward the hole exit. This is consistent with the known behaviors of nozzles and diffusers, respectively. More plots of the turbulent behavior in the delivery tube and in the crossflow are provided in Appendix C.

3.6.1 Trailing Edge Effects

At the trailing edge of the round holes, there is a recirculation region, associated with DSSN vortices and jet blow off (documented in section 3.5.2). Similar plots of streamlines and temperature fields are plotted in Figure 3.58-63 for the shaped holes to identify key behaviors.

In Figure 3.58, a recirculation region that extends almost the entire lateral span is observed in the console case even at the lowest blowing ratio. This is not a terrible disadvantage in the console case because the crossflow fluid is unable to go around the side and become entrained beneath the jet as it does in the cylindrical hole case. The recirculation region is interrupted near the z/pitch=0.5 plane due to the strong vertical jet formed by the laterally split jetting discussed previously. Indeed, a misshapen horseshoe vortex is formed in front of this strong vertical jet, easily observable in the streamlines and temperature field.

The features observed at a blowing ratio of 1 for the console hole (Figure 3.59) are quite similar to the features observed at blowing ratio 0.5. The recirculation region is larger in vertical and streamwise extents, but it is still interrupted at the hole intersections where the upward jet blows through it. In the lower part of the figure, the ends of the recirculation region are shown to be folded down vertically to meet the surface about 0.2 diameters from the intersection plane to make way for the strong vertical jet centered on the intersection plane.

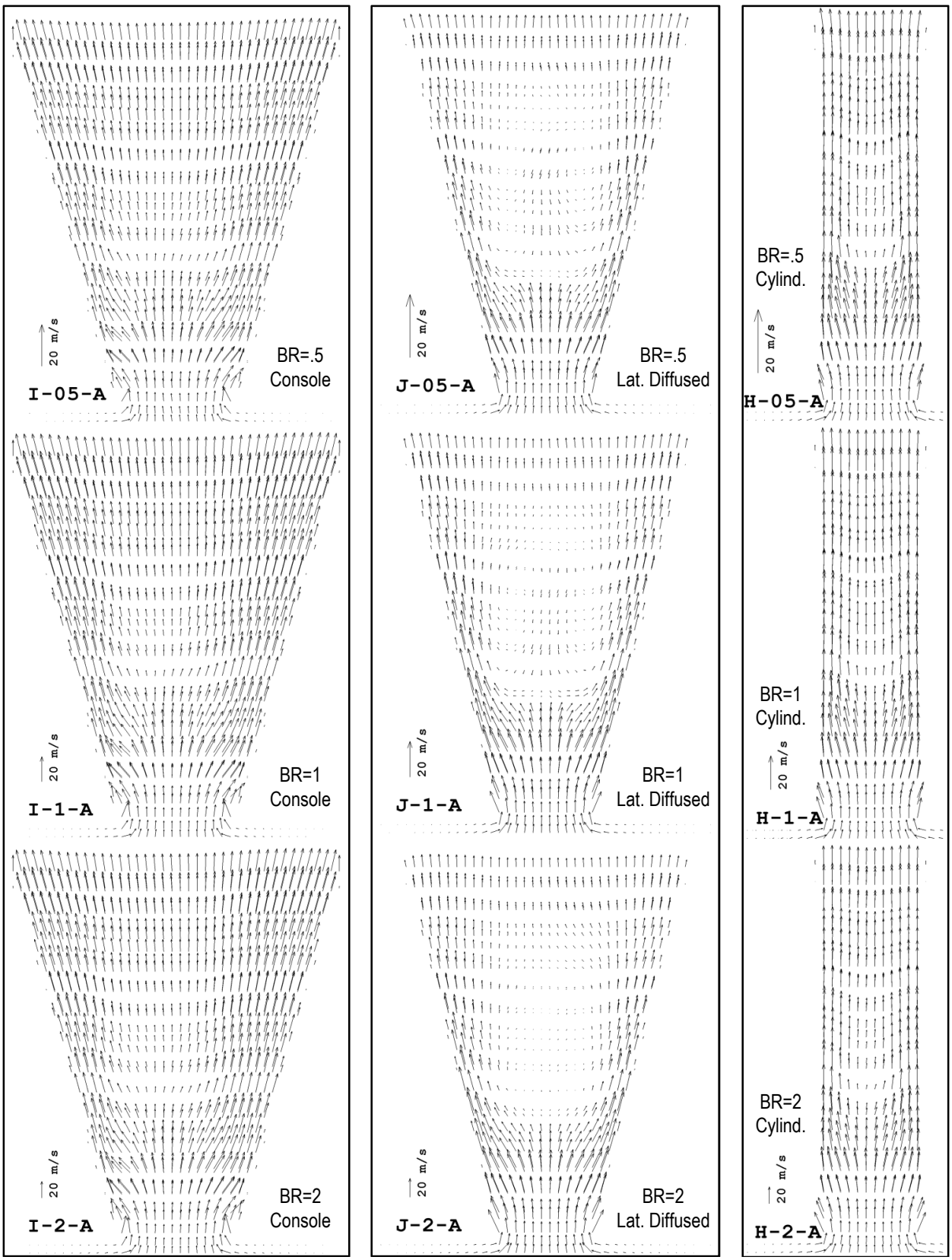

Figure 3.55: Vector fields on a widthwise slice of the middle of the delivery tube; view is normal to the slice

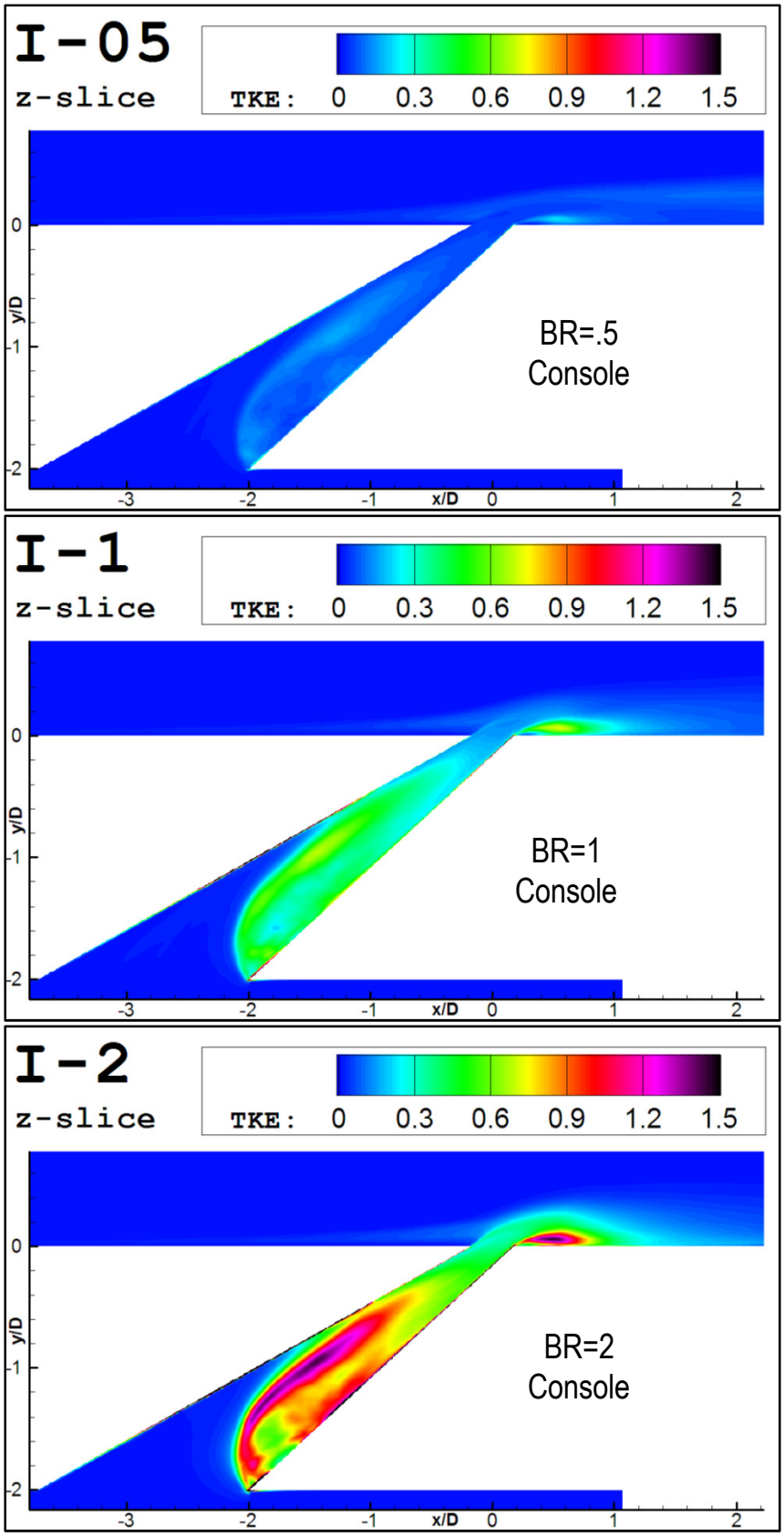

Figure 3.56: Turbulent kinetic energy in the console hole (z=0 slice)

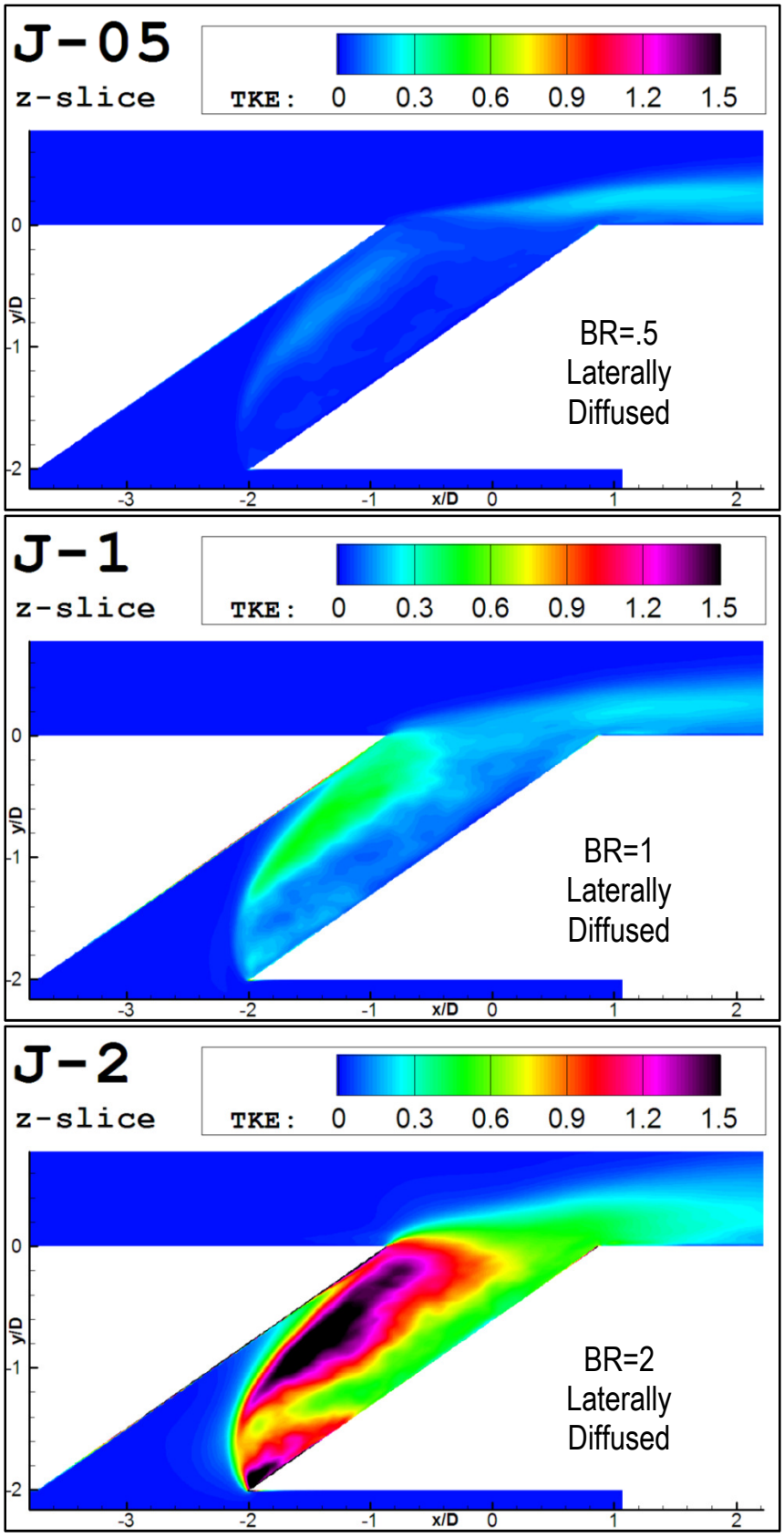

Figure 3.57: Turbulent kinetic energy in the laterally diffused hole (z=0 slice)

The features observed at a blowing ratio of 2 for the console hole (Figure 3.60) are quite similar to the features observed at lower blowing ratios. The recirculation region does not appear to grow significantly in vertical and streamwise extents, but it is still interrupted at the hole intersections where the upward jet blows through it. An organized lateral flow tendency is seen at the hole exit, although it is not clear whether this indicates a stable equilibrium of lateral flow being reached at the higher blowing ratio or insufficient time averaging.

In Figure 3.61, no recirculation region is observed in the laterally diffused case at the lowest blowing ratio. This is expected, because the modus operandi of the laterally diffused hole is to slow the coolant down to prevent blow off and prevent entrainment of the crossflow gas below the jet. The crossflow dips down into the center section of the hole, lending further credence to the idea that the recirculation region deep within the laterally diffused hole (discussed earlier) is thwarted at the top of the hole because of the convection and diffusion of x-momentum from the crossflow to the fluid in the hole.

In Figure 3.62, no recirculation region is observed in the wake of the hole at a higher blowing ratio, but the beginnings of a horseshoe-vortex-like recirculation at the leading edge of the hole can been seen to form. This is likely due to the increased vertical velocity at the upstream corners of the hole observed in Figure 3.51. If this is the culprit, one would expect this upstream phenomenon which is reminiscent of the horseshoe vortex ahead of the round holes would become stronger at higher blowing ratios because the vertical velocity at the upstream corners is further increased.

As predicted, the upstream recirculation region (horseshoe vortex) is more pronounced at the higher blowing ratio shown in Figure 3.63. No recirculation region is observed in the laterally diffused case behind the hole even at the highest blowing ratio of 2. Thus, it appears that in

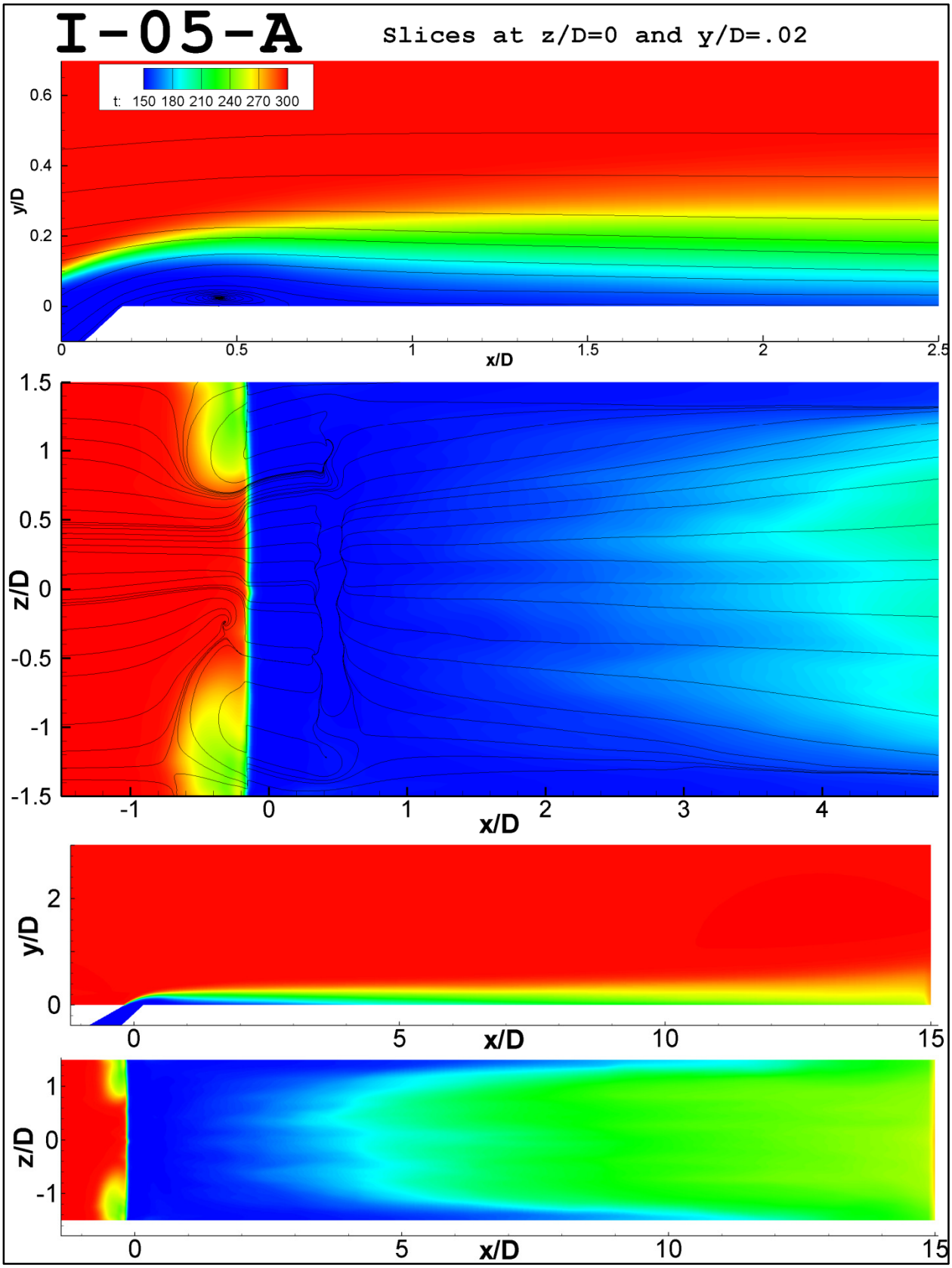

Figure 3.58: Streamlines and temperatures, BR=0.5, console geometry

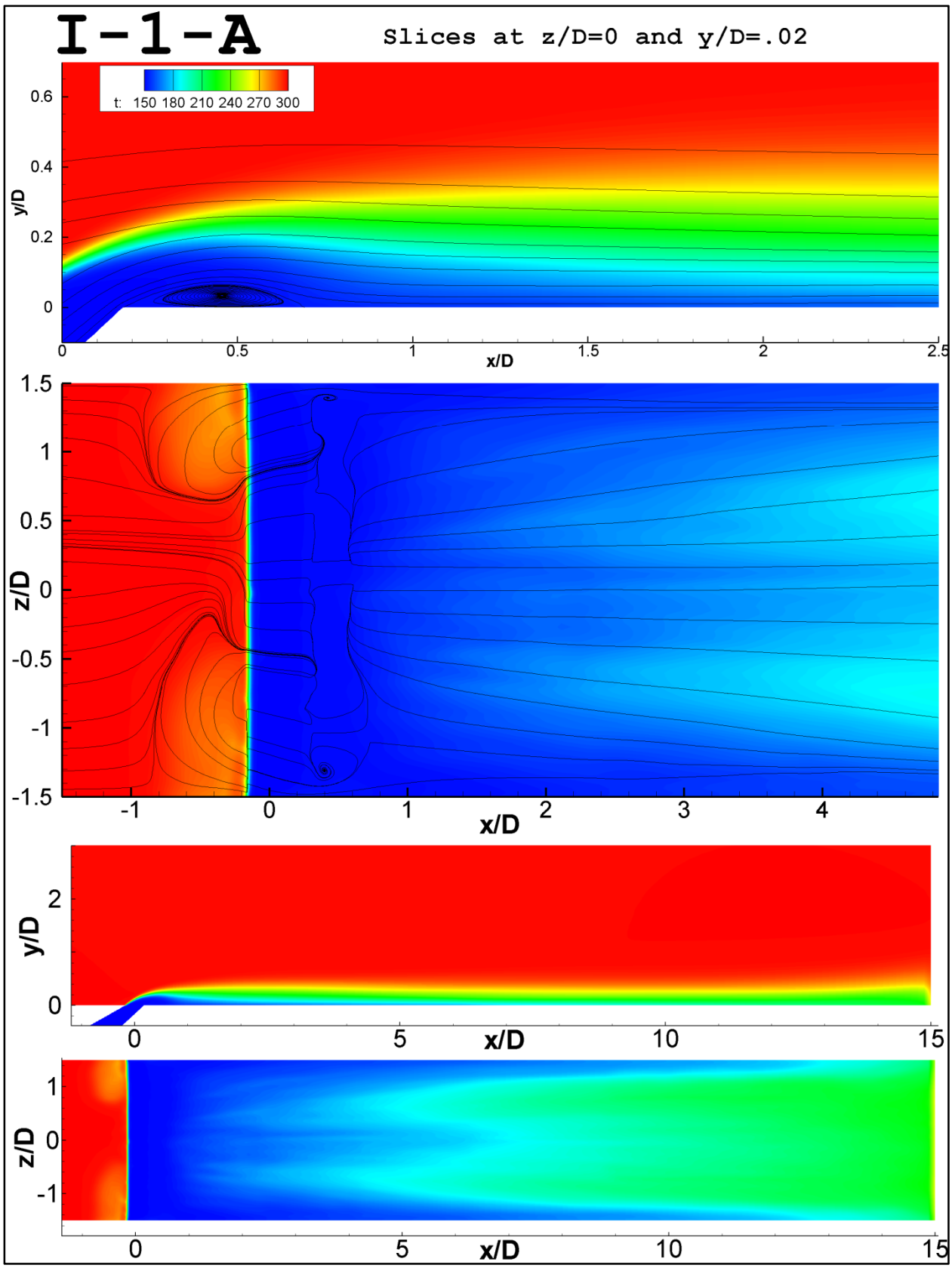

Figure 3.59: Streamlines and temperatures, BR=1, console geometry

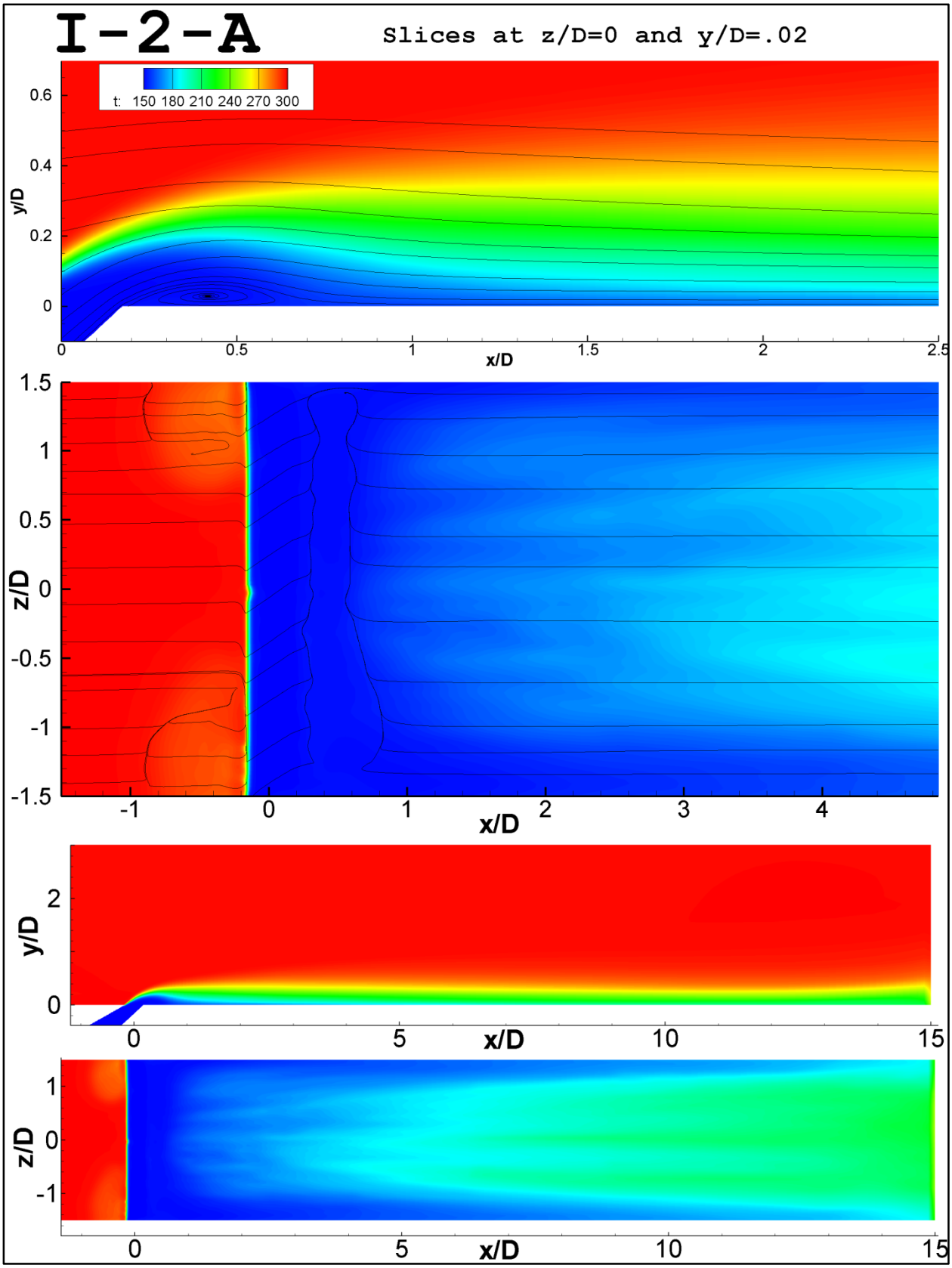

Figure 3.60: Streamlines and temperatures, BR=2, console geometry

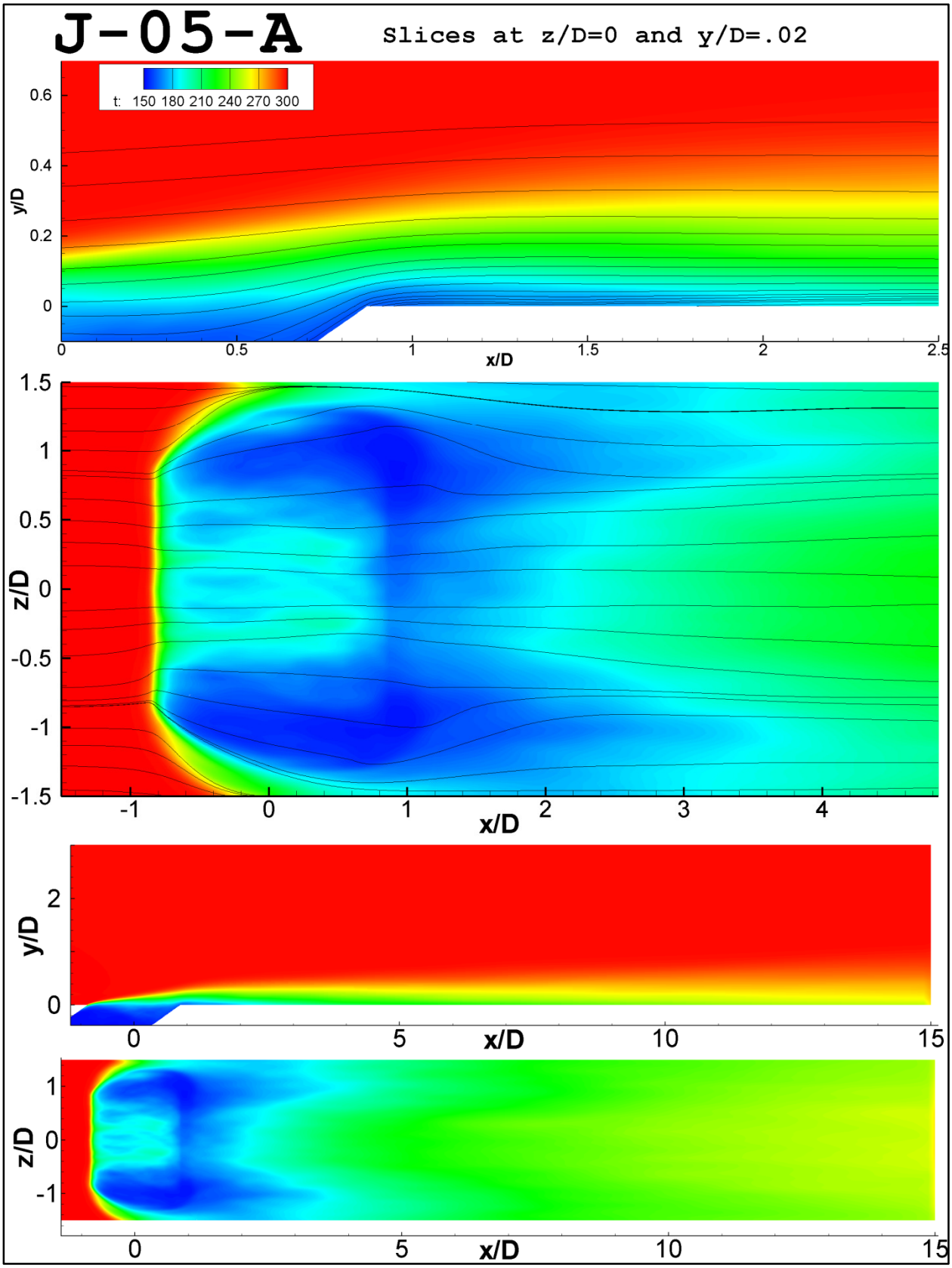

Figure 3.61: Streamlines and temperatures, BR=0.5, laterally diffused geometry

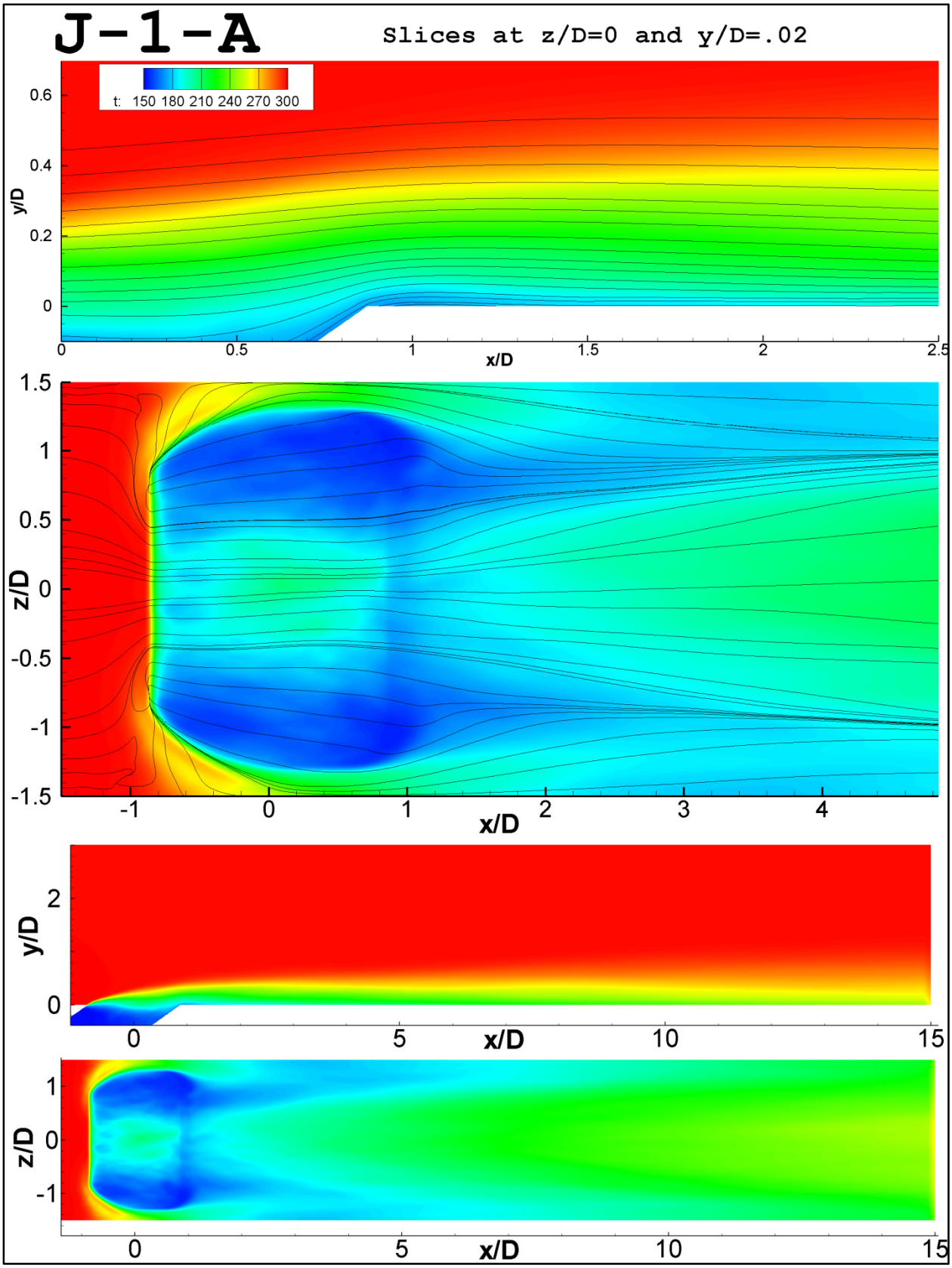

Figure 3.62: Streamlines and temperatures, BR=1, laterally diffused geometry

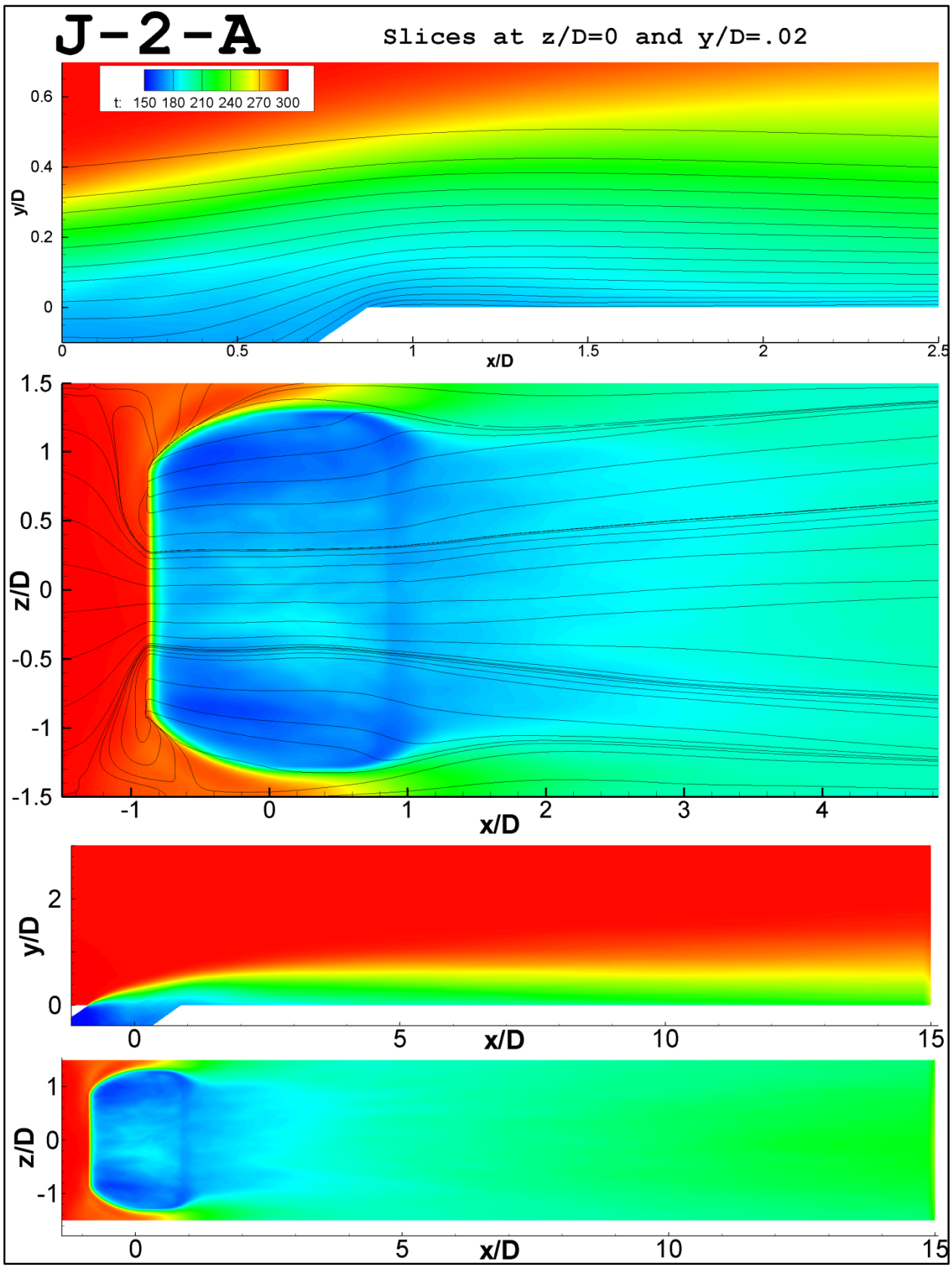

Figure 3.63: Streamlines and temperatures, BR=2, laterally diffused geometry

order to induce any sort of blow off in this geometry, a much higher mass flow rate of coolant would be required. This ability of the laterally diffused hole to issue more and more coolant and distribute it near the surface in a manner conducive to film cooling is why it is the industry standard. It is not, however, superior in terms of pressure loss. Pressure loss will be measured and documented later in this study.

3.6.2 Scaling by Blowing Ratio

In order to predict the performance of film cooling at varied blowing ratios, a scaling has been proposed and documented by Bogard (2007) (see Figure 3.64 for an example of this scaling applied with a logarithmic axis scales). The scaling was originally proposed for slot film cooling, but it has been extended to laterally averaged results from discrete film cooling holes. This will be the manner the scaling is employed in the current study. The intent is to equalize the "decay rate" of film cooling by assuming an inverse relationship between decay rate and blowing ratio. The results when such a scaling is applied are shown in Figure 3.65 and do indeed indicate an equalizing effect on slope between blowing ratios. The only cases that do not appear to follow the trend are the round holes at all but the lowest blowing ratio; this suggests that the scaling is useless when significant jet blow-off is encountered (Figure 3.64 shows the same trend

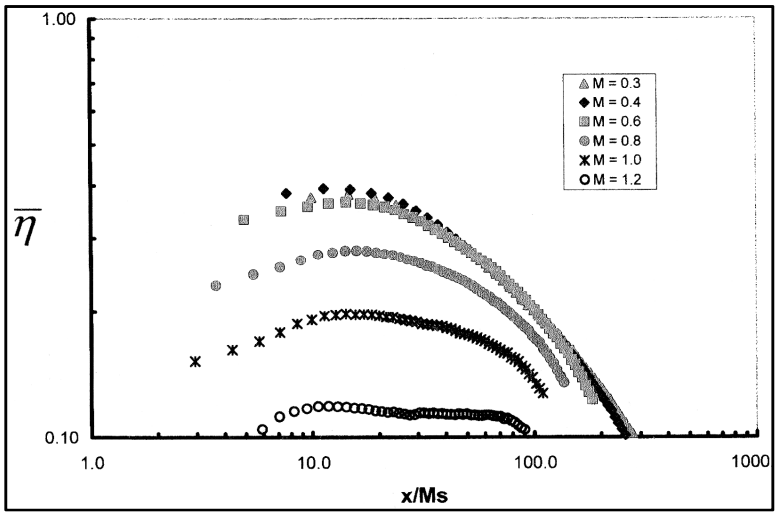

Figure 3.64: Scaling based on blowing ratio presented by Bogard (2007) for discrete holes

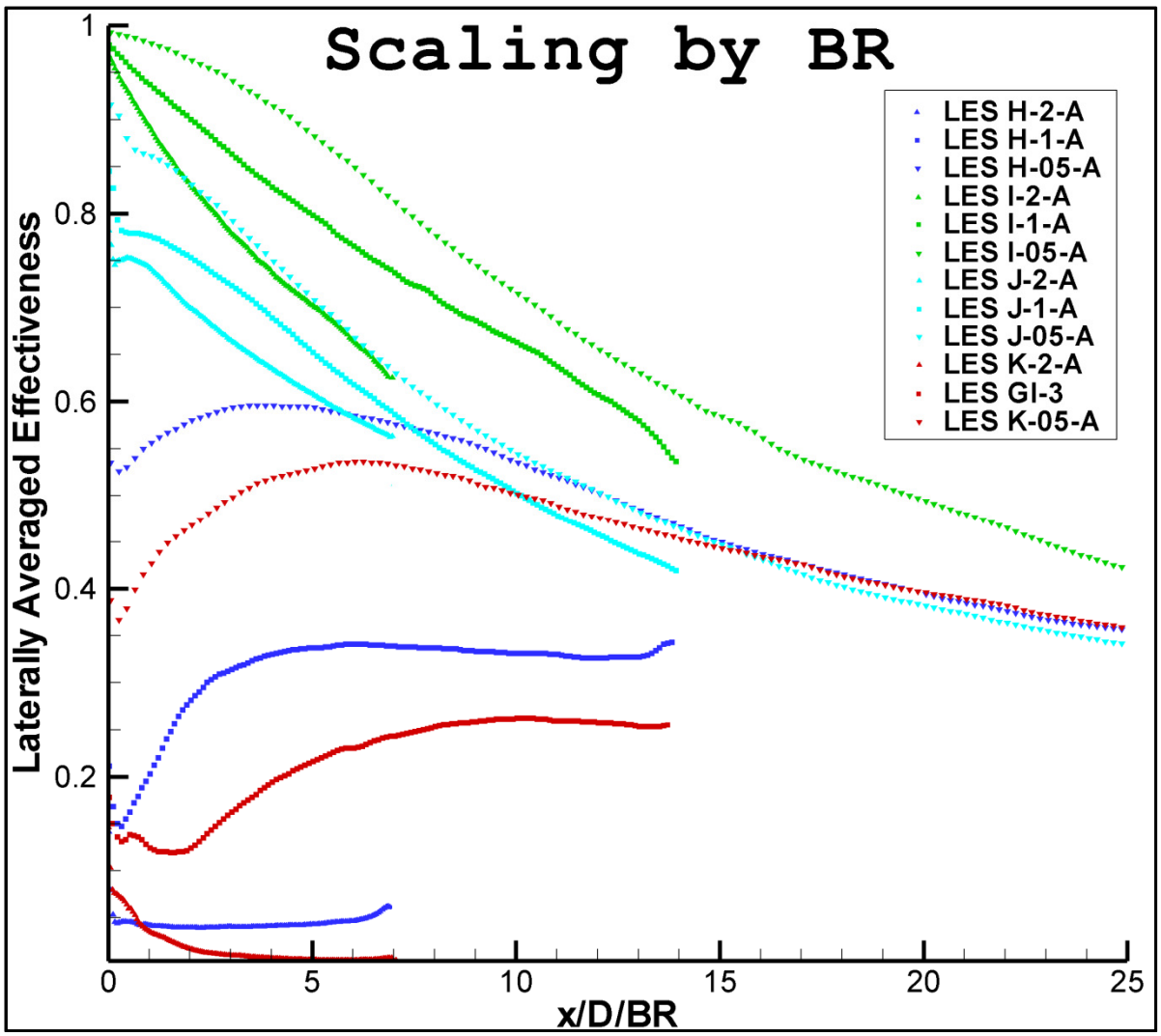

Figure 3.65: Scaling similar to that in Bogard (2007) for results from current study

observed in a discrete hole study with different operating conditions). This is consistent with the original intent of the scaling to be used on slot jets, which do not exhibit large amounts of blow-off due to the Coanda effect.

3.6.3 Penetration and Pressure Loss

In film cooling, since the purpose is to cover the surface with a thin film of cool air, any significant penetration of the jet into the mainstream is undesirable. Penetration does nothing to help lower the surface temperature, but wastes coolant and cools the process air (both of which decrease the efficiency of the cycle). Figure 3.66 and Figure 3.67 show the penetration of each

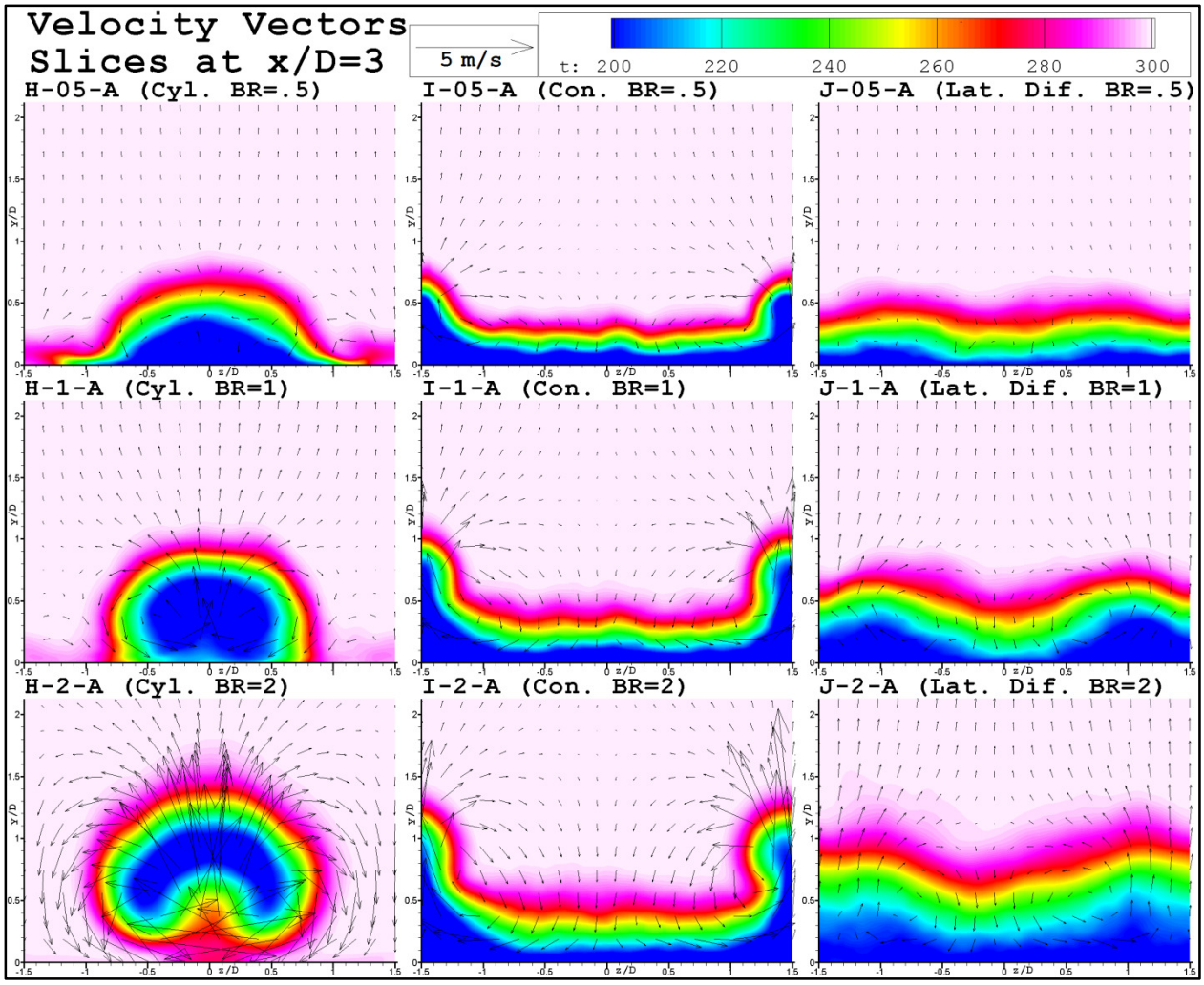

Figure 3.66: Slices of the temperature field from each issued jet at 3 hole diameters downstream taken perpendicular to the mainstream flow with superimposed velocity vectors

jet with respect to hole shape and blowing ratio at two downstream locations: three and ten hole diameters downstream of the hole.

Surprisingly, the console hole is seen to penetrate into the mainstream flow as far as the cylindrical hole at all blowing ratios. Thus, the vertical penetrating jets formed at the intersections of the consoles do not constitute only a minor nuance, but are a significant feature of the issued jet. This is further illustrated for the consoles in Figure 3.68 even for the lowest blowing ratio of 0.5.

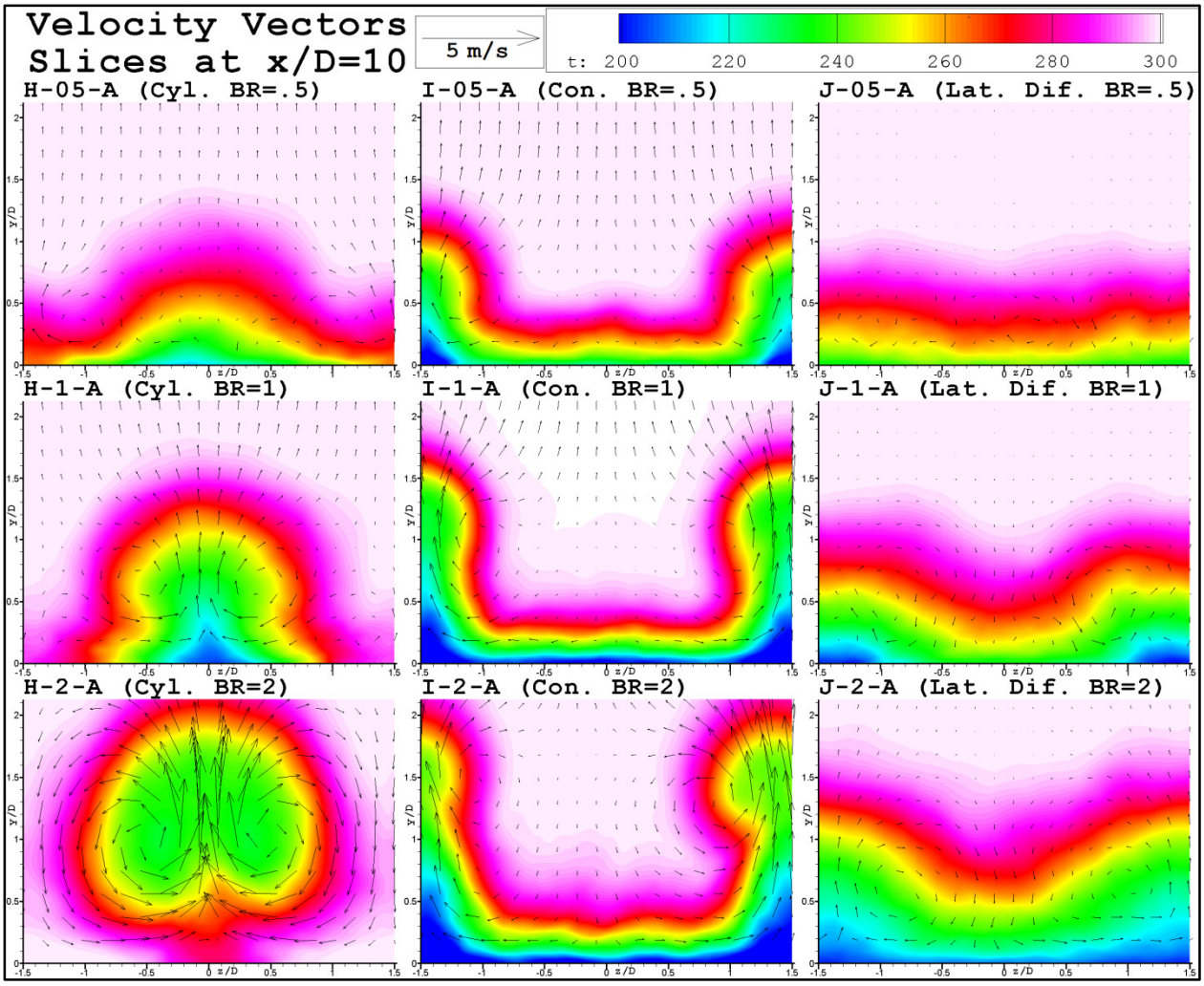

Figure 3.67: Slices of the temperature field from each issued jet at 10 hole diameters downstream taken perpendicular to the mainstream flow with superimposed velocity vectors

While jet penetration does not appear to be the greatest argument for the console geometry, pressure loss is one area in which the console hole performs quite well. Pressure loss is a method for measuring the tendency of film cooling to rob the crossflow fluid of momentum (and therefore efficiency). It is measured here in two ways. The first method, C_{PL} (defined in 3.11 and plotted in Figure 3.69), only takes into account the total pressure of the crossflow measured at a plane upstream of the hole (S_1) and downstream of it (S_2). The second method, C_{PL2} (defined in 3.12 and plotted in Figure 3.70), also takes into account the total pressure at a third

plane perpendicular to the flow in the plenum chamber (S_3). Plane S_1 is located at x/D=-4.5, plane S_2 is located at x/D=10, and S_3 is located at y/D=-5.

Note that the pressure loss (defined in 3.11 and plotted in Figure 3.69) for the console cases steadily decreases as the blowing ratio is increased, and becomes negative at BR=2 indicating that the downstream plane has even more momentum than the upstream plane due to the injected jet. This is true for the round hole as well, but to a lesser extent (and with much poorer adiabatic

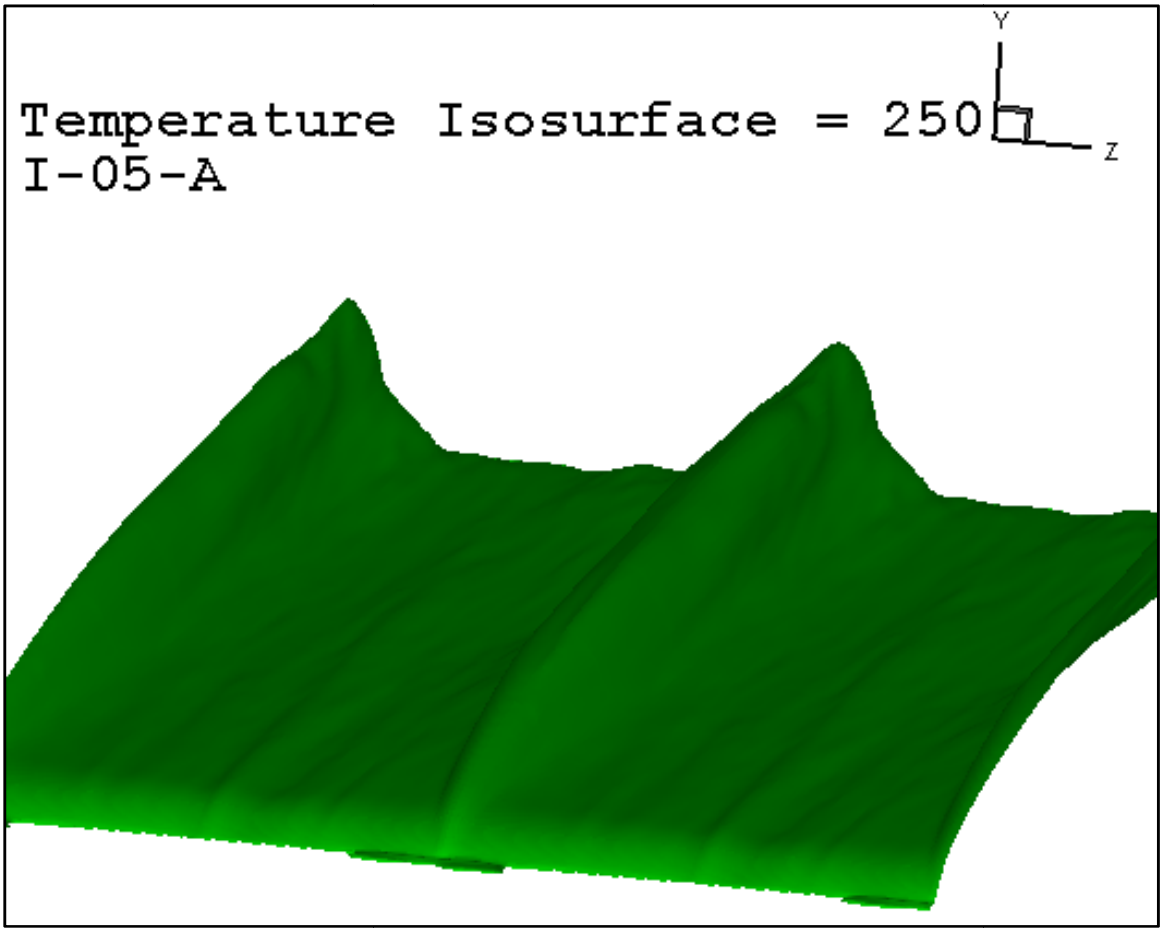

Figure 3.68: Further illustration of the penetrating jet in the console case at a different temperature isosurface, even at the lowest blowing ratio of 0.5

$$C_{PL} = \frac{\int^{S_1} P_{tot} dA - \int^{S_2} P_{tot} dA}{{}^1/_2 \rho_{inf} u_{inf} \int^{S_2} dA} \qquad (3.11)$$

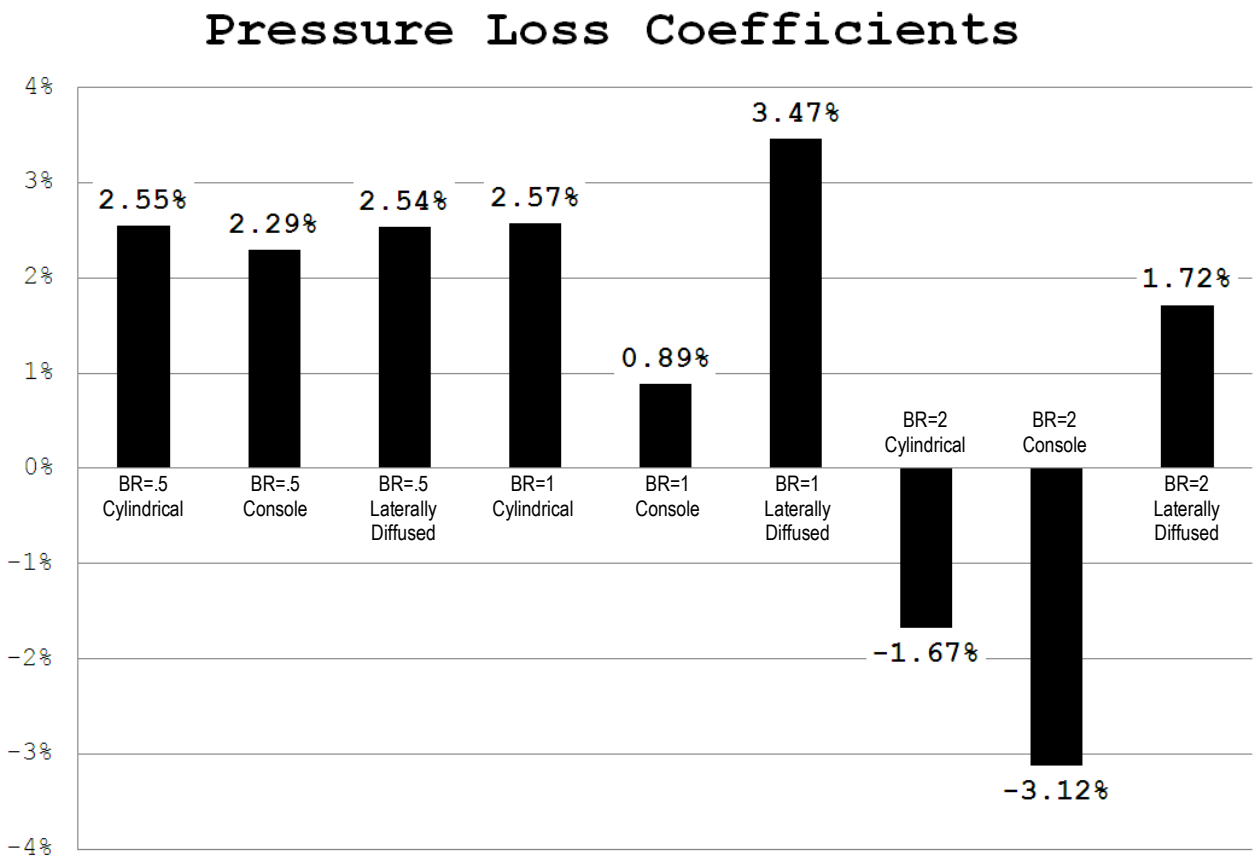

Figure 3.69: C_{PL} for each geometry and blowing ratio

effectiveness performance at this high blowing ratio, as previously documented). The disadvantage of the laterally diffused hole is also clear as the slower moving jet, while it does stick close to the surface well, robs the crossflow of more momentum than the other geometries do.

The same trends reported in the first method (3.11) of measuring pressure loss are confirmed via the second method in Figure 3.70. The method, defined in 3.12, includes a plane in the plenum chamber to account for the momentum imparted by the jet. The values no longer dip negative (which is impossible via this method because the momentum added to the flow in the negative C_{PL} cases comes from the jet, which passes though the plenum chamber's measurement plane), but the same trends of good and bad performance are observed.

$$C_{PL2} = \frac{\int^{S_1} P_{tot} dA + \int^{S_3} P_{tot} dA - \int^{S_2} P_{tot} dA}{{}^1/_2 \rho_{inf} u_{inf} \int^{S_2} dA} \tag{3.12}$$

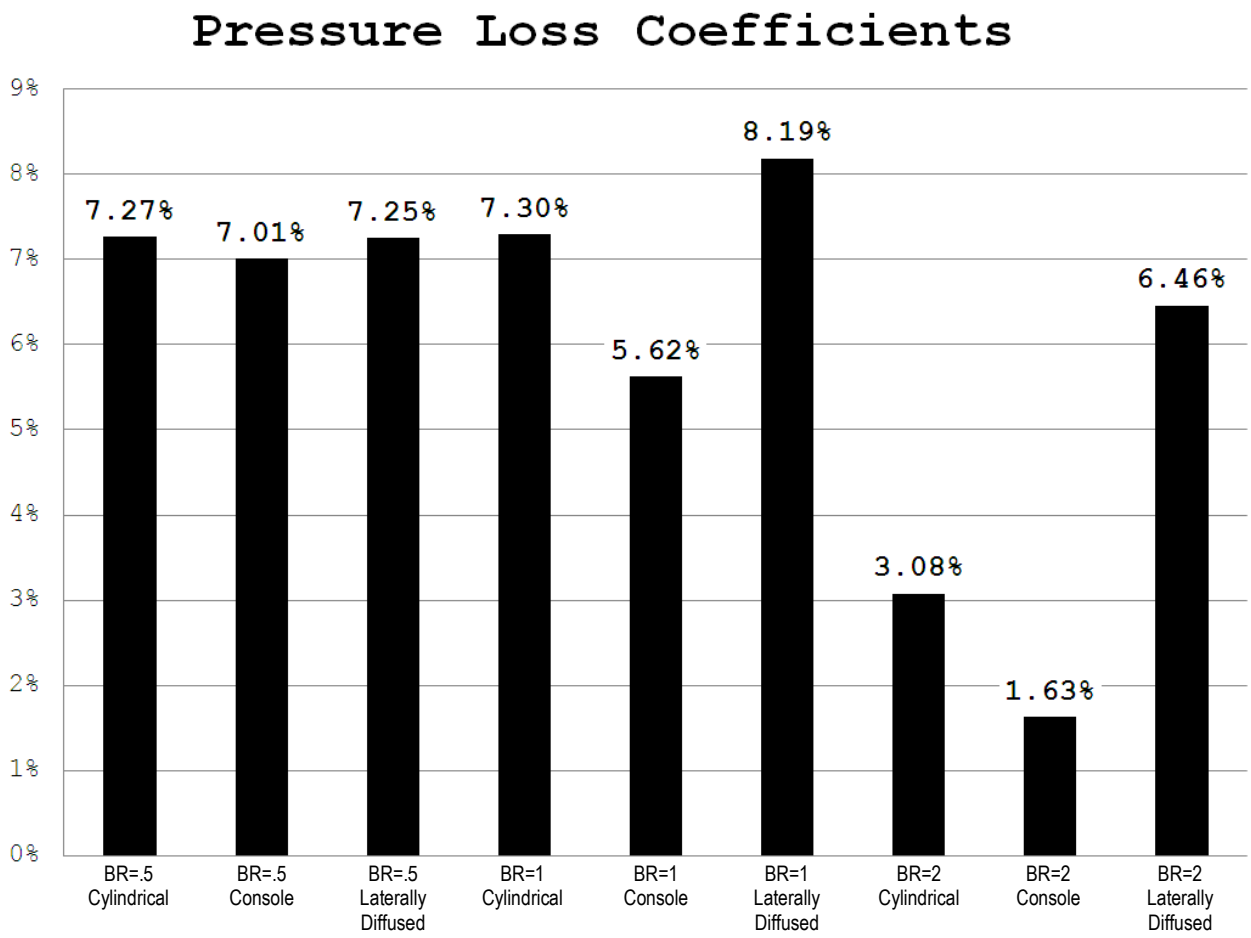

Figure 3.70: C_{PL2} for each geometry and blowing ratio

If one can deduce what parts of the jet contribute most to pressure loss, an effort can be made to isolate and minimize the features that cause the effect. This is the idea behind Figure 3.71 which shows dynamic pressure at a plane located ten hole diameters downstream of the hole. Values are normalized by the freestream dynamic pressure to yield a unitless measure.

Note that the parts of the console jet and cylindrical hole jet that blow off of the surface significantly have high momentum. This means that while the penetration may be undesirable

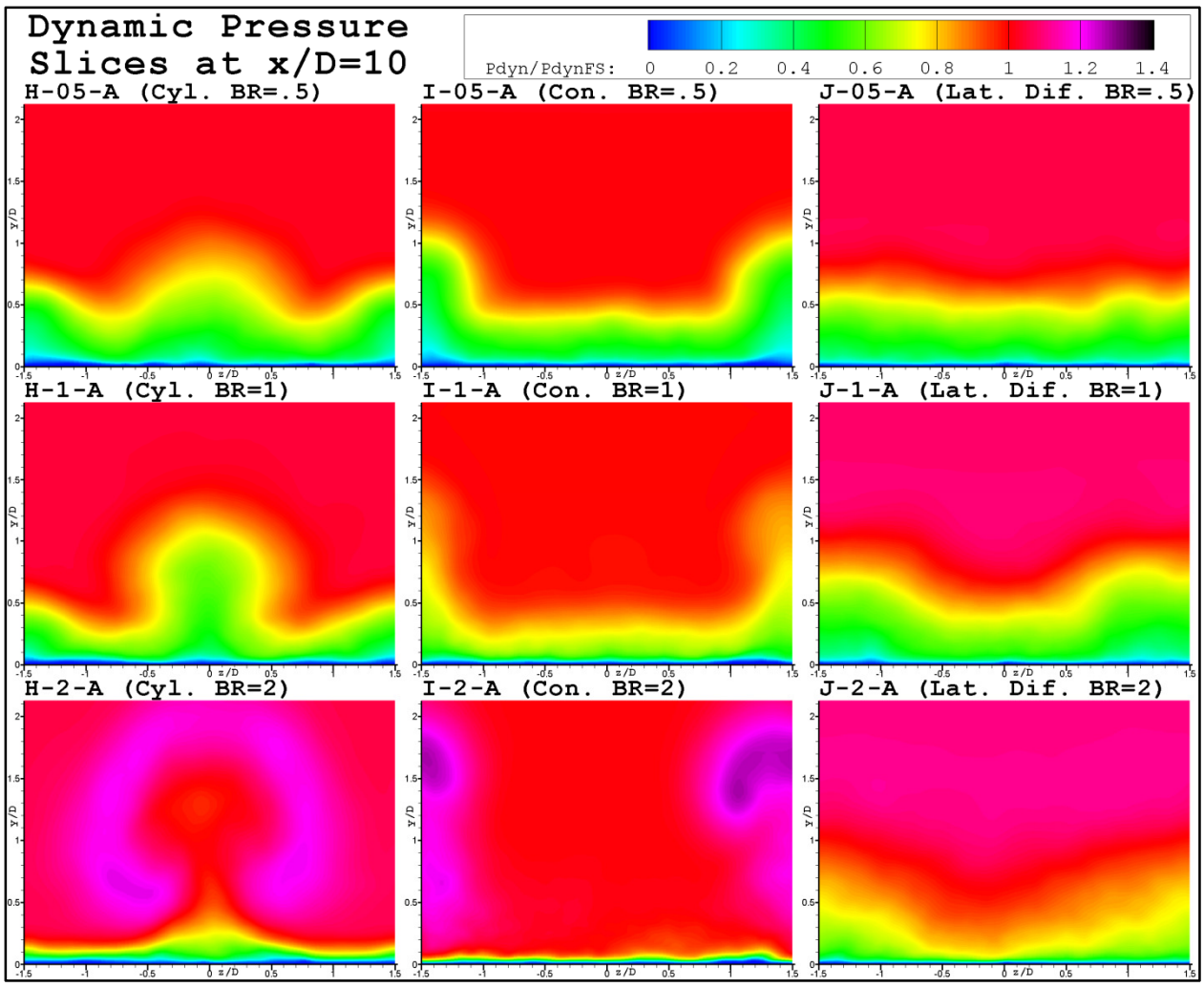

Figure 3.71: Local plots of dynamic pressure at downstream planes

from the point of view of wasted coolant and cooler process air, the aerodynamic performance of the penetrating parts of the jets is good.

3.6.4 Vorticial Structures

Coherent vorticial structures are created via shear near the hole and propagate downstream in film cooling cases, having an impact on the properties of the jet as related to film cooling. These structures are plotted in an instantaneous time series for the cylindrical (Figures 3.72-75), console (Figures 3.76-79), and laterally diffused (Figures 3.80-83) geometries at a blowing ratio of 1 and discussed in this section. All steps of the series shown are 200 physical time steps apart.

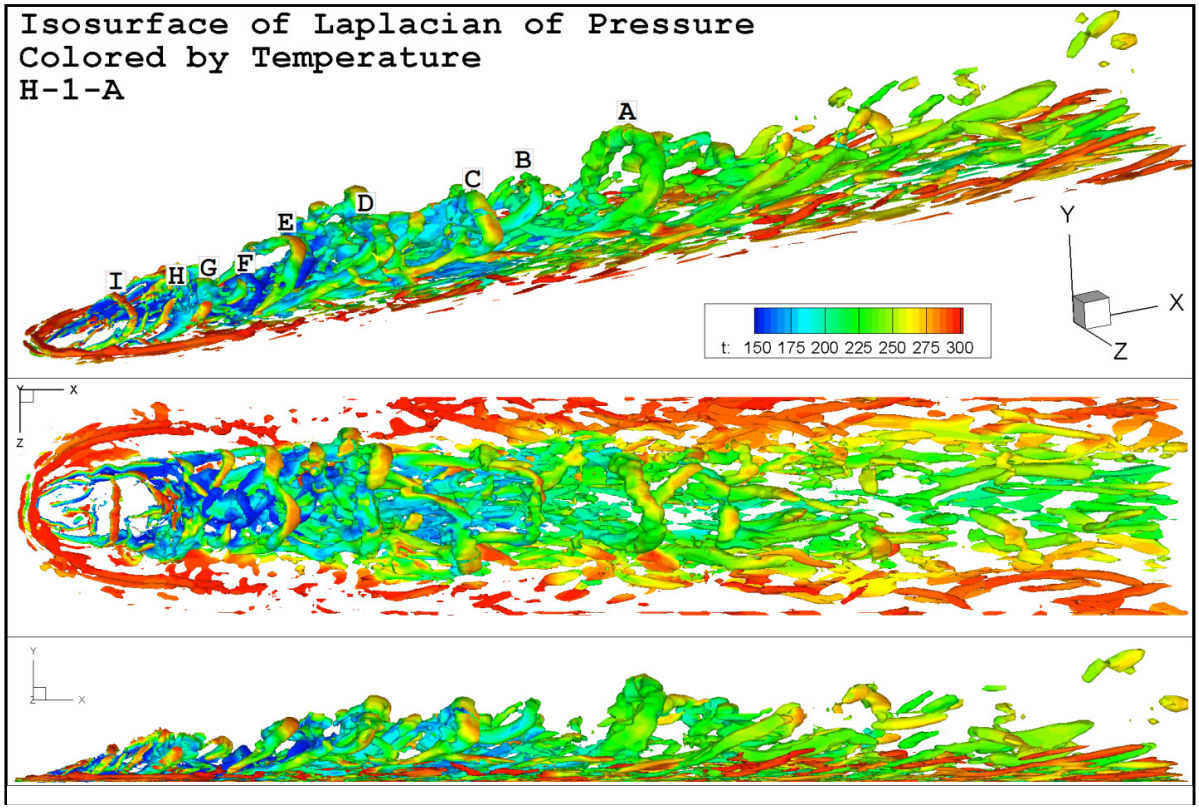

Figure 3.72: Identification of coherent structures in the round hole, L/D=3.5, BR=1 case

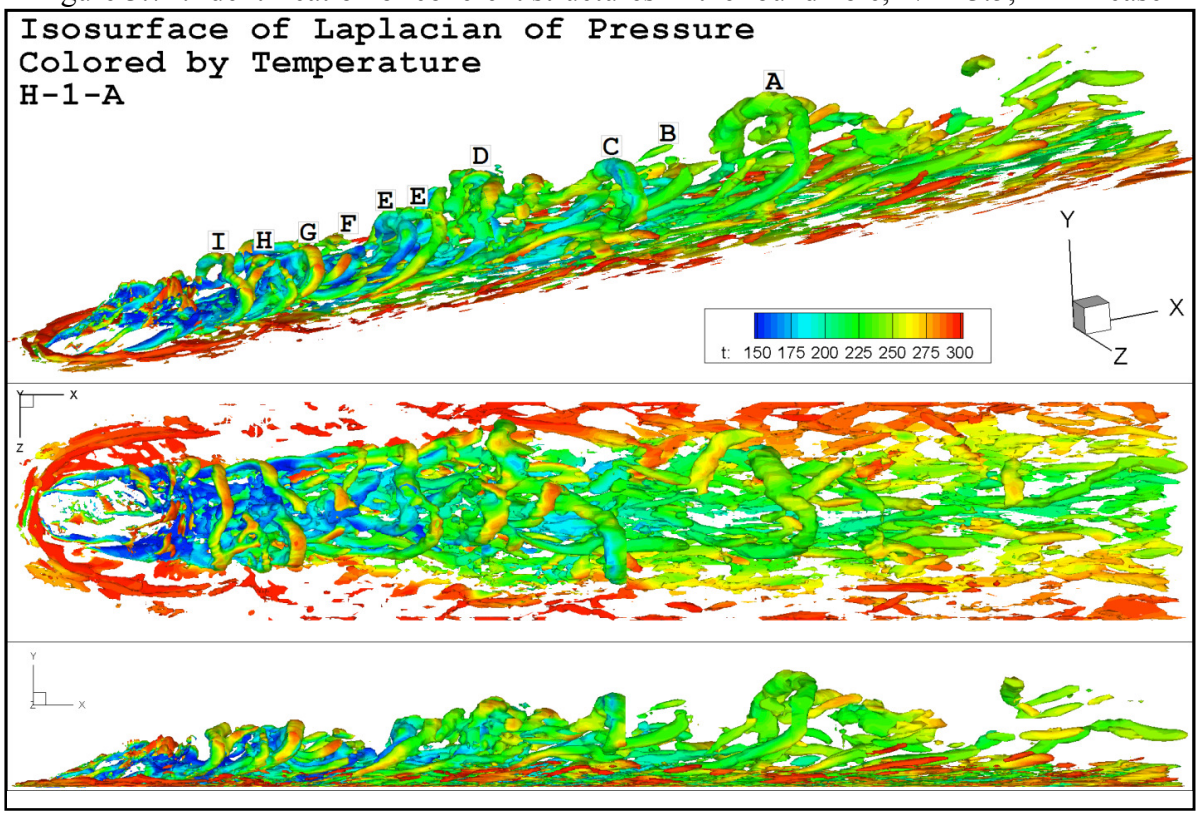

Figure 3.73: Identification of coherent structures in the round hole, L/D=3.5, BR=1 case

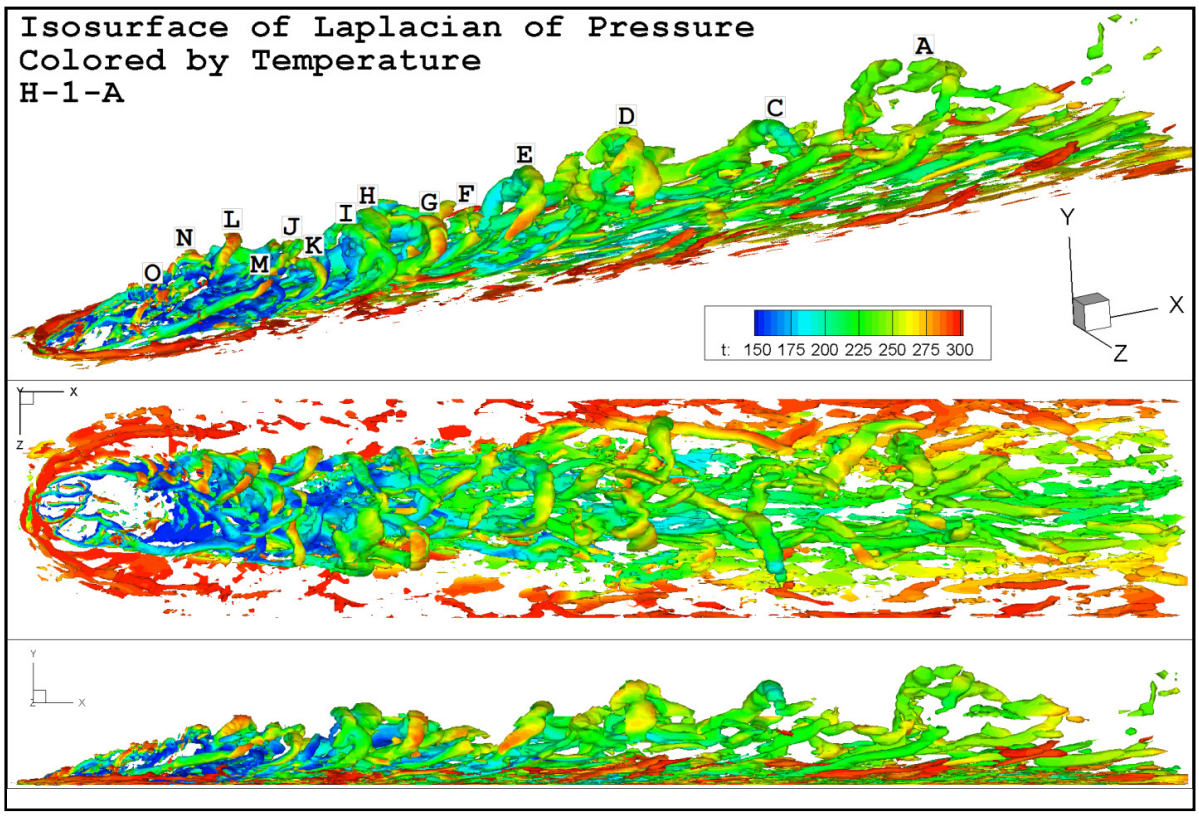

Figure 3.74: Identification of coherent structures in the round hole, L/D=3.5, BR=1 case

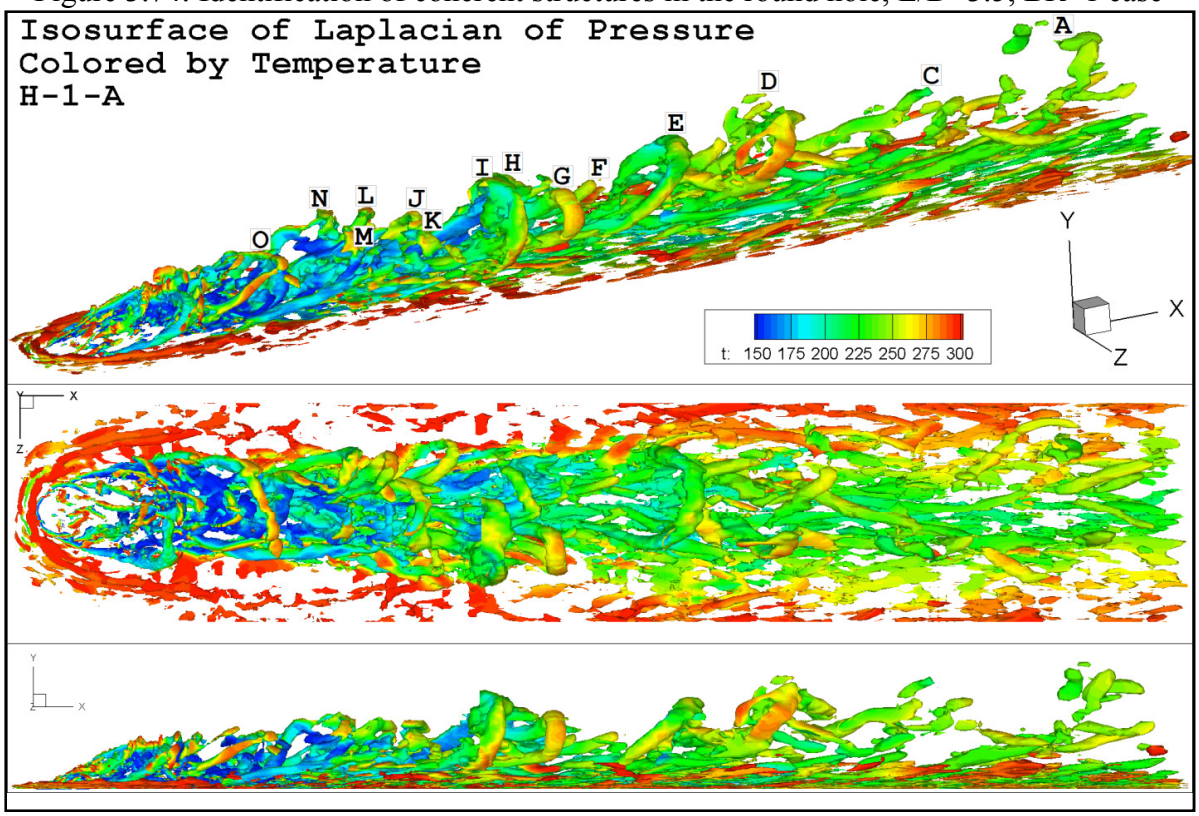

Figure 3.75: Identification of coherent structures in the round hole, L/D=3.5, BR=1 case

The vorticial structures present in the cylindrical hole, BR=1 case are illustrated in Figures 3.72-75. The hairpin vortices are tracked and labeled with capital letters in the four time instances. Comparisons of the hairpin locations to instantaneous local surface temperature plots did not yield a direct correlation. This indicates that while the hairpins are important features of the flow farther from the surface (with associated effects on mixing), they are not the most important factor in determining the surface effectiveness. The structures emanating from the immediate back side of the hole (such as DSSN vortices) seem to have a larger impact on the surface cooling character of the jet. The hairpin structures seem to be more responsible for increased jet penetration of the jet than any other factor, as they are consistently the features with the greatest vertical development.

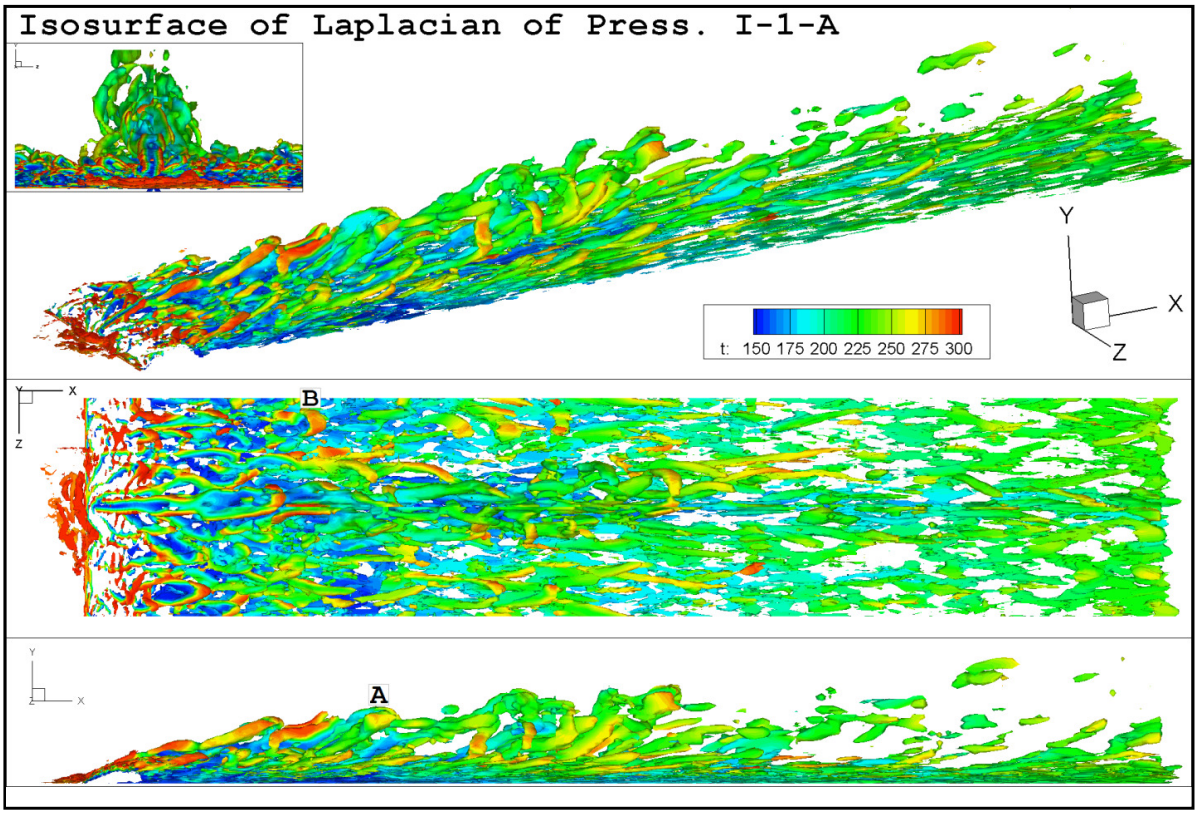

Figure 3.76: Identification of coherent structures in the console hole, BR=1 case

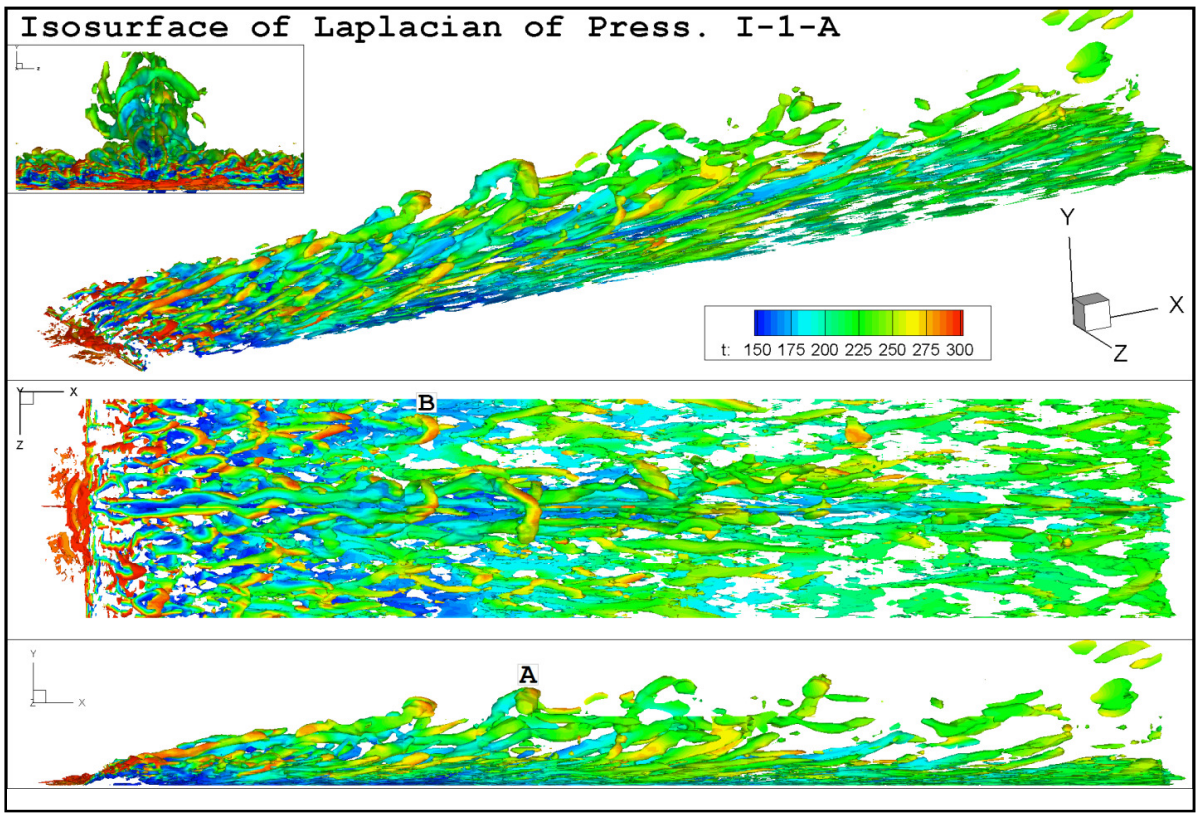

Figure 3.77: Identification of coherent structures in the console hole, BR=1 case

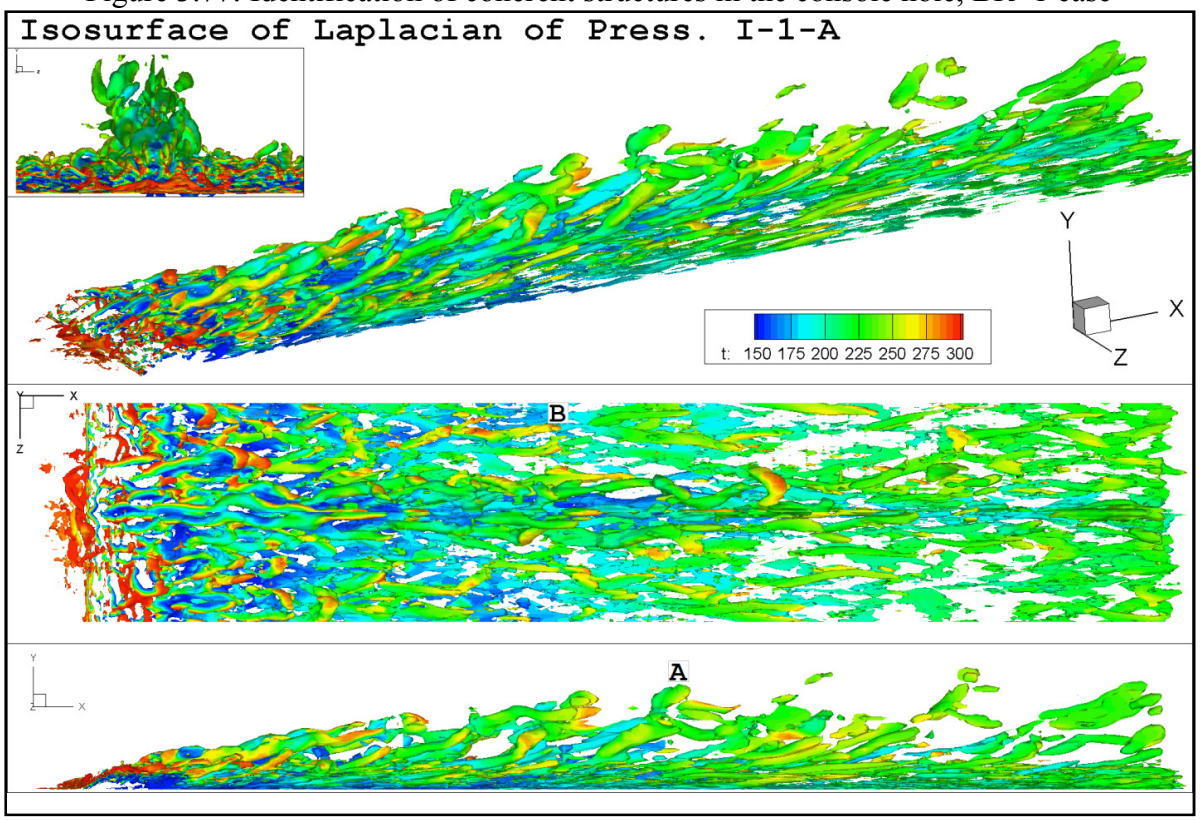

Figure 3.78: Identification of coherent structures in the console hole, BR=1 case

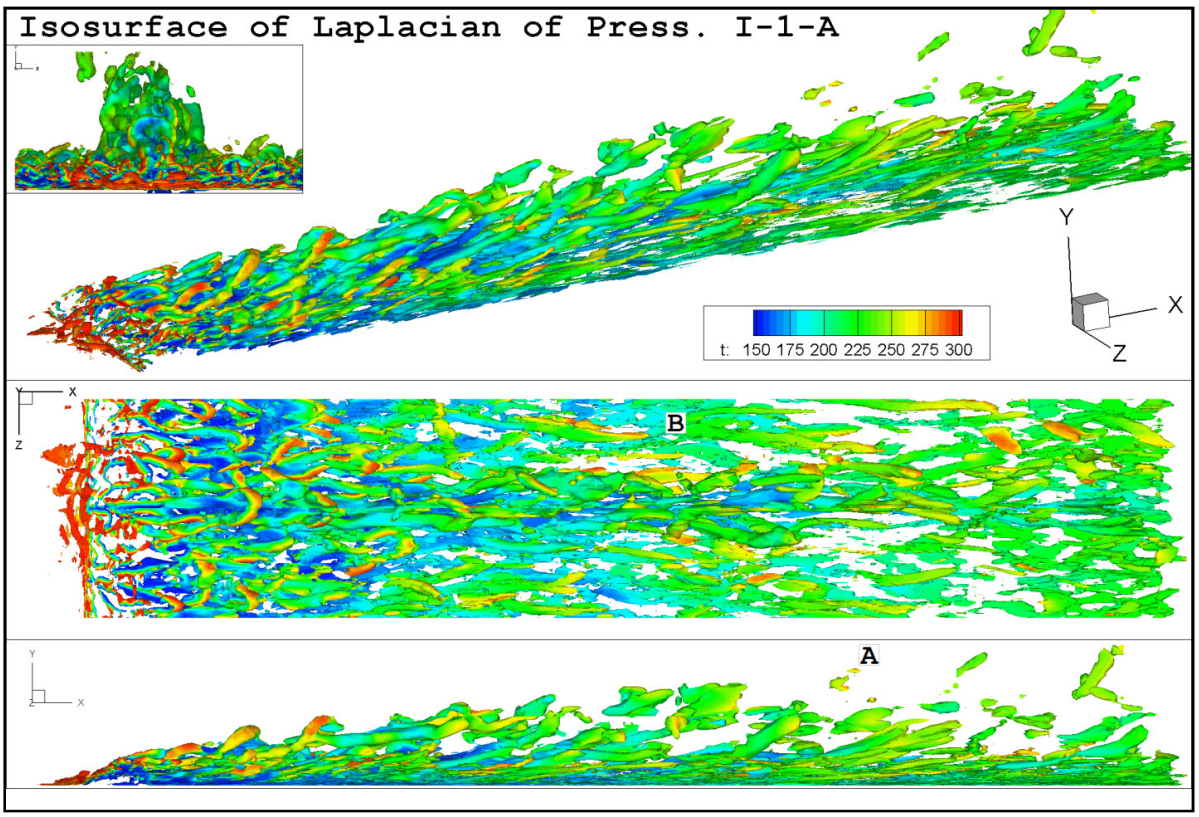

Figure 3.79: Identification of coherent structures in the console hole, BR=1 case

For the console case at a blowing ratio of unity (illustrated in the time series from Figures 3.76-79), two distinct types of hairpin structure are tracked. One occurs in the powerful, penetrating jet at the intersection of two consoles (shown centered on this time series of plots to more easily show the hairpins in the intersection jet), and the other closer to the centerline of an individual console hole. The intersection jet's hairpins (one is tracked and shown as A in the figures) are quite steady and occur at a predictable frequency. The smaller, shorter, and weaker hairpins (one is illustrated by B) are much more intermittent in nature and do not occur in an easily predictable manner. Neither of these hairpins are shown to have a significant effect on the instantaneous, local surface temperature plots, but both of the hairpin types are responsible for the greatest jet penetrations at their respective lateral locations (just as the hairpins in the cylindrical hole penetrated the crossflow more than any other structure).

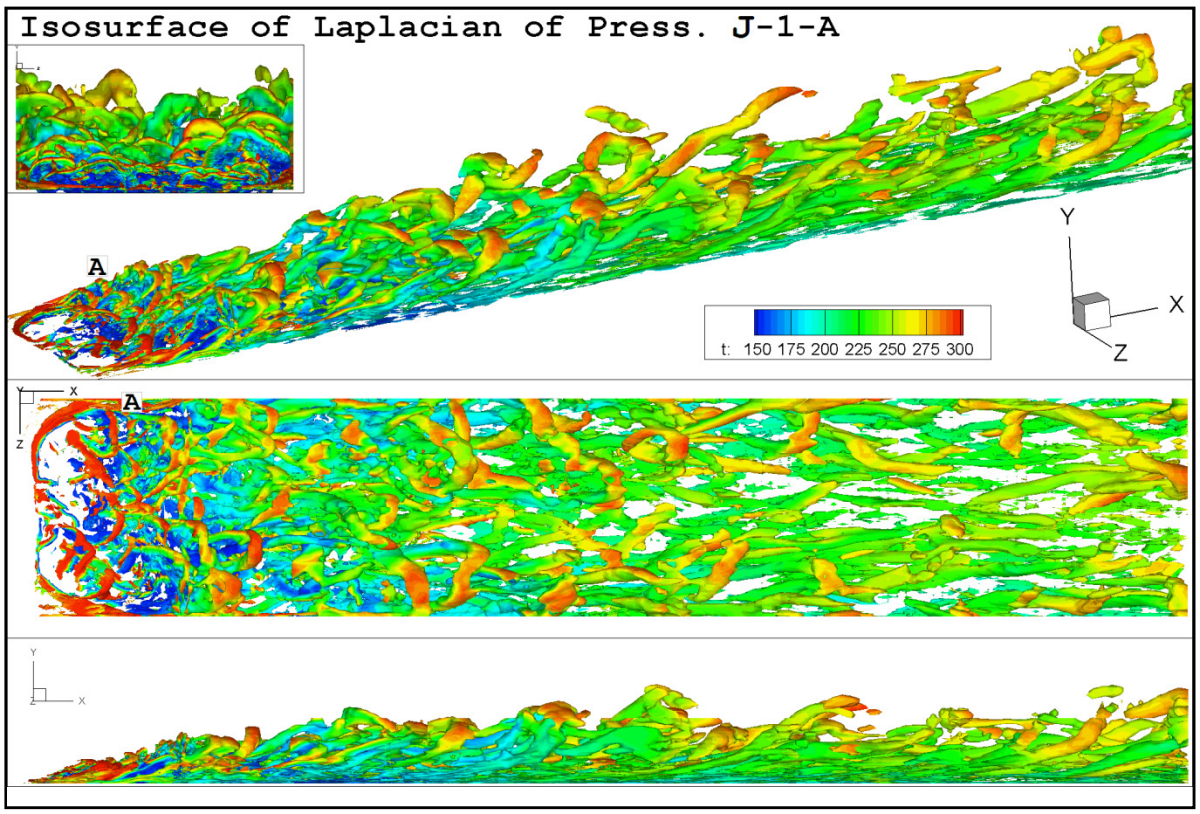

Figure 3.80: Identification of coherent structures in the round hole, L/D=3.5, BR=1 case

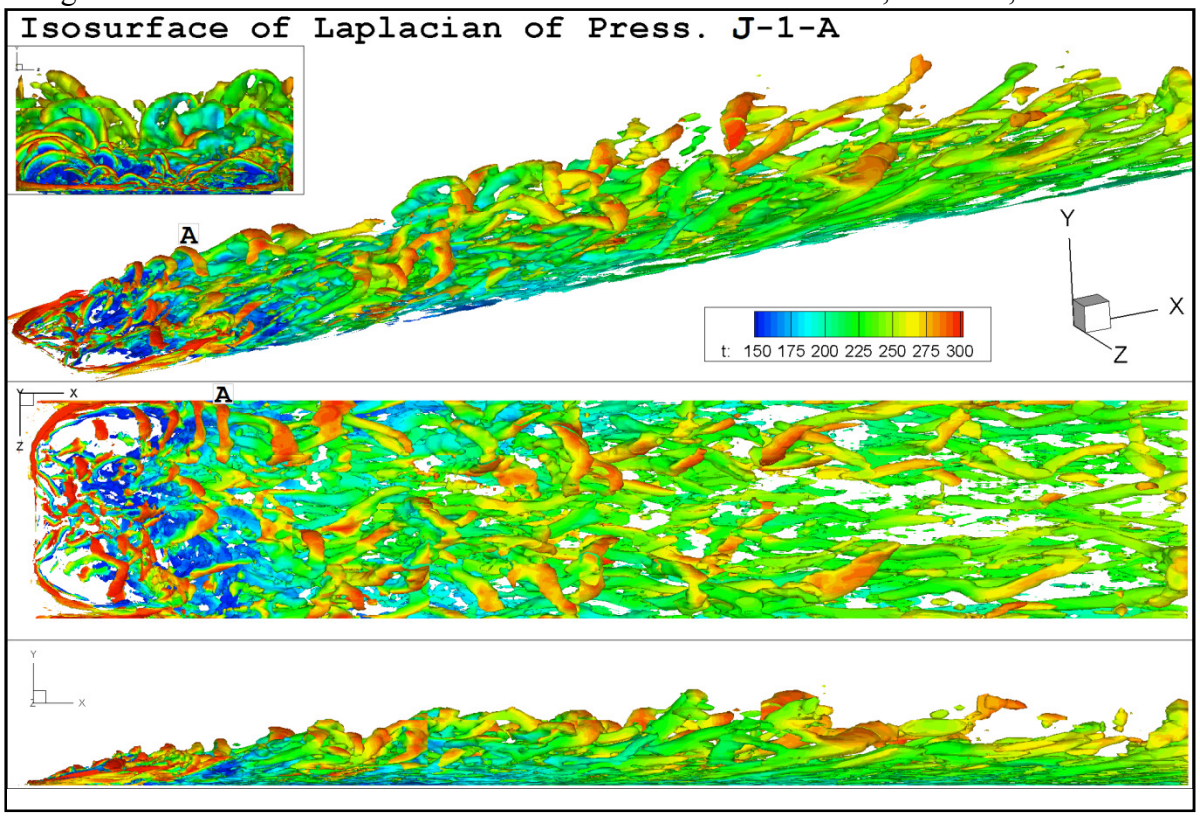

Figure 3.81: Identification of coherent structures in the round hole, L/D=3.5, BR=1 case

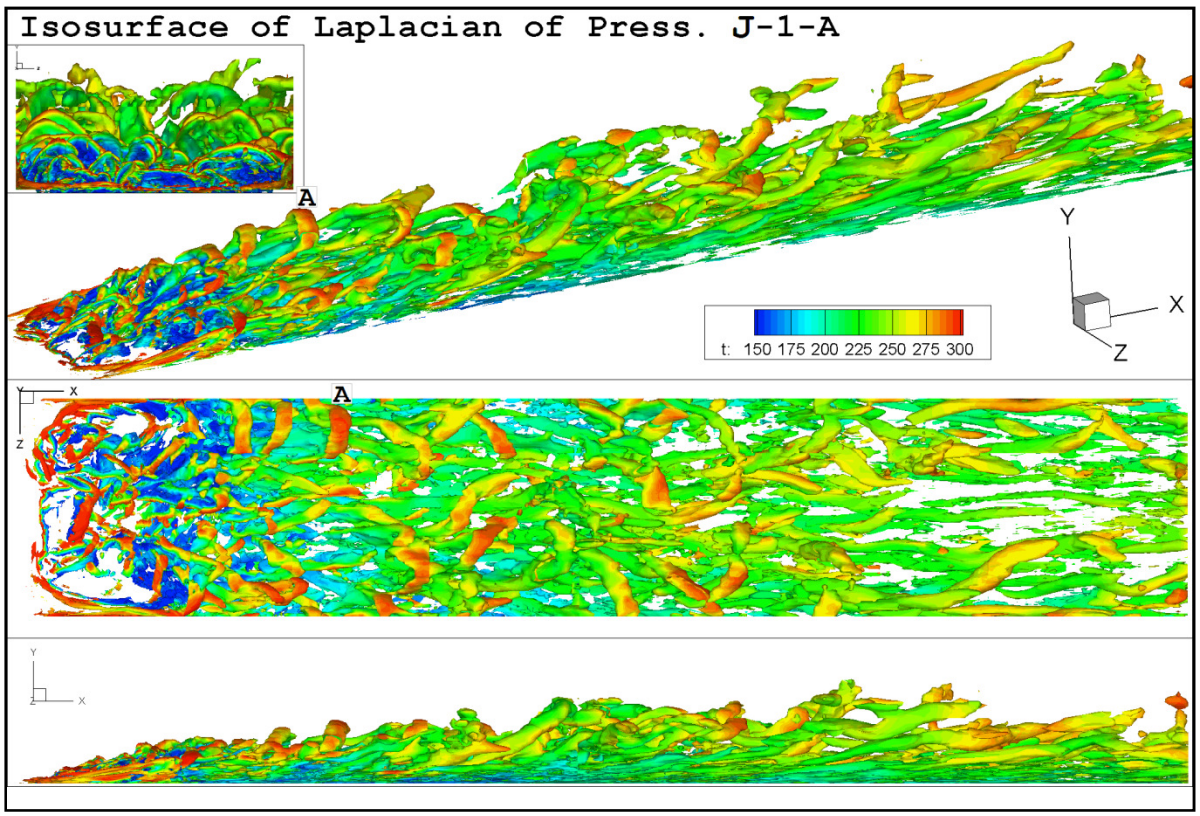

Figure 3.82: Identification of coherent structures in the round hole, L/D=3.5, BR=1 case

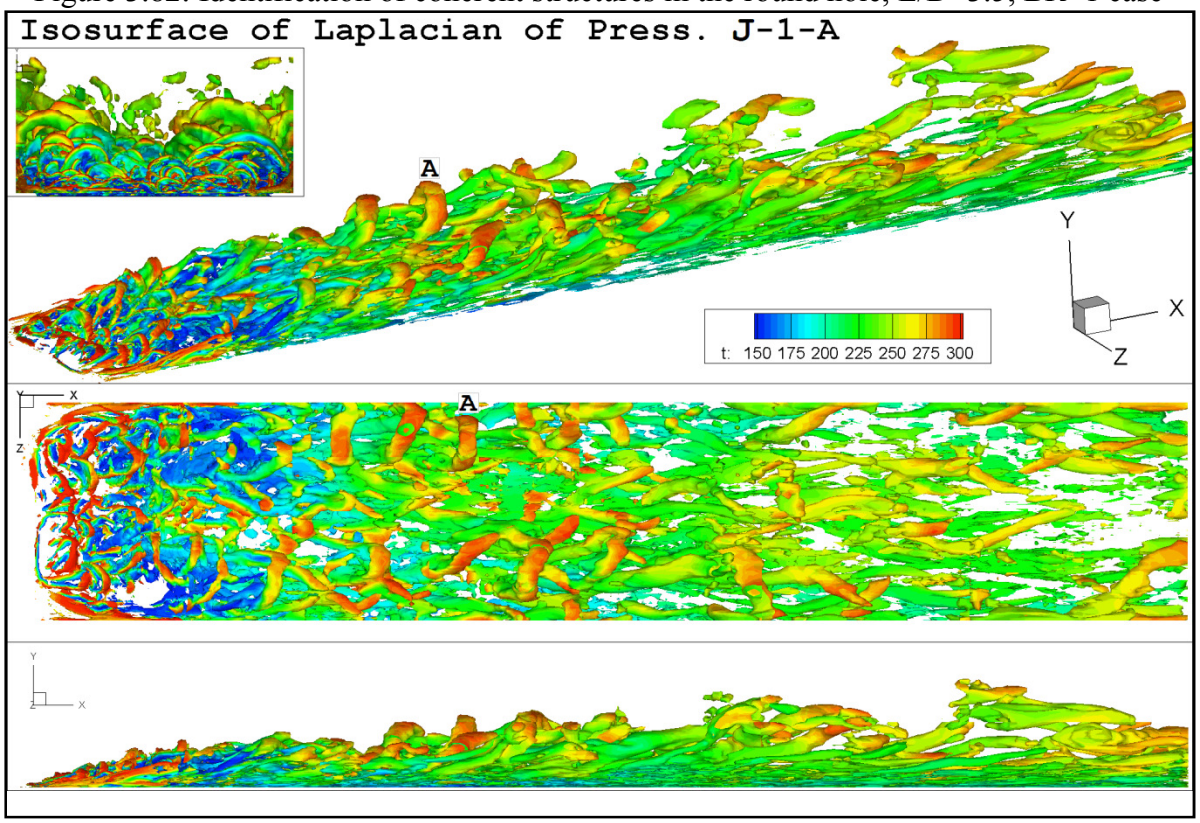

Figure 3.83: Identification of coherent structures in the round hole, L/D=3.5, BR=1 case

The laterally diffused hole at a blowing ratio of 1 (Figures 3.80-83) illustrates an amplified version of the smaller B-type hairpins found in the console hole case (which were not born from a strong vertical jet, but from a relatively weak, more uniform vertical flow. One such hairpin is tracked in the time series plots and is labeled A. The hairpins occur in a more predictable, periodic manner, but not as predictably as the A-type console hairpins or the cylindrical hole hairpins. There also appear to be two distinct sets of hairpins, one at either side (laterally) of the hole. This observation is consistent with the higher vertical velocity of the jet at the lateral sides (see Figure 3.51) due to the aforementioned split jetting effect around a centrally located separation bubble. No distinct evidence of the hairpin having a direct effect on the instantaneous surface temperature plots is observed. Again, the hairpins are responsible for the greatest penetrations of the jet into the crossflow.

Based on the observations in all three of the time series plots, it appears that the formation of hairpin vortices is detrimental to film cooling in that the hairpin penetrates the crossflow deeply without netting any discernable positive effects on the surface temperature distribution. Thus, hole shapes should avoid producing hairpins if at all possible, or at the least strive to make them weaker and smaller (whether they are caused by or are a result of the vertical development of the cooling jet, their presence does not appear to indicate good performance).

3.7 Conclusions

By performing large eddy simulations of film cooling from various discrete hole shapes at varied blowing ratios, the suitability and performance characteristics of different hole shapes has been investigated in this study.

In the case of cylindrical holes, shorter holes were found to have velocity profiles shifted more toward the front of the hole than longer holes at similar operating conditions. This shift

was tracked down the delivery tube and attributed to jetting which was given a longer distance to dissipate in the longer hole. The longer holes also consistently outperformed the shorter holes in terms of surface cooling effectiveness, indicating that the jetting effect is undesirable as exhibited in these simulations. In order to further study the effects of jetting, it is suggested that future simulations be performed with different plenum conditions (such as a crossflow) to examine what happens when the jetting is not confined to the front of the delivery tube and whether there are conditions in which the jetting affects the film cooling characteristics favorably.

In the two shaped geometries simulated, a split jetting effect was found and shown to direct coolant laterally around a central recirculation region rather than along the centerline of the delivery tube. This recirculation region was seen in the cylindrical hole, but since the hole did not expand laterally, no split jetting was exhibited. The diffuser shape of the laterally diffused hole aggravated the splitting of the jet, and the recirculation region extended to the exit plane of the hole where the crossflow interfered with it. The nozzle shape of the console hole helped to dissipate the recirculation region far below the exit plane, but the split jetting characteristics were still plainly visible in the console simulations.

The split jetting effect negatively affected the film cooling from the console hole more than the laterally diffused hole. Because the consoles met one another laterally at the surface, the split jets from adjacent holes were attempting to occupy the same space and impinged on one another. The result was a large penetration of coolant into the crossflow at the lateral locations where the consoles meet one another. Suggested remedies to this situation are a modification of the console shape (lateral diffuser angle or exit slot shape) to encourage more uniform coolant flow at the surface, providing some lateral spacing at the surface between the consoles for the coolant

to spill over onto without immediately running into the next console's coolant, or staggering the consoles slightly in the crossflow direction to prevent the split jets from impinging directly on one another.

Recirculation regions in the crossflow were recorded upstream of the coolant jets (in the form of horseshoe vortices) and downstream of the coolant jets. The effects of the horseshoe vortices on surface cooling were more pronounced in the lower blowing ratio cases. The in the cylindrical hole cases, DSSN vortices had a profound impact on many of the cases tested, and a detailed investigation of this region and any structures in it would be beneficial. In the console holes, a recirculation region directly downstream of the hole exit extended laterally across the entire span of the domain. This recirculation did not exhibit the adverse film cooling characteristics associated with downstream recirculation in other geometries because it extended the width of the domain, preventing the crossflow fluid from entering the recirculation region. No significant downstream recirculation was recorded in the laterally diffused geometries.

Overall, the performance of the shaped holes was dramatically better than the performance of the cylindrical holes in terms of surface adiabatic effectiveness, with the console holes performing slightly better than the laterally diffused holes. In terms of aerodynamic loss, the console and cylindrical hole far outperformed the laterally diffused hole. A future study optimizing angles and inlet/exit shapes for the console would be instructive. Also, measuring the performance of the console against other geometries in a turbulent crossflow would be enlightening, as the much thinner film that makes up much of the console's jet may suffer more than the more uniform, thicker jet effused from the laterally diffused hole.

4 Flow Field Study of Shaped Holes with L/D Close to 5[1]

4.1 Introduction

This flow field investigation will use LES to investigate the flow fields of laterally diffused, console, and cylindrical film cooling holes. While many of the earlier studies on film cooling focused on cylindrical holes, recent efforts have explored the role of hole shaping, particularly laterally and forward diffused holes. In a recent study, the benefits of the console hole shape were demonstrated by Sargison ae al. (2002a). The majority of the studies on shaped holes are either experimental (where the primary emphasis is on surface heat transfer and cooling effectiveness) or RANS computations (which cannot resolve flow unsteadiness and do not model turbulence anisotropic accurately). A key goal of the present work is to provide an understanding of the flow physics associated with hole shaping. Holes are inclined at an angle of 35 degrees to the surface, and Reynolds number (based on cylindrical hole diameter and mainstream flow velocity) will be 36,000. Asymmetric plenum boundary conditions and resulting flow fields within the delivery tube will be investigated to determine their impact on the effused jet's film cooling potential.

4.2 Numerical Method

The numerical methodology used to generate these results is laid out in a previous chapter, but it should be noted that an eddy viscosity limiter of 100 times the laminar viscosity is enforced to ensure stability. A physical time step corresponding to a CFL number of 0.5 is selected. The results are time-averaged until acceptable convergence is reached (typically requiring 15 flow-through times.

[1] (Leedom and Acharya 2008)

4.3 Grids and Boundary Conditions

The physical domain for the cylindrical hole configuration is shown in Figure 4.1. To reduce numerical uncertainty, a grid independence study is initially performed. Three grids are used in this study; all grids are multiblock and body fitted. The reference coordinate system used in this investigation is located on the plane of the film cooled surface in the center of the hole exit. The x direction extends in the downstream direction, and the y direction extends vertically upward perpendicular to the cooled surface.

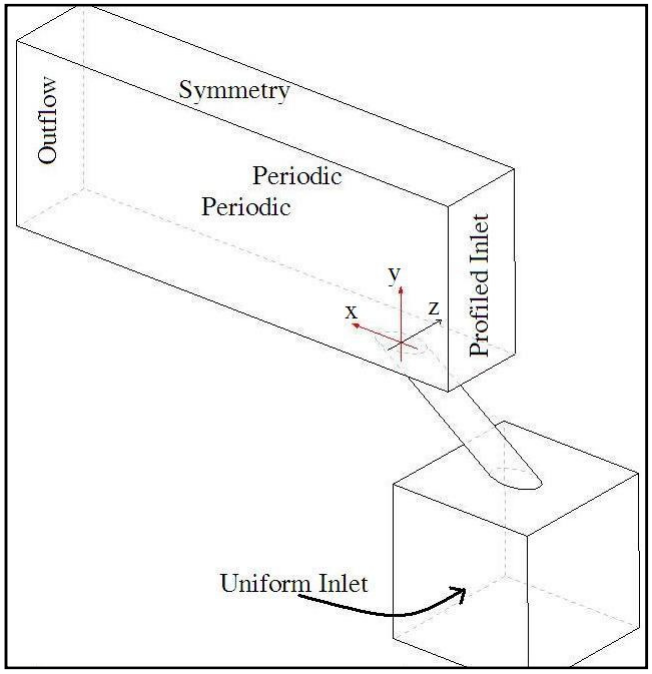

Figure 4.1: Flow Domain and Boundary Conditions

Details of the geometries are shown in Figure 4.2. It should be noted that for the laterally diffused case, the first third of the delivery tube length has a constant cross-section beyond which the lateral diffusion is initiated. For the console hole case, the lateral diffusion is accompanied by a longitudinal convergence of the hole so that the aerodynamic losses due to mixing of the coolant with the crossflow are minimized. In all three cases, the crossflow computational domain extends upstream of the cooling hole to x=-6cm (x/d=-3) and downstream of the hole to

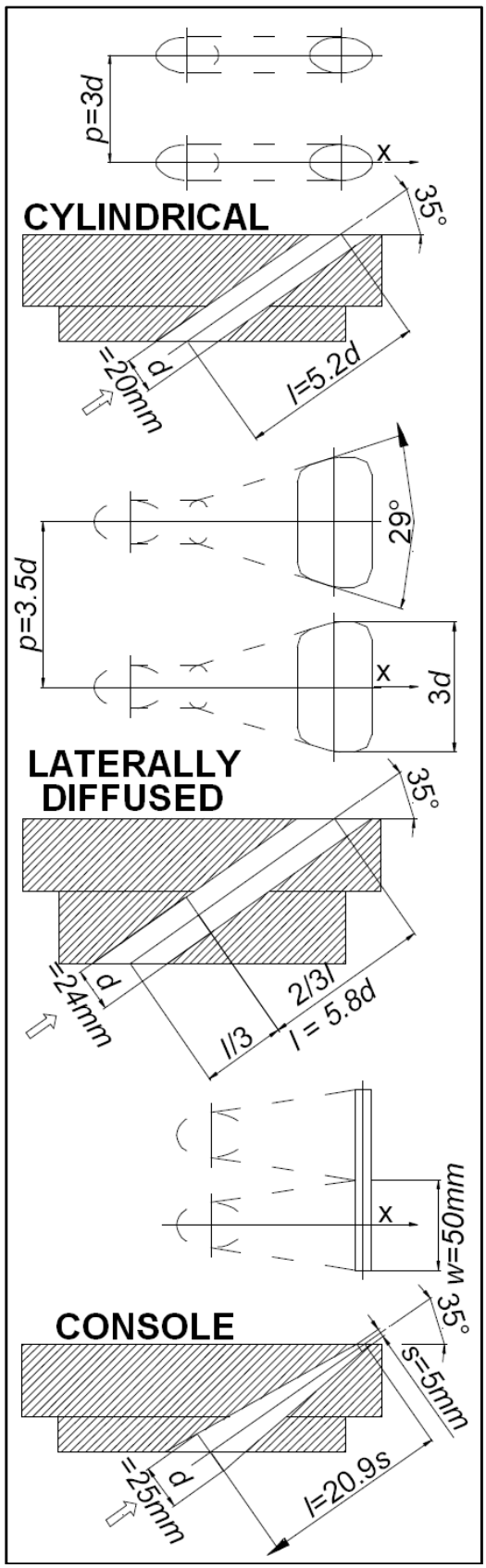

Figure 4.2: Details of simulated geometries drawn by Sargison et al. (2002a)

x=26cm (x/d=13). The plenum for all three cases is a 10cm cube with the coolant passage entrance centered on the top face. In all plots where length is nondimensionalized with hole diameter, the hole diameter referred to is the cylindrical hole diameter of 20mm.

Since LES solves for the time-dependent, resolved velocity field, the spatial and temporal distributions of velocity at the inlet are needed. When these inlet conditions have been available from experiments, investigators have used the measured first and second order statistics and length scales to reconstruct the correct inlet boundary condition. In the absence of measured velocity statistics at the inlet, specification of the inflow conditions is only ad hoc. Since experimental inlet data is not available in the present study, inlet turbulence is neglected and a velocity profile is prescribed.

Adiabatic, no-slip walls are used at all solid surfaces inside the plenum and on the cooled surface. The inlet to the plenum is uniform plug flow, but at the mainstream inlet a velocity profile is specified. The value of u_∞ is 26.48 m/s, and the inlet profile inside the boundary layer is given by:

$$u(y) = u_\infty \left(\frac{y}{\delta} \right)^{1/7} \qquad (4.1)$$

The boundary layer thickness (δ) of the profile introduced is 2d (40mm). A symmetry boundary condition is enforced on the top of the mainstream flow, and the sides of the mainstream flow are periodic in the z-direction. The temperature used for the mainstream flow is 300K and the coolant temperature is 320K (reference temperatures are reversed with coolant temperatures higher than crossflow, but for a density ratio close to unity, this reversal should have no significant impact on the flow field).

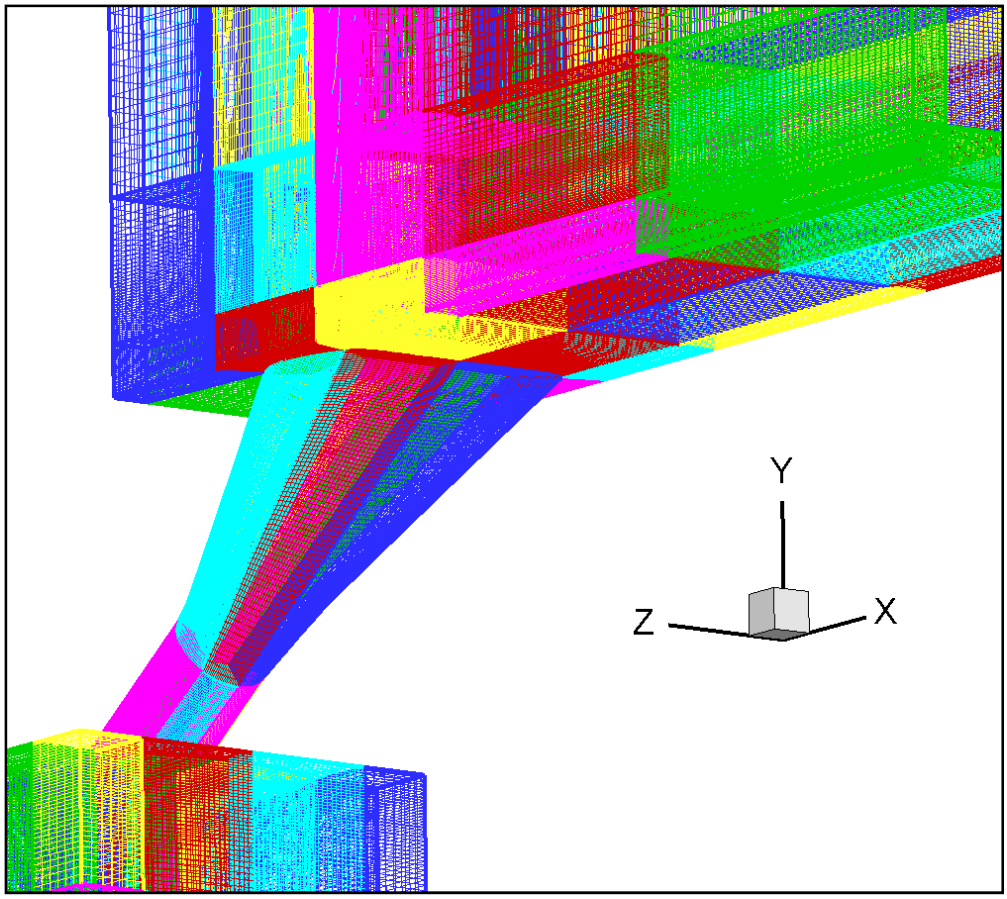

Figure 4.3: Multiblock Grid Example – Laterally Diffused Geometry

The flow domain is decomposed into approximately 150 logically hexahedral blocks that are divided up and distributed to different processors to solve. Production runs are performed on grids with ~4.2 million cells. An example of such a multiblock domain decomposition is shown in Figure 4.3.

The mainstream flow of each case has approximately 175, 110, and 45 cells in the x, y, and z directions respectively. The grid is refined near the wall to provide a first cell height y^+ between .3 and .4 over the majority of the blade surface. Within a y^+ of 10, ~23 grid points are located in the y-direction. In the x-direction, the mesh spacing values ranged from 6 near the hole to 70 near the end of the flow domain in y^+ wall units. In the x-direction, the mesh spacing values ranged from 19 near the hole to 51 near the end of the flow domain in y^+ wall units.

The flow quantity fixed between the three geometries is the mass flow rate of coolant per unit width of cooled blade surface. This makes the mass flow rate of coolant through one hole directly proportional to the pitch of the holes. The reference for the mass flow rate per unit width is the cylindrical hole case, whose mass flow rate corresponds to an I_{ideal} of 1.1 as defined through plenum pressure in the nomenclature section. This I_{ideal} was the criterion held constant in the experiments of Sargison et al. (2002a). In that investigation, to account for different hole sizes in the three geometries the pitch of the holes was varied in order to provide the same throat area per unit width of cooled surface. If the flow were choked (as it is in the follow-up investigation of Sargison et al. (2002b)), this procedure would provide equal flow rates in the three cases. In this investigation, since the flow is largely incompressible, it is appropriate to directly set the coolant mass flow rates per unit width equal so that a direct comparison between the different hole shapes can be made. In the results presented by Sargison et al. (2002a), the mass flux for each hole shape was different, and therefore the results of the present study are not compared with those from the experiments. Furthermore, the experimental inlet boundary conditions needed for LES of the flow are not documented (as discussed earlier in this section). This adds another level of uncertainty that precludes a direct comparison.

For this computational study, the various parameters for the different coolant hole geometries are shown in Table 4.1. As noted above, the parameter that is held constant in all these cases is the coolant mass flow rate per unit width in the pitch direction. This ensures that for a given blade or vane, all coolant hole configurations have the same coolant mass flow rate, and a direct comparison between the various cases can be made. With the mass flux held constant, the blowing ratio (BR) for each case becomes a function of the hole exit cross-sectional area. The BR is the largest for the console hole case and the smallest for the laterally diffused case.

Table 4.1: Paramaters of Simulated Cases

	Cylindrical	Laterally Diffused	Console
Flow/Width (kg s^{-1} m^{-1})	.10588	.10588	.10588
Pitch (mm)	60	82	50
Flow Rate (kg s^{-1})	0.0063528	0.0086822	0.0052940
Density Ratio	0.9375	0.9375	0.9375
Velocity Ratio	0.7212	0.2337	1.3168
Blowing Ratio	0.6761	0.2191	1.235

4.4 Grid Independence Study

A grid independence study is performed for the cylindrical hole geometry in order to provide confidence that the important flow features are well resolved at the level of grid refinement used in the production runs. Time-averaged results for the cylindrical hole case are obtained for grids having 1, 2, 4, and 8 million cells. The grids used in this grid independence study employed the same block decomposition, boundary conditions, and grid clustering ratios for each grid refinement level. The number of cells on all block edges is simultaneously scaled by a constant factor to generate a grid with the desired cell count.

The time-averaged u and v velocity components are shown in Figure 4.4. The data shown is taken directly downstream of the hole at an x/d location of 1. There were 75 cells, 95 cells, 108 cells, and 118 cells vertically in the mainstream flow for the 1, 2, 4, and 8 million cell grids respectively.

The results show that the flow solutions appear to be well converged at the four million cell level. The differences in the peak velocity between the four and eight million cell calculations are less than 3%. It should be noted that in this implementation of LES, the filter width changes with the width of the grid cells. This makes a formal grid independence study difficult because

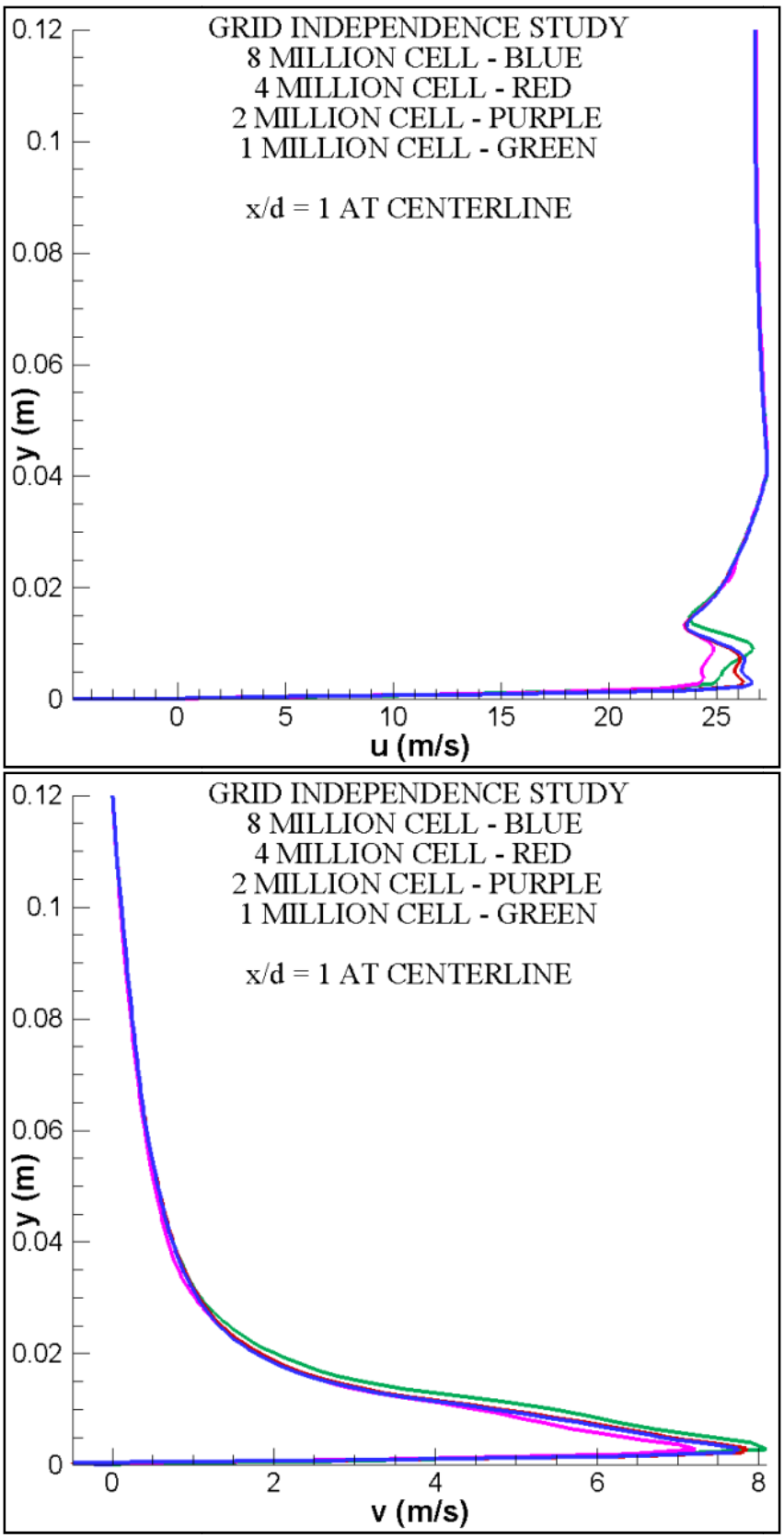

Figure 4.4: Grid Independence Study

the turbulent length scale beyond which the sub-grid scale model takes over becomes smaller with the grid spacing. This study should provide some measure of confidence that fine enough grids were used. All production grids in this section are approximately four million cells unless noted otherwise.

4.5 Results and Discussion

Plots of key time-averaged statistics are presented in the following figures for the center (z=0) plane of the jet; plots include the temperature (Figure 4.5), T_{rms} (Figure 4.6), turbulent kinetic energy (Figure 4.7), and u velocity (Figure 4.8). Each geometry has the same mass flow rate of coolant per unit width (pitch) so that a direct comparison can be made as described earlier. Note again that the temperature scales are inverted from the true situation in a turbine in that the coolant jet has a nondimensional temperature of one and the crossflow is at a nondimensional temperature of zero.

Figure 4.8 and Figure 4.5 show distinct differences in the mean velocity and temperature profiles between the different cases. The results show that the console's performance is superior to the laterally diffused and cylindrical holes in terms of jet penetration into the crossflow. This is best illustrated by comparing the temperature contours in Figure 4.5. The cylindrical hole case shows higher penetration and mixing in the jet and wake regions, while the console case shows that most of the coolant jet penetrates to less than .4d and covers the wall without mixing much with the crossflow. The velocity contours in Figure 4.8 illustrate that for the cylindrical hole case, there is significant jetting effect in the coolant delivery tube, with the peak velocities shifted toward the leeward side of the hole. For the laterally diffused case, the jetting effect is essentially eliminated, and the exit profile appears more uniform. The console hole geometry also exhibits higher velocities on the leeward side of the coolant hole exit. In examining the

TKE profiles (Figure 4.7), it is clear that the highest turbulence levels are generated near the jet exit and the leeward side of the jet, with the cylindrical hole turbulence levels being higher than those in the laterally diffused hole case. These higher turbulence levels for the cylindrical hole case contribute to the enhanced mixing between the coolant fluid and the crossflow as observed in the mean temperature distributions. For the console hole, the turbulence at the hole exit is the lowest (due to the flow acceleration imposed by the delivery tube geometry); however, the high-speed, leeward side of the jet is associated with greater turbulence that shows up as a local region of high turbulence intensity near the wall in the vicinity of x/d of 1 (Figure 4.7). Interestingly, the T_{rms} plots (Figure 4.6) indicate that their peak values originate from the windward side of the coolant jet as it encounters the crossflow and propagates downstream. Note that the peak kinetic energy levels are found on the leeward side of the jet, making a case for a direct spatial correlation between the velocity and temperature fluctuations weak. The console hole has the

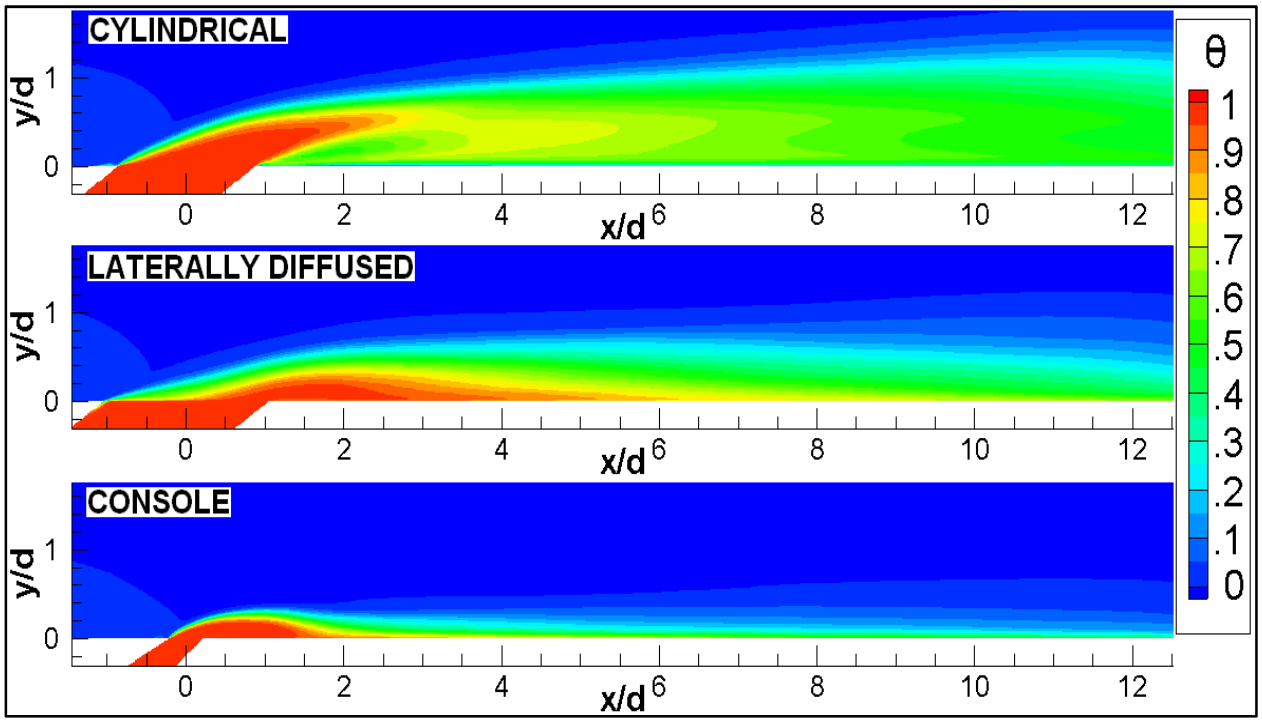

Figure 4.5: Time-averaged Nondimensional Temperature on the z=0 Midplane

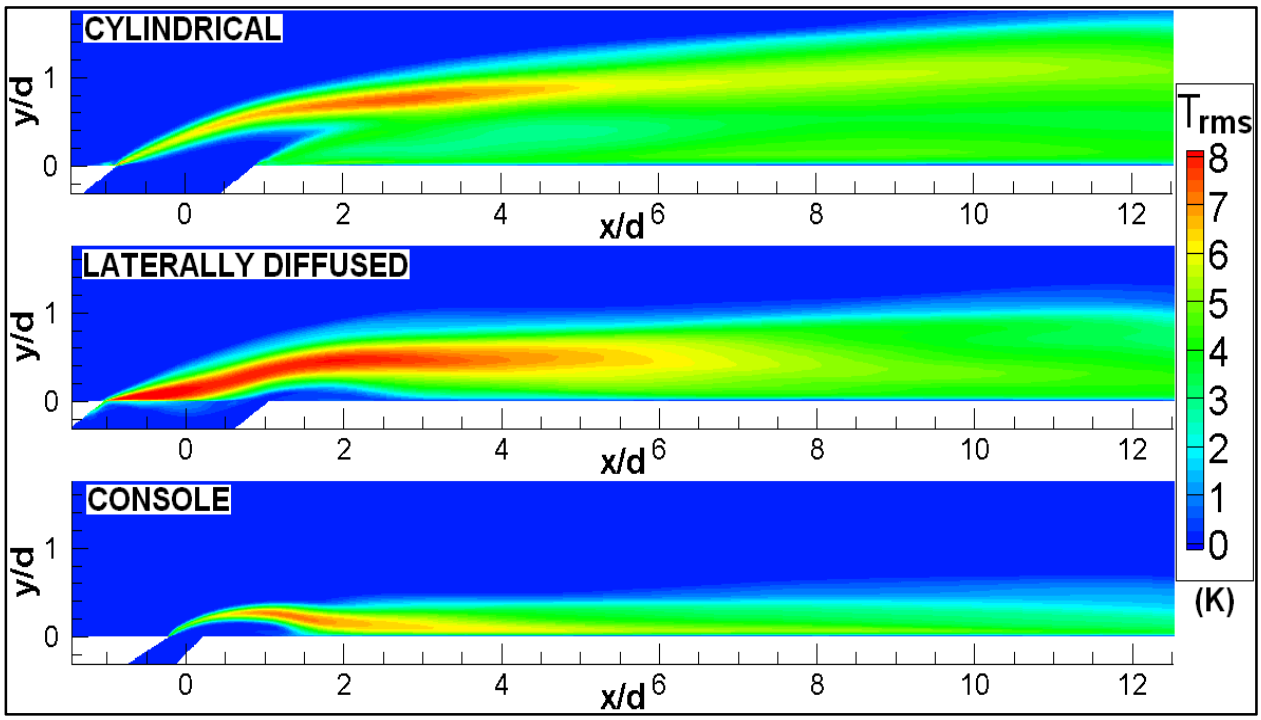

Figure 4.6: Root-mean-square of Temperature Plotted on the z=0 Midplane

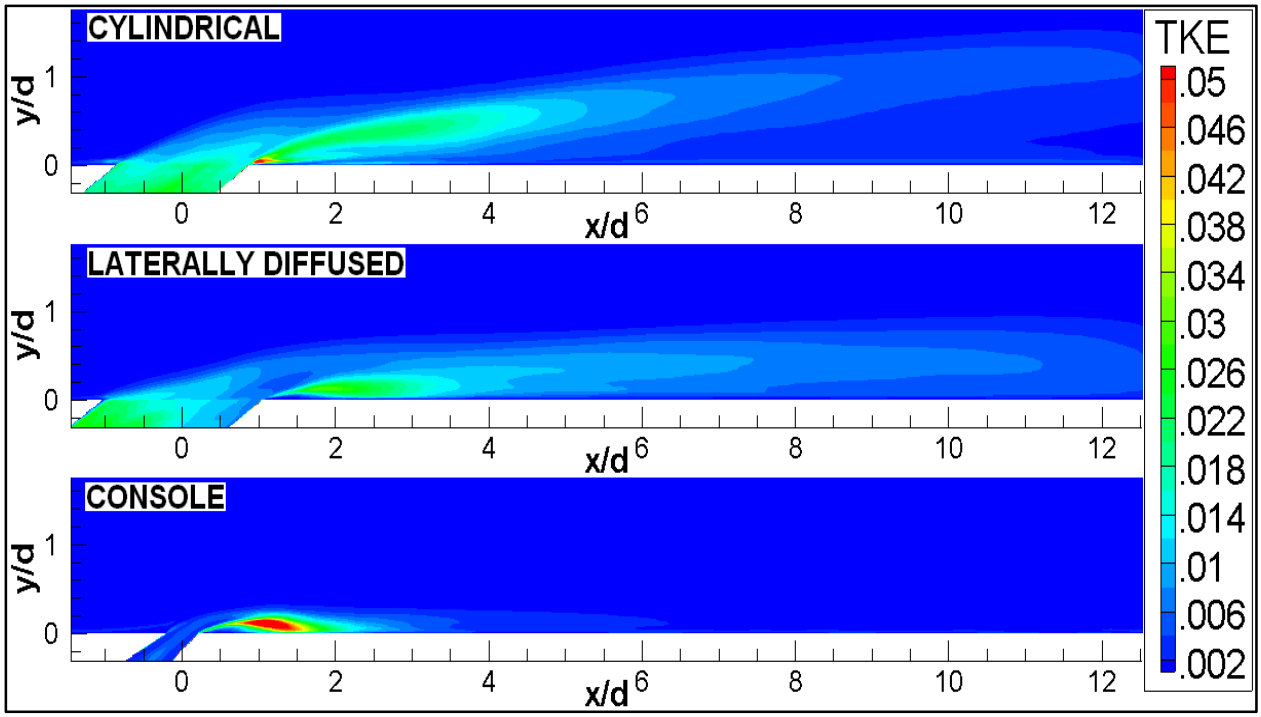

Figure 4.7: Normalized Turbulent Kinetic Energy on the z=0 Midplane

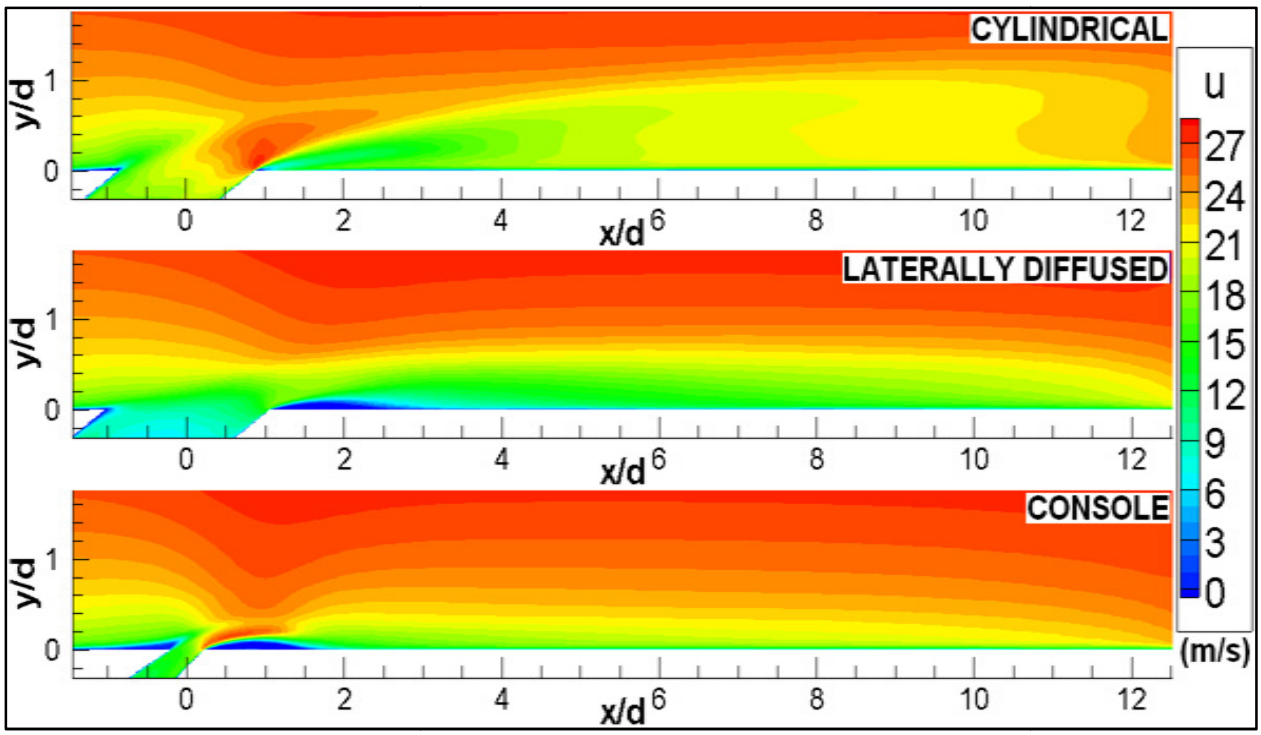

Figure 4.8: u-velocity on the z=0 Midplane

lowest T_{rms} values and the lowest spatial distribution of the high kinetic energy region; this indicates that the console jet does not have as much turbulent fluctuation as the other cases. Therefore, the console is associated with lower levels of turbulent mixing of the jet with the crossflow.

Figure 4.9 shows the cross-stream (in the y-z plane) distributions of the normalized temperature (θ) and streamwise vorticity (ω_x) at x/d=1, 3, and 7. The vorticity plots for the cylindrical holes show the traditional kidney pair vortices riding on top of wall vortices of the opposite sign. The wall vortices are an indication of crossflow entrainment beneath the coolant jet. Evidence of horse-shoe vortices deflected around the coolant jet can also be seen at x/d=1, but this dissipates further downstream. There is some inherent asymmetry in the kidney pair structure that will be discussed later. For the laterally diffused hole case, the kidney-pair structures are much smaller in size, further separated from each other (due to the greater lateral

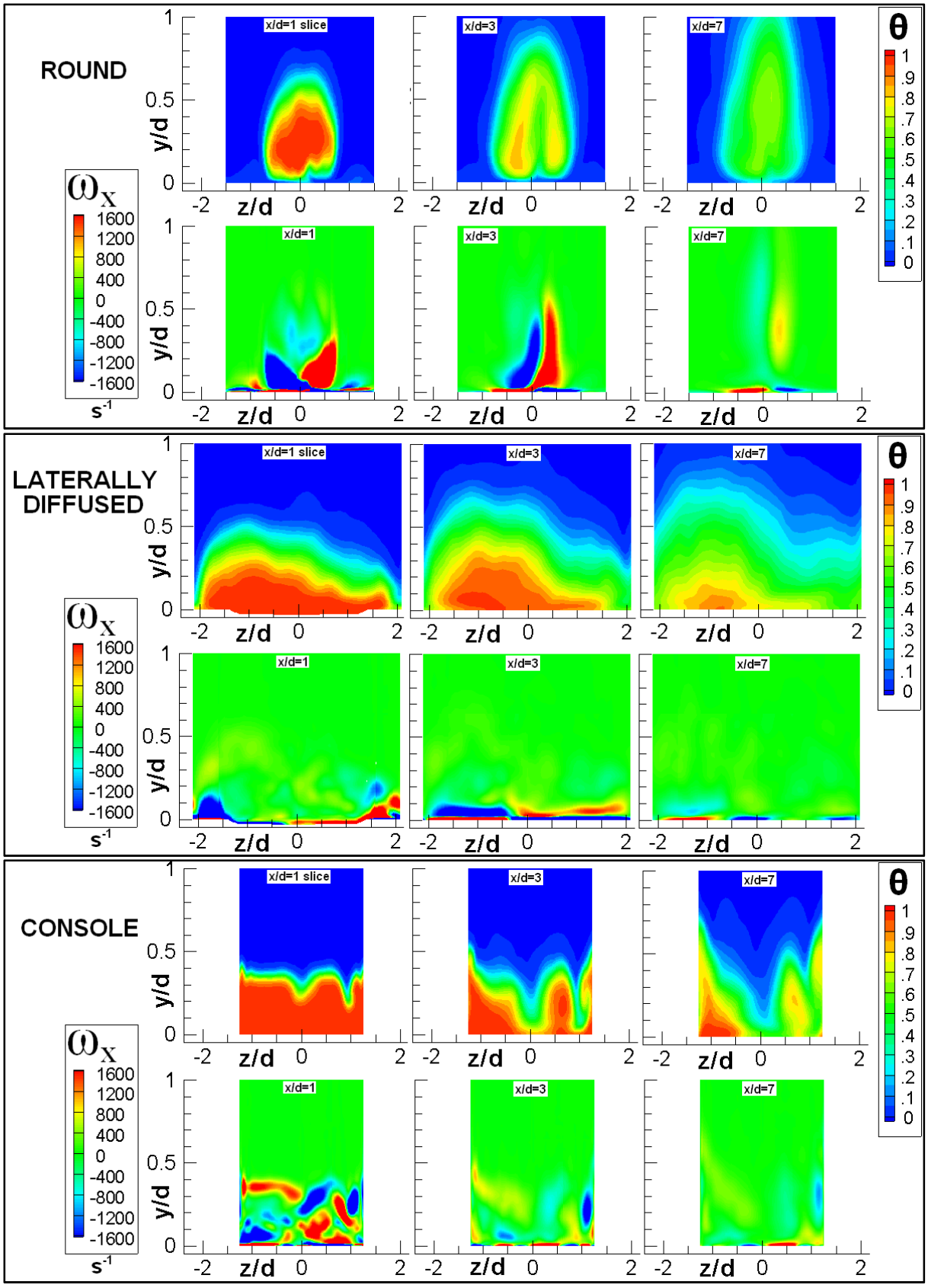

Figure 4.9: Temperature and ω_x Contour Slices at x/d=1, 3, and 7 for Each Geometry

spreading of the jet), and closer to the wall (due to reduced vertical penetration of the coolant jet into the crossflow). The console hole vorticity plot shows that the kidney pair is also considerably separated in the pitch direction compared to the cylindrical hole case. For both the console and the laterally diffused cases, the larger separation of the kidney vortices reduces the self-induced vorticity and lift-off of the coolant jet from the surface; this is evident in both the vorticity and temperature plots. The console holes show the kidney pair structure in the near field, but also show additional flow structures (discussed later) that originate in the coolant delivery tube and have the appearance of an anti-kidney pair riding on top of the kidney-pair vortices noted by Haven and Kurosaka (1997). The anti-kidney pair quickly dissipates the primary kidney pair vortex structure, but induces additional mixing and penetration along the periodic boundaries. This interaction along the periodic boundaries between neighboring holes when the consoles merge together into a slot at the surface is detrimental to the hole behaving as a uniform slot. Figure 4.10 shows the time-averaged vertical velocity component downstream of the console hole. In the center of the hole (where the issued jet is well attached), the vertical velocity is not as significant as at the edges of the hole, where adjacent console holes are merging. Strong upward flow exists at the edges of the hole; this is responsible for increased mixing and vertical penetration of the coolant jet along the periodic boundaries. From the temperature plots at x/d=3, it can be seen that while the center of the console flow stays close to the surface, the sides of the jet (where the console meets another console) penetrate further.

It is evident from Figure 4.9 that the significant size and strength of the kidney pair vortex structure for the cylindrical hole case causes the coolant jet to be lifted well above the surface, while for the shaped hole cases the kidney pair structures are smaller or dissipate rapidly. This behavior in the shaped geometries minimizes the cross-plane mixing and helps to keep the

coolant jet close to the surface. The cylindrical and laterally diffused hole cases show that in the jet wake, the mainstream air is entrained beneath the jet while in the console hole case this entrainment is not as pronounced. The u velocity plots (Figure 4.8) show that the laterally diffused hole (which has the lowest BR) slows down the flow more significantly than the other geometries. This potentially implies a lower aerodynamic efficiency for the blade as evidenced by the large pocket of slowly moving air downstream of the hole.

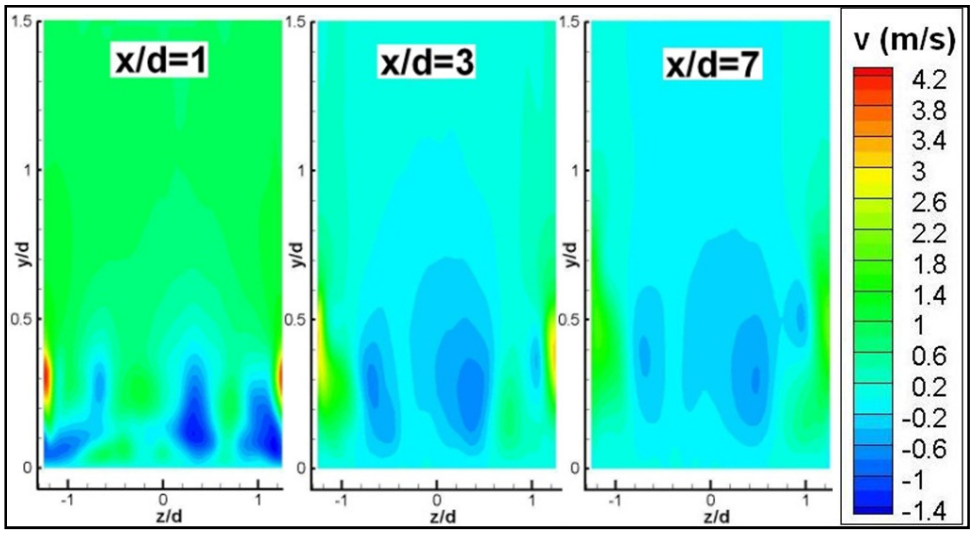

Figure 4.10: Time-averaged Vertical Velocity Downstream of the Console Hole

The flow inside the coolant delivery tube is complex and three-dimensional. The velocity field in a tube fed by a plenum often exhibits a zone of recirculation at the inlet to the delivery tube. In order to better understand the flow inside the tube, the component of velocity along the axis of the delivery tube is plotted for each geometry in Figure 4.11.

For all three geometries, a zone of separated flow forms in the lower part of the delivery tube, and this creates a jetting effect within the tube. The jetting produces a region of high velocity and separated flow within the tube, but these characteristics are different for each hole shape. In the cylindrical case, the jetting is most pronounced; the high-velocity region shifts toward the

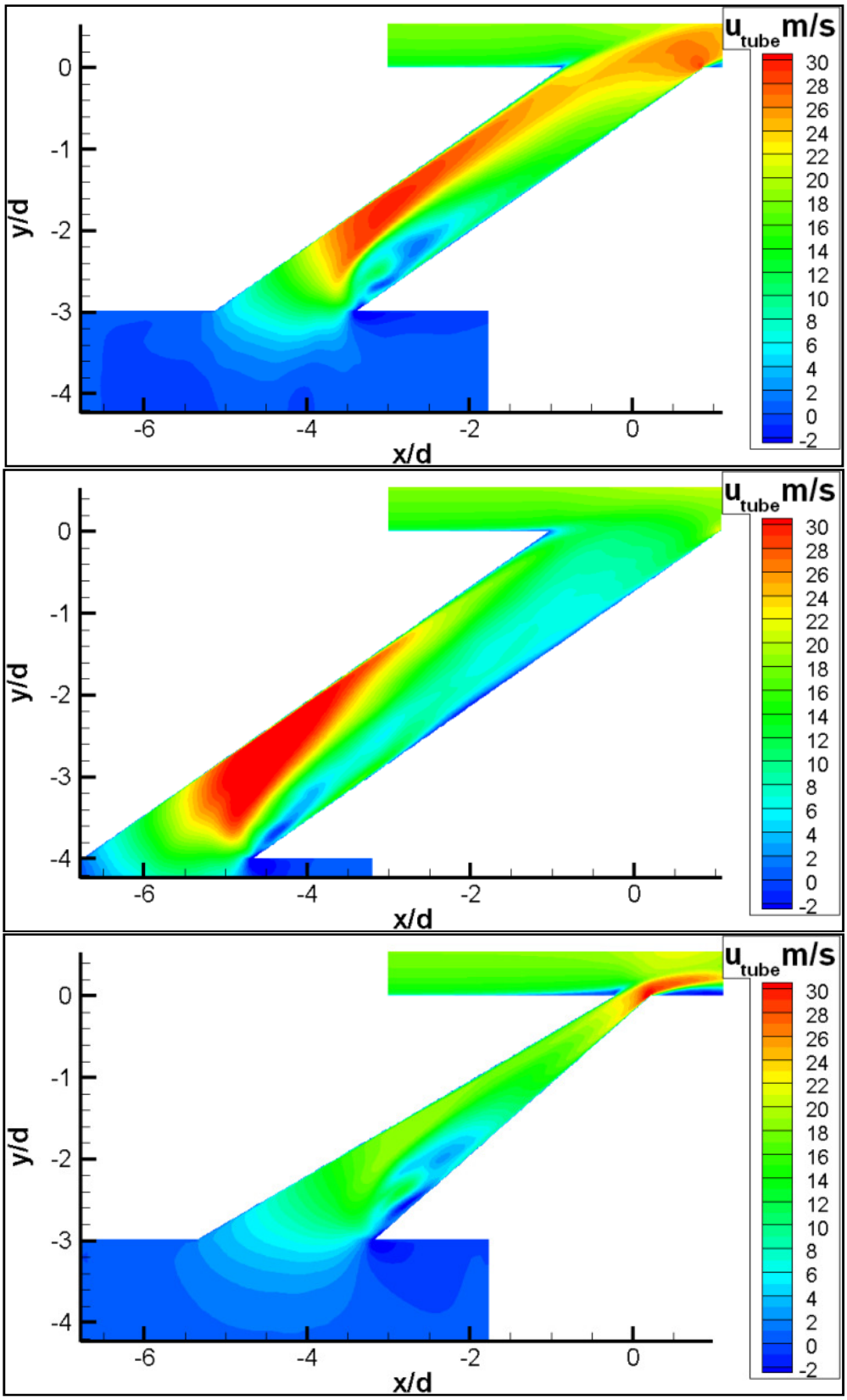

Figure 4.11: Midplane Plots of Velocity in the Direction of the Delivery Tube

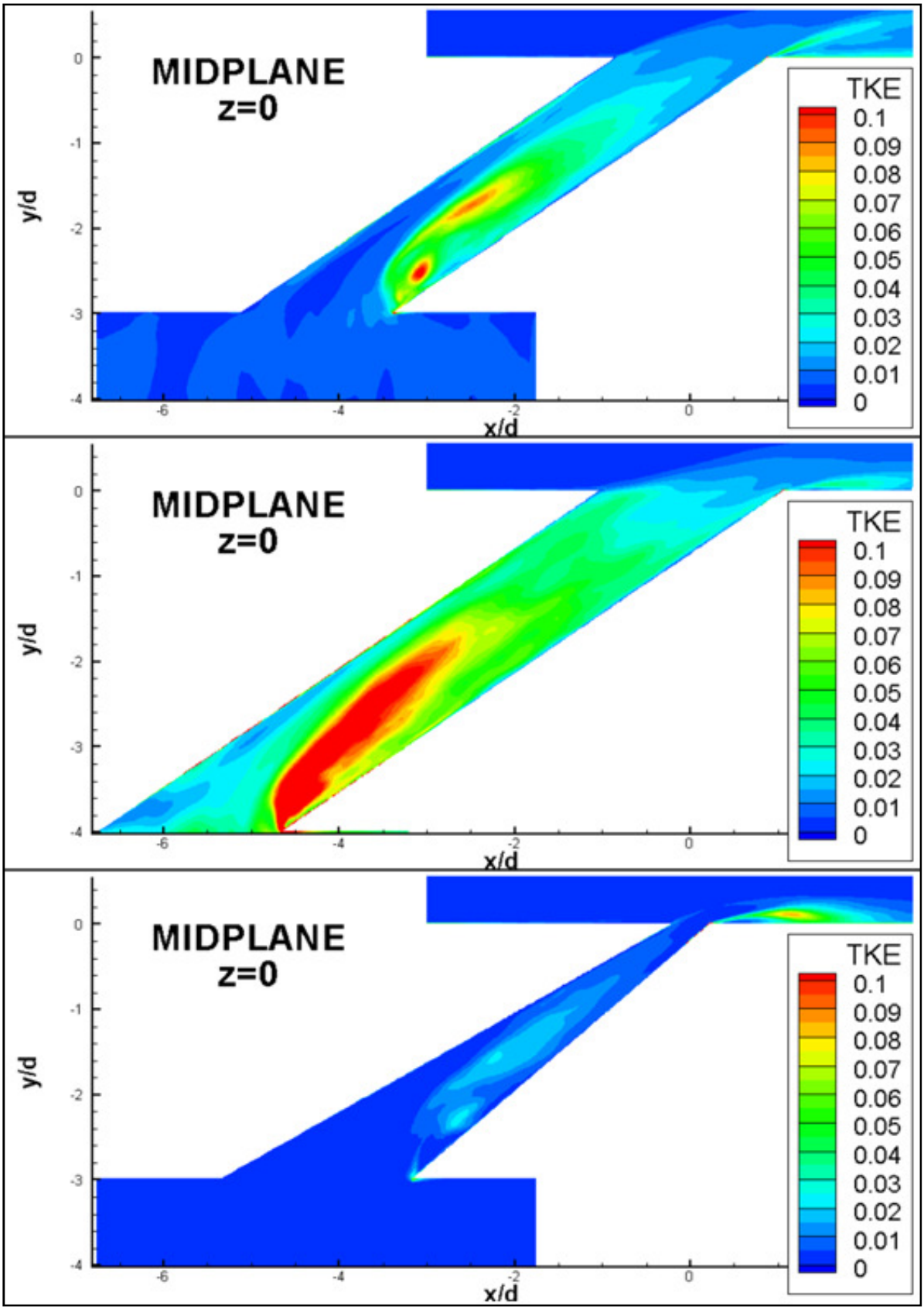

Figure 4.12: Nondimensional Turbulent Kinetic Energy in the Delivery Tube

leeward side of the hole at the exit. For the laterally diffused case, the high-velocity regions die down (via area expansion), and the velocity profiles at the exit appear more uniform. For the console case, the separation and jetting within the delivery tube are the weakest. High velocity gradients within the delivery tube are associated with high TKE (Figure 4.12). TKE is highest in the laterally diffused case, lower in the cylindrical case, and much lower in the console case. The lower TKE for the console case is beneficial in view of the reduced mixing between the coolant jet and the crossflow downstream of the hole. This reduced mixing effect is evident in the x-y temperature contour plots shown in Figure 4.5 earlier.

4.6 Anisotropy Investigation

RANS turbulence models which assume that all turbulence is isotropic have difficulty accurately predicting film cooling flow fields. Since LES does not have this restriction, second order statistics may be plotted to check whether or not this assumption of isotropic turbulence is correct.

Figure 4.13 shows the statistical averages of the velocity components at the x/d=3 plane for the cylindrical, laterally diffused, and console hole flow fields. Turbulence levels are clearly the highest in the jet region, and the turbulence is strongly anisotropic. The plots show that generally, $u_{rms}>w_{rms}>v_{rms}$. The magnitude of u_{rms} compared to that of v_{rms} is approximately twice as large, making the flow significantly anisotropic. Clearly, an isotropic turbulence model is inadequate for such a flow field.

4.7 Asymmetry Investigation

One unique aspect of this study is the use of an inlet boundary condition implemented on the side (z-face) of the feeding plenum chamber instead of the typical inlet on the bottom (y-face) of the plenum. This choice of inlet was made in order to more closely match the experimental case

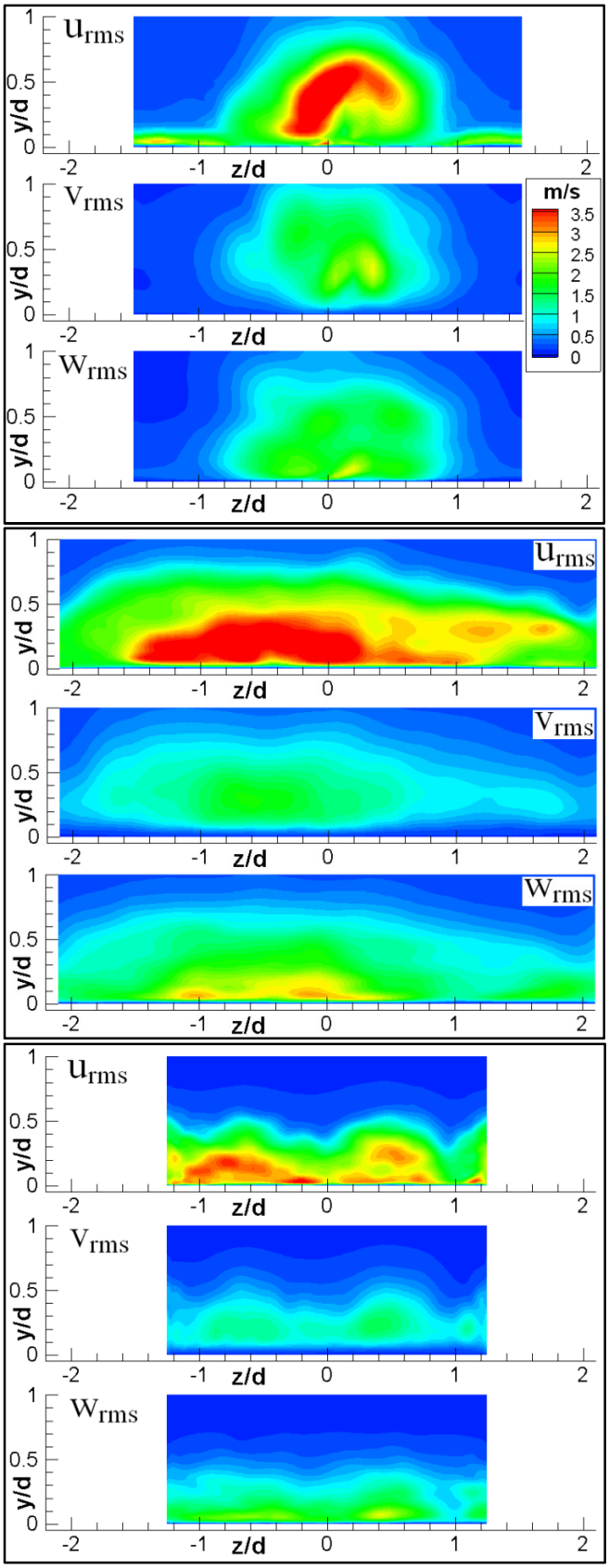

Figure 4.13: Second-order Statistics of Velocity 3 Hole Diameters Downstream of the Hole

by Sargison et al. (2002a) from which the geometries are derived. It was assumed at the beginning of the study that the low speed of the plenum's inlet flow would render it innocuous to the stronger effused jet. It turns out that this choice of inlet induces asymmetries in the flow field downstream of the hole that could significantly affect film cooling performance. This asymmetry is investigated thoroughly for the cylindrical hole case here.

Gritsch et al. (2003) have completed a study on the effects of internal coolant crossflow for internal crossflow velocities which are close to or exceed the mainstream flow velocity. The crossflow velocity in the present study is on the order of 3 percent of the mainstream flow velocity, and yet the direction of the flow into the plenum appears to be important.

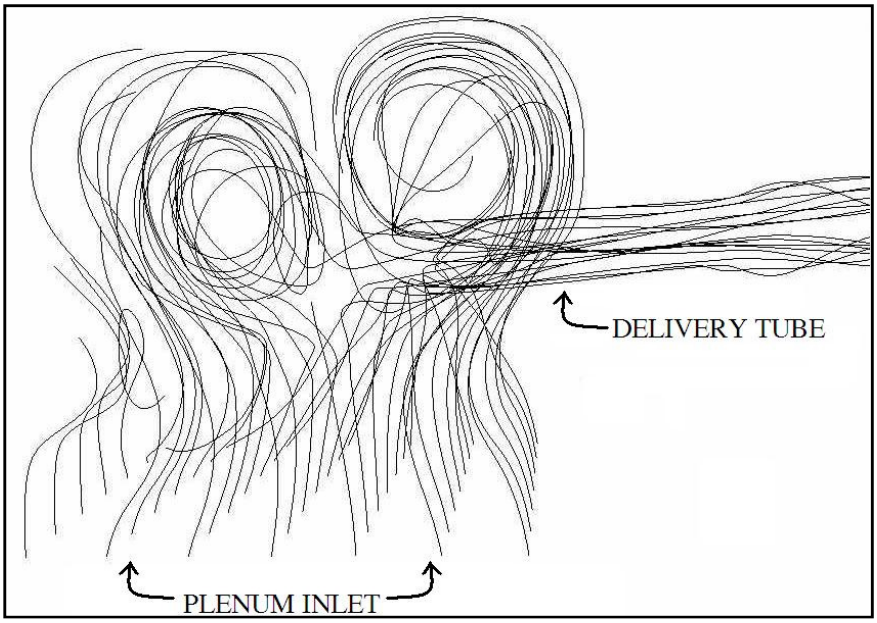

Figure 4.14: Streamtraces in the Plenum Chamber

The general flow pattern in the feeding plenum is evident in Figure 4.14, which shows the paths of some streamtraces released at the inlet plane of a time-averaged flow solution. The fluid in the plenum is organized into two weak, counter-rotating vortices in the plenum. These vortices are then stretched and strengthened as they are whisked into the coolant delivery tube.

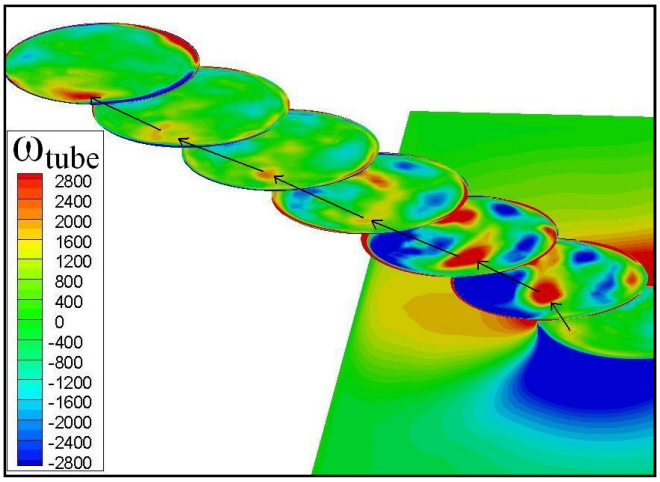

Figure 4.15: Cross sections showing vorticity (s^{-1}) along the axis of the cylindrical hole

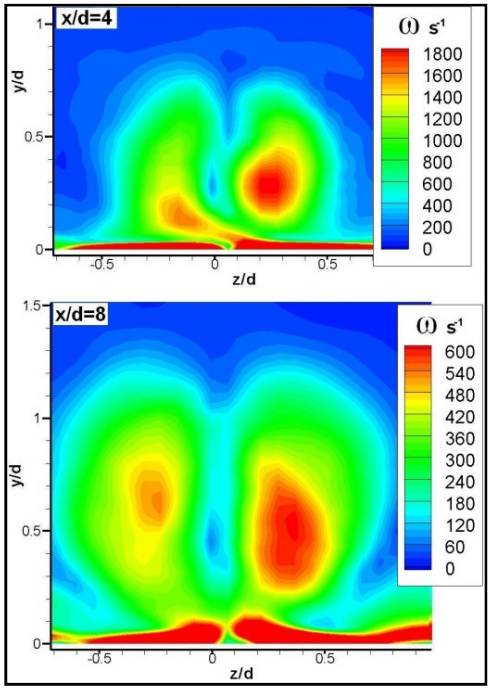

Figure 4.16: Vorticity Magnitudes Downstream of the Cylindrical Hole Case

It is suspected that some manifestation of the asymmetry in the feeding plenum survives the ride up the delivery tube and affects the flow field outside. The most obvious asymmetry in the flow up the coolant delivery tube is a pocket of vorticity in the direction of the tube that extends the length of the tube and is quite intense at the exit. This pocket is shown and tracked in Figure 4.15, and is also evident in flow downstream of the hole exit. Figure 4.16 shows the state of the

counter-rotating vortex pair (CVP) at downstream distances of x/d=4 and x/d=8. A plot of the magnitude (absolute value) of vorticity is used to easily compare relative strength between sides of the CVP. The side on which the pocket resides is skewed and weaker. This disruption of the CVP could have consequences for the near-field film cooling properties.

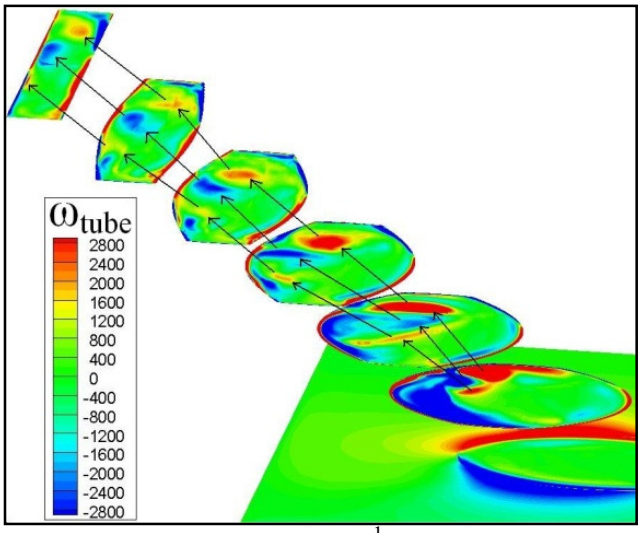

Figure 4.17: Cross-sections Showing Vorticity (s^{-1}) Along the Axis of the Console Hole

Evidence of similar pockets of vorticity in the console case is shown in Figure 4.17. Since there is no well-defined CVP downstream of console holes, it is more difficult to determine the effects of the pockets in this case. The laterally diffused hole did not have such well-defined pockets of vorticity spanning the delivery tube; this can either be attributed to the diffuser slowing the flow or the greater turbulent kinetic energy in the throat of the laterally diffused hole shown in Figure 4.7.

4.8 Conclusions

Large Eddy Simulations were performed for three cooling hole configurations: cylindrical holes, laterally diffused holes, and console holes. In all cases, the coolant mass flow rate per unit

width was held constant so that a direct comparison between the three cases could be made. The shaping of the film cooling holes is clearly an important consideration in the distribution and coverage of the coolant film. The console shape demonstrates reduced vertical penetration and improved coverage of the surface by the coolant film. However, higher jet-penetration and mixing is achieved in the vicinity of the console hole mergers; this points to the potential for additional improvements by changing the nature of the console hole's mergers. The turbulence generated in the near field of film cooling jets was found to be highly anisotropic. Vorticial structures found to emanate from the plenum chamber were tracked through the coolant delivery tube and effects on the issued jet were investigated. The importance of the choice of boundary condition for the feeding plenum chamber (even with low plenum velocities) was documented.

References

Azzi, A. and B. A. Jubran. "Numerical Modelling of Film Cooling from Converging Slot-Hole." *Heat Mass Transfer* 43 (2007): 381-388.

Baker, C. J. "The Oscillation of Horseshoe Vortex Systems." *Journal of Fluids Engineering* 113 (1991): 489-495.

Baldauf, S., A. Schulz, and S. Wittig. "High-Resolution Measurements of Local Effectiveness from Discrete Hole Film Cooling." *ASME Journal of Turbomachinery* 123 (2001): 758-765.

Bogard, D. G. "Fundamentals of Film Effectiveness Performance." In *Von Karman Institute for Fluid Dynamics Lecture Series: Film Cooling Science and Technology for Gas Turbines.* Rhode-Saint-Genese, Belgium. April 16-20, 2007.

Bons, J. P., C. D. MacArthur, and R. B. Rivir. "The Effect of High Free-Stream Turbulence on Film Cooling Effectiveness." *ASME Journal of Turbomachinery* 118 (1996): 814-824.

Brittingham, R. A. and J. H. Leylek. "A Detailed Analysis of Film Cooling Physics: Part IV - Compound-Angle Injection With Shaped Holes." *ASME Journal of Turbomachinery* 122 (2000): 133-145.

Bunker, R. S. "A Review of Shaped Hole Turbine Film Cooling Technology." *Journal of Heat Transfer* 127 (2005): 441-453.

Cortelezzi, L., and A. R. Karagozian. "On the Formation of the Counter-rotating Vortex Pair in Transverse Jets." *Journal of Fluid Mechanics* 446 (2001): 347-373.

Dhungel, S., A. Phillips, S. Ekkad, and J. D. Heidmann. "Experimental Investigation of a Novel Anti-Vortex Film Cooling Hole Design." In *Proceedings of ASME Turbo Expo 2007*. Montreal, Canada. May 14-17, 2007.

Ekkad, S. V., D. Zapata, and J. C. Han. "Film Effectiness Over a Flat Surface With Air and Carbon Dioxide Injection Through Compound Angle Holes Using a Transient Liquid Crystal Image Method." *ASME Journal of Turbomachinery* 119 (1997): 587-593.

Germano, M., U. Piomelli, P. Moin, and W. H. Cabot. "A Dynamic Subgrid-scale Eddy Viscosity Model." *Physics of Fluids* 3 (1991): 1760-1765.

Gritsch, M., A. Schulz, and S. Wittig. "Adiabatic Wall Effectiveness Measurements of Film-Cooling Holes With Expanded Exits." *ASME Journal of Turbomachinery* 120 (1998): 549-556.

Gritsch, M., A. Schulz, and S. Wittig. "Effect of Internal Coolant Crossflow on the Effectiveness of Shaped Film-Cooling Holes." *ASME Journal of Turbomachinery* 125 (2003): 547-554.

Gritsch, M., W. Colban, H. Schar, and K. Dobbeling. "The Effect of Hole Geometry on the Thermal Performance of Fan-Shaped Film Cooling Holes." *ASME Journal of Turbomachinery* 127 (2005): 718-725.

Guo, X., W. Schroder, and M. Meinke. "Large Eddy Simulations of Film Cooling Flows." *Computers & Fluids* 35 (2006): 587-606.

Harvey, A. D. "Generalized Turbulent Reacting Flow Code: Equations and Numerics." External release. *The Dow Chemical Company.* 2003.

Haven, B. A. and M. Kurosaka. "Kidney and Anti-kidney Vortices in Crossflow Jets." *Journal of Fluid Mechanics* 352 (1997): 27-64.

Heidmann, J. D. and S. Ekkad. "A Novel Antivortex Film-Cooling Hole Concept." *ASME Journal of Turbomachinery* 130 (2008): 31020.

Hyams, D. G. and J. H. Leylek. "A Detailed Analysis of Film Cooling Physics: Part III - Streamwise Inlection with Shaped Holes." *ASME Journal of Turbomachinery* 122 (2000): 122-132.

Iourokina, I.V. and S. K. Lele. "Towards Large Eddy Simulation of Film-Cooling Flows on a Model Turbine Blade Leading Edge." In *Proceedings of AIAA 43rd Aerospace Sciences Meeting and Exhibit.* Reno, Nevada. January 10-13, 2005.

Iourokina, I. V. and S. K. Lele. "Large Eddy Simulation of Film Cooling Flow Above a Flat Plate from Inclined Cylindrical Holes." In *Proceedings of ASME Joint U.S.-European Fluids Engineering Summer Meeting.* Miami, Florida. July 17-20, 2006a.

Iourokina, I. V. and S. K. Lele. "Large Eddy Simulation of Film-Cooling Above the Flat Surface with a Large Plenum and Short Exit Holes." In *Proceedings of AIAA 44th Aerospace Sciences Meeting and Exhibit.* Reno, Nevada. January 9-12, 2006b.

Jathar, K. N. and D. H. Leedom. In-house code. Louisiana State University, Baton Rouge, Louisiana. July 2007.

Jones, R., S. Acharya, and A. Harvey. "Improved Turbulence Modeling of Film Cooling Flow and Heat Transfer." In *Modeling and Simulation of Turbulent Heat Transfer*, by B. Sunden and M. Faghri, 113-144. Boston, Massachusetts: WIT Press, 2005.

Jumper, G. W., W. C. Elrod, and R. B. Rivir. "Film Cooling Effectiveness in High-Turbulence Flow." *ASME Journal of Turbomachinery* 113 (1991): 479-483.

Leedom, D. H., and S. Acharya. "Large Eddy Simuations of Film Cooling Flow Fields from Cylindrical and Shaped Holes." In *Proceedings of ASME Turbo Expo 2008*. Berlin, Germany. June 9-13, 2008.

Lund, T. S., X. Wu, and K. D. Squires. "Generation of Turbulent Inflow Data for Spatially-Developing Boundary Layer Simulations." *Journal of Computational Physics* 140 (1998): 233–258.

Lutum, E. and B. V. Johnson. "Influence of the Hole Length to Diameter Ratio on Film Cooling with Cylindrical Holes." *ASME Journal of Turbomachinery* 121 (1999): 209-216.

McGovern, K. T. and J. H. Leylek. "A Detailed Analysis of Film Cooling Physics: Part II - Compound-Angle Injection with Cylindrical Holes." *ASME Journal of Turbomachinery* 122 (2000): 113-121.

Morton, B. R. and A. Ibbetson. "Jets Deflected in a Crossflow." *Experimental Thermal and Fluid Science* 12 (1996): 112-133.

Muppidi, S. and K. Mahesh. "Study of Trajectories of Jets in Crossflow Using Direct Numerical Simulations." *Journal of Fluid Mechanics* 530 (2005): 81-100.

Muppidi, S. and K. Mahesh. "Direct Numerical Simulation of Round Turbulent Jets in Crossflow." *Journal of Fluid Mechanics* 574 (2007): 59-84.

Muppidi, S. and K. Mahesh. "Direct Numerical Sunulation of Passive Scalar Transport in Transverse Jets." *Journal of Fluid Mechanics* 598 (2008): 335-360.

Nasir, H., S. Acharya, and S. Ekkad. "Improved Film Cooling From Cylindrical Angled Holes with Triangular Tabs: Effect of Tab Orientations." *International Journal of Heat and Fluid Flow* 23 (2003): 657–668.

Okita, Y. and M. Nishiura. "Film Effectiveness Performance of an Arrowhead-Shaped Film-Cooling Hole Geometry." *Journal of Turbomachinery* 129 (2007): 331-339.

Peet, Y. V. and S. K. Lele. "Near Field of Film Cooling Jet Issued into a Flat Plate Boundary Layer: LES Study." In *Proceedings of ASME Turbo Expo 2008*. Berlin, Germany. June 9-13, 2008.

Peterson, S. D. and M. W. Plesniak. "Evolution of Jets Emanating from Short Holes into Crossflow." *Journal of Fluid Mechanics* 503 (2004): 57-91.

Pietrzyk, J. R., D. G. Bogard, and M. E. Crawford. "Hydrodynamic Measurements of Jets in Crossflow for Gas Turbine Film Cooling Applications." *ASME Journal of Turbomachinery* 111 (1989): 139-145.

Pietrzyk, J. R., D. G. Bogard, and M. E. Crawford. "Effects of Density Ratio on the Hydrodynamics of Film Cooling." *ASME Journal of Turbomachinery* 112 (1990): 437-443.

Renze, P., W. Schroder, and M. Meinke. "Hole Shape Comparison for Film Cooling Flows Using Large-Eddy Simulations." In *Proceedings of AIAA 45th Aerospace Sciences Meeting and Exhibit.* Reno, Nevada. January 8-11, 2007.

Renze, P., W. Schroder, and M. Meinke. "Large-Eddy Simulation of Film Cooling Flows at Density Gradients." *International Journal of Heat and Fluid Flow* 29 (2008a): 18-34.

Renze, P., W. Schröder, and M. Meinke. "Large-eddy Simulation of Film Cooling Flows with Variable Density Jets." *Flow Turbulence and Combustion* 80 (2008b): 119–132.

Sargison, J. E., S. M. Guo, M. L. G. Oldfield, G. D. Lock, and A. J. Rawlinson. "A Converging Slot-Hole Film-Cooling Geometry—Part 1: Low-Speed Flat-Plate Heat Transfer and Loss." *ASME Journal of Turbomachinery* 124 (2002a): 453-460.

Sargison, J. E., S. M. Guo, M. L. G. Oldfield, G. D. Lock, and A. J. Rawlinson. "A Converging Slot-Hole Film-Cooling Geometry—Part 2: Transonic Nozzle Guide Vane Heat Transfer and Loss." *Journal of Turbomachinery* 124 (2002b): 461-471.

Sargison, J. E., S. M. Guo, M. L. G. Oldfield, G. D. Lock, and A. J. Rawlinson. "Flow Visualisation of the External Flow From a Converging Slot-Hole." *Experiments in Fluids* 38 (2005): 304–318.

Saumweber, S., A. Schultz, and S. Wittig. "Free-Stream Turbulence Effects on Film Cooling with Shaped Holes." *ASME Journal of Turbomachinery* 125 (2003): 65-73.

Saumweber, C. and A. Schulz. "Interaction of Film Cooling Rows: Effects of Hole Geometry and Row Spacing on the Cooling Performance Downstream of the Second Row of Holes." *ASME Journal of Turbomachinery* 126 (2004): 237-246.

Saumweber, C. and A. Schulz. "Comparison of the Cooling Performance of Cylindrical and Fan-Shaped Cooling Holes with Special Emphasis on the Effect of Internal Coolant Fross-Flow." In *Proceedings of ASME Turbo Expo 2008*. Berlin, Germany. June 9-13, 2008a.

Saumweber, C. and A. Schulz. "Effect of Geometry Variation on the Cooling Perfromance of Fan-Shaped Cooling Holes." In *Proceedings of ASME Turbo Expo 2008*. Berlin, Germany. June 9-13, 2008b.

Saumweber, C. and A. Shulz. "Free-Stream Effects on the Cooling Performance of Cylindrical and Fan Shaped Cooling Holes." In *Proceedings of ASME Turbo Expo 2008*. Berlin, Germany. June 9-13, 2008c.

Schmidt, D., B. Sen, and D. Bogard. "Film Cooling with Compound Angle Holes: Adiabatic Effectiveness." *ASME Journal of Turbomachinery* 118 (1996): 800-806.

Sen, B., D. L. Schmidt, and D. G. Bogard. "Film Cooling with Compund Angle Holes: Heat Transfer." *ASME Journal of Turbomachinery* 118 (1996): 800-806.

Sinha, A. K., D. G. Bogard, and M. E. Crawford. "Film Cooling Effectiveness Downstream of a Single Row of Holes with Variable Density Ratio." *Transactions of the ASME* 113 (1991): 442-449.

Smagorinsky, J. "General Circulation Experiments on the Primitive Equations." *Monthly Weather Review* 91 (1963): 99-164.

Thole, K., M. Gritsch, A. Schulz, and S. Wittig. "Flowfield Measurements for Film-Cooling Holes With Expanded Exits." *ASME Journal of Turbomachinery* 120 (1998): 327-336.

Tyagi, M. and S. Acharya. "Large Eddy Simulation of Film Cooling Flow From an Inclined Cylindrical Jet." *Transactions of the ASME* 125 (2003): 734-742.

Walters, D. K. and J. H. Leylek. "A Systematic Computational Methodology Applied to a Three-Dimensional Film-Cooling Flowfield." *ASME Journal of Turbomachinery* 119 (1997): 777-785.

Walters, D. K. and J. H. Leylek. "A Detailed Analysis of Film-Cooling Physics: Part I - Streamwise Injection With Cylindrical Holes." *ASME Journal of Turbomachinery* 122 (2000a): 102-112.

Walters, D. K. and J. H. Leylek. "Impact of Film-Cooling Jets on Turbine Aerodynamic Losses." *ASME Journal of Turbomachinery* 122 (2000b): 537-545.

Waye, S. K. and D. G. Bogard. "High-Resolution Film Cooling Effectiveness Measurements of Axial Holes Embedded in a Transverse Trench With Various Trench Configurations." *Transactions of the ASME* 129 (2007): 294-302.

Appendix A: Letter Granting Permission to Reprint

Beth Darchi <DarchiB@asme.org> **Mon, Oct 13, 2008 at 2:00 PM**
To: David Leedom <dleedo1@gmail.com>

Dear Mr. Leedom:
It is our pleasure to grant you permission to use ASME paper "Large Eddy Simuations of Film Cooling Flow Fields from Cylindrical and Shaped Holes, " by Leedom, D.H. and Acharya, S., ASME Turbo Expo, 2008, paper number GT2008-51009, cited in your letter for inclusion in your master thesis entitled Numerical Investigation of Film Cooling Fluid Flow and Heat Transfer Using Large Eddy Simulations to be published by Louisiana State University.

As is customary, we ask that you ensure full acknowledgment of this material, the author(s), source and ASME as original publisher on all printed copies being distributed.

Many thanks for your interest in ASME publications.

Sincerely,
Beth Darchi
Permissions & Copyrights
ASME, 3 Park Avenue
New York, NY 10016
T: 212-591-7700
F: 212-591-7841
E: darchib@asme.org

Appendix B: Flow Field Validation

These are more plots of validation to experimental data provided by Dr. Bogard. All x locations mentioned are with respect to a datum located at the leading edge of the hole on the surface.

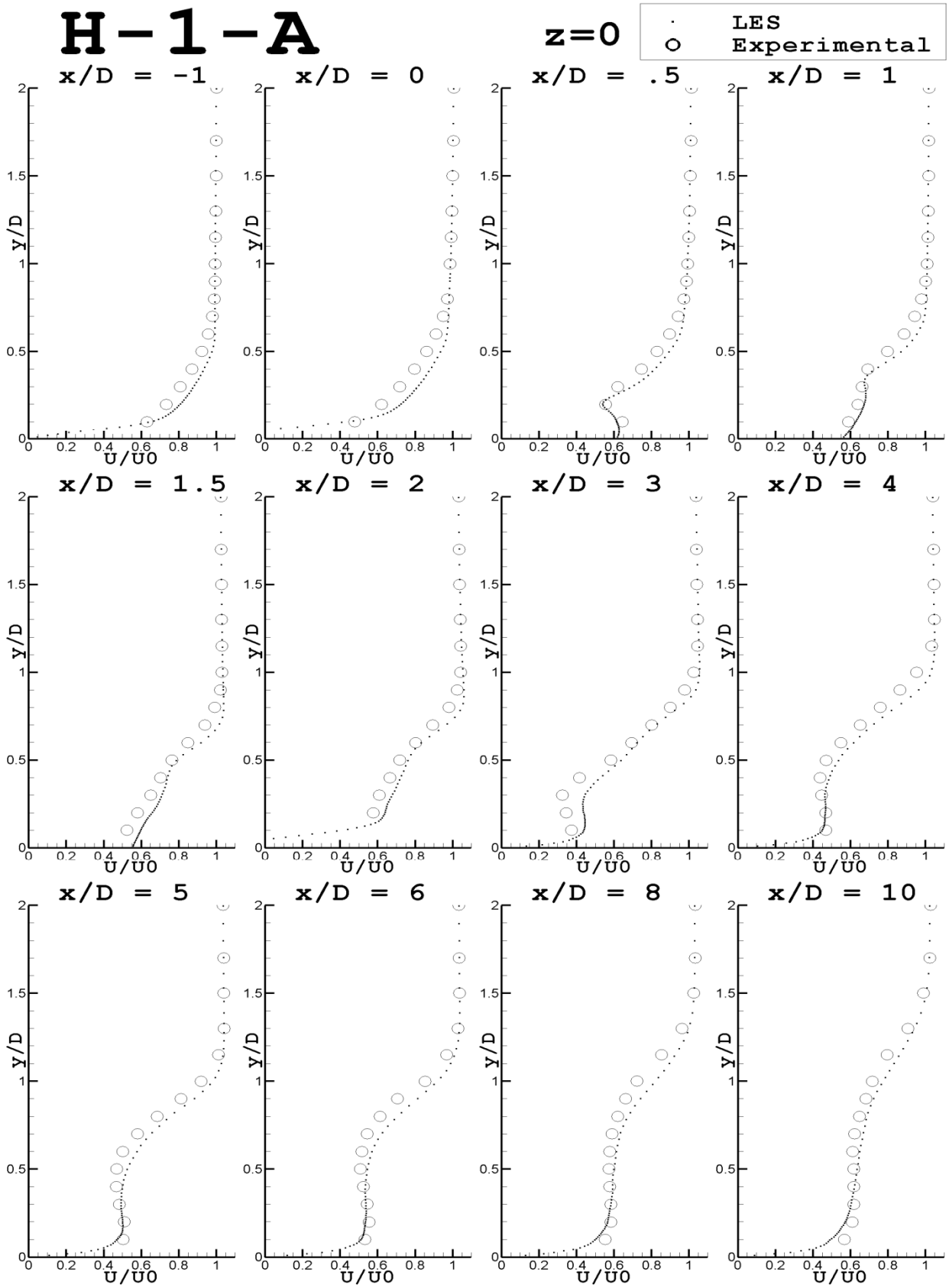

Figure 0.1: Blowing Ratio 1, L/D 3.5, u velocity

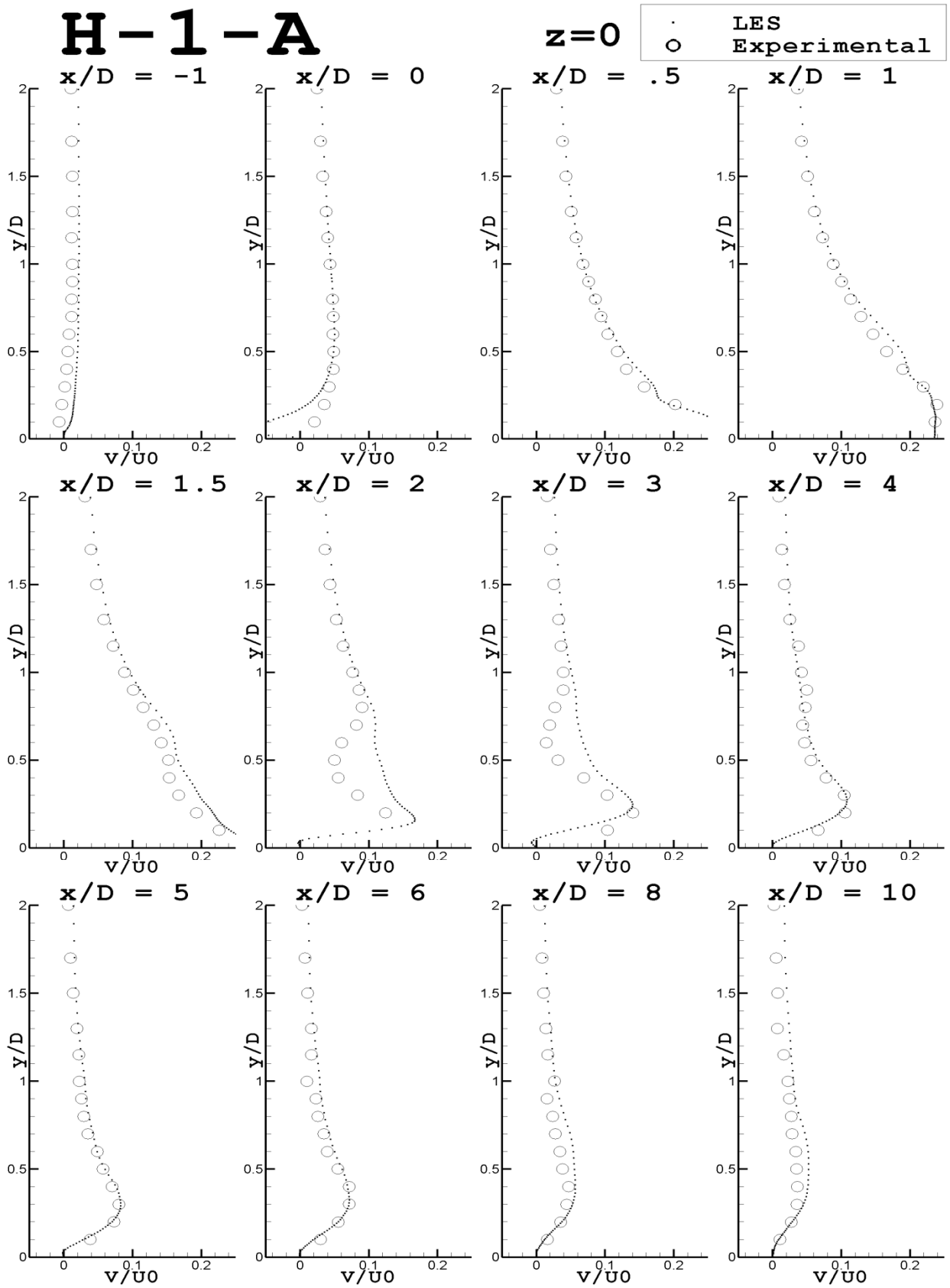

Figure 0.2: Blowing Ratio 1, L/D 3.5, v velocity

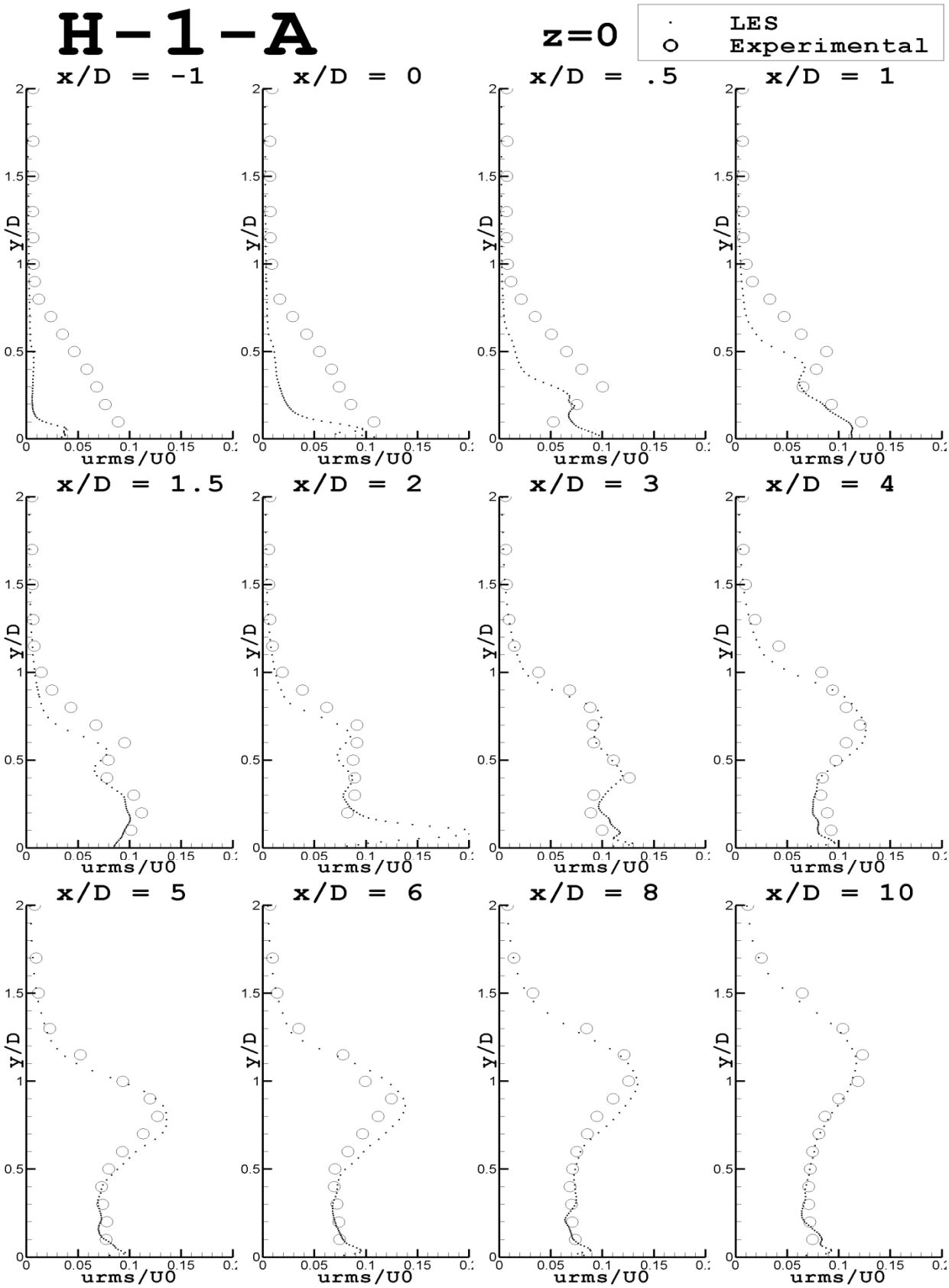

Figure 0.3: Blowing Ratio 1, L/D 3.5, root mean square of u velocity

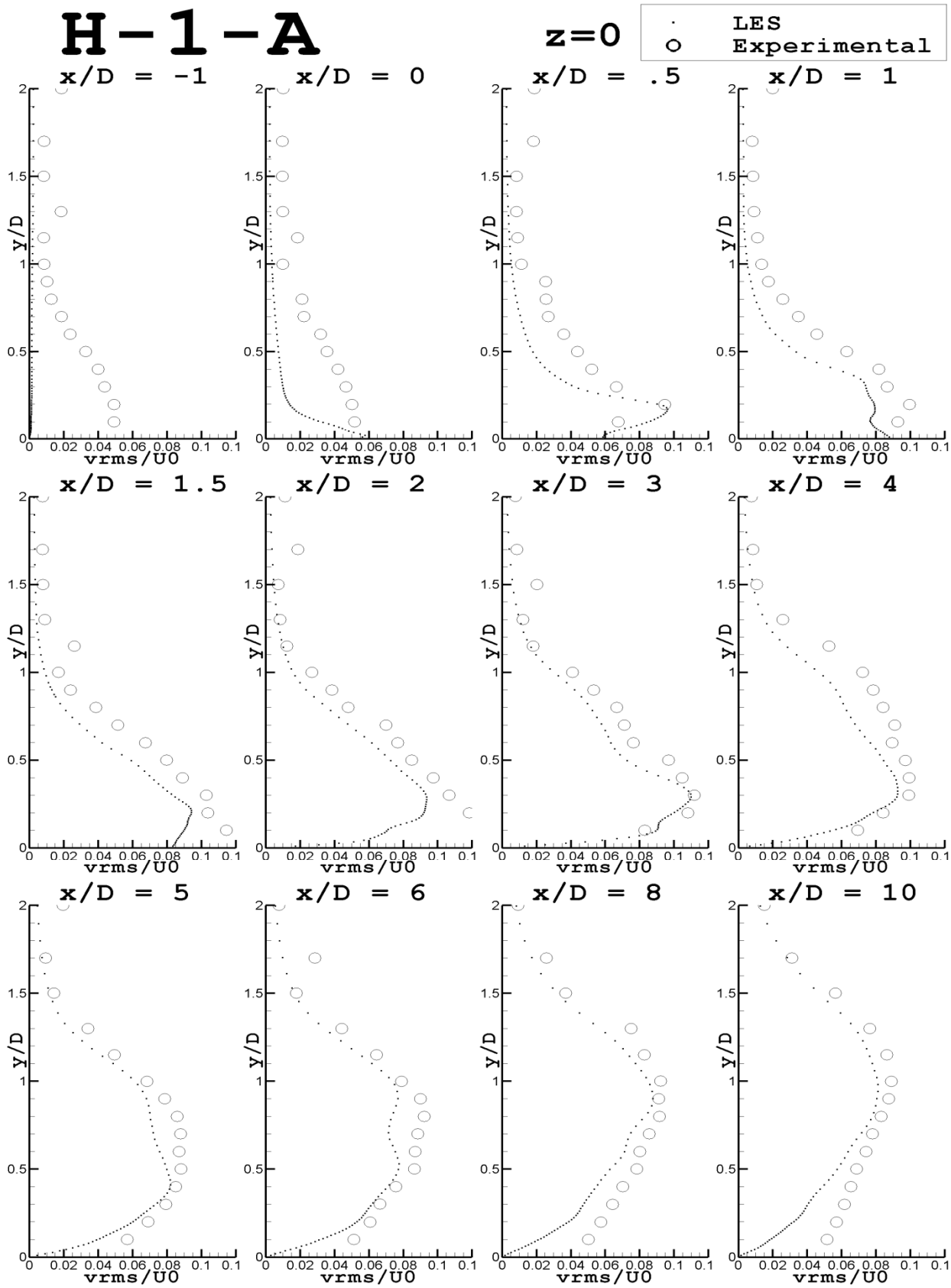

Figure 0.4: Blowing Ratio 1, L/D 3.5, root mean square of v velocity

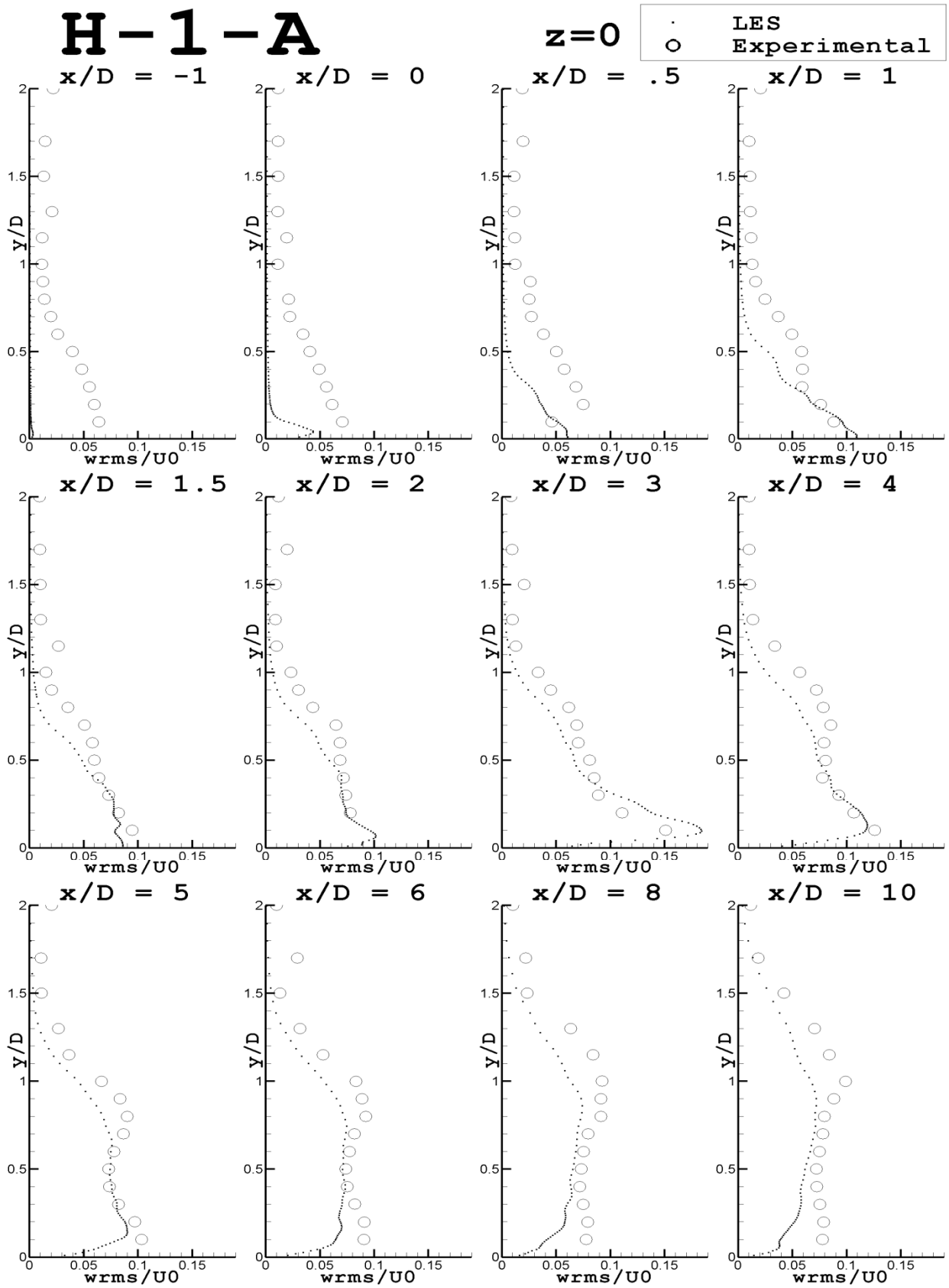

Figure 0.5: Blowing Ratio 1, L/D 3.5, root mean square of w velocity

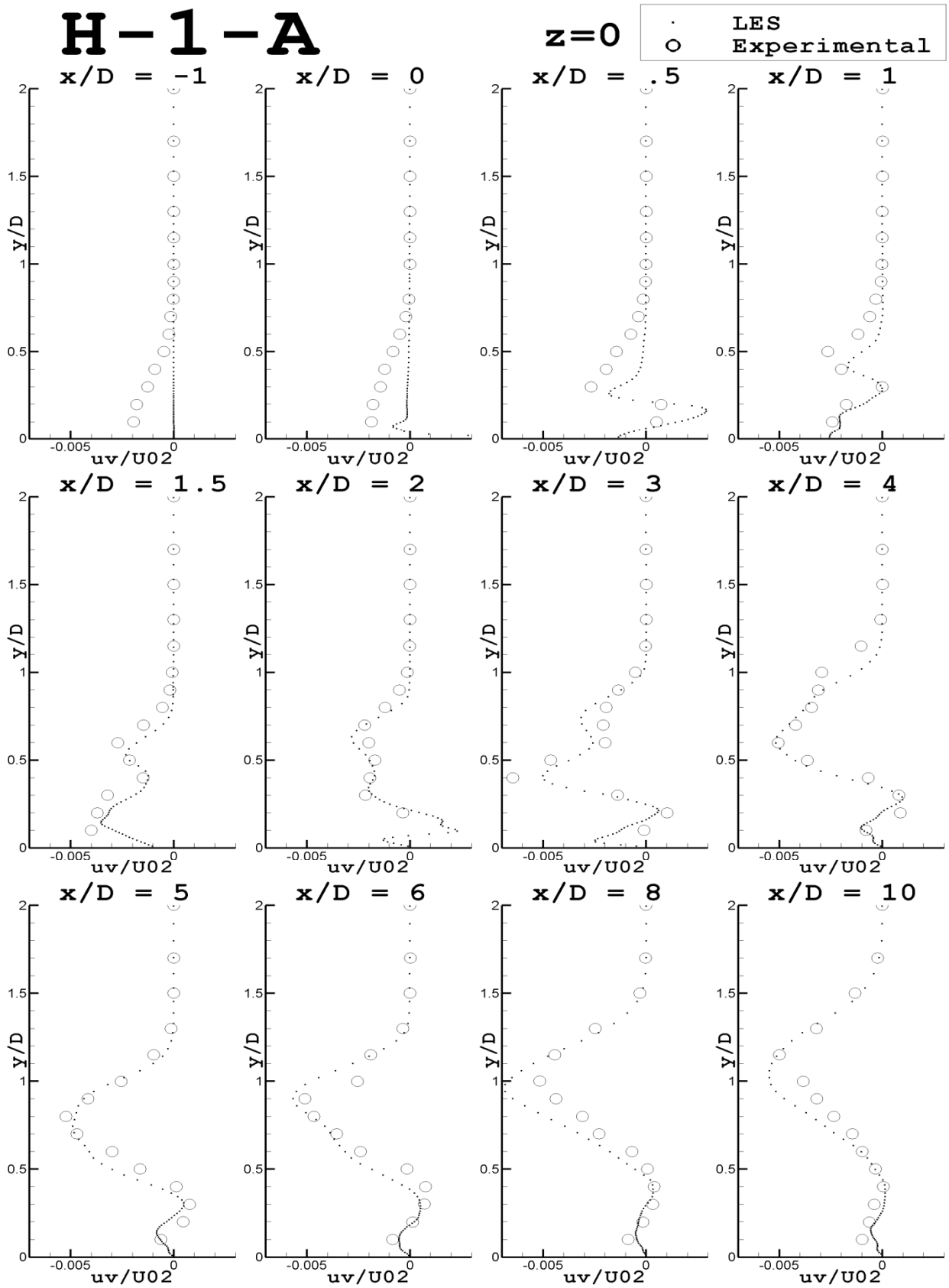

Figure 0.6: Blowing Ratio 1, L/D 3.5, u-v shear stress

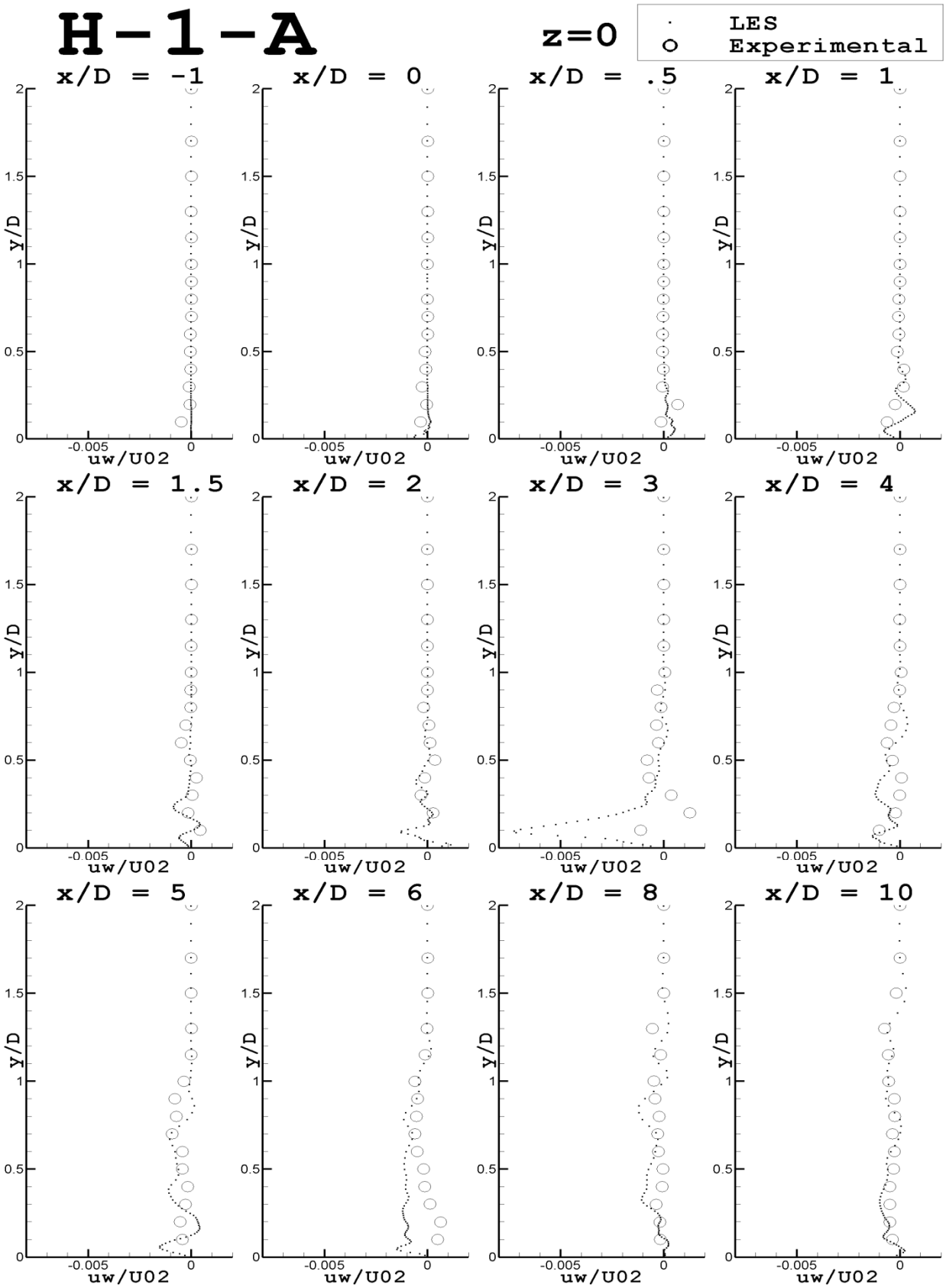

Figure 0.7: Blowing Ratio 1, L/D 3.5, u-w shear stress

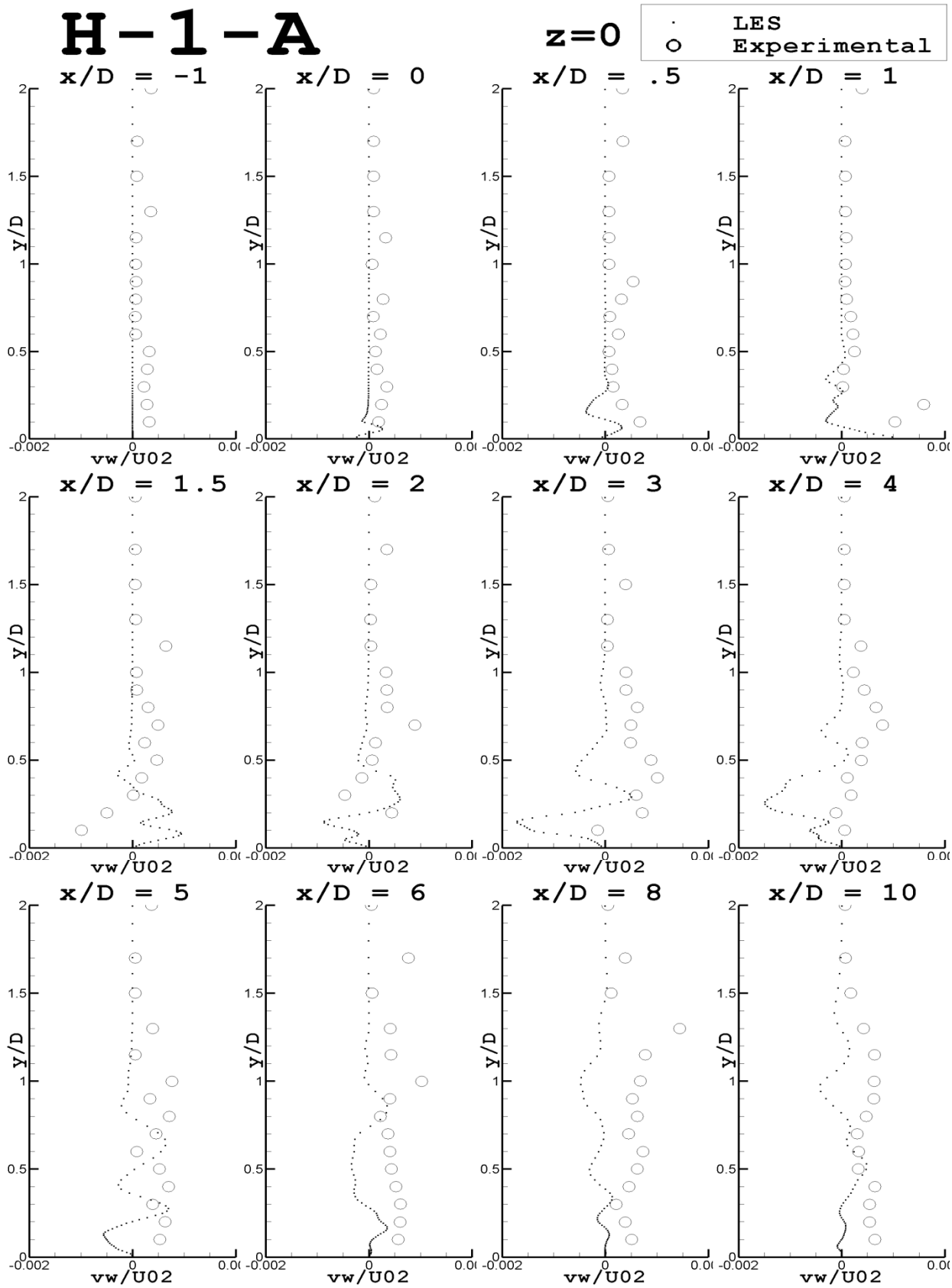

Figure 0.8: Blowing Ratio 1, L/D 3.5, v-w shear stress

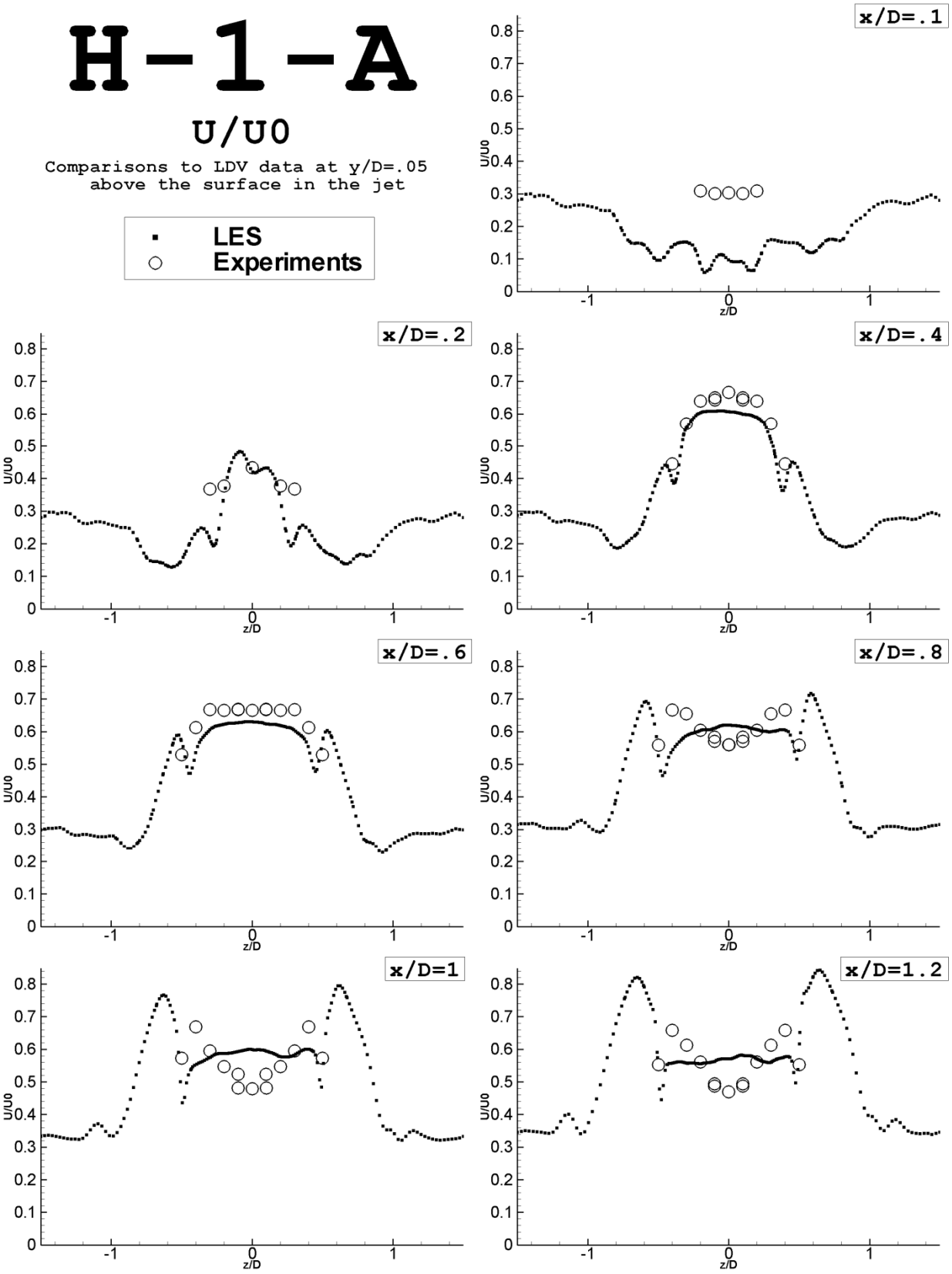

Figure 0.9: Blowing Ratio 1, L/D 3.5, u velocity

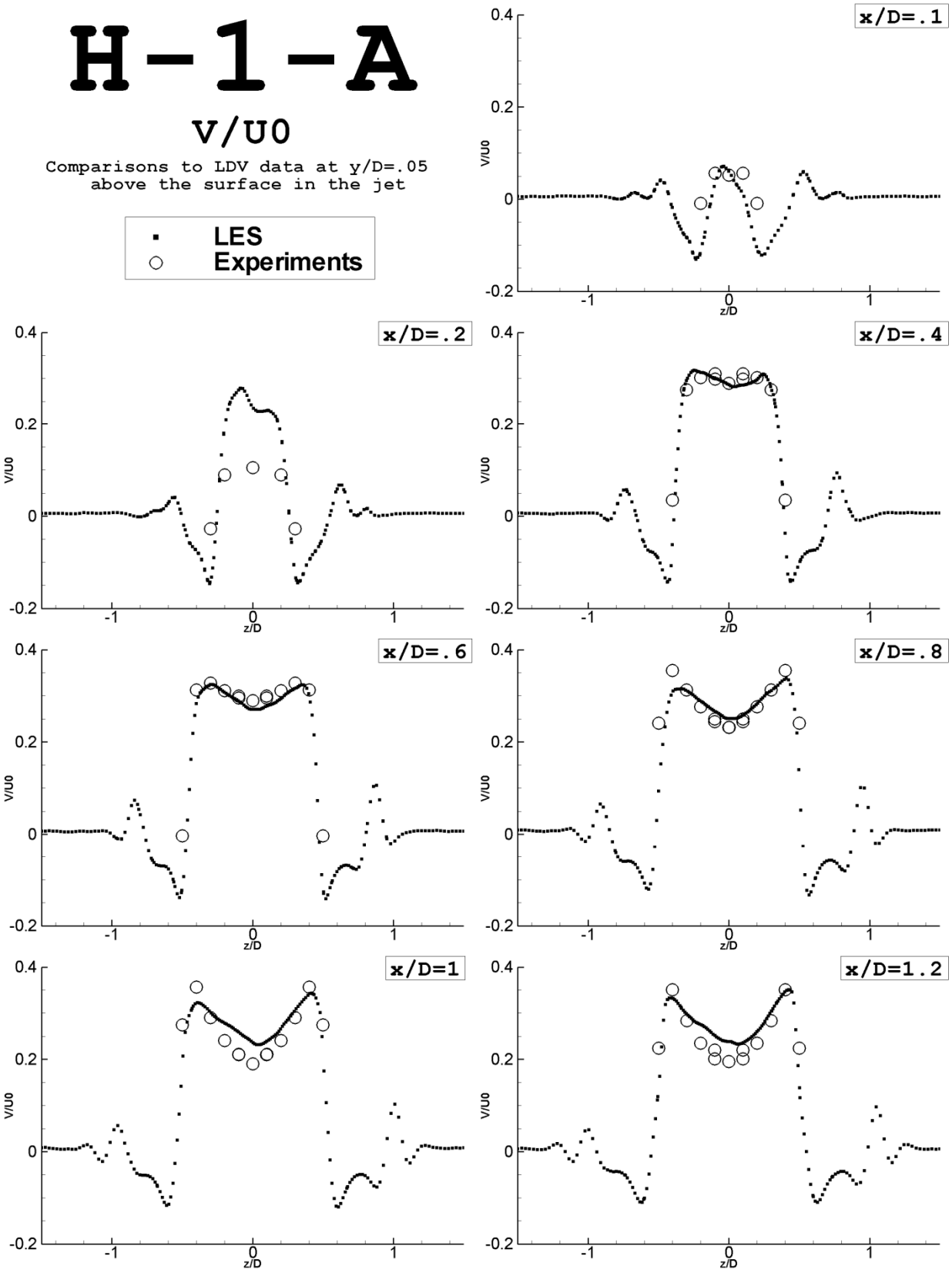

Figure 0.10: Blowing Ratio 1, L/D 3.5, v velocity

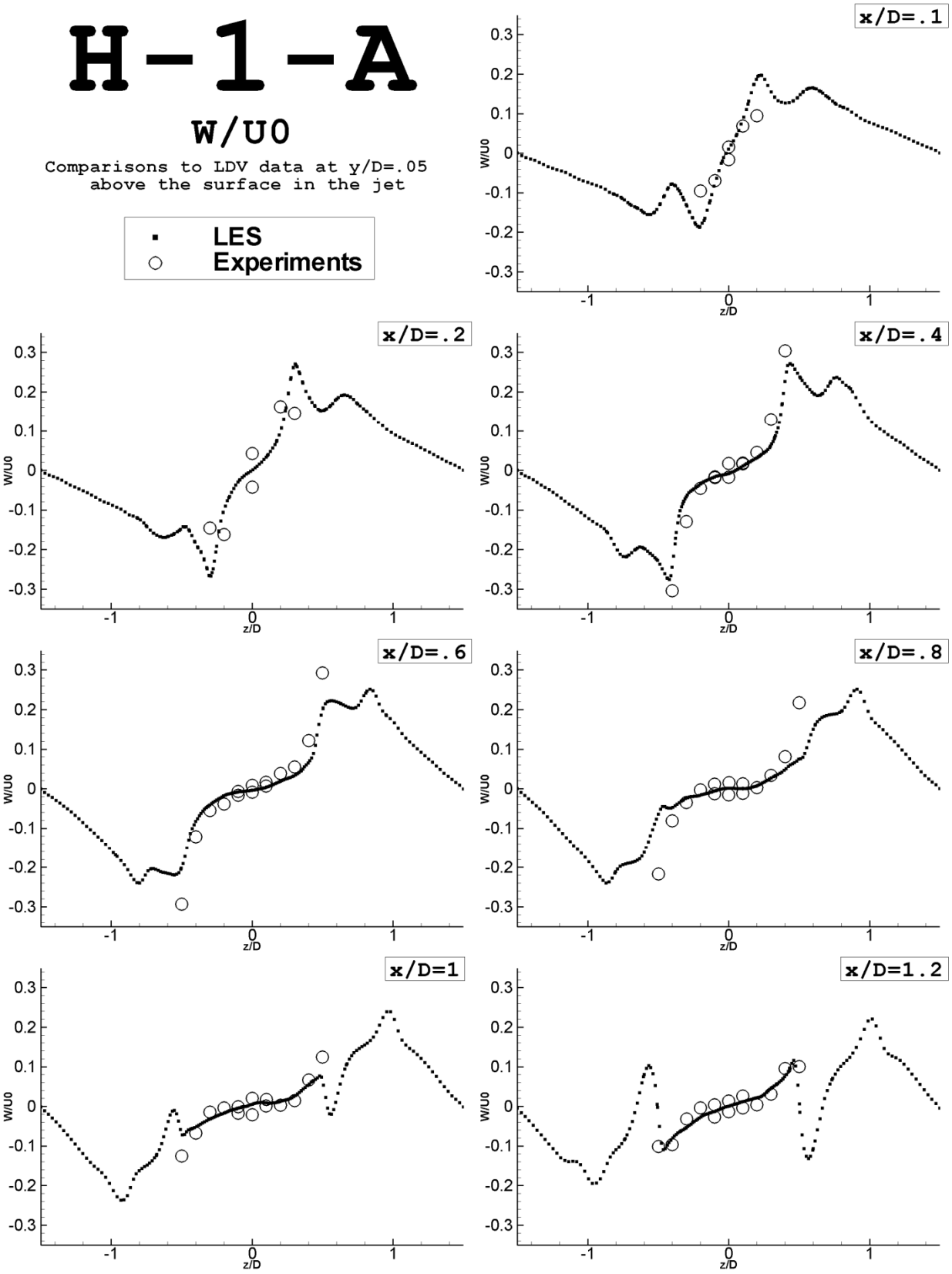

Figure 0.11: Blowing Ratio 1, L/D 3.5, w velocity

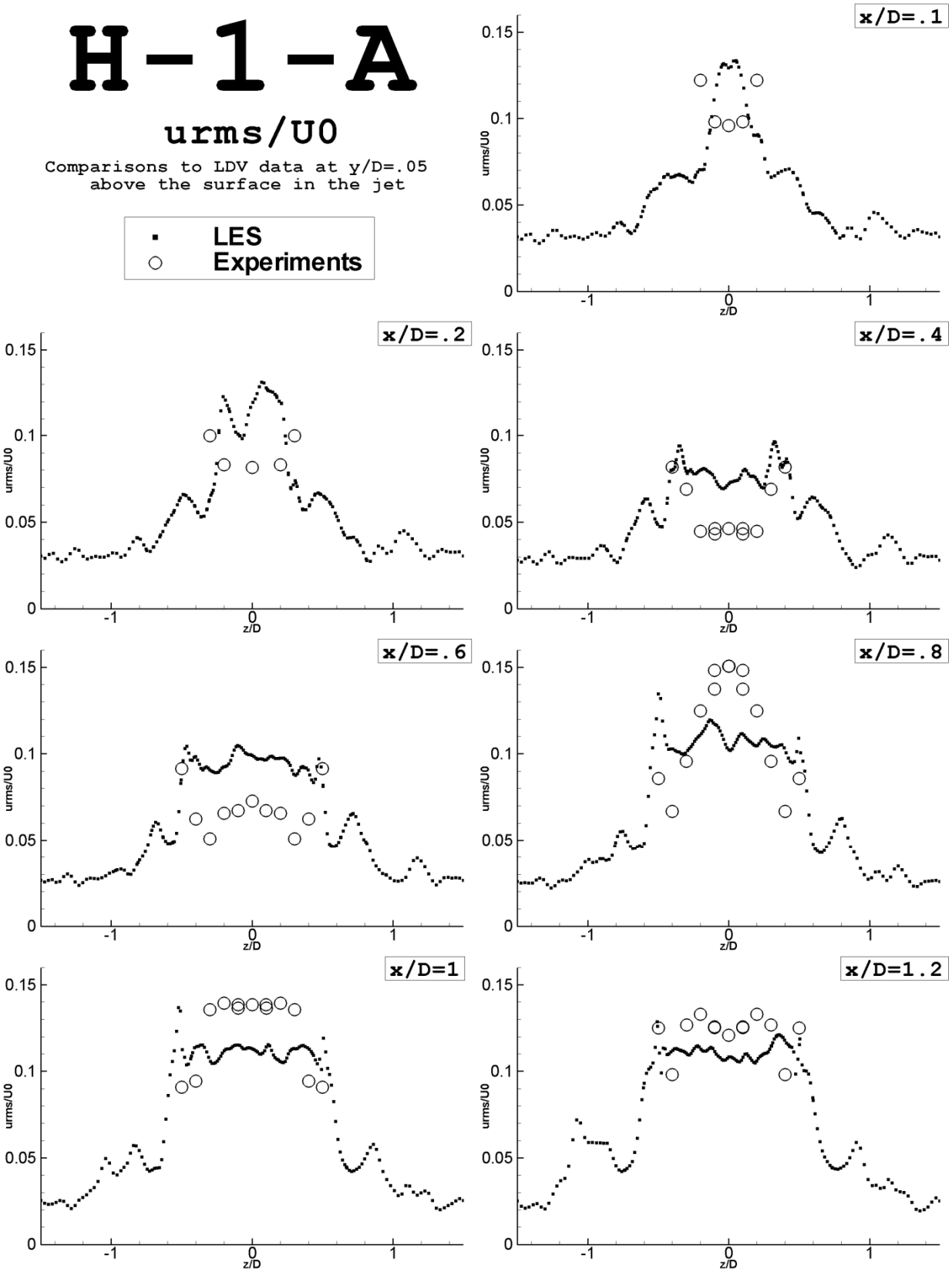

Figure 0.12: Blowing Ratio 1, L/D 3.5, root mean square of u velocity

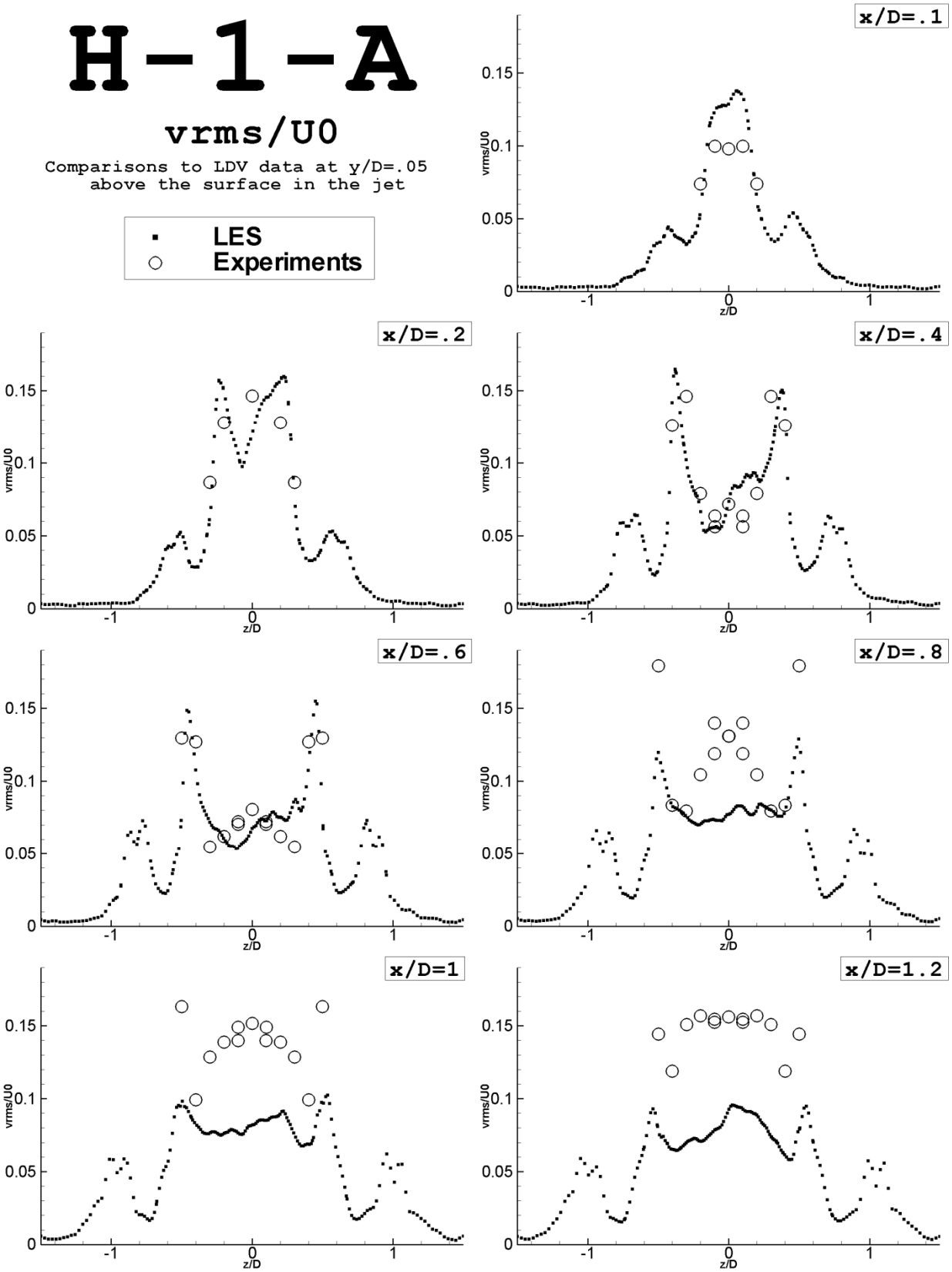

Figure 0.13: Blowing Ratio 1, L/D 3.5, root mean square of v velocity

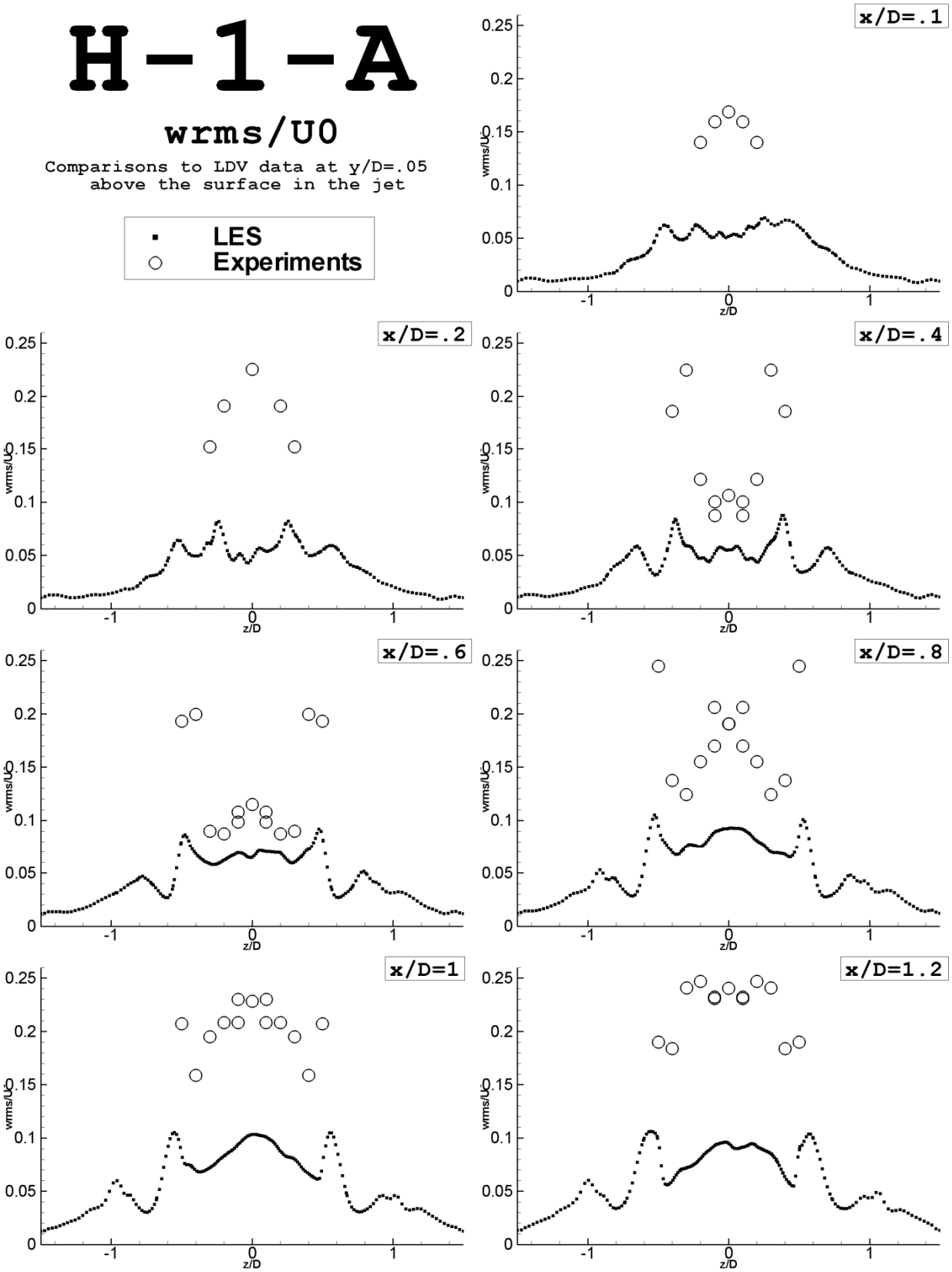

Figure 0.14: Blowing Ratio 1, L/D 3.5, root mean square of w velocity

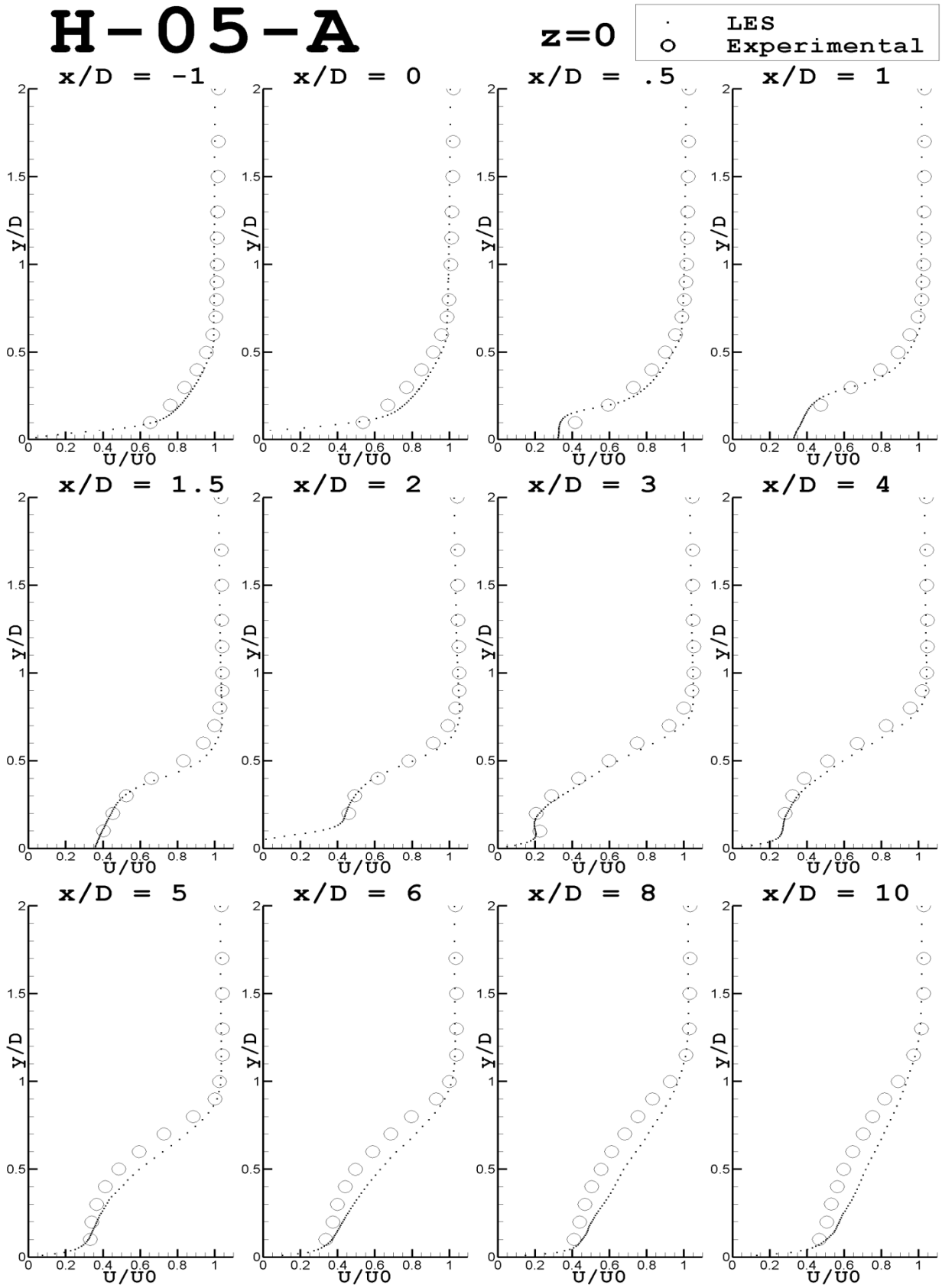

Figure 0.15: Blowing Ratio 0.5, L/D 3.5, u velocity

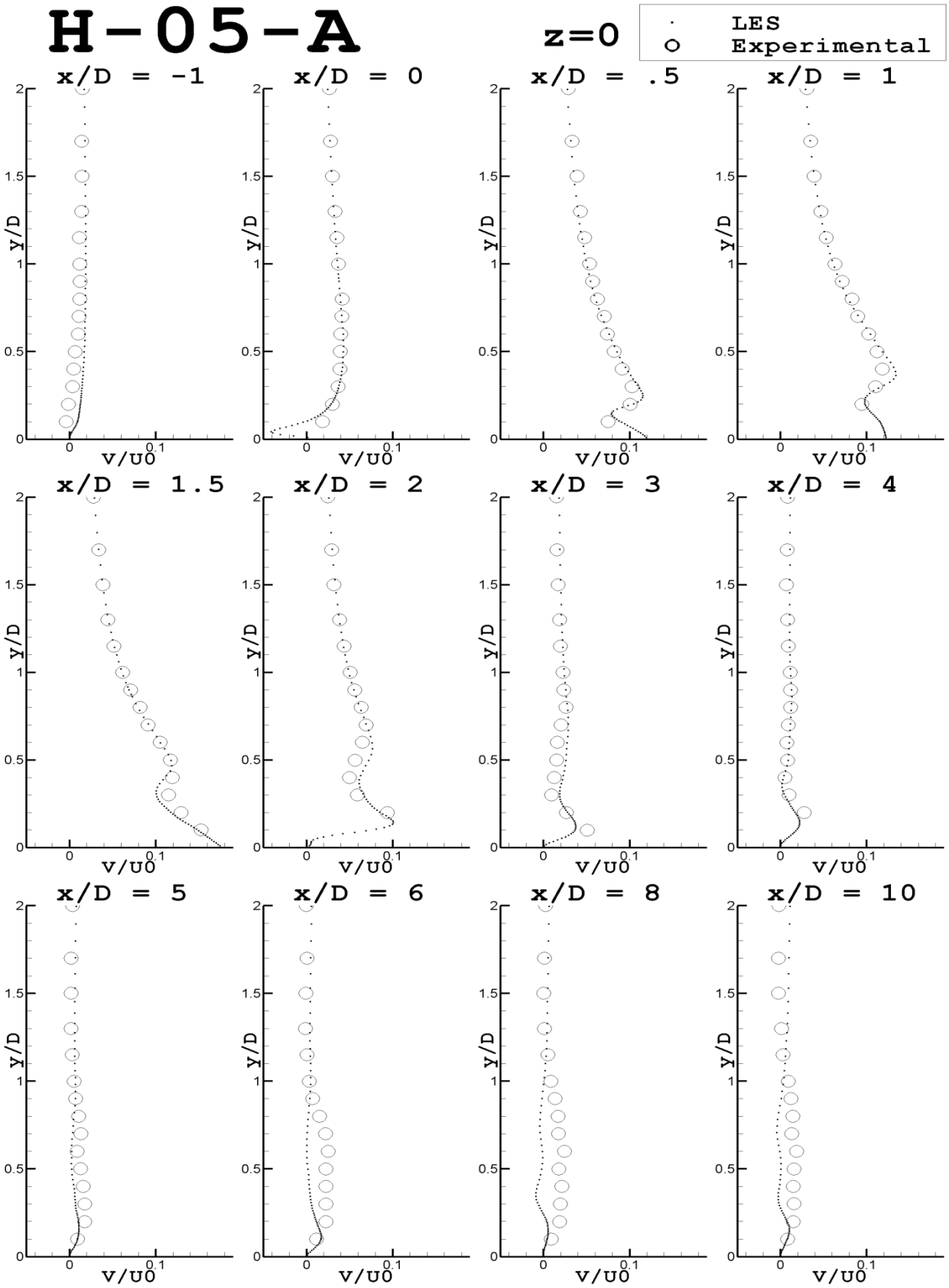

Figure 0.16: Blowing Ratio 0.5, L/D 3.5, v velocity

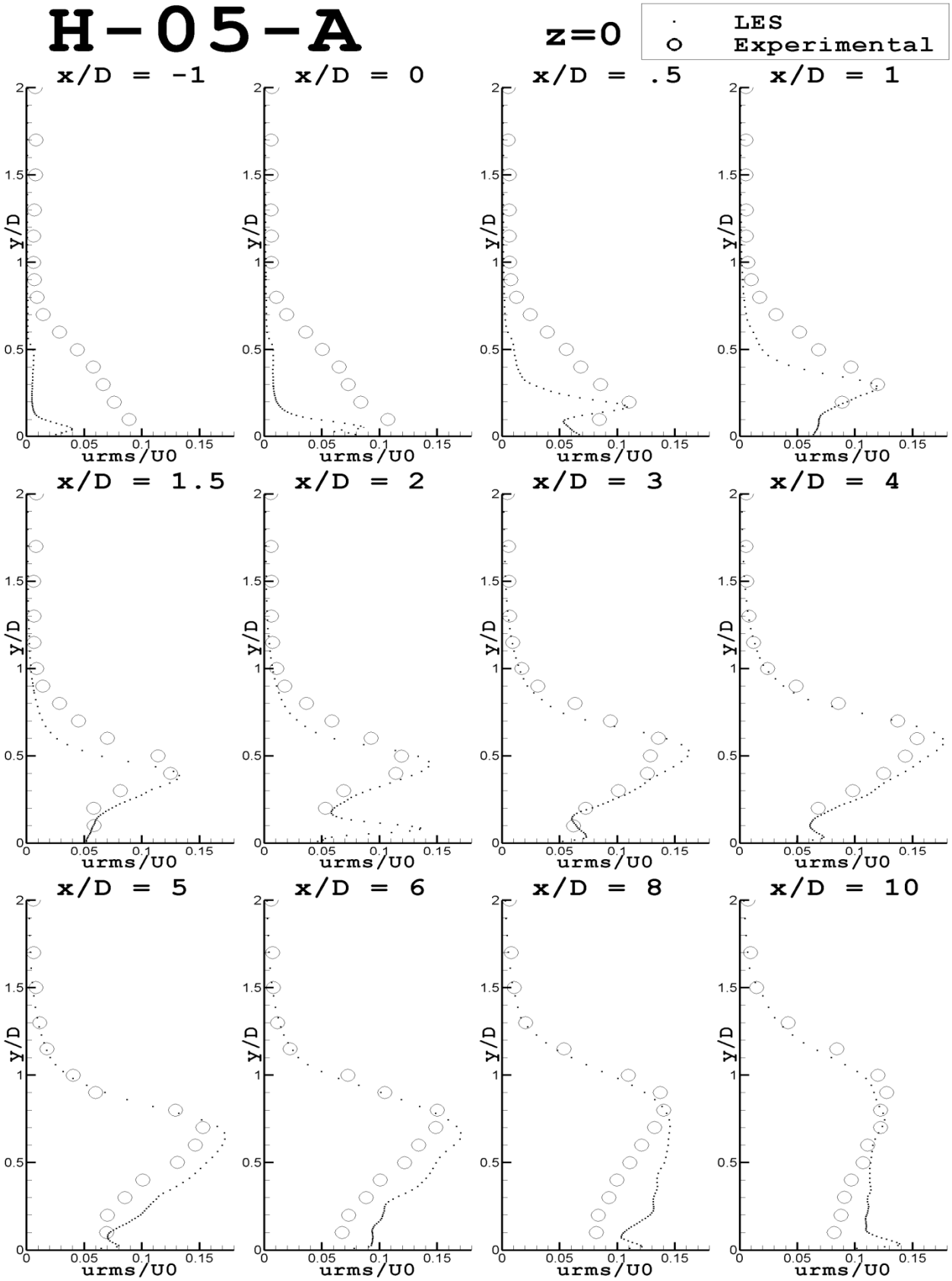

Figure 0.17: Blowing Ratio 0.5, L/D 3.5, root mean square of u velocity

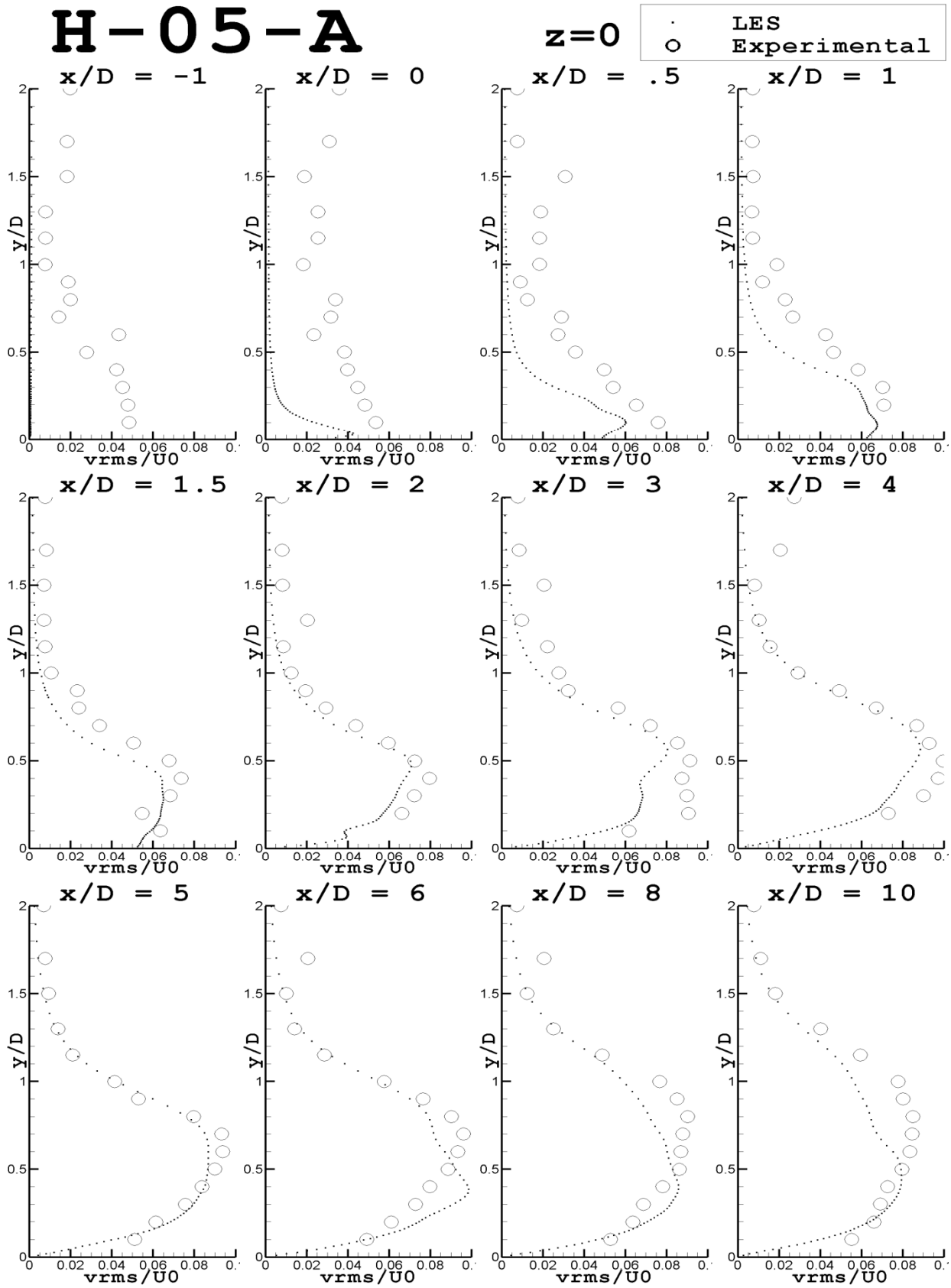

Figure 0.18: Blowing Ratio 0.5, L/D 3.5, root mean square of v velocity

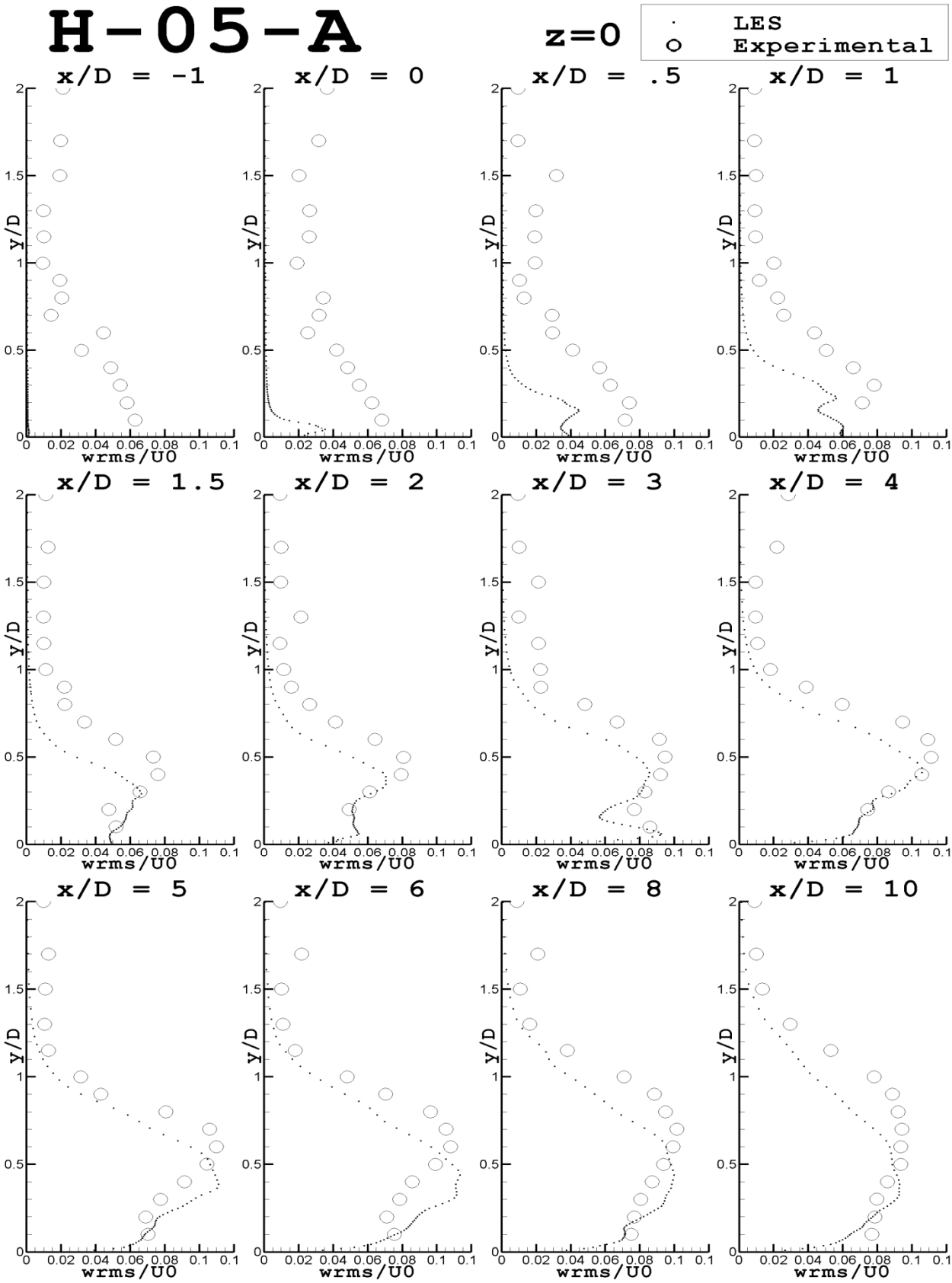

Figure 0.19: Blowing Ratio 0.5, L/D 3.5, root mean square of w velocity

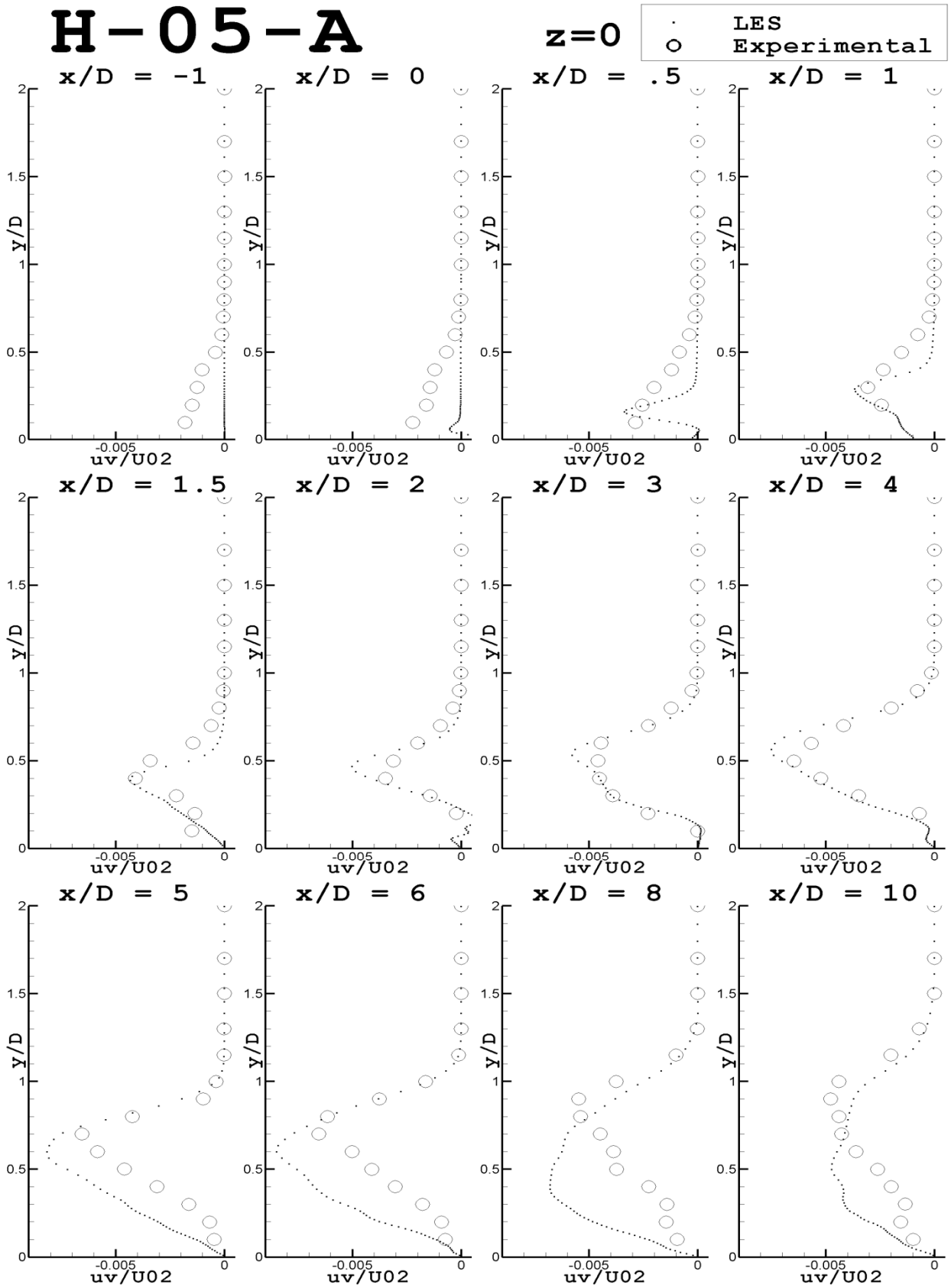

Figure 0.20: Blowing Ratio 0.5, L/D 3.5, u-v shear stress

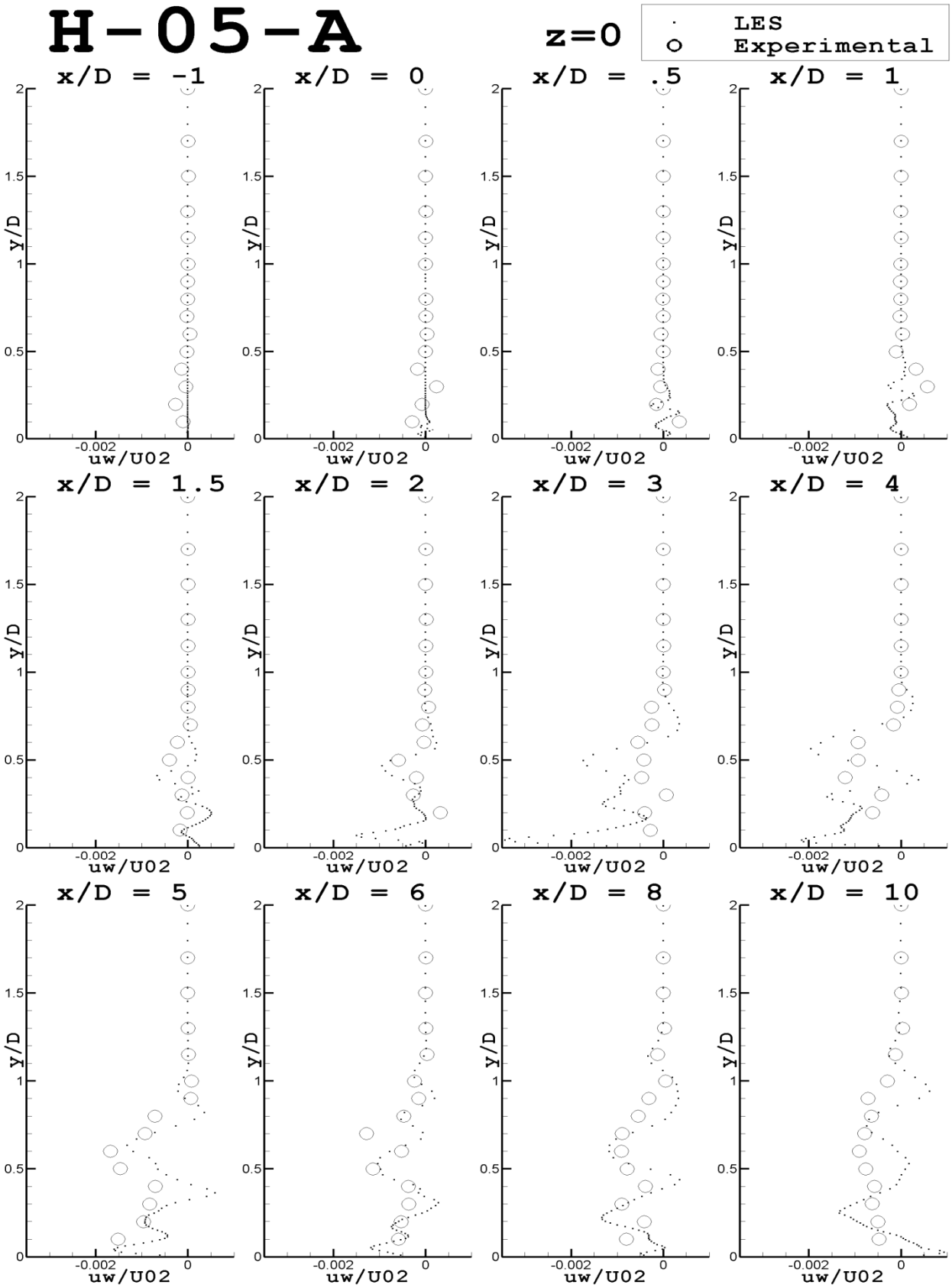

Figure 0.21: Blowing Ratio 0.5, L/D 3.5, u-w shear stress

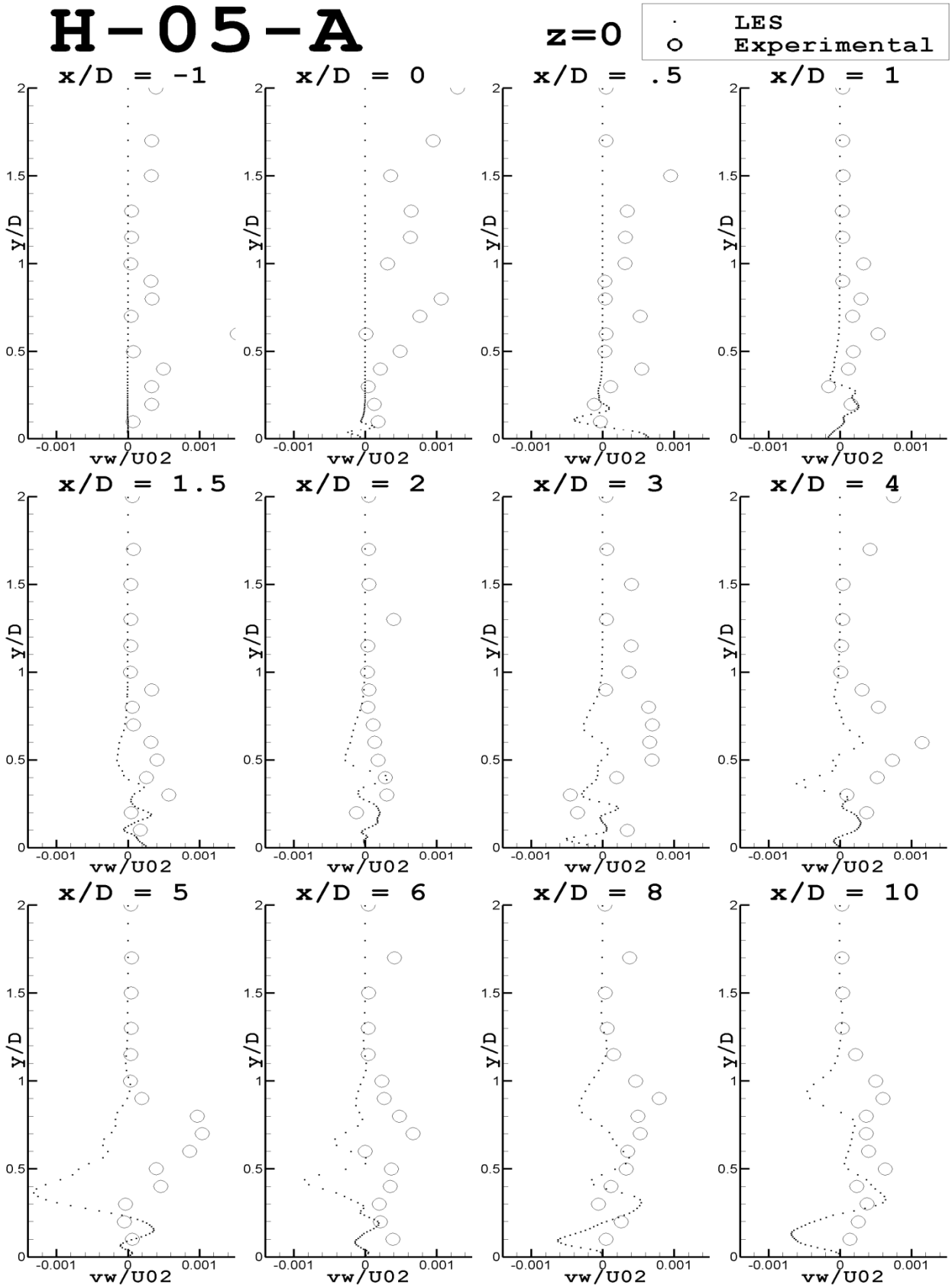

Figure 0.22: Blowing Ratio 0.5, L/D 3.5, v-w shear stress

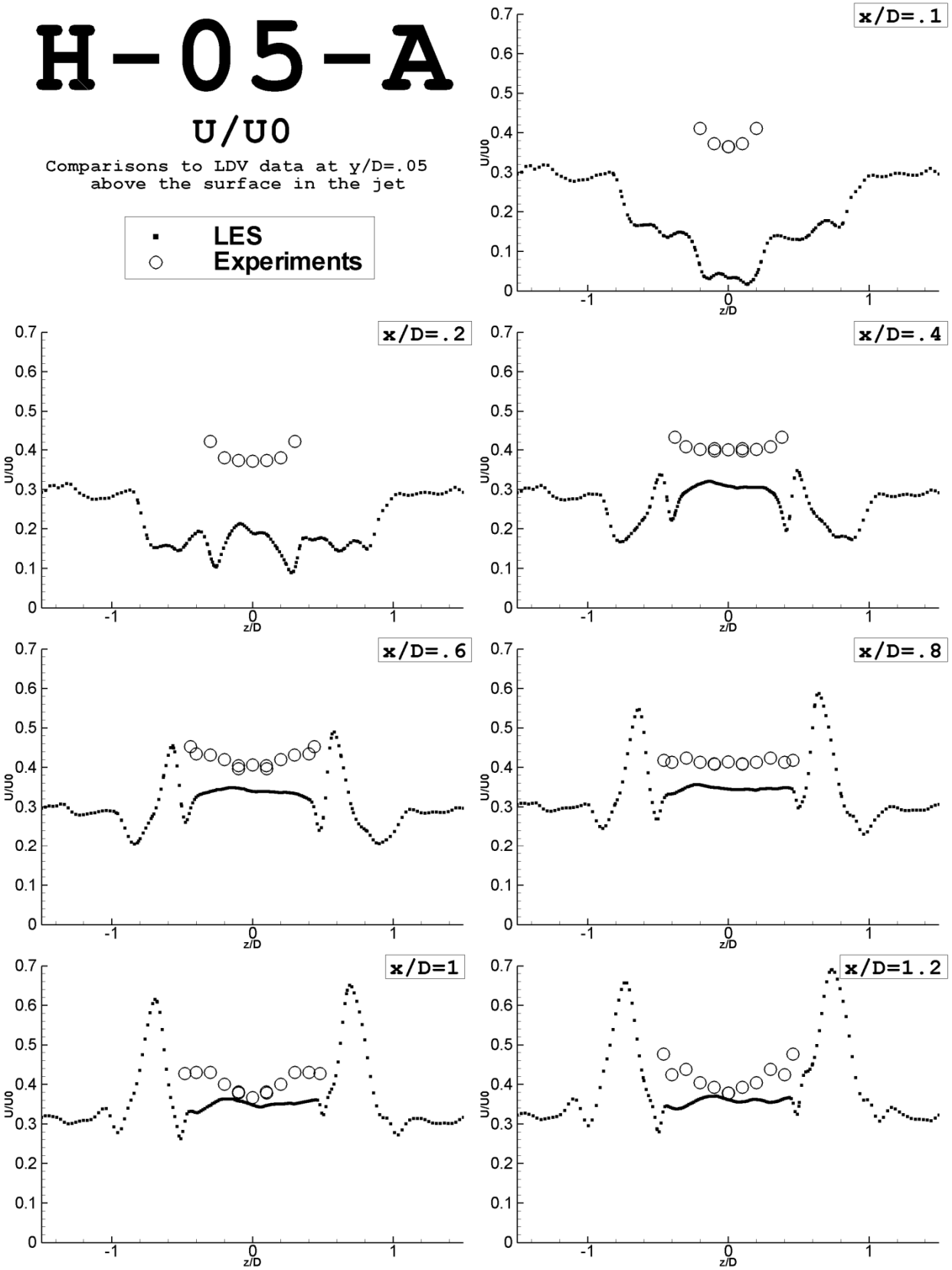

Figure 0.23: Blowing Ratio 0.5, L/D 3.5, u velocity

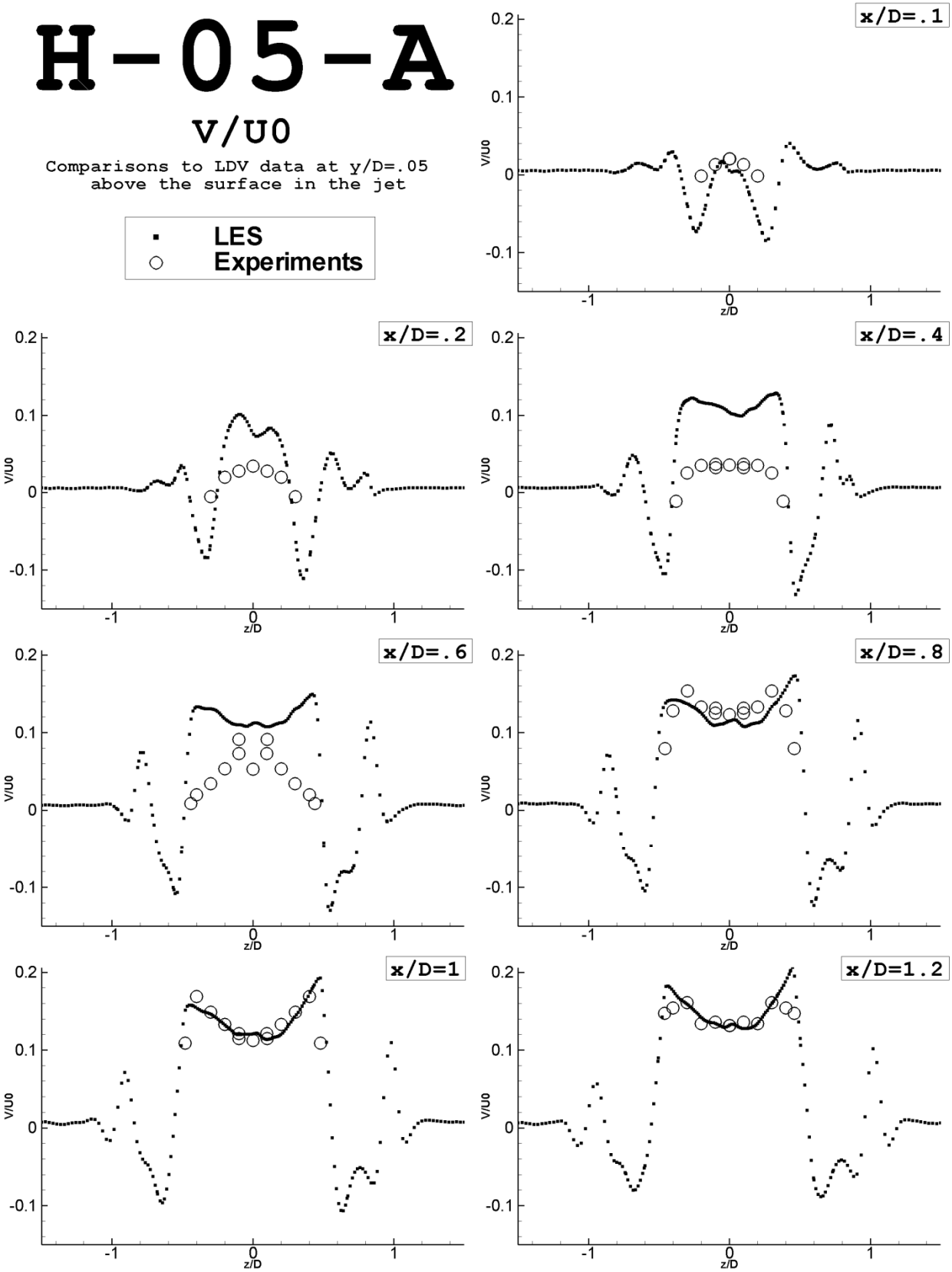

Figure 0.24: Blowing Ratio 0.5, L/D 3.5, v velocity

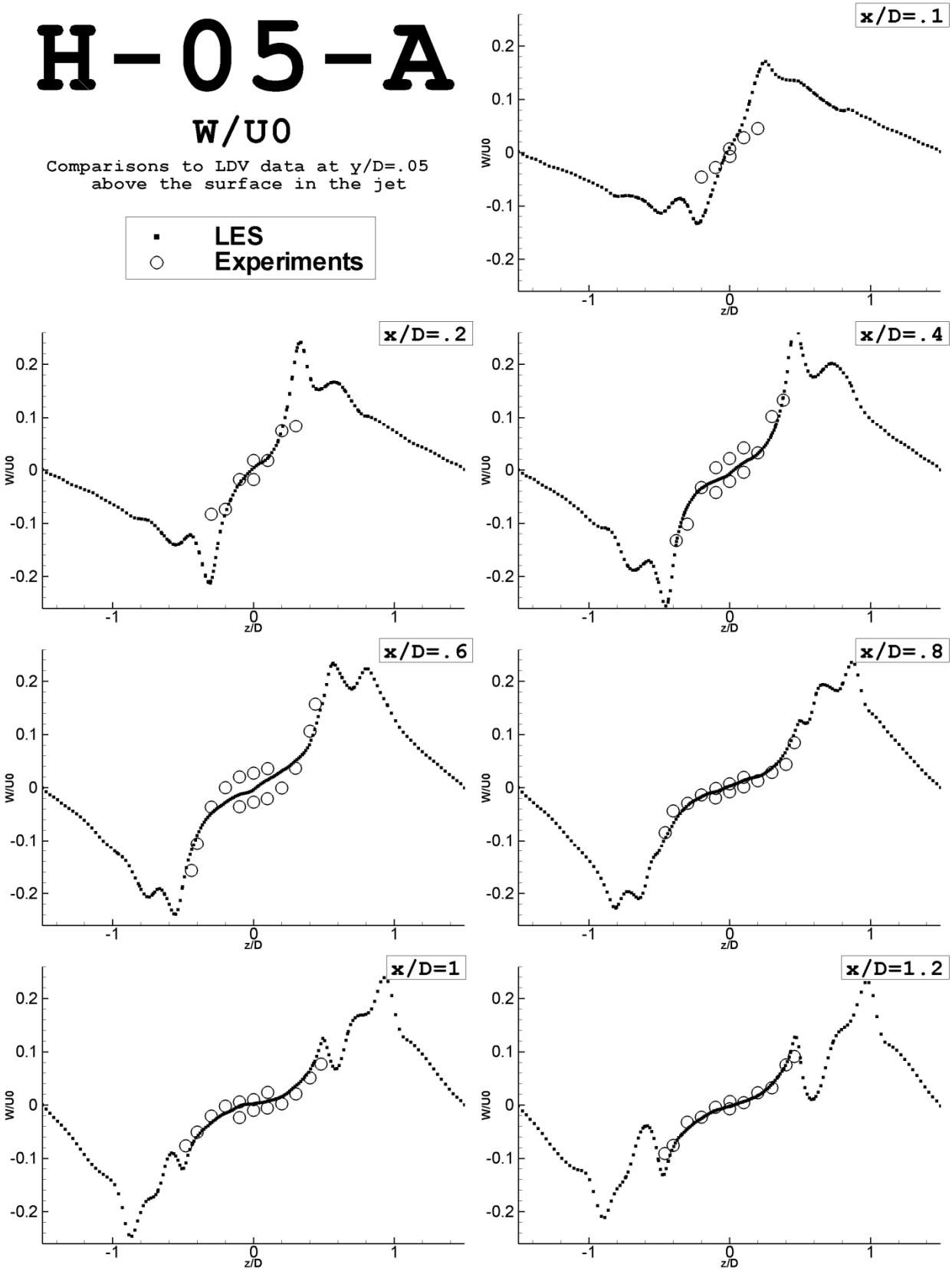

Figure 0.25: Blowing Ratio 0.5, L/D 3.5, w velocity

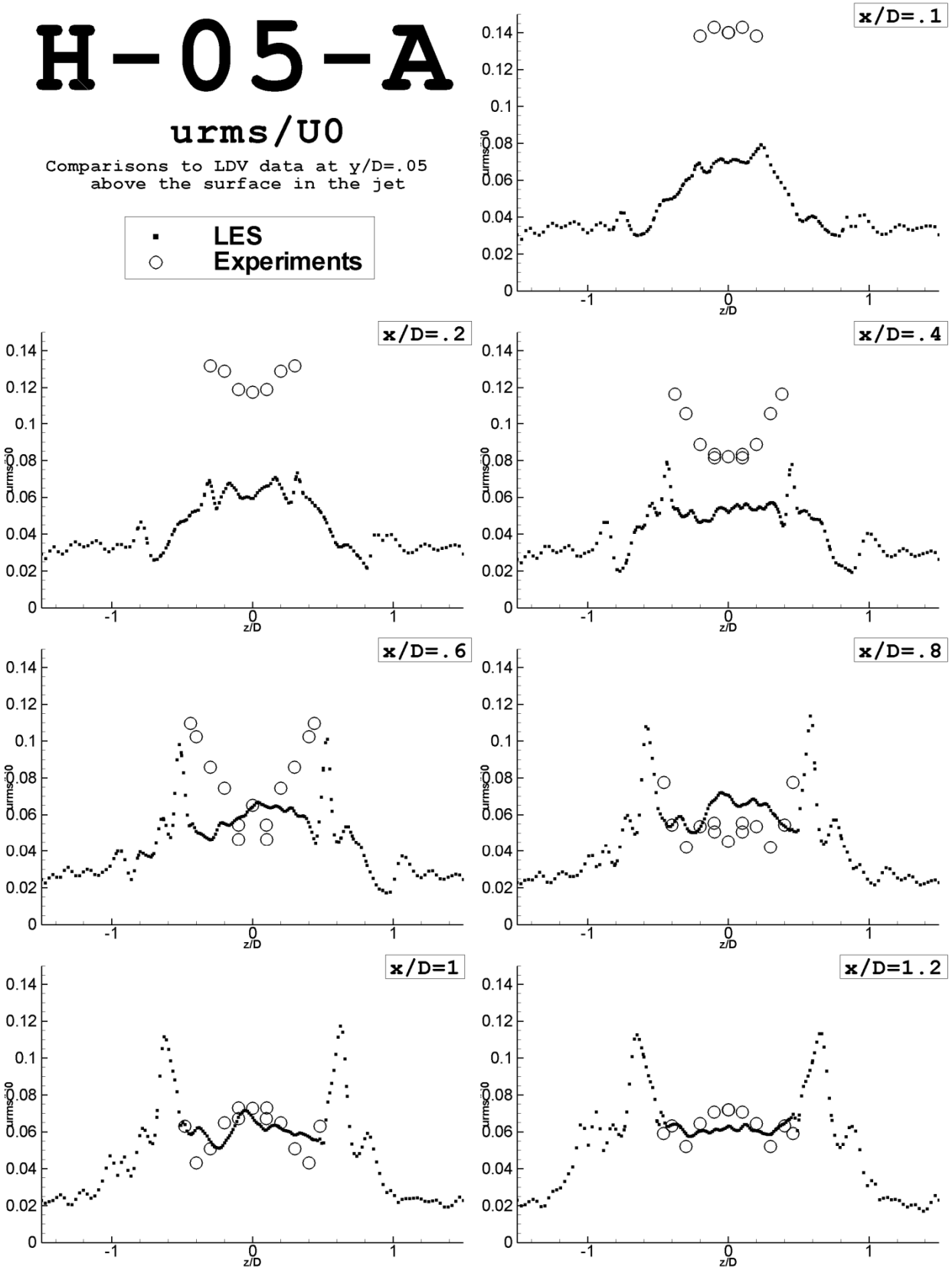

Figure 0.26: Blowing Ratio 0.5, L/D 3.5, root mean square of u velocity

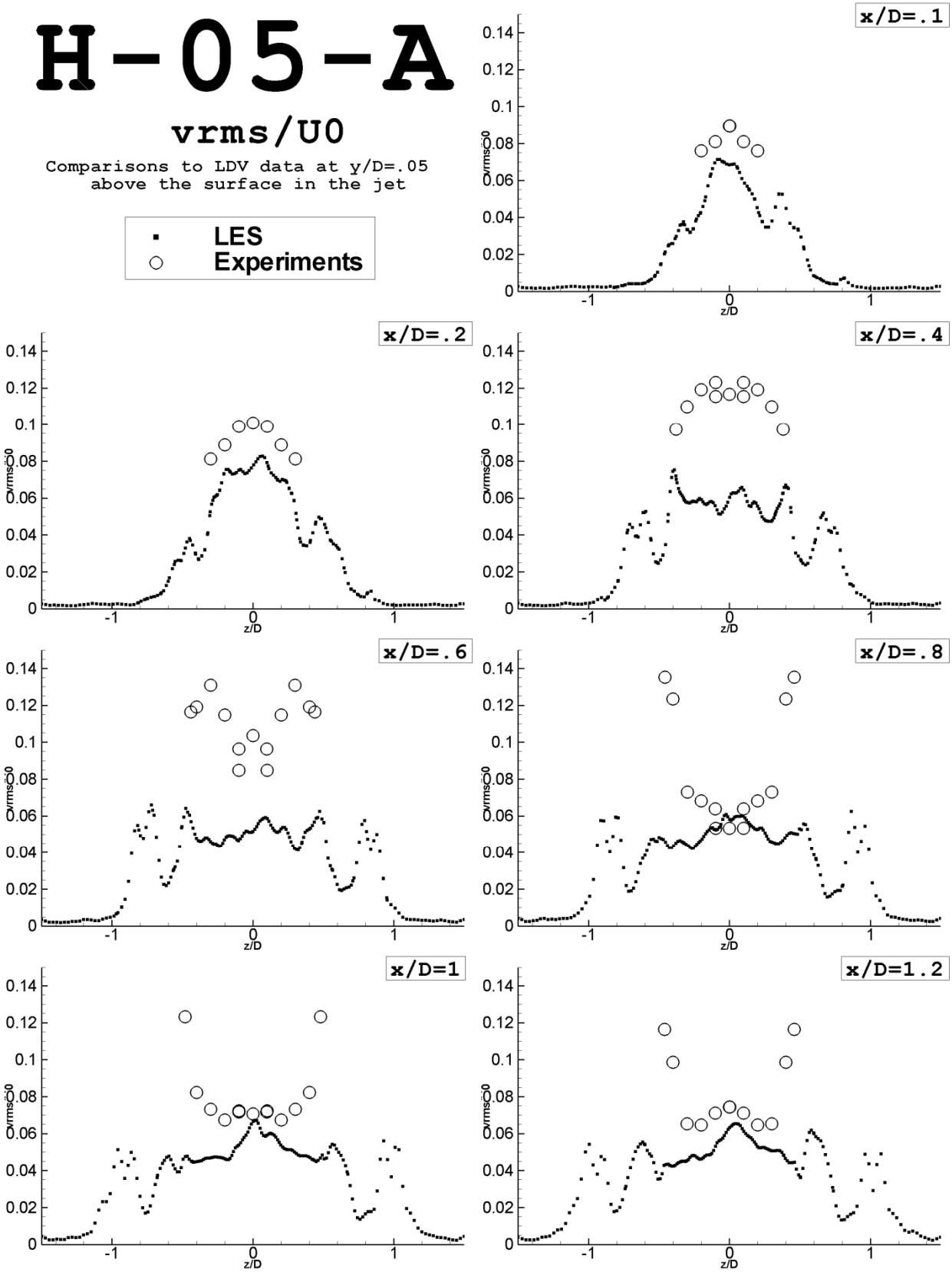

Figure 0.27: Blowing Ratio 0.5, L/D 3.5, root mean square of v velocity

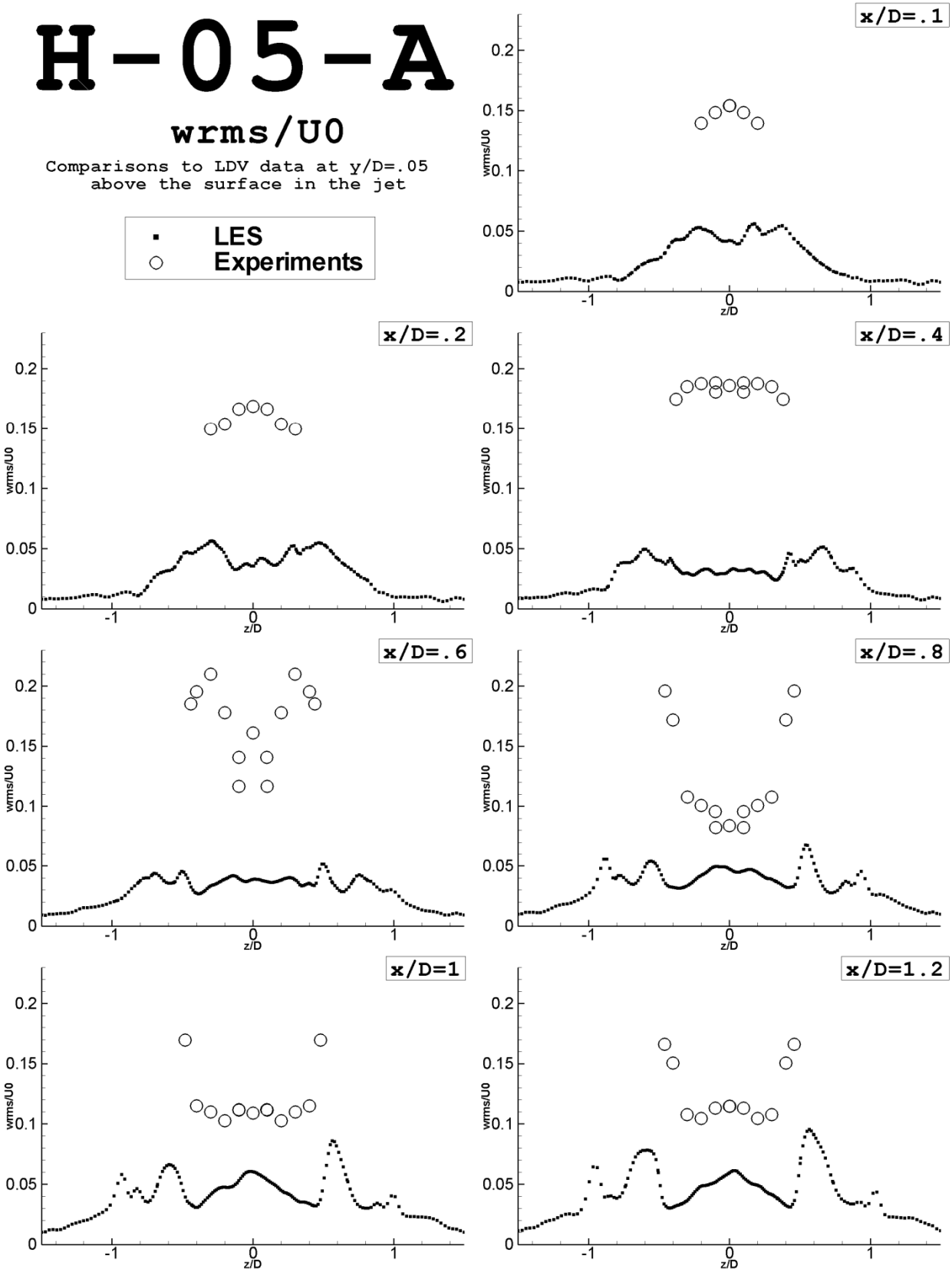

Figure 0.28: Blowing Ratio 0.5, L/D 3.5, root mean square of w velocity

Appendix C: Turbulence Plots

These are additional plots showing contours of turbulence at various locations in each case. The x-slice contours are shown stacked vertically from top to bottom at x/d locations of 1, 3, 5, and 10. Each figure is labeled by run name, and these may be referenced in Table 3.1 and Table 3.2.

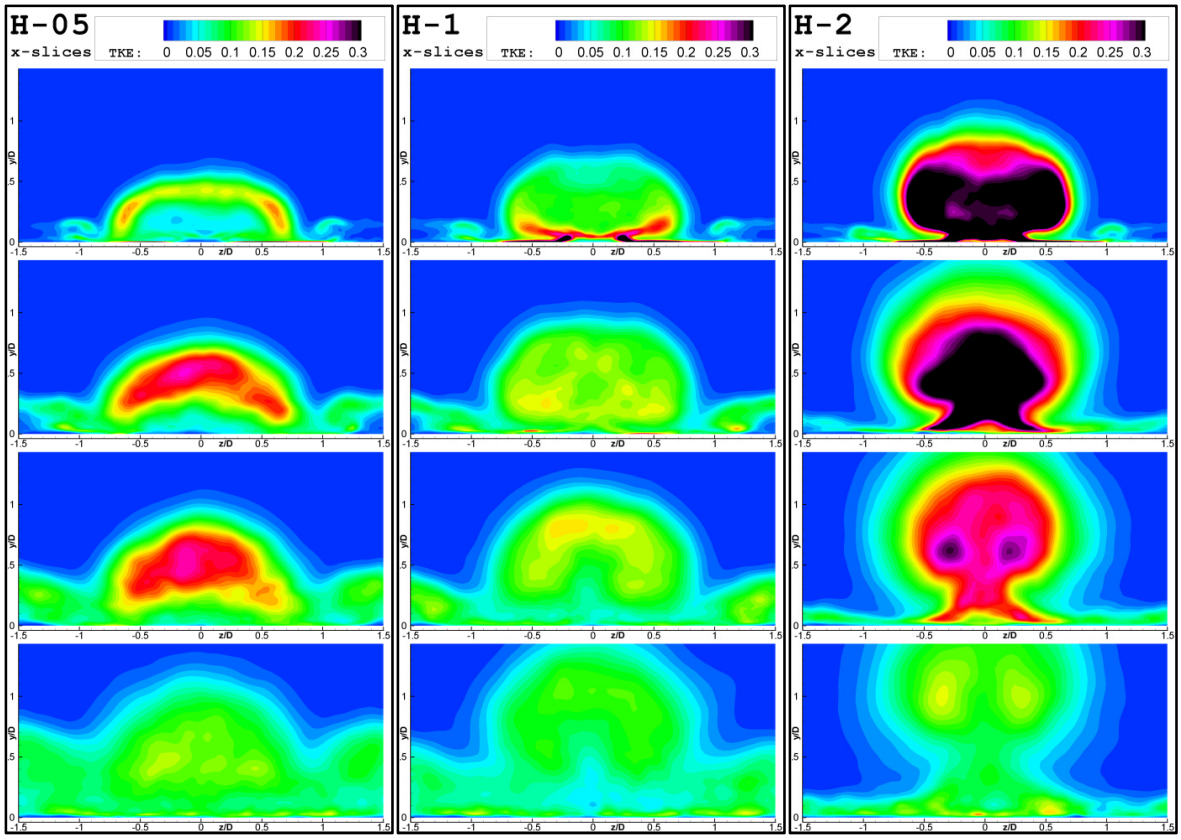

Figure 0.29: Turbulent kinetic energy x-slice contours – Cylindrical hole, L/D=3.5

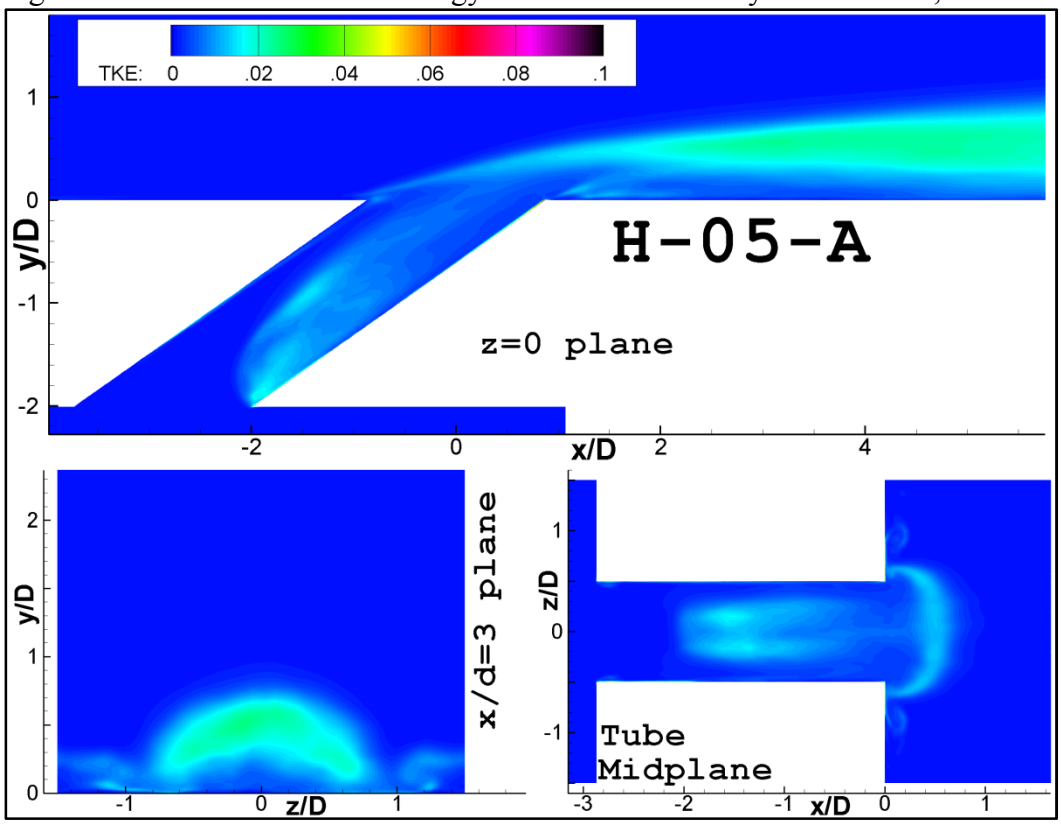

Figure 0.30: Turbulent kinetic energy plots – Cylindrical hole, L/D=3.5, BR=0.5

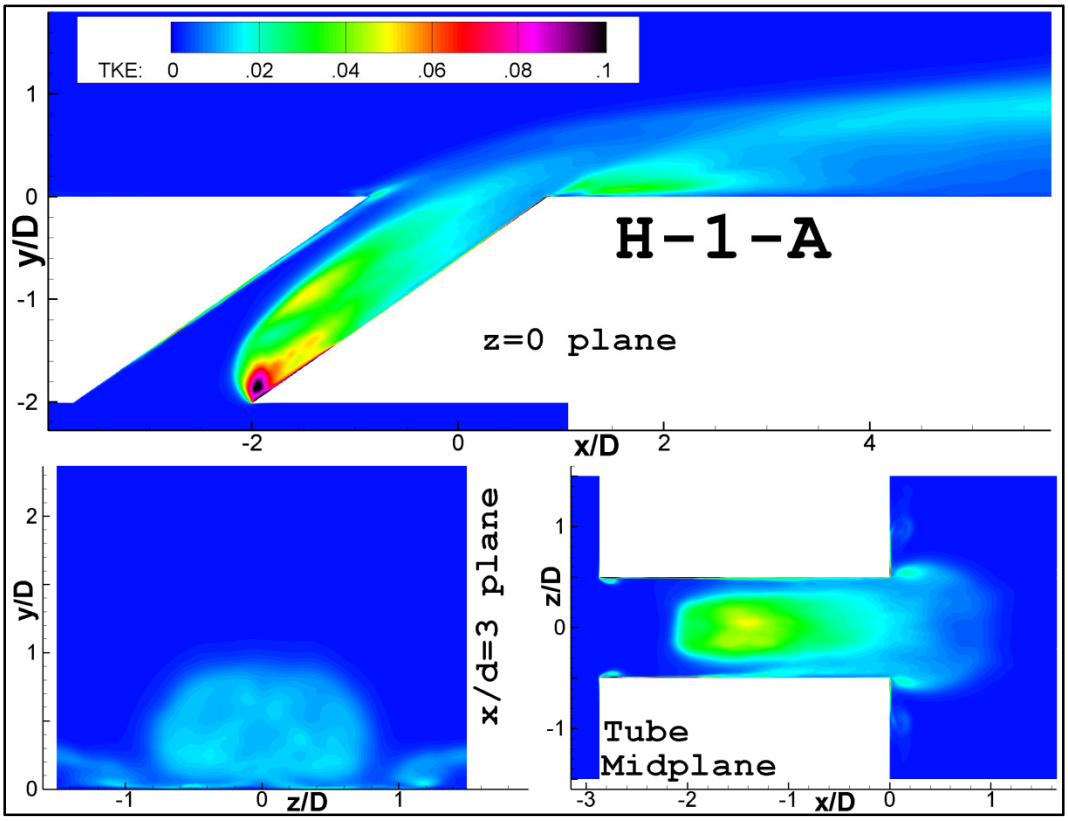

Figure 0.31: Turbulent kinetic energy plots – Cylindrical hole, L/D=3.5, BR=1

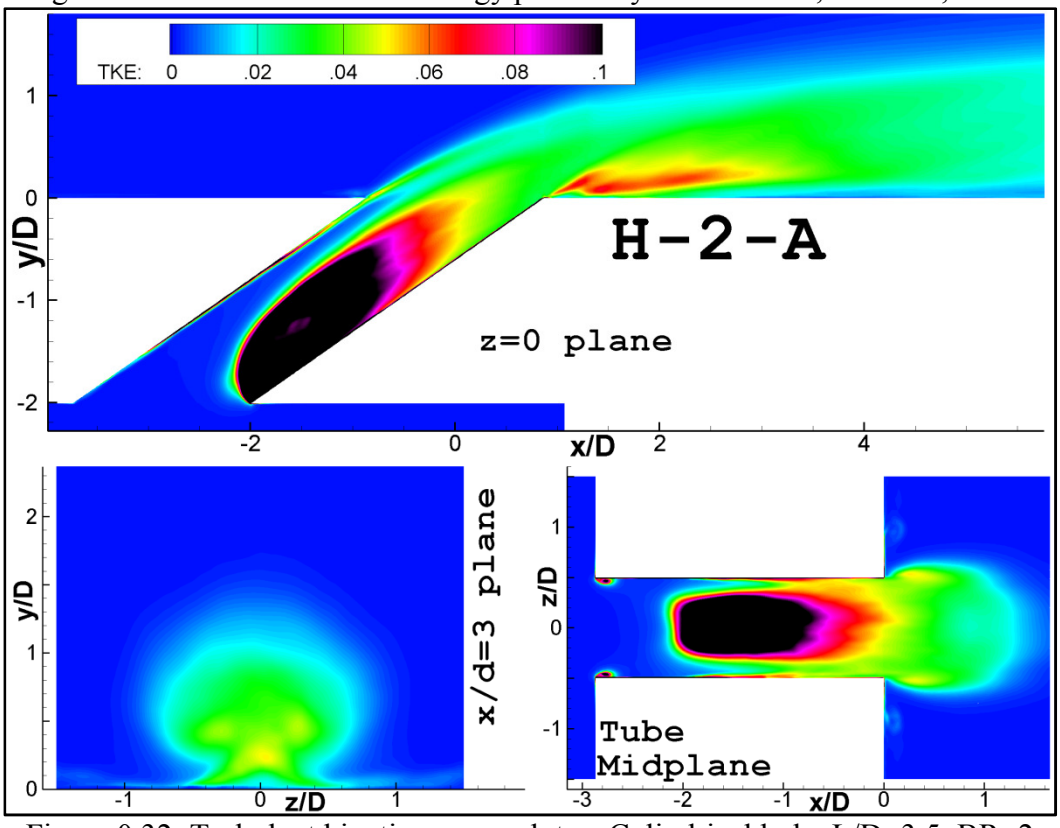

Figure 0.32: Turbulent kinetic energy plots – Cylindrical hole, L/D=3.5, BR=2

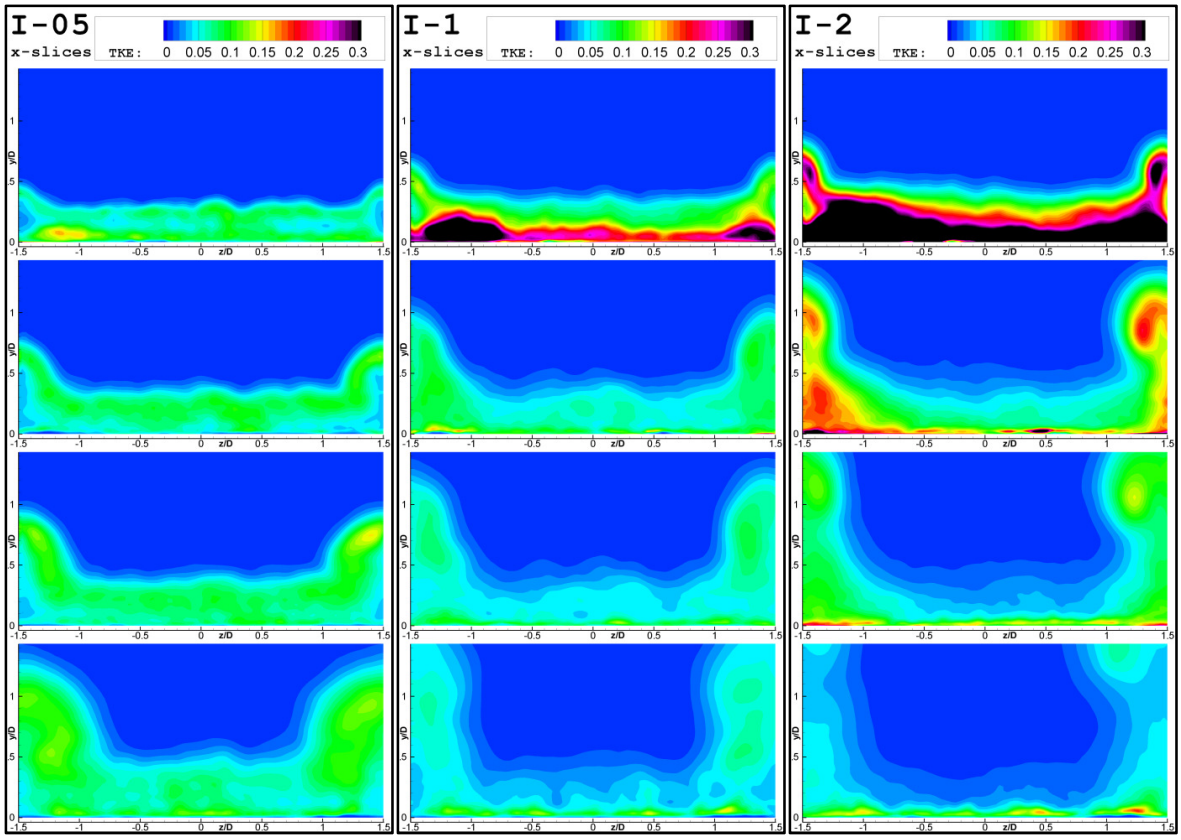

Figure 0.33: Turbulent kinetic energy x-slice contours – Console hole

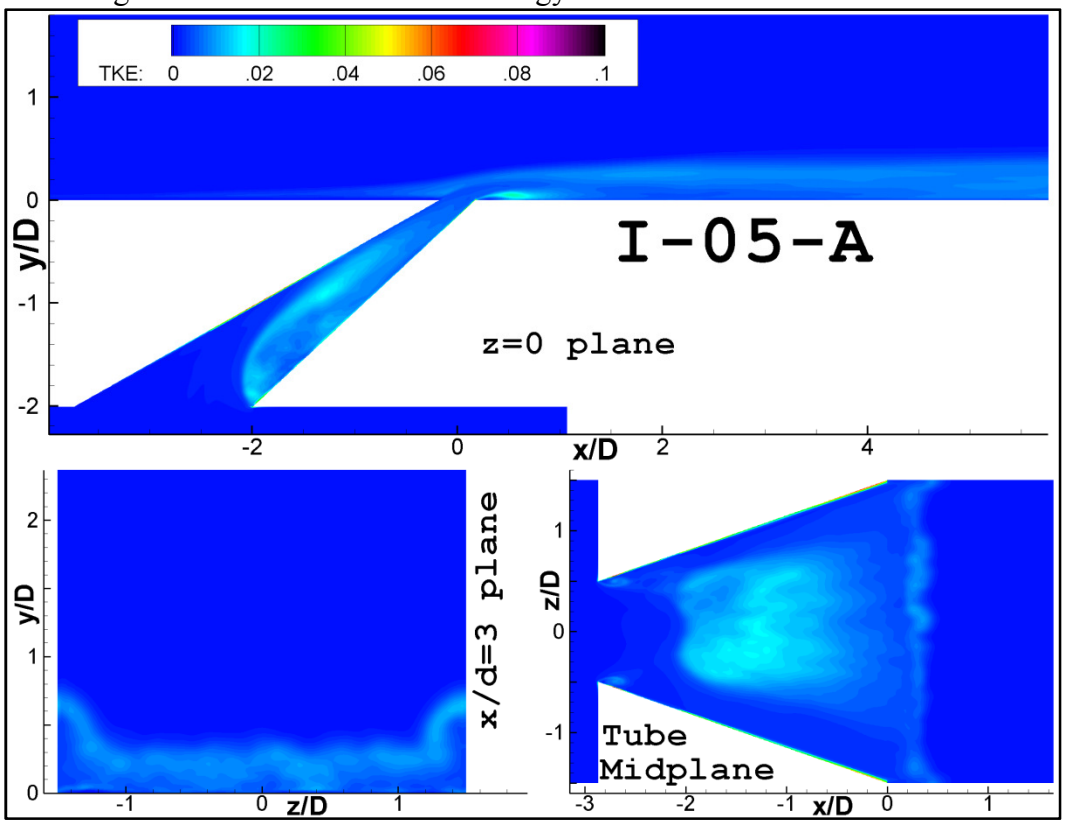

Figure 0.34: Turbulent kinetic energy plots – Console hole, BR=0.5

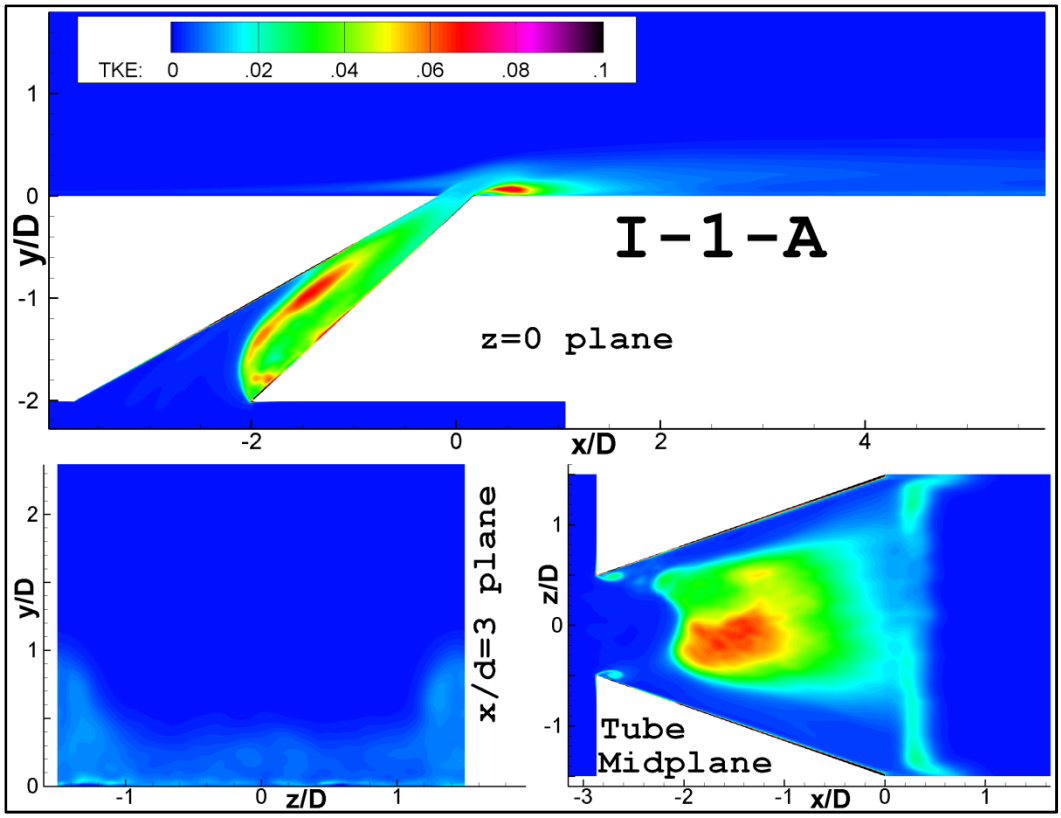

Figure 0.35: Turbulent kinetic energy plots – Console hole, BR=1

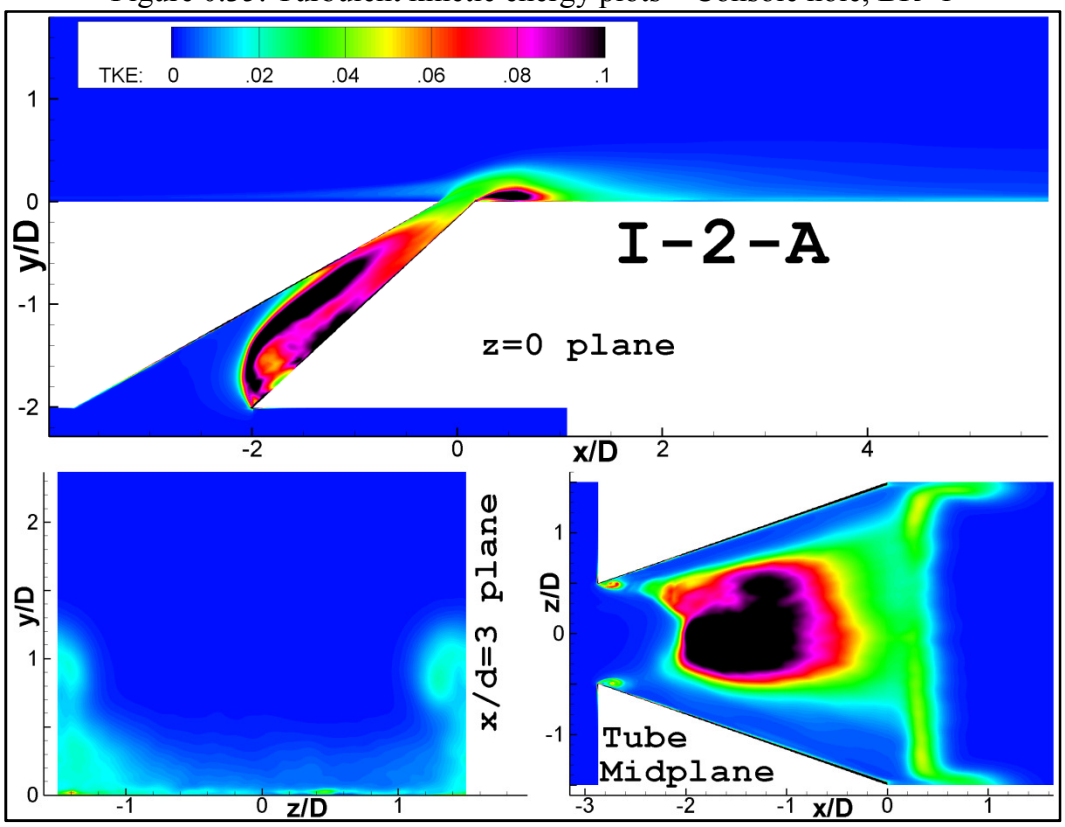

Figure 0.36: Turbulent kinetic energy plots – Console hole, BR=2

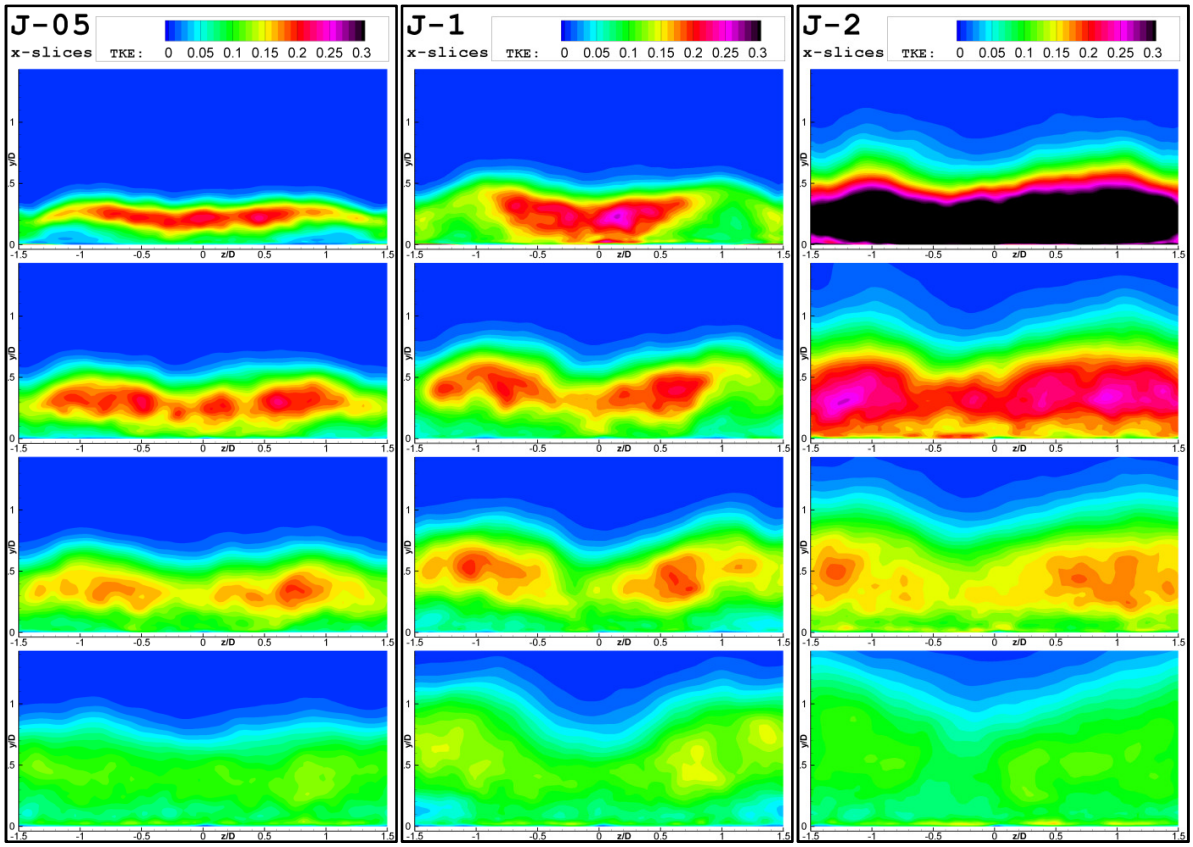

Figure 0.37: Turbulent kinetic energy x-slice contours – Laterally diffused hole

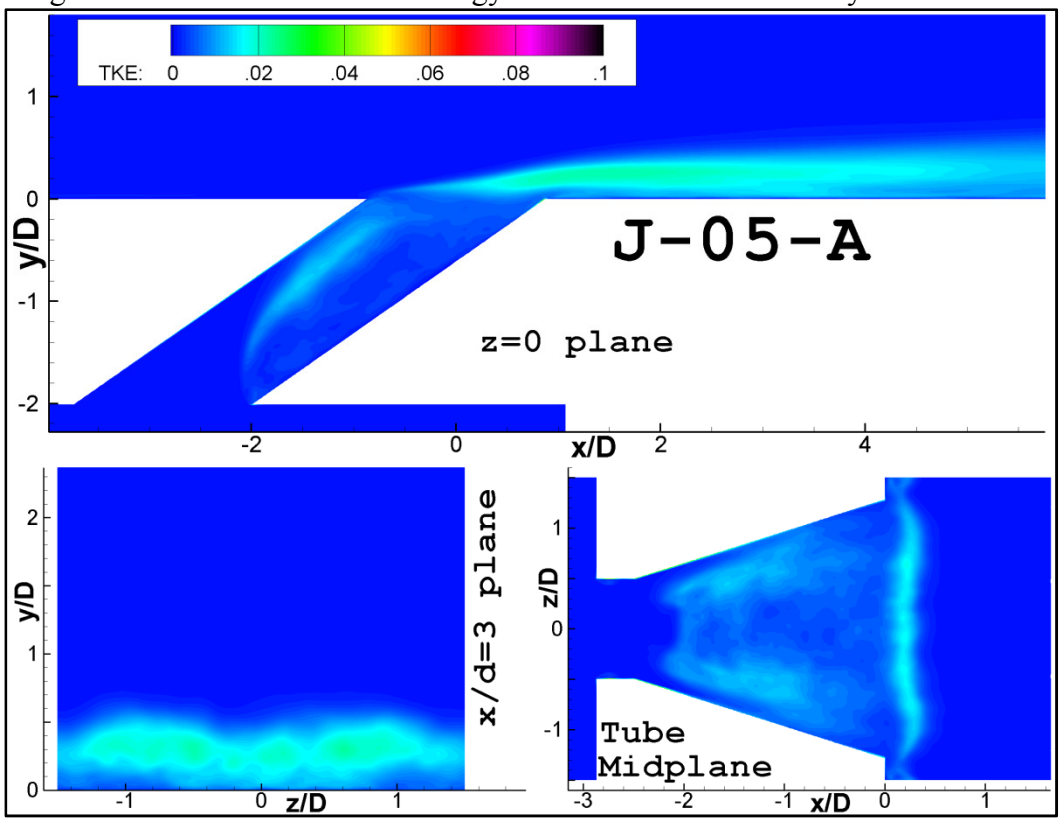

Figure 0.38: Turbulent kinetic energy plots – Laterally diffused hole, BR=0.5

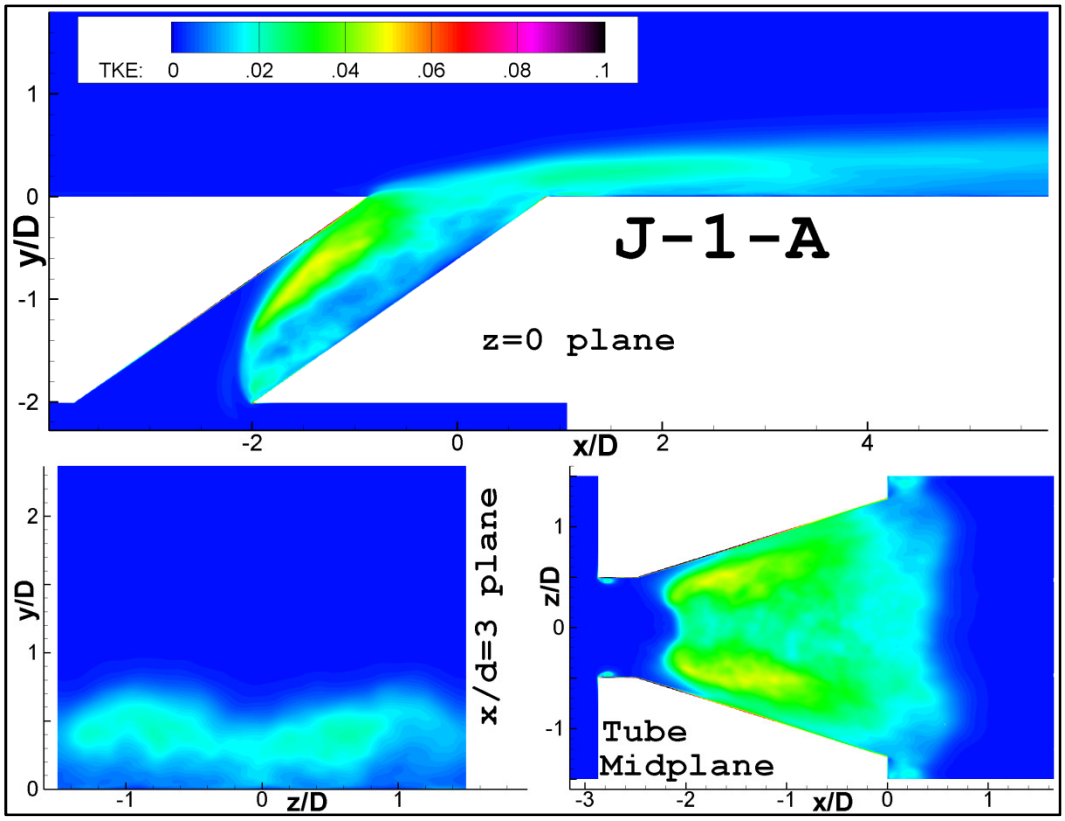

Figure 0.39: Turbulent kinetic energy plots – Laterally diffused hole, BR=1

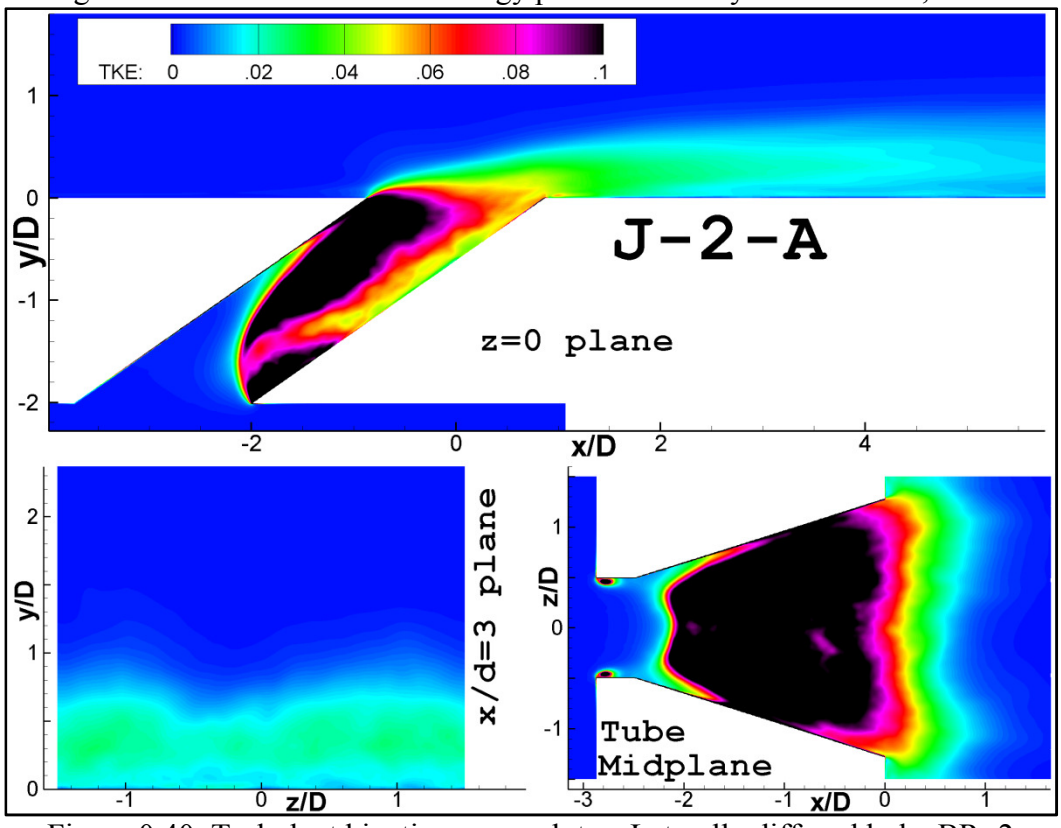

Figure 0.40: Turbulent kinetic energy plots – Laterally diffused hole, BR=2

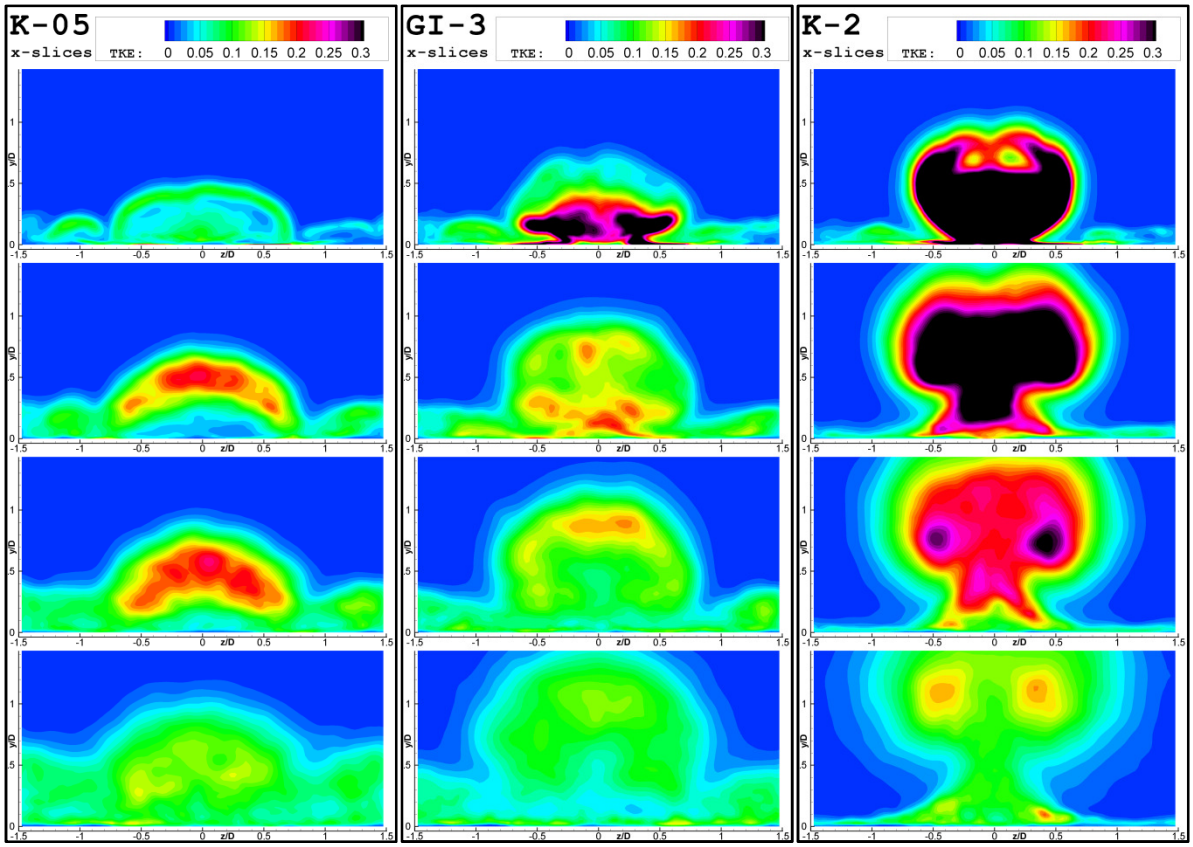

Figure 0.41: Turbulent kinetic energy x-slice contours – Cylindrical hole, L/D=1.75

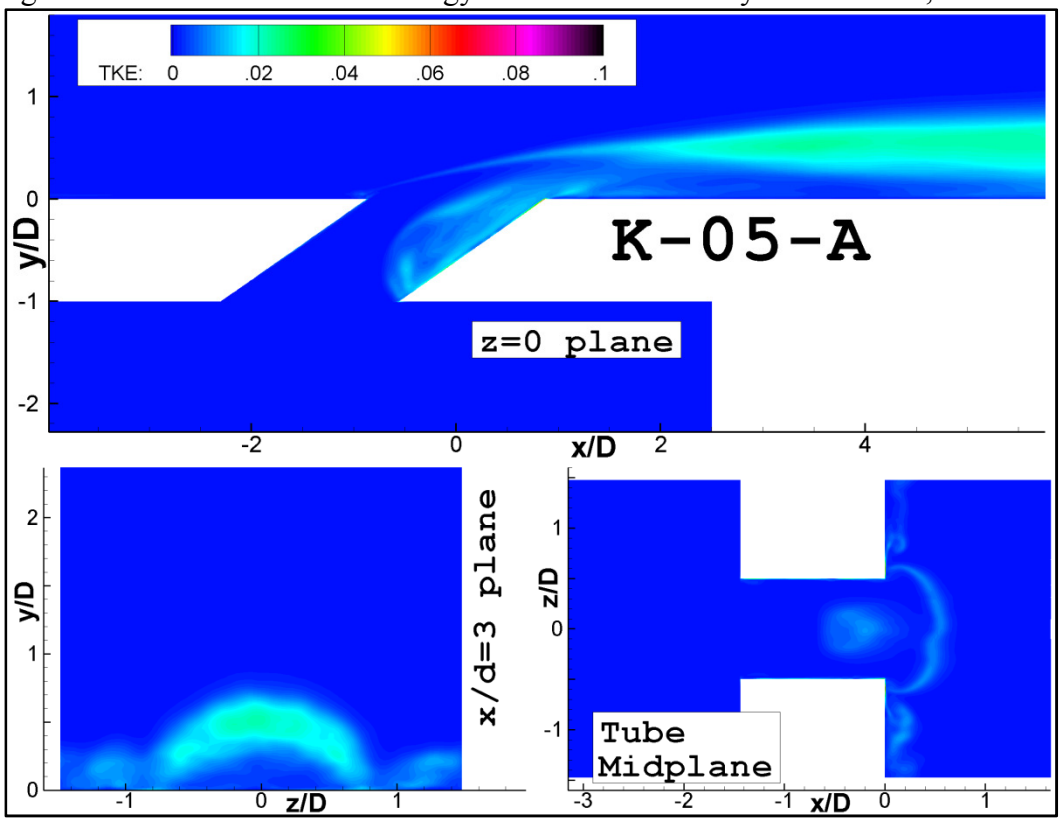

Figure 0.42: Turbulent kinetic energy plots – Cylindrical hole, L/D=1.75, BR=0.5

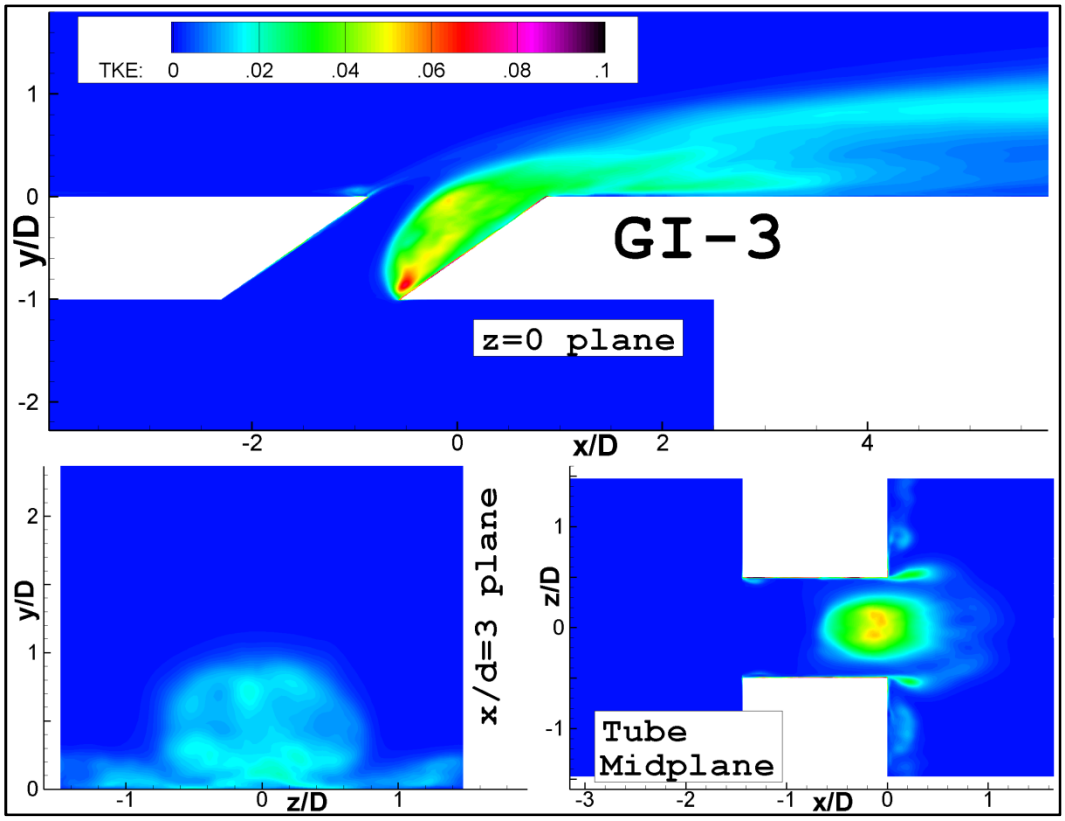

Figure 0.43: Turbulent kinetic energy plots – Cylindrical hole, L/D=1.75, BR=1

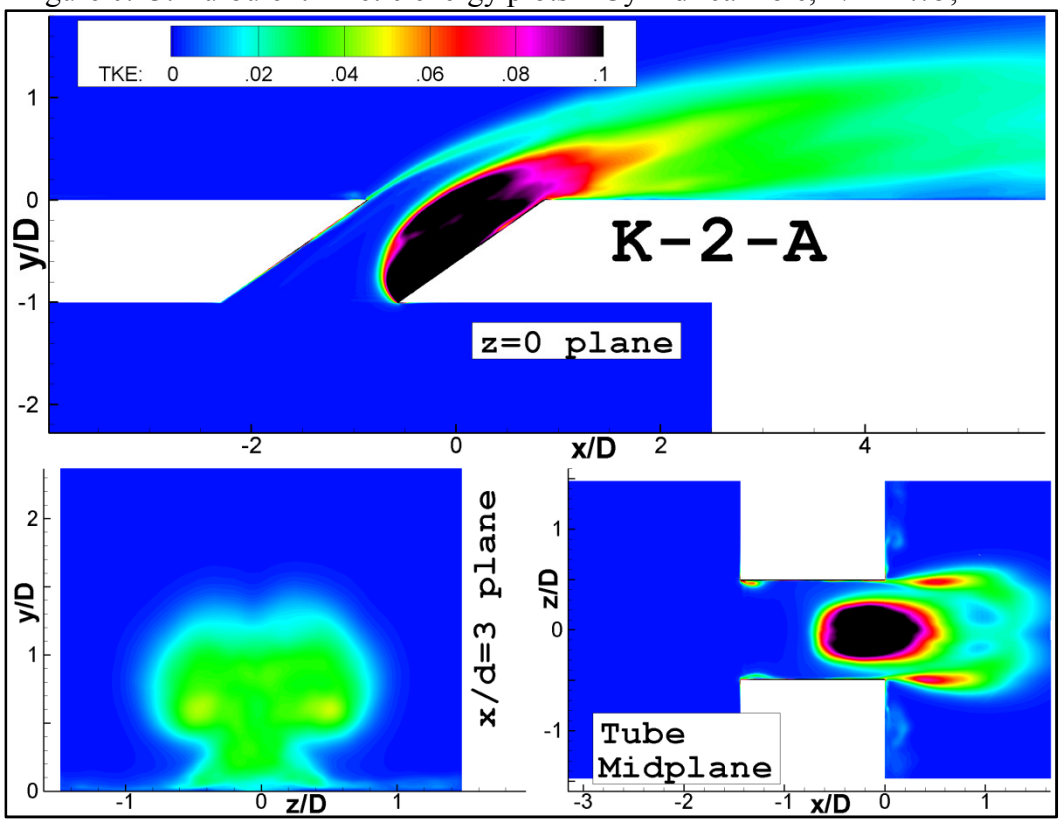

Figure 0.44: Turbulent kinetic energy plots – Cylindrical hole, L/D=1.75, BR=2

Vita

David Houston Leedom was born in Denison, Texas in December 1984 to parents David Lawrence Leedom and Linda Lee Leedom. He attended primary school in Bossier City, Louisiana and Shreveport, Louisiana, graduating from Airline High School in May 2003 with his private pilot certificate. He then moved to Baton Rouge, Louisiana to pursue a bachelor's degree, interning at TAC Air Shreveport (as a flight line technician), at the 93rd Bomb Squadron at Barksdale AFB (as a GS-3), and Lockheed Martin Aeronautics Company in Fort Worth, Texas (as an engineering intern in F-16 flight test) over summers. He was involved in the LSU Formula SAE car efforts, raced shifter karts, and performed at air shows in a Pitts Special. He received his Bachelor of Science in Mechanical Engineering from Louisiana State University in May 2007, graduating *cum laude* and with his instrument rating. He continued studies and research at Louisiana State University, and obtained his Master of Science in Mechanical Engineering in May 2009 with his commercial pilot certificate.